Frontiers of Biomechanics 2

Yoshitaka Kameo
Ken-ichi Tsubota
Taiji Adachi

Bone Adaptation

In Silico Approach

Springer

Frontiers of Biomechanics

Volume 2

Aims and Scope:

Biomechanics is a rapidly expanding field that focuses on exploring the mechanics of structure–function relationships underlying the functionality of living systems with the aim of gaining insights for medical applications. The field cuts across diverse disciplines: physics, biology, medicine, mechanical engineering, and biomedical engineering, and incorporates principles and concepts from these fields in the study of living systems and their dynamics.

A major objective of this series is to pioneer new frontiers of biomechanics by including concepts and ideas from new research frontiers yet to be addressed within the existing paradigm of biomechanics. The series highlights the role of mechanics in the realization of multicomponent and hierarchical interactions that characterize living systems, based on the context of open systems. The series also presents in-depth coverage of cutting-edge research in frontiers of biomechanics that explores fundamental concepts of what constitutes life, based on mechanics as an entity of energy principles and information science. It is hoped that this series will develop as an open system (analogous to living systems) that is admissible of future research dynamics and expansion in the field of biomechanics.

Distinctive features of the series:

- Each volume will cover core topics in the frontiers of biomechanics.
- The series will be multidisciplinary in that it will consist of volumes written by authors who are at the forefront of research in diverse fields including physics, mechanical engineering, biology, and medicine.
- Each volume will place emphasis on not only providing readers with new knowledge and techniques in biomechanics, but also presenting the underlying concepts and principles concisely and precisely so that the readers are able to discern unresolved and challenging problems in biomechanics.
- The series aims to contribute to further expansion and development of the field of biomechanics by including concepts and ideas from new research frontiers yet to be addressed within the existing paradigm of biomechanics.

More information about this series at http://www.springer.com/series/13453

Yoshitaka Kameo • Ken-ichi Tsubota
Taiji Adachi

Bone Adaptation

In Silico Approach

Springer

Yoshitaka Kameo
Institute for Frontier Life
and Medical Sciences
Kyoto University
Kyoto, Japan

Taiji Adachi
Institute for Frontier Life
and Medical Sciences
Kyoto University
Kyoto, Japan

Ken-ichi Tsubota
Graduate School of Engineering
Chiba University
Chiba, Japan

ISSN 2199-8515 ISSN 2199-8523 (electronic)
Frontiers of Biomechanics
ISBN 978-4-431-56512-3 ISBN 978-4-431-56514-7 (eBook)
https://doi.org/10.1007/978-4-431-56514-7

Library of Congress Control Number: 2017954322

This Springer imprint is published by Springer Nature
The registered company is Springer Japan KK
The registered company address is: Shiroyama Trust Tower, 4-3-1 Toranomon, Minato-ku, Tokyo 105-6005, Japan

Preface

For centuries, what is life has remained a central question in life science. This series highlights living systems as open systems emerging from multicomponent and hierarchical interactions and the role of mechanics in the realization of such systems. It covers cutting-edge research in the new frontiers of biomechanics that explores the fundamental concepts of what constitutes life, based on principles of energy and information.

Traditionally, biomechanics has been concerned mainly with the dynamics of biological bodies and mechanical behaviors of tissues, cells, and biomolecules. Recently, the field has progressed to incorporate multiscale structure-function relationships that underlie biological phenomena. To contribute to the further development of biomechanics, this series aims to explore the core concepts of "what makes life what it is" and how the functionality of dynamical living systems are realized and maintained. Consequently, the series attempts to answer the question, "what is life?"

Taking a keen look at our life from birth to death highlights the following observations:

- First, development and growth of a living organism occur through highly orchestrated multiple morphogenetic events including cell division, proliferation, and differentiation that initiate tissue/organ formation. These processes evolve systematically right from conception to maturity, giving rise to a fully formed and functional organism.
- Second, living systems maintain their structure and functionality through elaborate homeostatic processes, and they possess adaptive capabilities such as wound healing and remodeling that enable them to adapt and respond to changes in their surroundings.
- Third, living systems, such as humans, succumb to diseases, infections, or injuries that lead to system breakdown and subsequent loss of functionality or even death.

Overall, these phases in a life cycle of a living system involve mechanical processes at different spatiotemporal levels and result from coupling interactions between mechanical and biochemical processes. Biomechanics dealt with in this series is concerned with quantitative analyses and approaches aimed at elucidating the fundamental mechanisms that underlie these coupling interactions that collectively build living systems.

Considering that a living system is an open system exchanging energy and mass with its surroundings, the processes outlined above are dynamical in nature and comprise both linear and nonlinear and stable and unstable events and bifurcation processes that lead to "emerging selectivity," which determines how the sequences of events occurring in living systems emerge from dynamical complexities with large degrees of freedom. In such a dynamical open system, the most intrinsic processes are those mediated by the complex and spatiotemporally hierarchical interactions among the numerous system components.

Interestingly, mechanical phenomena are inherent in the dynamics of complex living systems and play important roles in the emergence of order that makes life what it is. Thus, a mechanistic approach is fundamental to understanding living systems. Mechanics referred to here is not just the classical Newtonian mechanics dealing with forces but, in a broader sense, one that encompasses areas ranging from statistical thermodynamics and electromagnetism to quantum mechanics. Research involving these energy-based disciplines will in the near future become multidisciplinary and ultimately yield new disciplines that treat life as a creation of information.

From the viewpoint of structural dynamics, thermodynamics, and fluid dynamics, the analyses of a living system based on the principles of energy and mass will naturally extend to include physical as well as biological information. This will enable the formulation of more descriptive models for a better understanding of the complex biological interactions, such as genetic transcription network, cell signaling cascade, and cell-cell communication, and the dynamics of macroscopic living systems.

A major objective of this series is to pioneer new frontiers of biomechanics by including concepts and ideas from new research frontiers yet to be addressed within the existing paradigm of biomechanics. In other words, the series presents a novel energy- and information-based perspective of life that extends from the classical energy-based understanding. We believe that this series will make a strong contribution toward the expansion of our understanding of "interactions and feedbacks" that are necessary for adaptive responses exhibited by living systems.

A future milestone of the series is to understand complex open systems, such as the brain, the nervous system, and the immune system: systems that are born and maintained homeostatically based on energy and information and whose functionality changes dynamically through the interaction with the surrounding environment. In this regard, the series is intended to develop as an open system (analogous to living systems) that is admissible of future research dynamics and expansion in the field of biomechanics.

Physical forces play an essential role in establishing and maintaining the vital functions of our bodies. It is well known that a variety of biological processes in living organisms, such as cell differentiation, morphogenesis, growth, remodeling, and regeneration, are largely regulated by mechanical factors. The skeletal system, a leading topic of research, has been studied for several years with the objective of identifying the contribution of physical forces in living systems. The skeletal system has a remarkable ability to adapt its structure and function to its mechanical environment via continual remodeling and regeneration. In light of the progress made through state-of-the-art research in this field, the principal objective of this book is to initiate a discussion on skeletal mechanics by elucidating bone adaptation through the lens of in silico modeling.

The sophisticated bone structure of the human body is a result of the collaborative activities of numerous bone cells that interact with their mechanical environment. It is extremely important to understand the mechanism underlying the self-organized regulation of bone adaptation, both from the clinical and scientific points of view. Maintenance of the load-bearing function of the skeleton over the lifetime of an individual is critical to preventing locomotive syndrome caused by osteoporosis and osteoarthritis in our aging society. Furthermore, an abnormality in the skeletal and immune systems—collectively known as osteoimmunology—triggers bone destruction associated with rheumatoid arthritis. To deal with such serious health problems that can significantly affect the quality of life, it is crucial to investigate the cellular mechanism underlying bone adaptation. This approach would provide a deeper understanding of the well-organized dynamics of living systems that emerge from complex cellular interactions. This can also provide a clue toward answering the question, "What makes life what it is?"

Recent advances in cellular and molecular biology, along with improved imaging techniques and omics technologies such as genomics, transcriptomics, and proteomics, have revealed single-cellular and multi-cellular activities associated with bone adaptation and their underlying molecular mechanisms via complex intercellular signaling. In addition to the experimental approach, the parallel usage of mathematical modeling and computer simulation has remarkably enhanced our understanding of bone adaptation by linking cellular and molecular dynamics to organ and tissue behaviors. Such active research has accelerated the development of novel technologies and drugs toward the treatment of bone diseases. Thus, even though studies of the bone fall under the category of classical research, these continue to raise important and intriguing questions on the intrinsic nature of living systems.

This book focuses on the systems biomechanics of bone adaptation through remodeling that provides a multiscale model for it, spanning the cellular, tissue, and organ levels. The mathematical model explained in each section provides concrete examples of *in silico* approaches for bone adaptation. It will be immensely useful for readers interested in bone morphology and metabolism and will serve as an effective bridge connecting mechanics, cellular and molecular biology, and medical sciences. These *in silico* approaches toward exploring the mechanisms by which the functioning of dynamic living systems is established and maintained have potential

for facilitating the efforts of graduate students and young researchers pioneering new frontiers in biomechanics. The authors sincerely hope that this book will evoke a "eureka" moment for readers and, as an added incentive, they will enjoy reading its contents.

We would like to acknowledge the following students, colleagues, and mentors for their contributions to this book. It is our pleasure to thank Hiroshi Kamioka and Jenneke Klein-Nulend for imaging a single osteocyte canaliculus and revising Chap. 2 of the manuscript. We wish to express our gratitude to Masaki Hojo for the valuable comments and useful suggestions provided for Chaps. 3, 4, 5, and 13. We are grateful to Narumichi Sato for imaging the lacuno-canalicular porosity in Chap. 4. We are also grateful to Yoshihiro Tomita for his continuous support and useful discussions regarding computational modeling in Chaps. 8, 11, 12, and 14. We sincerely thank Masao Tanaka for the helpful comments on Chap. 8. We thank Hiroshi Sakaue for developing mathematical models and computing codes and for gathering and analyzing numerical data for Chap. 8. We would like to express our gratitude to Scott J. Hollister for his valuable comments on Chap. 11. We also thank Tomonori Yamada and Yusuke Suzuki for developing computing codes and gathering numerical data and Akitake Makinouchi for his continuous support toward Chap. 13.

Kyoto, Japan — Yoshitaka Kameo
Chiba, Japan — Ken-ichi Tsubota
Kyoto, Japan — Taiji Adachi

Contents

Chapter 1
Overview: *In Silico* Approaches to Understand Bone Adaptation

Abstract In this chapter, we provide an overview of our *in silico* modeling approaches based on a bottom-up perspective to understanding bone adaptation. For investigating the underlying cellular mechanism, we propose a mathematical model of trabecular bone remodeling that considers cellular mechanosensing and intercellular communication. Through remodeling simulations, this model is able to explain the phenomenological remodeling law to achieve locally uniform mechanical states at the tissue level. Furthermore, we present a model for trabecular surface remodeling based on the hypothesis that bone remodeling is driven by the local non-uniformity of stress distribution on the trabecular surface. The trabecular remodeling simulations incorporating this phenomenological model can successfully represent the functional adaptation of the trabecular architecture from the tissue level to the organ level.

Keywords Bone adaptation • Mechanical hierarchy • Mathematical model • Cell • Tissue • Organ

1.1 Introduction

Bone is a hard tissue that supports the body's weight and protects the various organs within the body. The internal structure and external form of bone adapt continually to the mechanical environment by remodeling and maintain its strength as a load-bearing organ. If long bones such as the femur and tibia were sliced open, cancellous bone would be found with an intricate network structure consisting of multiple trabeculae. This structure may be reminiscent of the well-designed supporting framework of buildings. Although the close relationship between the trabecular orientation and the applied mechanical load is generally recognized, how the functional bone structure is formed through remodeling is still an enigma. Clarifying the mechanism of bone adaptation is an important and fascinating problem not only in the fields of biology and medical sciences, but also in mechanics and engineering.

The earliest mechanical interpretation of bone structure dates back to *Wolff's Law*, often known as the law of bone transformation, which states a mathematical correspondence between trabecular arrangement and principal stress trajectories

Y. Kameo et al., *Bone Adaptation*, Frontiers of Biomechanics 2,
https://doi.org/10.1007/978-4-431-56514-7_1

(Brand 2010; Duda et al. 2010; Wolff 1870, 2010). The ability of bone to align its trabeculae with stress trajectories was interpreted as a self-regulated functional adaptation by remodeling (Roux 1881). For the quantitative evaluation of Wolff's doctrine, a number of *in vivo* experiments investigated the adaptive changes of bone under controlled mechanical conditions (Goldstein et al. 1991; Guldberg et al. 1997a, b). In parallel to the experimental works, several theories to account for bone adaptation have been proposed. An adaptive elasticity theory developed by Cowin and Hegedus (1976) is one of the successful continuum theories to describe an elastic material that adapts its structure to the applied load. According to this theory, a rate equation of bone morphological changes could be described as a function of mechanical stress/strain (Hegedus and Cowin 1976). While in their analytical study, bone structure and mechanics were simplified, computer simulations enabled us to handle more complex spatial and temporal information with remarkable improvements in our quantitative understanding of bone adaptation. Carter et al. (1987) and Huiskes et al. (1987) proposed a finite element procedure to predict the relationships between trabecular bone density and mechanical loading based on their own adaptive bone remodeling theories. These density-based simulation models were later extended to investigate the morphological changes in individual trabeculae as a result of bone adaptation (Mullender et al. 1994; Weinans et al. 1992). Thus, mathematical modeling and computer simulation—the so-called *in silico* approaches—have played an important role in the history of bone adaptation research. The objective of this book is to reconsider the underlying mechanism of bone adaptation through *in silico* approaches by taking into account up-to-date research findings ranging from those at the cellular level, to the tissue level, and up to the organ level.

The process of bone remodeling is intimately associated with the hierarchy of bone structure and function. Figure 1.1 shows the multiscale bone structure from the cellular level to the organ level. The remodeling in cancellous bone results from the repetition of bone resorption by osteoclasts and bone formation by osteoblasts on individual trabecular surfaces, which is called the remodeling cycle (Parfitt 1994). This coordinated activity is believed to be orchestrated by osteocytes buried in calcified bone matrix (Bonewald 2011; Dallas et al. 2013; Nakashima et al. 2011; Tatsumi et al. 2007), which account for about 90% of bone cells. From an anatomical point of view, the osteocyte network via slender cell processes housed in the lacuno-canalicular porosity seems to be suitable for sensing the surrounding mechanical environment (Cowin et al. 1991; Himeno-Ando et al. 2012; Sugawara et al. 2005). Moreover, the flow of interstitial fluid in the lacuno-canalicular porosity is considered to work as a mechanical cue that initiates an osteocytic response (Burger and Klein-Nulend 1999; Kameo et al. 2016; Weinbaum et al. 1994), as well as enhances the transport of signaling molecules (Ciani et al. 2014; Fritton and Weinbaum 2009; Price et al. 2011).

In order to comprehensively understand the entire process of bone functional adaptation by considering the intrinsic hierarchy ranging from the cellular level to the organ level, mathematical modeling and computer simulation have become more and more indispensable. In this chapter, we provide an overview of our

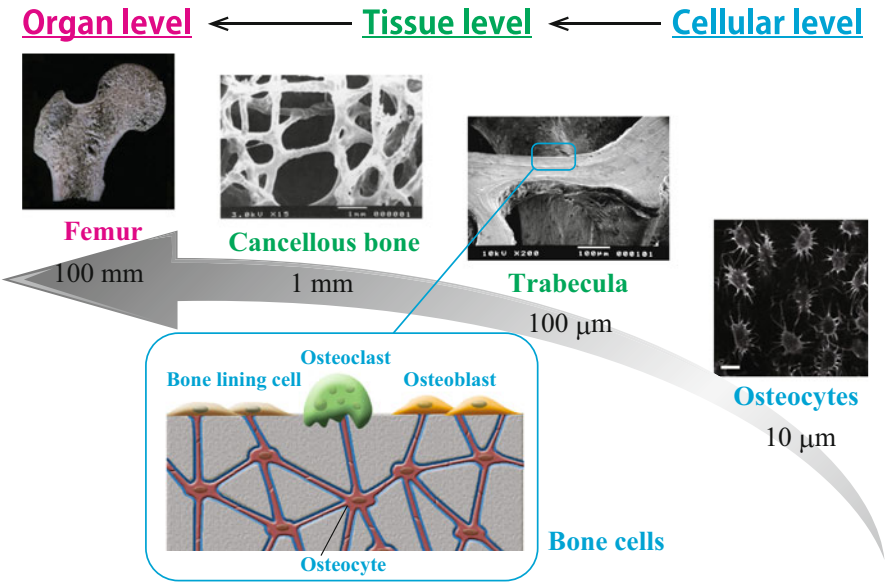

Fig. 1.1 Hierarchical structure of bone from cellular to organ level

multiscale modeling and *in silico* approaches based on a bottom-up perspective to investigate bone adaptation to mechanical load and the underlying cellular activities, as shown in Fig. 1.2. First, we introduce a mathematical model of trabecular bone remodeling that considers the cellular mechanical response to the interstitial fluid flow and intercellular communication in Sect. 1.2. Through the trabecular remodeling simulations at the tissue level, this model is shown to have the potential to represent the phenomenological law of bone transformation toward a locally uniform mechanical state of stress or strain in the trabecula. Next, based on the hypothesis that bone remodeling is driven according to the non-uniformity of local stress on the trabecular surface, we present a model to describe trabecular bone adaptation from the tissue level to the organ level in Sect. 1.3. The successful use of this phenomenological model is shown to reproduce highly organized trabecular architecture in whole bone. Finally, we present questions that remain unanswered and the future research directions.

1.2 Modeling Bone Adaptation from Cellular to Tissue Level

Bone adaptation is a biological event that results from cooperative metabolic activities of numerous bone cells influenced by mechanical environment. One of the most essential cellular activities that regulate bone adaptation is a mechanotransduction, i.e., the process by which mechanosensory cells transduce

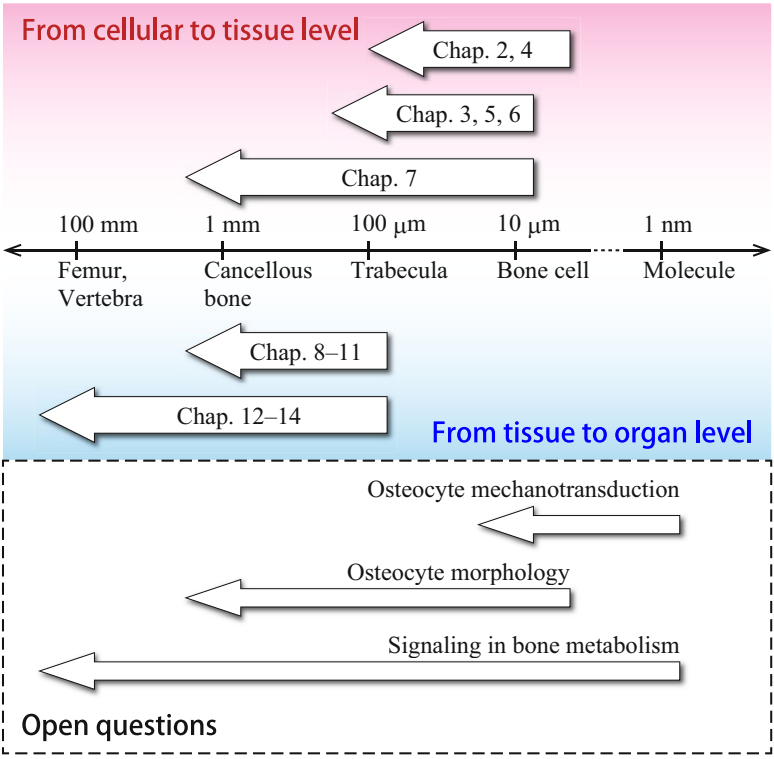

Fig. 1.2 Overview of multiscale modeling and *in silico* approaches

mechanical signals into biochemical signals. An experimental study using isolated osteocytes, which are considered to be mechanosensory cells, showed that the mechanosensitivity of the cell processes is higher than that of the cell bodies (Adachi et al. 2009b). However, there is still a significant gap between the strain required for cellular responses such as the influx of calcium ions or nitric oxide production ($\varepsilon = 1$–10%) and the strain in bone tissue caused by daily activities ($\varepsilon = 0.01$–0.1%). Taking into account this contradictory finding, interstitial fluid flow in the lacuno-canalicular porosity is thought to play an important role as an amplifier of mechanical stimuli given to osteocytes (Weinbaum et al. 1994).

To gain a deeper understanding of the multiscale bone adaptation, we have adopted a bottom-up perspective in which knowledge obtained at the microscopic scale is pieced together to reveal a macroscopic phenomenon. We visualized a single osteocyte process within a canaliculus and reconstructed a three-dimensional model with the help of ultra-high voltage electron microscope (UHVEM) tomography (Kamioka et al. 2012). Using the obtained image-based model, we simulated the microscopic fluid flow in the pericellular space to identify the effects of the geometric complexity of the canaliculus and osteocyte process (Chap. 2). From a more macroscopic viewpoint, the spatially averaged interstitial fluid flow in the

lacuno-canalicular porosity can be regarded as seepage flow in porous bone tissue. The macroscopic fluid flow in an individual trabecula was analyzed by Biot's poroelastic theory (Chap. 3). In the poroelastic analysis, the effects of the lacuno-canalicular microstructure on the seepage flow are reflected in the value of permeability, which can be estimated using a cross-sectional image of a single trabecula (Chap. 4). Based on these findings, we developed a mathematical model for trabecular bone remodeling, incorporating the mechanical hierarchy ranging from microscopic cellular activities to macroscopic bone tissue adaptation, where flow stimuli to osteocytes are assumed to be a driving force for bone remodeling (Chap. 5). The validity of this model has been shown through remodeling simulations for single trabeculae subjected to a cyclic uniaxial load (Chap. 5) and a cyclic bending load (Chap. 6). Furthermore, remodeling simulations for a cancellous bone specimen demonstrated the functional adaptation of the consisting multiple trabeculae and the corresponding uniformalization of the stress in the cancellous bone (Chap. 7). These results suggest that the proposed model can represent the phenomenological remodeling law to achieve local uniform stress states at the tissue level. This finding could be useful in developing a more macroscopic remodeling model, which is introduced in the following sections.

1.3 Modeling Bone Adaptation from Tissue to Organ Level

The bottom-up modeling to link information from the cellular level to the tissue level is an effective approach to clarify the underlying cellular mechanism of bone adaptation. However, this approach requires a tremendous number of parameters to characterize a whole organ composed of millions of cells. To capture the essential features of macroscopic organ dynamics emerging from complex cellular interactions, phenomenological modeling, in which a phenomenon is represented using only a few meaningful parameters, is a powerful strategy. From a historical point of view, prior to bottom-up models that consider cellular activities, several phenomenological models for bone adaptation such as Frost's mechanostat theory (Frost 1987, 2003) were proposed in order to refine Wolff's Law. So far, a variety of computer simulation models of adaptive bone remodeling have been developed in combination with finite element methods (Carter et al. 1987; Huiskes et al. 1987). In most of these remodeling simulations, the associated cellular activities were designed to be governed by some mechanical factors at the tissue level such as stress and strain (Gerhard et al. 2009). These models are distinctively characterized by the assumption that each mechanosensory cell intrinsically "knows" the reference value of the specific mechanical quantity at the state of remodeling equilibrium.

In contrast to the conventional remodeling models (Carter et al. 1987; Huiskes et al. 1987), we proposed a novel rate equation for trabecular surface remodeling toward a uniform stress state at the tissue level (Chap. 8), inspired by the cellular-to-tissue-level simulations mentioned in the previous section. This rate equation

assumes that trabecular surface remodeling is driven by the local non-uniformity of stress distribution, i.e., bone is formed at the site with convex stress distribution and resorbed at the site with concave stress distribution. The originality of our remodeling model lies in the phenomenological hypothesis that each mechanosensory cell can acknowledge the local variation in the mechanical state in the neighboring tissue through a bone cell network. This hypothesis is supported by the experimental findings that the propagation distance of cell-to-cell calcium signaling induced by mechanical stimuli is limited within several hundred micrometers (Adachi et al. 2009a; Huo et al. 2008). The fundamental features of the remodeling model have been investigated through computer simulations for two-dimensional single trabeculae (Chap. 8), two-dimensional cancellous bone specimens (Chaps. 8 and 9), and three-dimensional cancellous bone specimens (Chap. 11), with discussions about the distribution of mechanical quantities on the trabecular surface (Chap. 10). Moreover, the proposed remodeling rate equation has been applied to organ-level remodeling simulations using the models of two-dimensional (Chap. 12) and three-dimensional (Chap. 13) human proximal femurs. Surprisingly, the simulations successfully reproduced highly complex trabecular architecture similar to that in the actual femur. These results indicate that a simple remodeling law to achieve local uniform stress states at the tissue level can realize bone functional adaptation at the organ level. The three-dimensional trabecular remodeling simulation has also been applied to predict the effects of a spinal fixation screw on trabecular structural changes in a vertebral body (Chap. 14), demonstrating a potential for future clinical applications.

1.4 Open Questions and Future Directions

Although our multiscale mathematical modeling and computer simulation have revealed much about the underlying mechanism of bone adaptation, some unanswered questions remain, which should be addressed in future work (see Fig. 1.2).

1.4.1 Osteocyte Mechanotransduction

The molecular mechanism of osteocyte mechanotransduction is a fascinating and challenging research topic. Osteocytes are believed to convert mechanical information from the surrounding interstitial fluid flow into signals that regulate gene expression and protein synthesis through complex intracellular and extracellular ultrastructures, such as the cytoskeleton, plasma membrane, and proteoglycan, all of which are mechanically linked together. However, the relationship between the ultrastructure of osteocytes and mechanotransduction is poorly understood. The first step in clarifying the whole picture of this physiological event is to develop a constitutive model of a single osteocyte within a fluid-filled lacuno-canalicular

porosity by explicitly modeling the associated cellular components. The mechanical properties of each component should be carefully determined in reference to microscale experimental studies. The application of this osteocyte model to a fluid-structure interaction simulation can demonstrate the detailed mechanical behavior of the osteocyte in response to the interstitial fluid flow. By considering the experimental findings obtained through cellular and molecular biology, this modeling approach can provide insights into the underlying roles of mechanical cues that contribute to physiological and pathological phenomena in bone.

1.4.2 Osteocyte Morphology

Increasing evidence suggests that the morphology of osteocytes is an essential factor that influences their mechanosensitivity to maintain physiological bone remodeling. An experimental study using early mice showed that osteocyte network formation in both cortical bone and cancellous bone was affected by mechanical loading (Sugawara et al. 2013). Indeed, there exists a significant structural difference in the osteocyte network between the parietal bone (flat bone) and tibia (long bone) in mice, reflecting physiologically different loading conditions (Himeno-Ando et al. 2012). It was also reported that pathologies resulting in different bone mineral densities, such as osteopenia, osteoarthritis, and osteopetrosis, are related to differences in the osteocyte morphology (van Hove et al. 2009). Thus, alterations in the micromechanical environment of osteocytes within a lacuno-canalicular porosity may affect osteocyte mechanotransduction via interstitial fluid flow. In order to investigate the relationship between microscopic osteocyte morphology and macroscopic bone adaptation, our multiscale modeling and *in silico* approaches extended by considering the variations in the osteocyte micromechanical environment will provide a useful platform.

1.4.3 Signaling in Bone Metabolism

While in this book we have highlighted the mechanical aspects of bone adaptation, it is inherently a biochemical process regulated by complex signaling cascades among a large number of bone cells. One of the most important signaling pathways involved in bone remodeling is the RANK–RANKL–OPG interaction, which is responsible for osteoclastogenesis (Wada et al. 2006). Advances in molecular biology have uncovered various cell-cell signaling pathways that influence bone mineral density. Based on these experimental findings, several drugs for bone pathologies targeting specific signaling molecules have been developed. These include bisphosphonate, parathyroid hormone (teriparatide), selective estrogen receptor modulator (SERM), anti-receptor activator of nuclear factor-κB ligand (RANKL) antibody (denosumab), and anti-sclerostic antibody (Kawai et al. 2011).

In spite of identifying individual signaling pathways, it is still difficult to predict the behavior of bone metabolism systems emerging from complex communication between bone cells. One of the effective strategies to integrate diverse experimental data is to construct a mathematical model of bone metabolism incorporating an entire signaling cascade. The *in silico* experiments based on this mathematical model can enhance our knowledge of the molecular mechanism of bone pathologies for diagnosis and treatment, and ultimately would help us understand the nature of bone homeostasis.

Thus, a comprehensive understanding of bone adaptation necessitates an interdisciplinary approach combining mechanics, cellular and molecular biology, and medical sciences. To successfully treat the hierarchy of bone structure and function, the synergistic interaction between the following two strategies is indispensable. One is to dig down into the detail of underlying molecular mechanisms that regulate bone metabolism from the viewpoint of reduction, and the other is to concentrate on the holistic behavior of bone as a biological system by integrating separate molecular mechanisms. We believe that in both strategies, multiscale mathematical modeling and computer simulation will provide powerful techniques to solve the long-standing enigma of bone adaptation.

1.5 Conclusion

In this chapter, we introduced multiscale modeling and *in silico* approaches to understand bone adaptation from the cellular level, over the tissue level, and up to the organ level. To clarify the underlying cellular mechanism, we developed a mathematical model of trabecular bone remodeling based on a bottom-up perspective that considers cellular mechanosensing and intercellular communication. Through the trabecular remodeling simulations at the tissue level, this remodeling model was suggested to have the potential to represent the phenomenological law of bone transformation toward a locally uniform mechanical state. To distill the essence of the mechanical aspects of bone adaptation, we proposed a rate equation for trabecular surface remodeling based on the phenomenological hypothesis that bone remodeling is driven by the local non-uniformity of stress distribution at the tissue level. The trabecular remodeling simulations incorporating this rate equation reproduced the adaptive changes in trabecular architecture at the tissue level and the organ level. The complementary usage of two remodeling models with different characteristics could contribute to the comprehensive understanding of bone functional adaptation.

References

Adachi T, Aonuma Y, Taira K, Hojo M, Kamioka H (2009a) Asymmetric intercellular communication between bone cells: propagation of the calcium signaling. Biochem Biophys Res Commun 389(3):495–500. https://doi.org/10.1016/j.bbrc.2009.09.010

Adachi T, Aonuma Y, Tanaka M, Hojo M, Takano-Yamamoto T, Kamioka H (2009b) Calcium response in single osteocytes to locally applied mechanical stimulus: differences in cell process and cell body. J Biomech 42(12):1989–1995. https://doi.org/10.1016/j.jbiomech.2009.04.034

Bonewald LF (2011) The amazing osteocyte. J Bone Miner Res 26(2):229–238. https://doi.org/10.1002/jbmr.320

Brand RA (2010) Biographical sketch Julius Wolff, 1836-1902. Clin Orthop Relat Res 468 (4):1047–1049. https://doi.org/10.1007/s11999-010-1258-z

Burger EH, Klein-Nulend J (1999) Mechanotransduction in bone - role of the lacuno-canalicular network. FASEB J 13:S101–S112

Carter DR, Fyhrie DP, Whalen RT (1987) Trabecular bone-density and loading history: regulation of connective tissue biology by mechanical energy. J Biomech 20(8):785–794. https://doi.org/10.1016/0021-9290(87)90058-3

Ciani C, Sharma D, Doty SB, Fritton SP (2014) Ovariectomy enhances mechanical load-induced solute transport around osteocytes in rat cancellous bone. Bone 59:229–234. https://doi.org/10.1016/j.bone.2013.11.026

Cowin SC, Hegedus DH (1976) Bone remodeling I: theory of adaptive elasticity. J Elast 6 (3):313–326. https://doi.org/10.1007/bf00041724

Cowin SC, Mosssalentijn L, Moss ML (1991) Candidates for the mechanosensory system in bone. J Biomech Eng 113(2):191–197. https://doi.org/10.1115/1.2891234

Dallas SL, Prideaux M, Bonewald LF (2013) The osteocyte: an endocrine cell and more. Endocr Rev 34(5):658–690. https://doi.org/10.1210/er.2012-1026

Duda GN, Haas NP, Bergmann G (2010) Founding of the Julius Wolff Institut Charite - Universitatsmedizin berlin. Clin Orthop Relat Res 468(4):1050–1051. https://doi.org/10.1007/s11999-010-1238-3

Fritton SP, Weinbaum S (2009) Fluid and solute transport in bone: flow-induced mechanotransduction. Annu Rev Fluid Mech 41:347–374. https://doi.org/10.1146/annurev.fluid.010908.165136

Frost HM (1987) Bone "mass" and the "mechanostat": a proposal. Anat Rec 219(1):1–9. https://doi.org/10.1002/ar.1092190104

Frost HM (2003) Bone's mechanostat: a 2003 update. Anat Rec A Discov Mol Cell Evol Biol 275A(2):1081–1101. https://doi.org/10.1002/ar.a.10119

Gerhard FA, Webster DJ, van Lenthe GH, Muller R (2009) In silico biology of bone modelling and remodelling: adaptation. Philos Trans R Soc A 367(1895):2011–2030. https://doi.org/10.1098/rsta.2008.0297

Goldstein SA, Matthews LS, Kuhn JL, Hollister SJ (1991) Trabecular bone remodeling: An experimental model. J Biomech 24:135–150

Guldberg RE, Caldwell NJ, Guo XE, Goulet RW, Hollister SJ, Goldstein SA (1997a) Mechanical stimulation of tissue repair in the hydraulic bone chamber. J Bone Miner Res 12(8):1295–1302. https://doi.org/10.1359/jbmr.1997.12.8.1295

Guldberg RE, Richards M, Caldwell NJ, Kuelske CL, Goldstein SA (1997b) Trabecular bone adaptation to variations in porous-coated implant topology. J Biomech 30(2):147–153

Hegedus DH, Cowin SC (1976) Bone remodeling II: small strain adaptive elasticity. J Elast 6 (4):337–352. https://doi.org/10.1007/bf00040896

Himeno-Ando A, Izumi Y, Yamaguchi A, Iimura T (2012) Structural differences in the osteocyte network between the calvaria and long bone revealed by three-dimensional fluorescence morphometry, possibly reflecting distinct mechano-adaptations and sensitivities. Biochem Biophys Res Commun 417(2):765–770. https://doi.org/10.1016/j.bbrc.2011.12.031

Huiskes R, Weinans H, Grootenboer HJ, Dalstra M, Fudala B, Slooff TJ (1987) Adaptive bone-remodeling theory applied to prosthetic-design analysis. J Biomech 20(11–12):1135–1150. https://doi.org/10.1016/0021-9290(87)90030-3

Huo B, XL L, Hung CT, Costa KD, QB X, Whitesides GM, Guo XE (2008) Fluid flow induced calcium response in bone cell network. Cell Mol Bioeng 1(1):58–66. https://doi.org/10.1007/s12195-008-0011-0

Kameo Y, Ootao Y, Ishihara M (2016) Poroelastic analysis of interstitial fluid flow in a single lamellar trabecula subjected to cyclic loading. Biomech Model Mechanobiol 15(2):361–370. https://doi.org/10.1007/s10237-015-0693-x

Kamioka H, Kameo Y, Imai Y, Bakker AD, Bacabac RG, Yamada N, Takaoka A, Yamashiro T, Adachi T, Klein-Nulend J (2012) Microscale fluid flow analysis in a human osteocyte canaliculus using a realistic high-resolution image-based three-dimensional model. Integr Biol 4 (10):1198–1206. https://doi.org/10.1039/c2ib20092a

Kawai M, Modder UI, Khosla S, Rosen CJ (2011) Emerging therapeutic opportunities for skeletal restoration. Nat Rev Drug Discov 10(2):141–156. https://doi.org/10.1038/nrd3299

Mullender MG, Huiskes R, Weinans H (1994) A physiological approach to the simulation of bone remodeling as a self-organizational control process. J Biomech 27(11):1389–1394

Nakashima T, Hayashi M, Fukunaga T, Kurata K, Oh-hora M, Feng JQ, Bonewald LF, Kodama T, Wutz A, Wagner EF, Penninger JM, Takayanagi H (2011) Evidence for osteocyte regulation of bone homeostasis through RANKL expression. Nat Med 17(10):1231–1234. https://doi.org/10.1038/nm.2452

Parfitt AM (1994) Osteonal and hemi-osteonal remodeling: the spatial and temporal framework for signal traffic in adult human bone. J Cell Biochem 55(3):273–286

Price C, Zhou X, Li W, Wang L (2011) Real-time measurement of solute transport within the lacunar-canalicular system of mechanically loaded bone: direct evidence for load-induced fluid flow. J Bone Miner Res 26(2):277–285. https://doi.org/10.1002/jbmr.211

Roux W (1881) Der zuchtende Kampf der Teile, oder die 'Teilauslese' im Organismus (Theorie der 'funktionellen Anpassung'). Wilhelm Engelmann, Leipzig

Sugawara Y, Kamioka H, Honjo T, Tezuka K, Takano-Yamamoto T (2005) Three-dimensional reconstruction of chick calvarial osteocytes and their cell processes using confocal microscopy. Bone 36(5):877–883. https://doi.org/10.1016/j.bone.2004.10.008

Sugawara Y, Kamioka H, Ishihara Y, Fujisawa N, Kawanabe N, Yamashiro T (2013) The early mouse 3d osteocyte network in the presence and absence of mechanical loading. Bone 52 (1):189–196. https://doi.org/10.1016/j.bone.2012.09.033

Tatsumi S, Ishii K, Amizuka N, Li MQ, Kobayashi T, Kohno K, Ito M, Takeshita S, Ikeda K (2007) Targeted ablation of osteocytes induces osteoporosis with defective mechanotransduction. Cell Metab 5(6):464–475. https://doi.org/10.1016/j.cmet.2007.05.001

van Hove RP, Nolte PA, Vatsa A, Semeins CM, Salmon PL, Smit TH, Klein-Nulend J (2009) Osteocyte morphology in human tibiae of different bone pathologies with different bone mineral density – is there a role for mechanosensing? Bone 45(2):321–329. https://doi.org/10.1016/j.bone.2009.04.238

Wada T, Nakashima T, Hiroshi N, Penninger JM (2006) RANKL-RANK signaling in osteoclastogenesis and bone disease. Trends Mol Med 12(1):17–25. https://doi.org/10.1016/j.molmed.2005.11.007

Weinans H, Huiskes R, Grootenboer HJ (1992) The behavior of adaptive bone-remodeling simulation models. J Biomech 25(12):1425–1441. https://doi.org/10.1016/0021-9290(92)90056-7

Weinbaum S, Cowin SC, Zeng Y (1994) A model for the excitation of osteocytes by mechanical loading-induced bone fluid shear stresses. J Biomech 27(3):339–360

Wolff J (1870) Ueber die innere Architectur der Knochen und ihre Bedeutung für die Frage vom Knochenwachstum. Virchows Arch Pathol Anat Physiol 50:389–450

Wolff J (2010) The classic on the inner architecture of bones and its importance for bone growth (reprinted from virchows arch pathol anat physiol, vol 50, pg 389-450, 1870). Clin Orthop Relat Res 468(4):1056–1065. https://doi.org/10.1007/s11999-010-1239-2

Chapter 2
Microscopic Fluid Flow Analysis in an Osteocyte Canaliculus

Abstract This chapter describes a computational analysis of the interstitial fluid flow in a single osteocyte canaliculus, which is closely associated with cellular mechanotransduction. A three-dimensional simulation model of an osteocyte process within a canaliculus was reconstructed based on serial tomographic images obtained by ultra-high voltage electron microscopy. The fluid flow simulation predicts the generation of highly inhomogeneous flow patterns in the pericellular space, owing to the microscopic surface roughness of the canalicular wall and the osteocyte process. These flow patterns may contribute to the amplification of mechanical stimuli to osteocytes through deformation of cytoskeletal elements in the cell processes.

Keywords Interstitial fluid flow • Osteocyte canaliculus • Osteocyte process • Computational fluid dynamics • Ultra-high voltage electron microscopy

2.1 Introduction

Changes in bone mass and structure owing to remodeling are regulated by the metabolic activities of bone cells in response to mechanical loading. Among bone cells, osteocytes, the most abundant cell type in bone tissue, are believed to orchestrate osteoclastic bone resorption and osteoblastic bone formation (Nakashima et al. 2011; Tatsumi et al. 2007). Osteocytes are considered the most likely mechanosensory cells (Adachi et al. 2009a, b, c; Bonewald 2011; Cowin et al. 1991) from an anatomical point of view since they form a complex intercellular network via slender cell processes housed in the lacuno-canalicular porosity inside the mineralized bone matrix (Kamioka et al. 2001, 2009; Sugawara et al. 2005).

The mechanism by which mechanosensory cells transduce mechanical signals into biochemical signals, in a process known as mechanotransduction for bone remodeling, remains unclear. Several experimental and theoretical studies suggest that the flow of the interstitial fluid in the lacuno-canalicular porosities induced by dynamic loading plays a pivotal role in the activation of osteocytes (Burger and

This Chapter was adapted from Kamioka et al. (2012) with permission from The Royal Society of Chemistry.

Y. Kameo et al., *Bone Adaptation*, Frontiers of Biomechanics 2,
https://doi.org/10.1007/978-4-431-56514-7_2

Klein-Nulend 1999; Fritton and Weinbaum 2009; Knothe Tate et al. 1998; Weinbaum et al. 1994). Weinbaum et al. (1994) performed a poroelastic analysis of bone tissue to show that osteocytes can be activated by flow-induced shear stress on the surface membranes of their processes. Subsequent studies identified additional factors that amplify the cellular strain, such as tethering elements connecting the osteocyte processes to the canalicular wall (Han et al. 2004; You et al. 2001) and integrin-mediated focal attachments of the cell processes to the canalicular wall (Wang et al. 2007). However, the apparent complexity of the microstructural features of canaliculi and the osteocyte processes makes it difficult to judge the validity of any hypothesis regarding mechanotransduction. To investigate the effects of their complex geometries, it is essential to obtain high-resolution, preferably three-dimensional, morphological data of the canaliculi and cell processes within real bone.

In this chapter, we visualize a single osteocyte process within a canaliculus and create a three-dimensional model with the help of ultra-high voltage electron microscope (UHVEM) tomography. Using this image-based model for computational fluid dynamics analysis, we simulated the patterns of interstitial fluid flow in the pericellular space between the osteocyte process and the canalicular wall to identify the effects of geometric complexity of the canaliculus on the flow profiles that drive cellular mechanotransduction.

2.2 Three-Dimensional Reconstruction of Osteocytes in Canaliculi

For observation of osteocytes in canaliculi, cortical bone samples (surgical waste) were obtained from the femur of a male donor (aged 62 years) without any metabolic bone disease, during a joint replacement surgery. Informed consent was obtained from the donor. Using UHVEM tomography (Kamioka et al. 2009; Martone et al. 2000; Takaoka et al. 2008) at accelerating voltages of 2 MeV, we visualized the osteocyte processes within canaliculi at a nanometer scale in 1-μm-thick sections of the human bone and reconstructed three-dimensional models.

Figure 2.1 shows a series of tomographic images for a transverse cross-section through a canaliculus containing an osteocyte process. These images are obtained from one image plane at 10-voxel intervals. Each tomographic image consisted of 500 pixels × 500 pixels, with a final pixel size of 1.7 nm. The total stack of tomographic images contained 700 images per virtual slice with a 1-voxel thickness of 0.86 nm. A tethering element (Fig. 2.1, TE), connecting the osteocyte process to the canalicular wall, was observed. Both transversely sectioned (Fig. 2.1, cross-section, CS) and longitudinally sectioned (Fig. 2.1, LS) collagen fibrils were observed in considerable abundance. It was clear that the contour of the canalicular wall was determined by the collagen fibrils running parallel to the cell process (Fig. 2.1, $Z = 40$, white star) and by others running in a direction perpendicular to

the cell process (Fig. 2.1, $Z = 10$, black star). With regard to the cell process, a protuberance was observed, forming a discontinuity in the otherwise smooth and tube-like structure of the osteocyte process (Fig. 2.1, $Z = 20$). Protuberances like

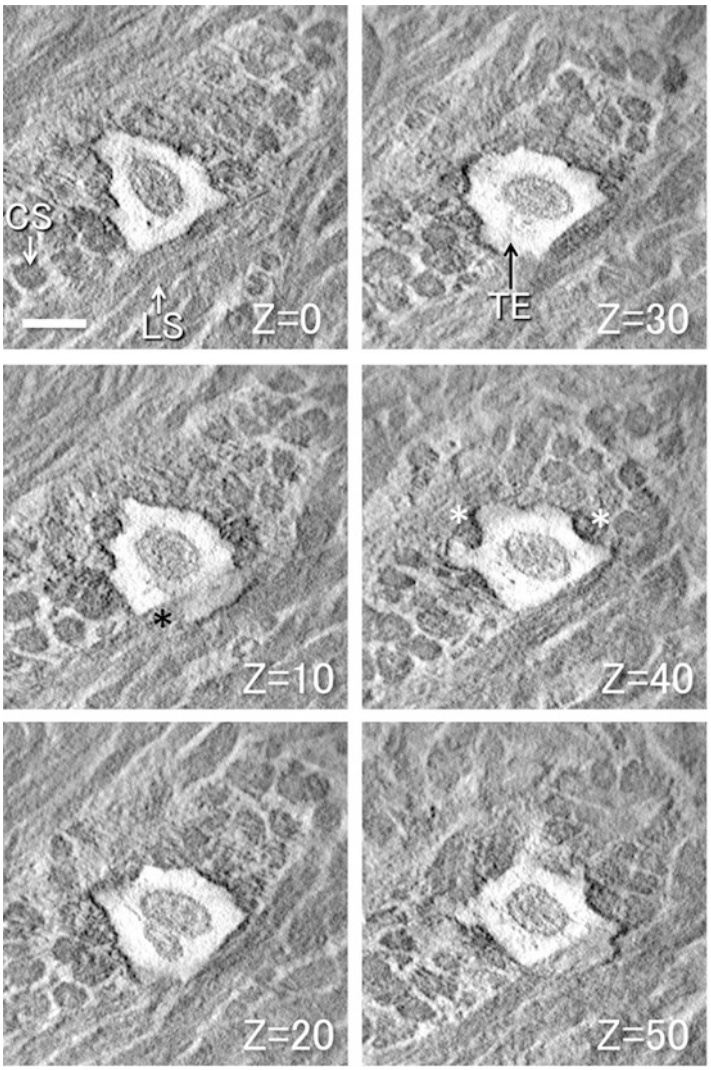

Fig. 2.1 Serial tomographic images of a transverse cross-section of a canaliculus containing an osteocyte process. These images are obtained at 10-voxel intervals (8.6 nm intervals) along the *Z*-direction. *TE* indicates tethering fibers that occupy the space between the cell process and the canalicular wall. *CS* indicates cross-section of a collagen fibril and *LS* indicates longitudinal section of a collagen fibril. The *white star* indicates a collagen fibril that runs along the cell process, and the *black star* indicates a collagen fibril that runs in a direction perpendicular to the cell process. Bar = 200 nm (This figure was adapted from Kamioka et al. (2012) with permission from The Royal Society of Chemistry)

these have been observed earlier and seem to be a natural feature of osteocyte processes (McNamara et al. 2009).

We generated a three-dimensional reconstruction of a single canaliculus containing an osteocyte process (Fig. 2.2) by using serial tomographic images from Fig. 2.1. Three-dimensional reconstruction clearly illustrates that the osteocyte process runs through the center of its canaliculus, without direct attachment to the canalicular wall (Fig. 2.2a–c). Furthermore, a three-dimensional distribution of collagen fibrils was apparent (Fig. 2.2d–e). The contour of the canalicular wall was

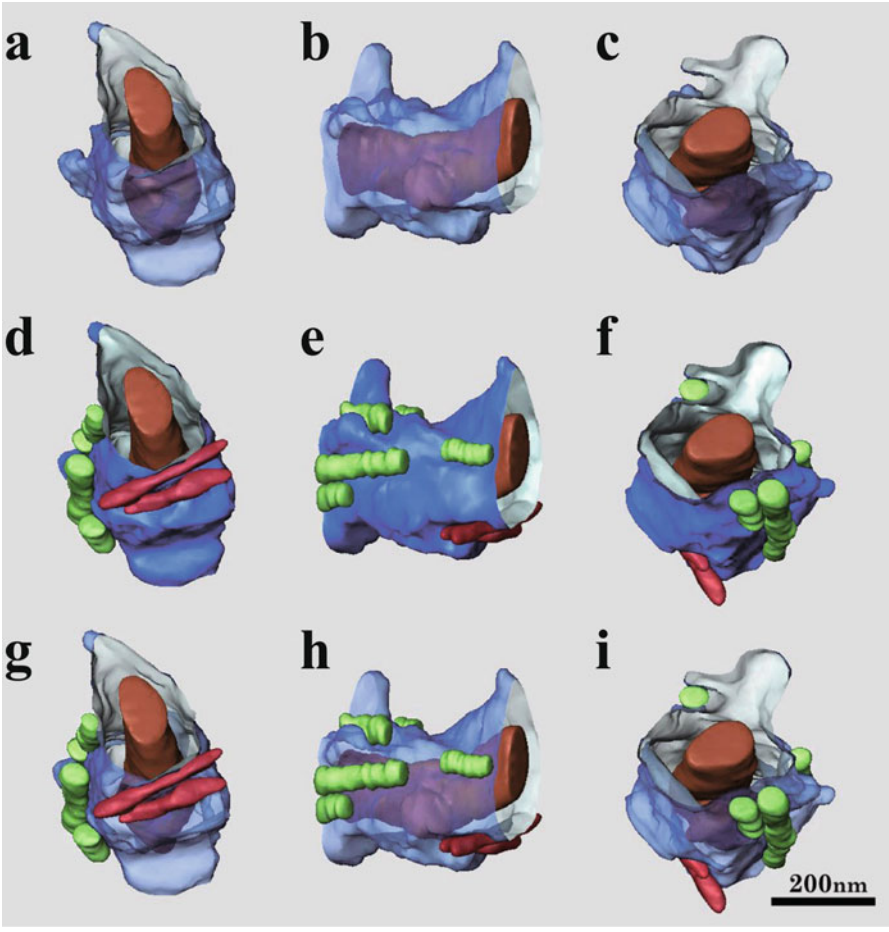

Fig. 2.2 Three-dimensional reconstruction of a single canaliculus containing an osteocyte process. The osteocyte process is shown in orange, the canalicular wall is shown in *blue*, the collagen fibrils running parallel to the cell process are shown in *green*, and the collagen fibrils running in a direction perpendicular to the cell process are shown in *red* (This figure was adapted from Kamioka et al. (2012) with permission from The Royal Society of Chemistry)

determined by linear collagen fibrils running parallel to the cell process (green; Fig. 2.2d–i) and in a direction perpendicular to the cell process (red; Fig. 2.2d–i).

2.3 Computational Fluid Flow Analysis

The fluid flow in the pericellular space between the osteocyte process and the canalicular wall was numerically analyzed by the lattice Boltzmann method (Chen and Doolen 1998; Takeishi et al. 2015). This is a computational fluid dynamics method in which a discretized Boltzmann equation, i.e., lattice Boltzmann equation, is solved to simulate the flow. The macroscopic flow profiles obtained by the lattice Boltzmann equation were shown to be equivalent to those obtained by the Navier-Stokes equation, i.e., Newtonian fluid flow.

In the lattice Boltzmann method, the fluid dynamics are expressed by the propagation and collision processes of mesoscopic particles that move on a regular lattice. This lattice represents a discretization of both three-dimensional coordinate space and particle velocity space. Each node in the lattice is connected to the 27 neighboring nodes in our implementation; this model is called D3Q27. Using a number density distribution function of the particles f_i, with a discretized velocity $\boldsymbol{c_i}$, the fluid dynamics are described by the following equation:

$$f_i(\boldsymbol{x} + \boldsymbol{c_i}\Delta t, t + \Delta t) - f_i(\boldsymbol{x}, t) = -\frac{\Delta t}{\tau}\left[f_i(\boldsymbol{x}, t) - f_i^{\mathrm{eq}}(\boldsymbol{x}, t)\right] - F_i(\boldsymbol{x}, t)\Delta t, \quad (2.1)$$

where the Bhatnagar-Gross-Krook (BGK) approximation was applied in the process of particle collisions. In the above equation, $\boldsymbol{x}$ is the position within the lattice, t is the time, Δt is the time step, τ is the BGK relaxation time, and F_i is the external body force. The local equilibrium distribution f_i^{eq} is given by

$$f_i^{\mathrm{eq}}(\boldsymbol{x}, t) = \omega_i \frac{\rho}{m}\left[1 + \frac{3\boldsymbol{c_i}\cdot\boldsymbol{v}}{c^2} + \frac{9(\boldsymbol{c_i}\cdot\boldsymbol{v})^2}{2c^4} - \frac{3\boldsymbol{v}\cdot\boldsymbol{v}}{2c^2}\right], \quad (2.2)$$

where ω_i is the weight that depends on the value of $|\boldsymbol{c_i}|$, m is the mass of a particle, and c is the lattice speed defined as the ratio of the lattice interval Δx to the time step Δt ($c = \Delta x/\Delta t$). The macroscopic density ρ and velocity $\boldsymbol{v}$ are, respectively, calculated by

$$\rho(\boldsymbol{x}, t) = \sum_{i=1}^{27} m f_i(\boldsymbol{x}, t), \quad (2.3)$$

$$\boldsymbol{v}(\boldsymbol{x},t)=\frac{\sum_{i=1}^{27} m\boldsymbol{c_i}f_i(\boldsymbol{x},t)}{\rho(\boldsymbol{x},t)} \tag{2.4}$$

The kinematic viscosity of the fluid ν satisfies the following relation:

$$\nu-\frac{c^2}{3}\left(\tau-\frac{\Delta t}{2}\right) \tag{2.5}$$

2.4 Model of Osteocyte Canaliculi

Based on the three-dimensional visualization of a canaliculus with an osteocyte process (discussed in Sect. 2.2) image-based simulation models of the pericellular fluid space between the cell process and the canalicular wall were constructed from two different canaliculi. One model is of an almost straight canaliculus and the other is that of a bifurcating canaliculus. These models were discretized by a regular lattice with a Cartesian coordinate system (x, y, z), where the z-direction was set as the direction perpendicular to the plane of the section used for tomographic reconstruction. The lengths of the canalicular models along the z-direction were set to 134 for the straight canaliculus ($\Delta x = 3.4$ nm) and to 124 for the bifurcating canaliculus ($\Delta x = 7.0$ nm). The total number of nodes was 574,617 for the straight canaliculus and 1,417,997 for the bifurcating canaliculus.

The boundary condition at the surface of the cell process and the canalicular wall was a no-slip condition. The periodic boundary condition at the inlet and outlet was applied by connecting these with an imaginary channel whose cross-section changes smoothly from one end to the other. The fluid flow was generated by the uniform body force along the z-direction. We set the kinematic viscosity at 10^{-6} m^2/s and the acceleration of the body force at 10^6 m/s^2. Here, we assumed that the kinematic viscosity of interstitial fluid has the same value as that of salt water. The value of acceleration of the body force has been determined with reference to the fluid pressure gradient in a canaliculus obtained by poroelastic analysis: ~ 1 Pa/nm (Weinbaum et al. 1994). These parameter values produce an extremely low Reynolds number flow, which is governed by the Stokes equation, i.e., the inertia is negligible, because the dimension of the channel is only several hundred nanometers. Under the above mechanical conditions, we simulated the flow profiles in steady state inside the canaliculi.

2.5 Interstitial Fluid Flow in Osteocyte Canaliculi

To investigate the effect of microscopic surface roughness of the canalicular wall, which is created by collagen fibrils, on the flow profiles in the pericellular space, we conducted computational fluid dynamics analysis by using the lattice Boltzmann method. The fluid flow profiles in an almost straight canaliculus and in a bifurcating canaliculus are shown in Figs. 2.3 and 2.4, respectively.

Figure 2.3a shows the distribution of the absolute value of fluid velocity and the corresponding streamlines. In spite of the irregular surface of the canalicular wall and a protuberance on the osteocyte process, the streamlines follow the shape of the pericellular space and no vortexes were observed because Stokes flow was assumed by setting an extremely low Reynolds number. Although the flow in the canaliculus is laminar, the value of fluid velocity on a given streamline is remarkably position-dependent. To describe the flow profiles more explicitly, the distribution of the absolute value of fluid velocity in cross-sections of the canaliculus is demonstrated in Fig. 2.3b, which shows the distribution in four longitudinal cross-sections including the z-axis, and in Fig. 2.3c, which shows the distribution in five x–y cross-sections viewed from $-$z-direction. These figures demonstrate that fluid velocity is high in regions where the space between the osteocyte process and the canalicular wall is relatively large and low in regions where this space is relatively small. As shown in Fig. 2.3b, ii and c, ii, relatively low fluid velocity was observed in the regions where the roughness of the surrounding canalicular wall is higher. In addition, it must be noted that the absolute value of fluid velocity in the upper region in Fig. 2.3b, iv was about two times larger than that in the lower region, despite the apparent similarity of the dimensions of the upper and lower regions of the channel.

The distribution of the absolute value of fluid velocity and the corresponding streamlines in the bifurcating canaliculus are shown in Fig. 2.4a, and the fluid velocity distribution in x–y cross-sections viewed from $-$z-direction in Fig. 2.4b. Even though the canaliculus has a bifurcation, the flow was exactly laminar and there was no vortex at all. The fluid flow inside each branch of channels depends on the direction of external body force, which is determined by the surrounding mechanical environment *in vivo*. Here, we focused on the flow profiles in the lower branch where the value of the fluid velocity was comparatively large. Figure 2.4b shows that the characteristics of the obtained inhomogeneous flow pattern were similar to those observed in the case of the straight canaliculus (Fig. 2.3c), i.e., the fluid velocity was higher in regions where the space between the osteocyte process and the canalicular wall was large compared to that in regions where the space was small.

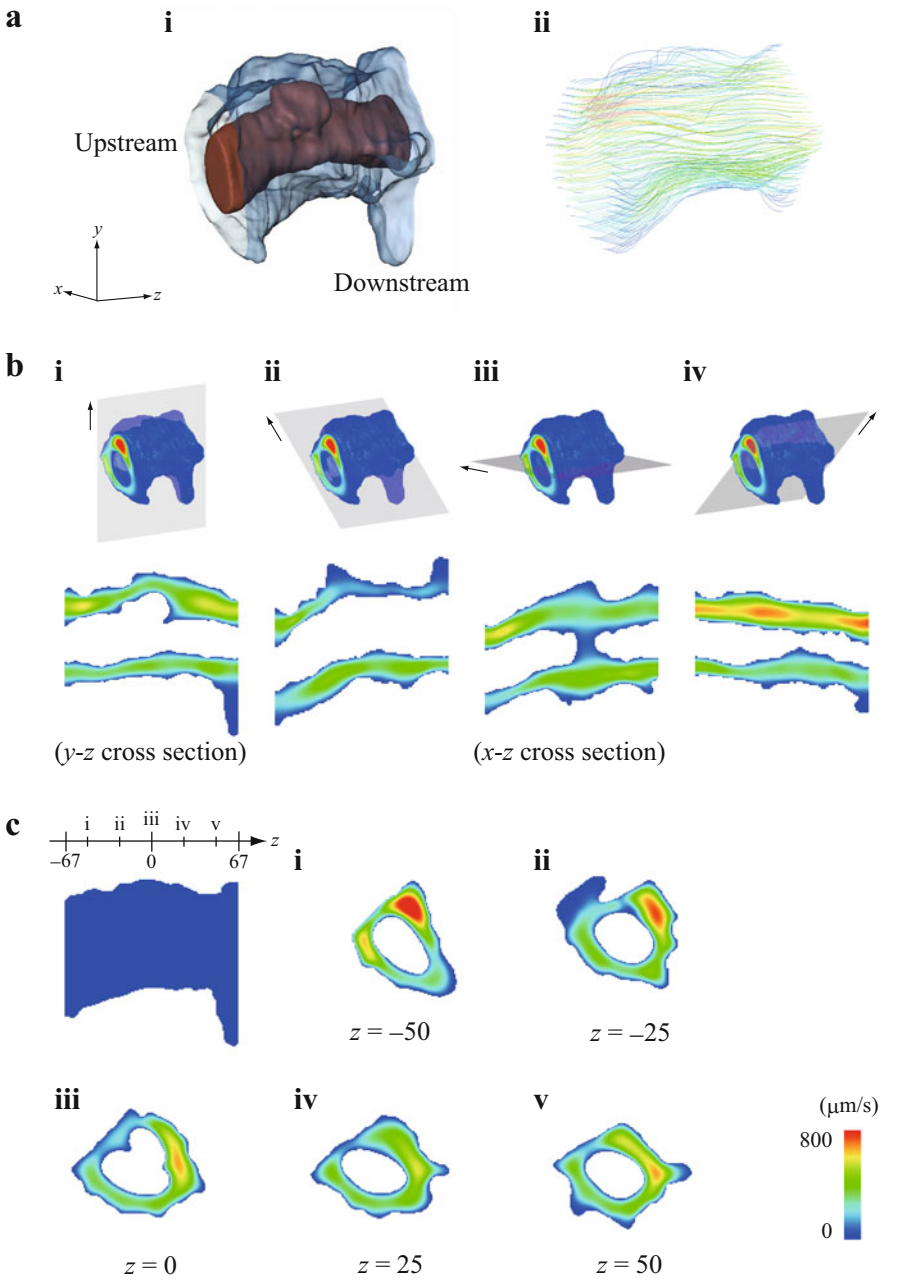

Fig. 2.3 Computational fluid flow analysis in an almost straight osteocyte canaliculus. (**a**) (*i*) A three-dimensional model of a single canaliculus with an osteocyte process. (*ii*) Distribution of the absolute value of fluid velocity on stream lines. (**b**) Distribution of the absolute value of fluid velocity in four cross-sections of a canaliculus including the *z*-axis: (*i*) the *y*–*z* cross-section, (*ii*) the cross-section rotated 45 degrees clockwise from the *y*–*z* plane, (*iii*) the *x*–*z* cross-section, (*iv*)

2.6 Importance of Canalicular Microstructure in Osteocyte Mechanosensing

Previous theoretical models designed to elucidate the manner in which mechanical loads placed on a whole bone organ are transduced to the osteocyte, are predominantly based on the assumption that the canalicular wall is relatively smooth and symmetrical (Han et al. 2004; Wang et al. 2007; Weinbaum et al. 1994; You et al. 2001). Assuming that fluid flow occurs around the osteocyte because of the loads placed upon the bone, the models would predict this flow to be relatively homogeneous. Yet, we found that the canalicular wall made up of collagen fibers is far from smooth, and the distance between the osteocyte process and the canalicular wall varies considerably. In addition, we found that the osteocyte process is smooth, but contains protuberances as has been described previously by Kamioka et al. (2004). Therefore, we reconstructed a three-dimensional model of the pericellular fluid space around an osteocyte process, containing a protuberance, and used computational fluid dynamics analysis at the microscopic scale to analyze the patterns of interstitial fluid flow.

As shown in Fig. 2.3a, b, although the flow of interstitial fluid in the canaliculus was always laminar due to an extremely low Reynolds number, even in a bifurcating canaliculus, we found that the surface roughness of the canalicular wall induces a complex distribution of fluid velocities. Both fluid flow simulations demonstrated higher fluid velocities in those regions of the canaliculus where the space between the osteocyte process and the canalicular wall was large because fluid tends to flow along the path of least resistance. This phenomenon was previously described in a flow simulation using an idealized canalicular model (Anderson and Tate 2008). Inhomogeneous flow patterns may induce strains in cytoskeletal elements of the osteocyte process, thereby amplifying mechanical stimuli. This effect can be dominant, especially considering that fiber-like tethering elements may have a role in amplifying mechanical stimuli in the cell process (Han et al. 2004; You et al. 2001). More reconstructions of osteocyte processes should be made and more fluid flow simulations should be performed to approximate the range of possible flow patterns. However, our calculations in two types of representative canaliculi clearly illustrate that the flow profiles remarkably depend on the size of the local space of the channels.

Fig. 2.3 (continued) the cross-section rotated 45 degrees clockwise from the x–z plane. (**c**) Distribution of the absolute value of fluid velocity in the x–y cross-section as viewed from the −z-direction: (*i*) $z = -50$, (*ii*) $z = -25$, (*iii*) $z = 0$, (*iv*) $z = 25$, (*v*) $z = 50$ (unit: Δx) (This figure was adapted from Kamioka et al. (2012) with permission from The Royal Society of Chemistry)

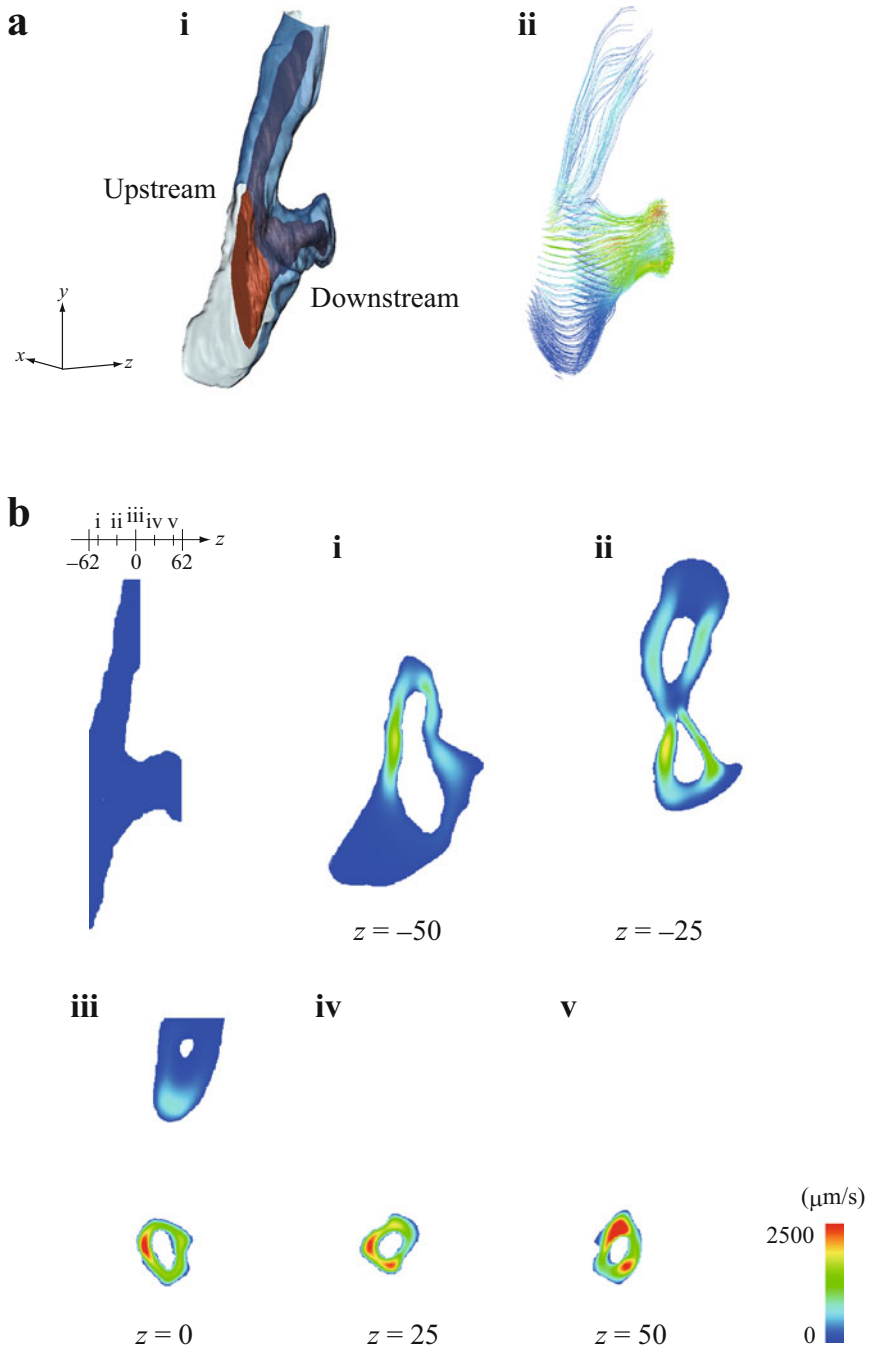

Fig. 2.4 Computational fluid flow analysis in a bifurcating osteocyte canaliculus. (**a**) (*i*) A three-dimensional model of a bifurcating canaliculus with an osteocyte process. (*ii*) Distribution of the absolute value of fluid velocity on stream lines. (**b**) Distribution of the absolute value of fluid velocity in the *x*–*y* cross-section as viewed from the −z-direction: (*i*) $z = -50$, (*ii*) $z = -25$, (*iii*) $z = 0$, (*iv*) $z = 25$, (*v*) $z = 50$ (unit: Δx) (This figure was adapted from Kamioka et al. (2012) with permission from The Royal Society of Chemistry)

2.7 Conclusion

In this chapter, we visualized canaliculi with osteocyte processes inside a cortical bone sample excised from a human femur by using UHVEM tomography. By stacking the serial tomographic images obtained, a single canaliculus containing an osteocyte process was three-dimensionally reconstructed. For the computational fluid dynamics analysis, image-based three-dimensional simulation models of the pericellular fluid space between the cell process and the canalicular wall were constructed for two different canaliculi: a straight canaliculus and a bifurcating canaliculus. Under the assumption that the interstitial fluid flow in a canaliculus is Newtonian with a low Reynolds number, we simulated the flow profiles in steady state inside the canaliculi by the lattice Boltzmann method.

The computational fluid flow analysis showed that the flow of interstitial fluid in the canaliculus was always laminar, even in a bifurcating canaliculus, and the magnitude of fluid velocity was strongly position-dependent, owing to the irregular surface of the canalicular wall and a protuberance on the osteocyte process. In particular, high fluid velocity was observed in regions of the canaliculus where the space between the osteocyte process and the canalicular wall was relatively large because fluid flows along the path of least resistance. These results suggest the possibility that the inhomogeneous flow patterns contribute to amplification of the mechanical stimuli to osteocytes by inducing strains in cytoskeletal elements of the cell processes.

References

Adachi T, Aonuma Y, Ito S, Tanaka M, Hojo M, Takano-Yamamoto T, Kamioka H (2009a) Osteocyte calcium signaling response to bone matrix deformation. J Biomech 42 (15):2507–2512. https://doi.org/10.1016/j.jbiomech.2009.07.006

Adachi T, Aonuma Y, Taira K, Hojo M, Kamioka H (2009b) Asymmetric intercellular communication between bone cells: propagation of the calcium signaling. Biochem Biophys Res Commun 389(3):495–500. https://doi.org/10.1016/j.bbrc.2009.09.010

Adachi T, Aonuma Y, Tanaka M, Hojo M, Takano-Yamamoto T, Kamioka H (2009c) Calcium response in single osteocytes to locally applied mechanical stimulus: differences in cell process and cell body. J Biomech 42(12):1989–1995. https://doi.org/10.1016/j.jbiomech.2009.04.034

Anderson EJ, Tate MLK (2008) Idealization of pericellular fluid space geometry and dimension results in a profound underprediction of nano-microscale stresses imparted by fluid drag on osteocytes. J Biomech 41(8):1736–1746. https://doi.org/10.1016/j.jbiomech.2008.02.035

Bonewald LF (2011) The amazing osteocyte. J Bone Miner Res 26(2):229–238. https://doi.org/10.1002/jbmr.320

Burger EH, Klein-Nulend J (1999) Mechanotransduction in bone - role of the lacuno-canalicular network. FASEB J 13:S101–S112

Chen S, Doolen GD (1998) Lattice Boltzmann method for fluid flows. Annu Rev Fluid Mech 30:329–364. https://doi.org/10.1146/annurev.fluid.30.1.329

Cowin SC, Mosssalentijn L, Moss ML (1991) Candidates for the mechanosensory system in bone. J Biomech Eng 113(2):191–197. https://doi.org/10.1115/1.2891234

Fritton SP, Weinbaum S (2009) Fluid and solute transport in bone: flow-induced mechanotransduction. Annu Rev Fluid Mech 41:347–374. https://doi.org/10.1146/annurev.fluid.010908.165136

Han YF, Cowin SC, Schaffler MB, Weinbaum S (2004) Mechanotransduction and strain amplification in osteocyte cell processes. Proc Natl Acad Sci U S A 101(47):16689–16694. https://doi.org/10.1073/pnas.0407429101

Kamioka H, Honjo T, Takano-Yamamoto T (2001) A three-dimensional distribution of osteocyte processes revealed by the combination of confocal laser scanning microscopy and differential interference contrast microscopy. Bone 28(2):145–149. https://doi.org/10.1016/S8756-3282(00)00421-X

Kamioka H, Sugawara Y, Honjo T, Yamashiro T, Takano-Yamamoto T (2004) Terminal differentiation of osteoblasts to osteocytes is accompanied by dramatic changes in the distribution of actin-binding proteins. J Bone Miner Res 19(3):471–478. https://doi.org/10.1359/jbmr.040128

Kamioka H, Murshid SA, Ishihara Y, Kajimura N, Hasegawa T, Ando R, Sugawara Y, Yamashiro T, Takaoka A, Takano-Yamamoto T (2009) A method for observing silver-stained osteocytes in situ in 3-um sections using ultra-high voltage electron microscopy tomography. Microsc Microanal 15(5):377–383. https://doi.org/10.1017/s1431927609990420

Kamioka H, Kameo Y, Imai Y, Bakker AD, Bacabac RG, Yamada N, Takaoka A, Yamashiro T, Adachi T, Klein-Nulend J (2012) Microscale fluid flow analysis in a human osteocyte canaliculus using a realistic high-resolution image-based three-dimensional model. Integr Biol 4(10):1198–1206. https://doi.org/10.1039/c2ib20092a

Knothe Tate ML, Knothe U, Niederer P (1998) Experimental elucidation of mechanical load-induced fluid flow and its potential role in bone metabolism and functional adaptation. Am J Med Sci 316(3):189–195

Martone ME, Deerinck TJ, Yamada N, Bushong E, Ellisman MH (2000) Correlated 3D light and electron microscopy: use of high voltage electron microscopy and electron tomography for imaging large biological structures. J Histotechnol 23(3):261–270

McNamara LM, Majeska RJ, Weinbaum S, Friedrich V, Schaffler MB (2009) Attachment of osteocyte cell processes to the bone matrix. Anat Rec 292(3):355–363. https://doi.org/10.1002/ar.20869

Nakashima T, Hayashi M, Fukunaga T, Kurata K, Oh-hora M, Feng JQ, Bonewald LF, Kodama T, Wutz A, Wagner EF, Penninger JM, Takayanagi H (2011) Evidence for osteocyte regulation of bone homeostasis through rankl expression. Nat Med 17(10):1231–1234. https://doi.org/10.1038/nm.2452

Sugawara Y, Kamioka H, Honjo T, Tezuka K, Takano-Yamamoto T (2005) Three-dimensional reconstruction of chick calvarial osteocytes and their cell processes using confocal microscopy. Bone 36(5):877–883. https://doi.org/10.1016/j.bone.2004.10.008

Takaoka A, Hasegawa T, Yoshida K, Mori H (2008) Microscopic tomography with ultra-HVEM and applications. Ultramicroscopy 108(3):230–238. https://doi.org/10.1016/j.ultramic.2007.06.008

Takeishi N, Imai Y, Yamaguchi T, Ishikawa T (2015) Flow of a circulating tumor cell and red blood cells in microvessels. Phys Rev E 92(6). https://doi.org/10.1103/PhysRevE.92.063011

Tatsumi S, Ishii K, Amizuka N, Li MQ, Kobayashi T, Kohno K, Ito M, Takeshita S, Ikeda K (2007) Targeted ablation of osteocytes induces osteoporosis with defective mechanotransduction. Cell Metab 5(6):464–475. https://doi.org/10.1016/j.cmet.2007.05.001

Wang Y, McNamara LM, Schaffler MB, Weinbaum S (2007) A model for the role of integrins in flow induced mechanotransduction in osteocytes. Proc Natl Acad Sci U S A 104(40):15941–15946. https://doi.org/10.1073/pnas.0707246104

Weinbaum S, Cowin SC, Zeng Y (1994) A model for the excitation of osteocytes by mechanical loading-induced bone fluid shear stresses. J Biomech 27(3):339–360

You L, Cowin SC, Schaffler MB, Weinbaum S (2001) A model for strain amplification in the actin cytoskeleton of osteocytes due to fluid drag on pericellular matrix. J Biomech 34(11):1375–1386

Chapter 3
Macroscopic Fluid Flow Analysis in a Poroelastic Trabecula

Abstract This chapter deals with a poroelastic analysis of the interstitial fluid flow in individual trabeculae. We employed an analytical approach to investigate the response of the interstitial fluid pressure within a single trabecula to the applied cyclic loading. By assuming a single trabecula as a two-dimensional poroelastic material, we present an analytical solution for the interstitial fluid pressure in a single trabecula as a summation of the transient and steady-state responses by solving the governing equations for the quasi-static poroelasticity. The results suggest the possibility that osteocytes embedded in the neighborhood of the trabecular surface play a primary role as mechanosensory cells during the bone remodeling process.

Keywords Interstitial fluid flow • Trabecula • Mechanosensory cell • Cyclic load • Poroelasticity

3.1 Introduction

An individual trabecula in cancellous bone is a porous material consisting of a calcified bone matrix and interstitial fluid within a lacuno-canalicular porosity. The trabeculae within a living body are usually subjected to low-frequency cyclic loading owing to locomotion (1–2 Hz) and posture maintenance (15–20 Hz) (Weinbaum et al. 1994). The deformation of the bone matrix under such external loading induces a flow of interstitial fluid. Experimental and theoretical studies have shown that an interstitial fluid flow is likely to be a mechanical cue initiating an osteocytic response (Burger and Klein-Nulend 1999; Price et al. 2011; Weinbaum et al. 1994).

For a quantitative evaluation of an interstitial fluid flow present in bone tissue, Biot's poroelastic theory (Biot 1941, 1955) has been widely applied (Cowin 1999). Poroelasticity is a continuum theory that considers the mechanical behavior of a fluid-saturated porous medium based on the interactions between the elastic deformation of a solid matrix and the flow of an internal fluid. A number of analytical studies on fluid-saturated bones have employed a poroelastic approach that considers bone tissue as an isotropic material (Kameo et al. 2008; Zeng et al. 1994;

This Chapter was adapted from Kameo et al. (2009) with permission from Elsevier.

Y. Kameo et al., *Bone Adaptation*, Frontiers of Biomechanics 2,
https://doi.org/10.1007/978-4-431-56514-7_3

Zhang and Cowin 1994) or a transversely isotropic material (Remond and Naili 2005). In other studies, a poroelastic finite element method has been applied to quantify the fluid pressure behavior found in bone tissue (Manfredini et al. 1999; Pereira and Shefelbine 2014; Remond et al. 2008).

In this chapter, we describe an analytical investigation of the mechanical behavior of an individual poroelastic trabecula in response to physiological cyclic loading based on poroelasticity. We present an analytical solution for a fluid pressure that contains both the transient and steady-state responses in two-dimensional poroelastic materials subjected to cyclic axial and bending loads. Based on the solution obtained, we demonstrate how two parameters, i.e., the loading frequency and the axial-bending loading ratio, influence the interstitial fluid flow, which is associated with the mechanical stimuli to the osteocytes.

3.2 Theory of Poroelasticity

This section presents a summary of the linear poroelasticity. In this theory, the constitutive equations are based on the assumption that the pairing of stress and fluid pressure is linearly related to the pairing of strain and fluid variation. Using these constitutive relations, two governing equations can be obtained from the strain compatibility and fluid continuity equations, respectively.

3.2.1 Constitutive Relations

We used the linear poroelasticity (Coussy 2004; Detournay and Cheng 1993; Wang 2000) to describe the solid-fluid interaction in an individual trabecula under the assumption of small perturbations. In particular, we focused on the quasi-static mechanical behavior because the bone tissue within a living body is usually subjected to low-frequency cyclic loading from daily activities.

The Biot formulation of the constitutive equations for a fluid-saturated porous material is based on the assumption that both the infinitesimal deformation of the porous material and the interstitial fluid flow are expressed as a linear sum of the contributions of the stress and fluid pressure. The constitutive relations for isotropic poroelastic materials are expressed using the solid strain tensor ε_{ij}, total stress tensor σ_{ij}, interstitial fluid pressure p, and variation in fluid content ζ, defined as a variation in the volume of per unit volume of a porous material:

$$\varepsilon_{ij} = \frac{1}{2G}\left(\sigma_{ij} - \frac{\nu}{1+\nu}\sigma_{kk}\delta_{ij}\right) + \frac{\alpha}{3K}p\delta_{ij}, \tag{3.1}$$

$$\zeta = \frac{\alpha}{K}\frac{\sigma_{kk}}{3} + \frac{\alpha}{KB}p, \tag{3.2}$$

where σ_{kk} represents a sum of the three normal stresses using the Einstein summation convention for repeated subscripts, and δ_{ij} is the Kronecker delta, that is, $\delta_{ij} = 1$ if $i = j$, and $\delta_{ij} = 0$ if $i \neq j$. In the above equation, G, ν and K are the shear modulus, Poisson's ratio, and bulk modulus under drained conditions, respectively, that satisfy $K = 2G(1+\nu)/3(1-2\nu)$. The Biot-Willis coefficient α and Skempton coefficient B in Eqs. (3.1) and (3.2) are given by

$$\alpha = 1 - \frac{K}{K_s}, \tag{3.3}$$

$$B = \frac{1/K - 1/K_s}{\phi/K_f + 1/K - (1+\phi)/K_s}, \tag{3.4}$$

where K_s is the solid bulk modulus, K_f is the fluid bulk modulus, and ϕ is the porosity.

Assuming an isotropic flow through a porous material, which is governed by Darcy's law, the fluid flux component q_i is related to the fluid pressure gradient $p_{,i}$ as

$$q_i = -\frac{k}{\mu}p_{,i}, \tag{3.5}$$

where k is the intrinsic permeability and μ is the dynamic viscosity of the fluid. Equations (3.1), (3.2), and (3.5) are constitutive equations used for the linear poroelasticity.

3.2.2 *Governing Equations*

To investigate the quasi-static behavior of poroelastic materials, a linear momentum conservation equation without inertia terms, i.e., a stress equilibrium equation, is utilized. The stress equilibrium equation for a poroelastic material is

$$\sigma_{ji,j} + F_i = 0, \tag{3.6}$$

where F_i is the body forces component. Using the constitutive equation, Eq. (3.1); the equilibrium equation, Eq. (3.6), in the absence of body forces; and the displacement-strain relation,

$$\varepsilon_{ij} = \frac{1}{2}\left(u_{i,j} + u_{j,i}\right), \tag{3.7}$$

the strain compatibility equations lead to the following relationship between the sum of the three normal stresses σ_{kk} and the fluid pressure p:

$$\nabla^2\left[\sigma_{kk} + \frac{2\alpha(1-2\nu)}{(1-\nu)}p\right] = 0, \tag{3.8}$$

where ∇^2 represents the Laplace operator.

The equation of fluid continuity is expressed as

$$\frac{\partial \zeta}{\partial t} + q_{k,k} = Q, \tag{3.9}$$

where Q is the source density, i.e., the rate of fluid injection per unit volume of a porous solid. Using the constitutive equation, Eq. (3.2); Darcy's law, Eq. (3.5); the strain compatibility equation, Eq. (3.8); and Eq. (3.9) in the absence of a fluid source, the total stress tensor σ_{ij} and fluid pressure p satisfy the following diffusion equation:

$$c\nabla^2\left(\sigma_{kk} + \frac{3}{B}p\right) = \frac{\partial}{\partial t}\left(\sigma_{kk} + \frac{3}{B}p\right), \tag{3.10}$$

in which the diffusion coefficient c is given by

$$c = \frac{k}{\mu}\left[\frac{2GB^2(1-\nu)(1+\nu_u)^2}{9(1-\nu_u)(\nu_u-\nu)}\right], \tag{3.11}$$

where ν_u is the undrained Poisson's ratio, which is defined by

$$\nu_u = \frac{3\nu + \alpha B(1-2\nu)}{3 - \alpha B(1-2\nu)} \tag{3.12}$$

Equations (3.8) and (3.10) constitute the set of governing equations to be solved. Seven independent material properties are required for a poroelastic analysis: the permeability k, fluid viscosity μ, drained shear modulus G, drained Poisson's ratio ν, solid bulk modulus K_s, fluid bulk modulus K_f, and porosity ϕ.

3.3 Poroelastic Modeling of a Single Trabecula

To represent the mechanical behavior of a single trabecula within a living body, a poroelastic problem concerned with a two-dimensional poroelastic material under cyclic loading was formulated. The initial and boundary value problem presented was analytically solved for the fluid pressure by making use of the Laplace transform technique.

3.3.1 Formulation of Poroelastic Problem

For the model of a single trabecula, we considered a two-dimensional poroelastic material with a width of $2a$ in the x-direction, as shown in Fig. 3.1. This model represents the longitudinal cross-section of an individual cylindrical trabecula. To impose uniform external loadings, two rigid and impermeable plates were placed at the top and bottom of the sample. The edges of the model $x = \pm a$ were assumed to be drained, i.e., the fluid pressure p satisfies

$$p(x = \pm a, t) = 0 \tag{3.13}$$

Both the cyclic axial load per unit thickness $N(t)$ with amplitude N_0, and the cyclic bending moment per unit thickness $M(t)$ with amplitude M_0, were applied in the same phase along the y-direction through the plates at the initial time of $t = 0$. The boundary conditions for the stresses are given as

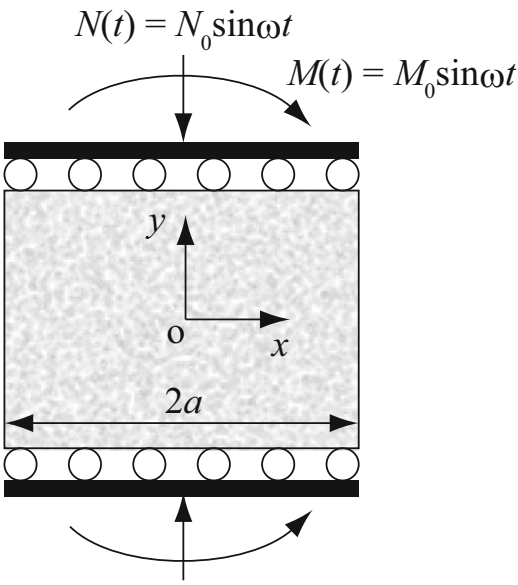

Fig. 3.1 Model of a single trabecula subjected to cyclic axial and bending loads (This figure was adapted from Kameo et al. (2009) with permission from Elsevier)

$$\int_{-a}^{a} \sigma_{yy} dx = -N(t) = -N_0 \sin \omega t, \tag{3.14}$$

$$\int_{-a}^{a} x\sigma_{yy} dx = -M(t) = -M_0 \sin \omega t, \tag{3.15}$$

where ω is the angular frequency of the applied cyclic loads. The initial condition of the poroelastic material was assumed to be at rest, that is, $\sigma_{ij}(x, t = 0) = 0$ and $p(x, t = 0) = 0$.

Considering the problem symmetry, the stress components σ_{ij} and fluid pressure p depend solely on x and t. Assuming no shear stresses throughout the poroelastic material, i.e., $\sigma_{xy}(x, t) = 0$, and stress-free edges $x = \pm a$, the stress equilibrium in the x-direction requires $\sigma_{xx}(x, t) = 0$. Under a plane strain condition in the z-direction, the constitutive relations yield the following:

$$\sigma_{kk} = (1 + \nu)\sigma_{yy} - (1 - 2\nu)\alpha p \tag{3.16}$$

Substituting Eq. (3.16) into Eqs. (3.8) and (3.10), the governing equations are reduced to

$$\frac{\partial^2}{\partial x^2}\left[\sigma_{yy} + \frac{\alpha(1 - 2\nu)}{(1 - \nu)} p\right] = 0, \tag{3.17}$$

$$c\frac{\partial^2}{\partial x^2}\left[\sigma_{yy} + \frac{3}{B(1 + \nu_u)} p\right] = \frac{\partial}{\partial t}\left[\sigma_{yy} + \frac{3}{B(1 + \nu_u)} p\right] \tag{3.18}$$

By introducing the following dimensionless values,

$$\left.\begin{aligned} x^* &= \frac{x}{a}, \quad t^* = \frac{ct}{a^2} \\ \sigma_{ij}^* &= \frac{2a\sigma_{ij}}{N_0}, \quad p^* = \frac{p}{B(1 + \nu_u)N_0/6a} \\ H &= \frac{1 - \nu}{\nu_u - \nu}, \quad \Omega = \frac{a^2\omega}{c}, \quad \Lambda = \frac{3M_0}{aN_0} \end{aligned}\right\}, \tag{3.19}$$

with the governing equations and boundary conditions, Eqs. (3.17) and (3.18) and Eqs. (3.13), (3.14), and (3.15) are rewritten as follows:

$$\frac{\partial^2}{\partial x^{*2}}\left(\sigma_{yy}^* + \frac{1}{H} p^*\right) = 0, \tag{3.20}$$

$$\frac{\partial^2}{\partial x^{*2}}\left(\sigma_{yy}^* + p^*\right) = \frac{\partial}{\partial t^*}\left(\sigma_{yy}^* + p^*\right), \tag{3.21}$$

$$p^*(x^* = \pm 1, t^*) = 0, \tag{3.22}$$

$$\int_{-1}^{1} \sigma_{yy}^{*} dx^{*} = -2 \sin \Omega t^{*}, \tag{3.23}$$

$$\int_{-1}^{1} x^{*} \sigma_{yy}^{*} dx^{*} = -\frac{2}{3} \Lambda \sin \Omega t^{*}, \tag{3.24}$$

Henceforth, H is a dimensionless stress coefficient, Ω is a dimensionless frequency, and Λ is the axial-bending loading ratio.

3.3.2 Analytical Solution for Fluid Pressure

We solved the initial and boundary value problem shown in the previous section analytically for fluid pressure p^{*}. The integration of Eq. (3.20) yields

$$\sigma_{yy}^{*}(x^{*}, t^{*}) + \frac{1}{H} p^{*}(x^{*}, t^{*}) = C_1(t^{*}) x^{*} + C_2(t^{*}), \tag{3.25}$$

where C_1 and C_2 are integration constants that depend solely on time t^{*}. Substituting $x^{*} = \pm 1$ into Eq. (3.25) using the diffusion equation, Eq. (3.21), C_1 and C_2 are expressed in the following form:

$$C_1(t^{*}) = \frac{1}{2} \left\{ \sigma_{yy}^{*}(1, t^{*}) - \sigma_{yy}^{*}(-1, t^{*}) \right\}, \tag{3.26}$$

$$C_2(t^{*}) = \frac{1}{2} \left\{ \sigma_{yy}^{*}(1, t^{*}) + \sigma_{yy}^{*}(-1, t^{*}) \right\} \tag{3.27}$$

Substituting Eq. (3.25) into Eq. (3.21) to eliminate the fluid pressure p^{*} leads to the following partial differential equation for the stress σ_{yy}^{*}:

$$\frac{\partial^2 \sigma_{yy}^{*}(x^{*}, t^{*})}{\partial x^{*2}} = \frac{\partial \sigma_{yy}^{*}(x^{*}, t^{*})}{\partial t^{*}} + \frac{H}{1 - H} \left\{ \frac{dC_1(t^{*})}{dt^{*}} x^{*} + \frac{dC_2(t^{*})}{dt^{*}} \right\} \tag{3.28}$$

By taking the Laplace transform of Eq. (3.28) with the assumption of no stress under the initial conditions, the fundamental solution of Eq. (3.28) is obtained as follows:

$$\begin{aligned} \tilde{\sigma}_{yy}^{*}(x^{*}, s) = {} & A(s) \cosh \sqrt{s} x^{*} + B(s) \sinh \sqrt{s} x^{*} \\ & - \frac{H}{1 - H} \left\{ \tilde{C}_1(s) x^{*} + \tilde{C}_2(s) \right\}, \end{aligned} \tag{3.29}$$

where the tilde (˜) signifies the Laplace transform, and $A(s)$ and $B(s)$ are unknown coefficients to be determined from the boundary conditions. Substituting $x^* = \pm 1$ into Eq. (3.29) and using the Laplace transform of Eqs. (3.26) and (3.27) yields

$$\tilde{C}_1(s) = (1-H)B(s)\sinh\sqrt{s}, \tag{3.30}$$

$$\tilde{C}_2(s) = (1-H)A(s)\cosh\sqrt{s} \tag{3.31}$$

Therefore, the substitution of Eqs. (3.30) and (3.31) into Eq. (3.29) leads to

$$\begin{aligned}\tilde{\sigma}^*_{yy}(x^*,s) = A(s)\{\cosh\sqrt{s}x^* - H\cosh\sqrt{s}\}+ \\ B(s)\{\sinh\sqrt{s}x^* - x^*H\sinh\sqrt{s}\}.\end{aligned} \tag{3.32}$$

The application of the Laplace transforms of the boundary conditions Eqs. (3.23) and (3.24), and the use of Eq. (3.32), yield

$$A(s) = -\frac{\frac{\Omega}{s^2+\Omega^2}\sqrt{s}}{\sinh\sqrt{s} - H\sqrt{s}\cosh\sqrt{s}}, \tag{3.33}$$

$$B(s) = -\frac{\Lambda\frac{\Omega}{s^2+\Omega^2}s}{3\sqrt{s}\cosh\sqrt{s} - \sinh\sqrt{s}(3+Hs)} \tag{3.34}$$

Thus, all of the unknown parameters are determined.

By substituting Eqs. (3.30), (3.31) and (3.32) into the Laplace transform of Eq. (3.25), the fluid pressure solution in the Laplace transformed domain is expressed as

$$\begin{aligned}\tilde{p}^*(x^*,s) = A(s)H\{\cosh\sqrt{s} - \cosh\sqrt{s}x^*\}+ \\ B(s)H\{x^*\sinh\sqrt{s} - \sinh\sqrt{s}x^*\}.\end{aligned} \tag{3.35}$$

The inverse Laplace transform of Eq. (3.35) with the help of the residue theorem eventually provides the solution of the fluid pressure in the form of the summation of the transient solution p^*_{trans} and the steady-state solution p^*_{steady}:

$$p^*(x^*,t^*) = p^*_{\text{trans}}(x^*,t^*) + p^*_{\text{steady}}(x^*,t^*), \tag{3.36}$$

$$\begin{aligned}p^*_{\text{trans}}(x^*,t^*) = 2\sum_{n=1}^{\infty}\frac{\Omega\lambda_n^2\sin\lambda_n(\cos\lambda_n - \cos\lambda_n x^*)}{(\lambda_n^4+\Omega^2)(\lambda_n - \sin\lambda_n\cos\lambda_n)}e^{-\lambda_n^2 t^*} \\ +2\Lambda\sum_{n=1}^{\infty}\frac{\Omega\mu_n^2(\sin\mu_n - \mu_n\cos\mu_n)(x^*\sin\mu_n - \sin\mu_n x^*)}{(\mu_n^4+\Omega^2)(\mu_n^2+\mu_n\sin\mu_n\cos\mu_n - 2\sin^2\mu_n)}e^{-\mu_n^2 t^*},\end{aligned} \tag{3.37}$$

$$p^*_{\text{steady}}(x^*, t^*) = (1 + \Lambda x^*)\sin \Omega t^* - \text{Im}\left[\left\{\frac{H\sqrt{i\Omega}\cosh\sqrt{i\Omega}x^* - \sinh\sqrt{i\Omega}}{H\sqrt{i\Omega}\cosh\sqrt{i\Omega} - \sinh\sqrt{i\Omega}} + \Lambda\frac{i\Omega H\sinh\sqrt{i\Omega}x^* + 3x^*\left(\sinh\sqrt{i\Omega} - \sqrt{i\Omega}\cosh\sqrt{i\Omega}\right)}{i\Omega H\sinh\sqrt{i\Omega} + 3\left(\sinh\sqrt{i\Omega} - \sqrt{i\Omega}\cosh\sqrt{i\Omega}\right)}\right\}e^{i\Omega t}\right], \tag{3.38}$$

where Im provides the imaginary part of the complex number, and λ_n and μ_n, respectively, are the n-th positive roots of

$$\frac{\tan\lambda_n}{\lambda_n} = H, \tag{3.39}$$

$$\frac{\tan\mu_n}{\mu_n} = \frac{3}{3 - H\mu_n^2} \tag{3.40}$$

Equations (3.36), (3.37), (3.38), (3.39), and (3.40) indicate that the fluid pressure p^* depends on three dimensionless parameters, H, Ω, and Λ. The dimensionless stress coefficient H is the parameter related to the material properties of the matrix material and interstitial fluid that constitute the poroelastic material. Both the dimensionless frequency Ω and the axial-bending loading ratio Λ are determined by the loading conditions representing the temporal and spatial characteristics.

3.4 Interstitial Fluid Pressure in Trabecula

This section first presents an overview of the results obtained regarding the fluid pressure behavior (Sect. 3.4.1), and follows with a more detailed description of the characteristics of the steady-state (Sect. 3.4.2) and transient (Sect. 3.4.3) responses.

3.4.1 Description of Fluid Pressure Behavior

As the dimensionless stress coefficient H increases, the effect of the fluid-to-solid coupling in a poroelastic material becomes negligible compared to that of a solid-to-fluid coupling, which is due to the fact that, for a large H, the matrix material supports much more of the mechanical load than the internal fluid. Indeed, it was reported that the distribution and evolution of the fluid pressure under cyclic loading are nearly independent of the value of H when H is larger than 50 (Kameo et al. 2008). In the current study, we focus on the dependence of the fluid pressure on the loading condition, and investigated the effects of dimensionless parameters Ω and Λ on the fluid pressure behavior, with $H = 100$.

The dimensionless frequency Ω defined in Eq. (3.19) represents the ratio of the characteristic time of the fluid pressure relaxation, $\tau_r = a^2/c$, to that of the applied load, $\tau_f = 1/\omega$. The fluid pressure distributions along the x-direction for $\Omega = 0.1$, 1, 10 and 100, with $\Lambda = 1$, are shown in Fig. 3.2. Figure 3.2a corresponds to the steady-state response p^*_{steady} plotted for eight phase points of equal length within a period, and Fig. 3.2b corresponds to the transient response p^*_{trans} plotted at $t^* = 0$, 0.01, 0.1 and 1. The fluid pressure evolution at $x^* = 0$ for $\Omega = 0.1$, 1, 10 and 100, with $\Lambda = 1$, is shown in Fig. 3.3. In each set of figures, the lower graph is an enlarged view of the upper graph from the initial time, $t^* = 0$, to the 1/12 period of the corresponding cyclic loading.

Referring to Eq. (3.19), the axial-bending loading ratio Λ indicates the ratio of the magnitude of the bending moment to that of the axial load. The fluid pressure distributions for $\Lambda = 0.1$, 1, 10 and 100, with $\Omega = 1$, are shown in Fig. 3.4. Figure 3.4a and b correspond to the steady-state response p^*_{steady} and the transient response p^*_{trans}, respectively.

For a quantification of the transient properties of the fluid pressure, we introduced two factors. The first factor is the half-value period of the transient stage $T_{1/2}$, which is defined by

$$T_{1/2} \equiv \frac{\Omega}{2\pi}\left(\int_{-1}^{1} \left|P^*_{\text{trans}}\right| dx^*\right)_{1/2}, \tag{3.41}$$

where $(\,)_{1/2}$ signifies the dimensionless time interval required for the quantity in parenthesis to decay to half of its initial value. The half-value period $T_{1/2}$ quantifies the decay rate of the integration value of p^*_{trans} over the width normalized by the period of applied cyclic loading. The second factor is the contribution of the transient response Π, which is defined by

$$\Pi \equiv \frac{\int_0^{\frac{2\pi}{\Omega}} \left(\int_{-1}^{1} \left|P^*_{\text{trans}}\right| dx^*\right) dt^*}{\int_0^{\frac{2\pi}{\Omega}} \left(\int_{-1}^{1} \left|P^*_{\text{steady}}\right| dx^*\right) dt^*} \tag{3.42}$$

This factor represents the ratio of the magnitude of the transient response to that of the steady-state response during the first period of the loading cycle. Both the half-value period of the transient stage $T_{1/2}$ and the contribution factor of the transient response Π are functions of the dimensionless frequency Ω and axial-bending loading ratio Λ when the dimensionless stress coefficient H is a constant. To identify the effects of Ω and Λ on the two factors above, which are associated with the transient properties, Figs. 3.5 and 3.6 show $T_{1/2}$ and Π plotted three-dimensionally versus $\log_{10}\Lambda$ and $\log_{10}\Omega$, respectively.

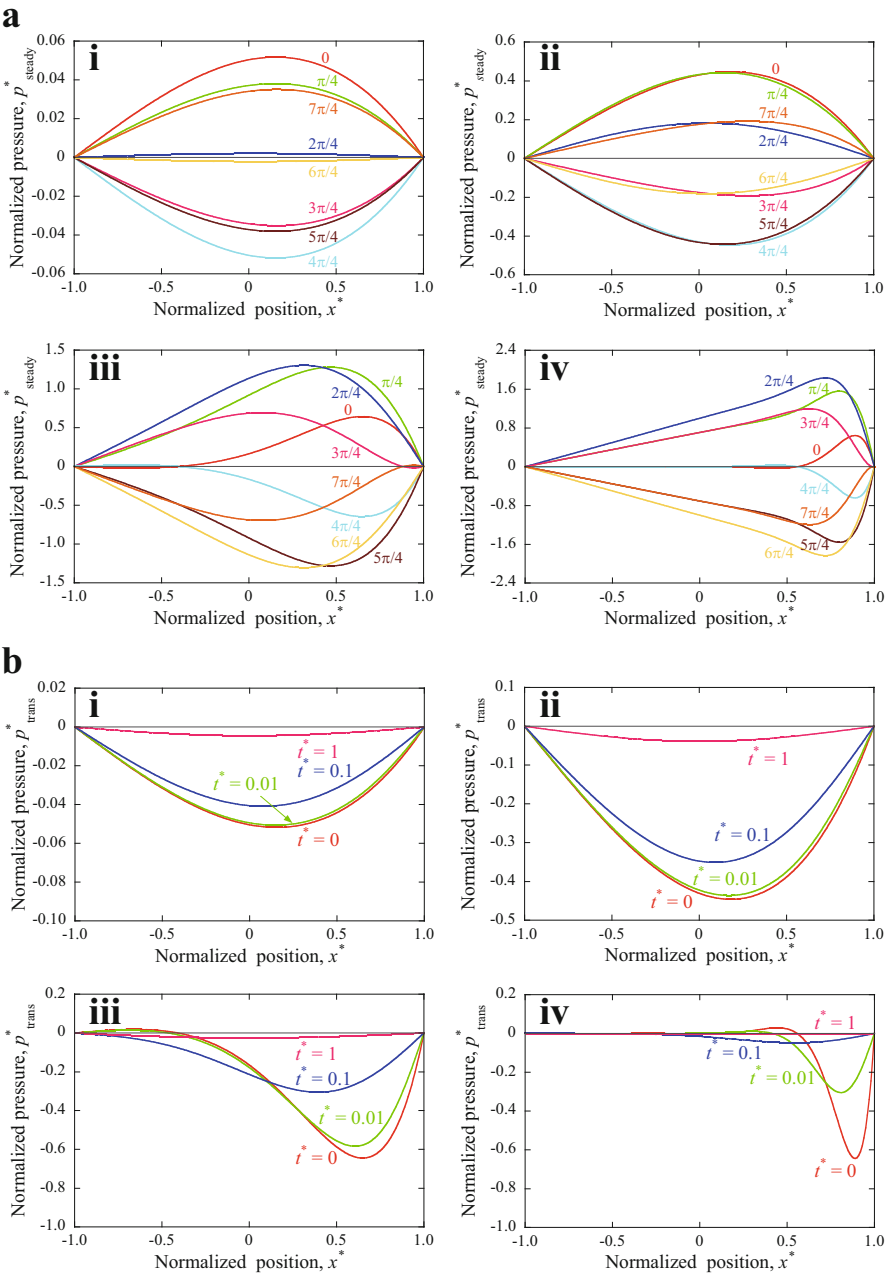

Fig. 3.2 Fluid pressure distribution along the x-direction for $\Lambda = 1$: (**a**) steady-state response (*i*) $\Omega = 0.1$, (*ii*) $\Omega = 1$, (*iii*) $\Omega = 10$, and (*iv*) $\Omega = 100$, and (**b**) transient response (*i*) $\Omega = 0.1$, (*ii*) $\Omega = 1$, (*iii*) $\Omega = 10$, and (*iv*) $\Omega = 100$ (This figure was adapted from Kameo et al. (2009) with permission from Elsevier)

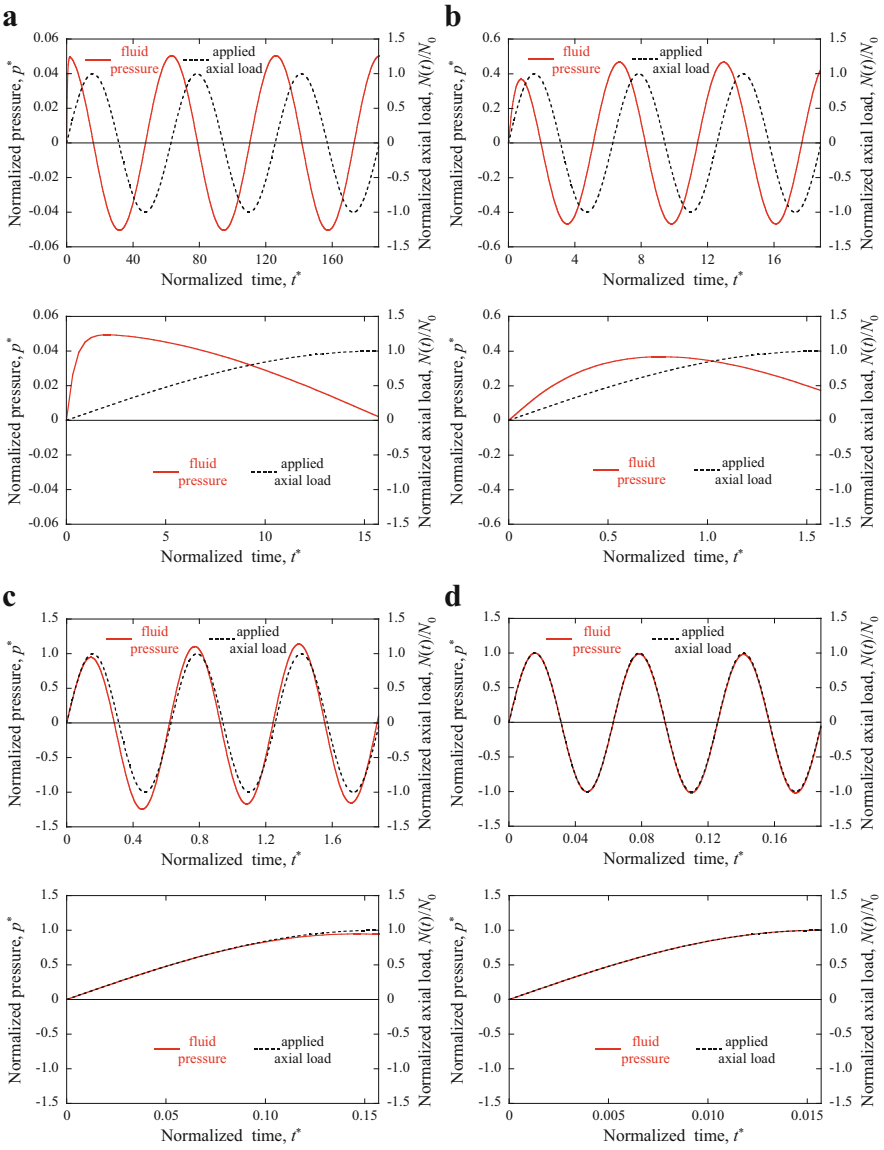

Fig. 3.3 Fluid pressure evolution at $x^* = 0$ for $\Lambda = 1$ (**a**) $\Omega = 0.1$, (**b**) $\Omega = 1$, (**c**) $\Omega = 10$, and (**d**) $\Omega = 100$. Each of the lower graphs is an enlarged view of the upper graph from $t^* = 0$ to the 1/12 period of the corresponding cyclic loading (This figure was adapted from Kameo et al. (2009) with permission from Elsevier)

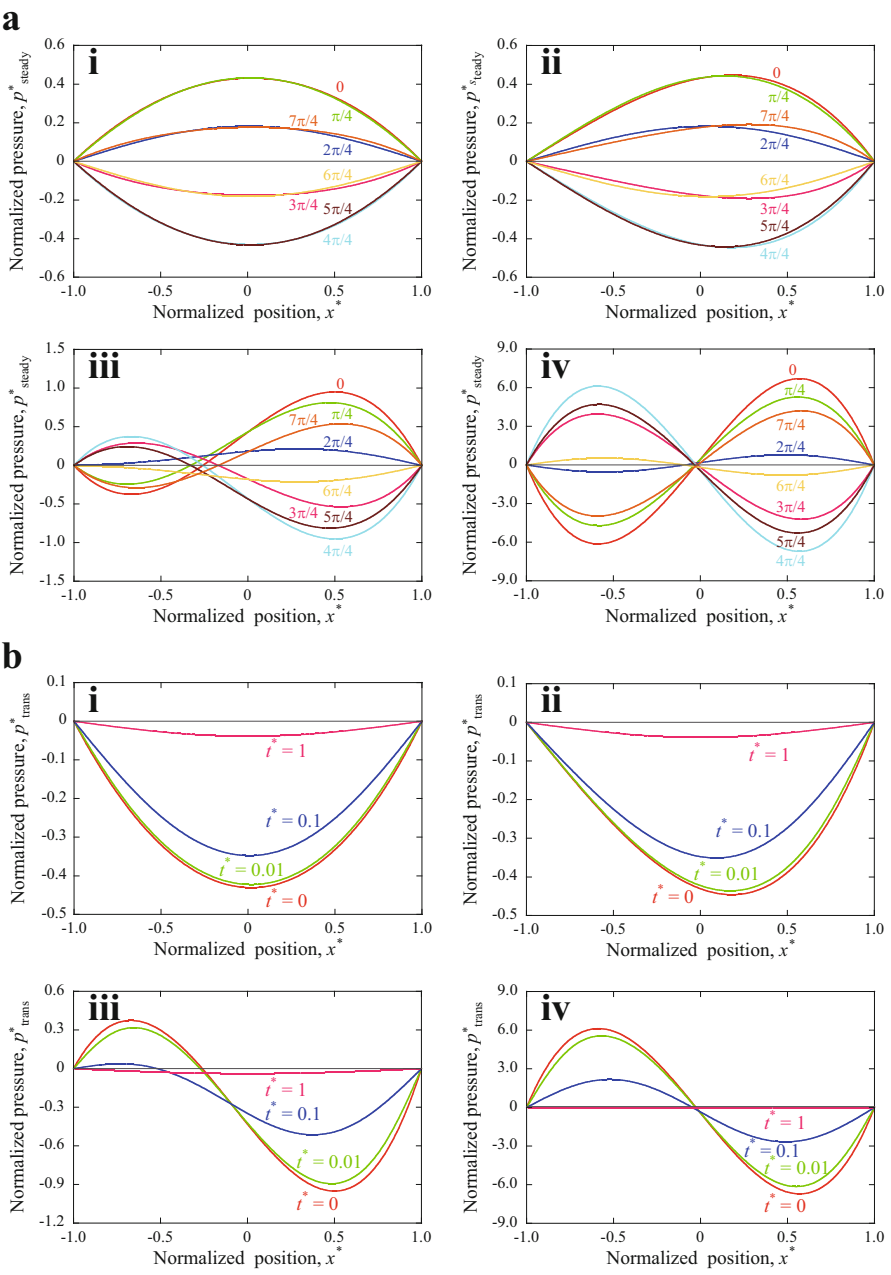

Fig. 3.4 Fluid pressure distribution along the x-direction for $\Omega = 1$: (**a**) steady-state response (*i*) $\Lambda = 0.1$, (*ii*) $\Lambda = 1$, (*iii*) $\Lambda = 10$, and (*iv*) $\Lambda = 100$, and (**b**) transient response (*i*) $\Lambda = 0.1$, (*ii*) $\Lambda = 1$, (*iii*) $\Lambda = 10$, and (*iv*) $\Lambda = 100$ (This figure was adapted from Kameo et al. (2009) with permission from Elsevier)

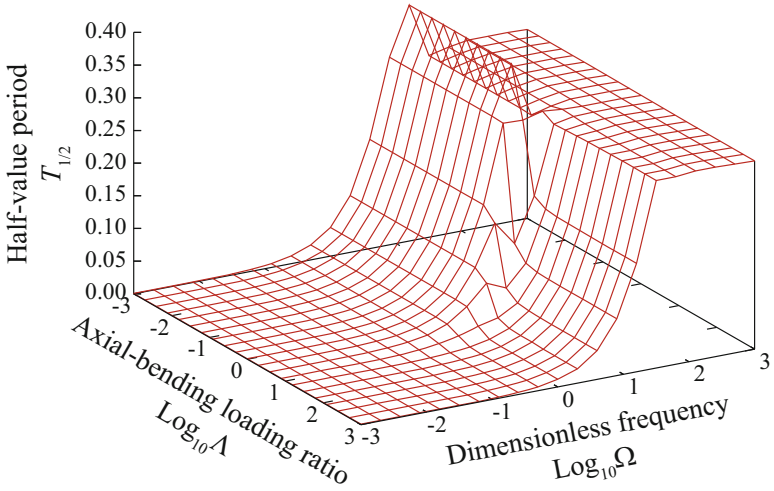

Fig. 3.5 The half-value period of the transient stage $T_{1/2}$ versus $\log_{10}\Lambda$ and $\log_{10}\Omega$ (This figure was adapted from Kameo et al. (2009) with permission from Elsevier)

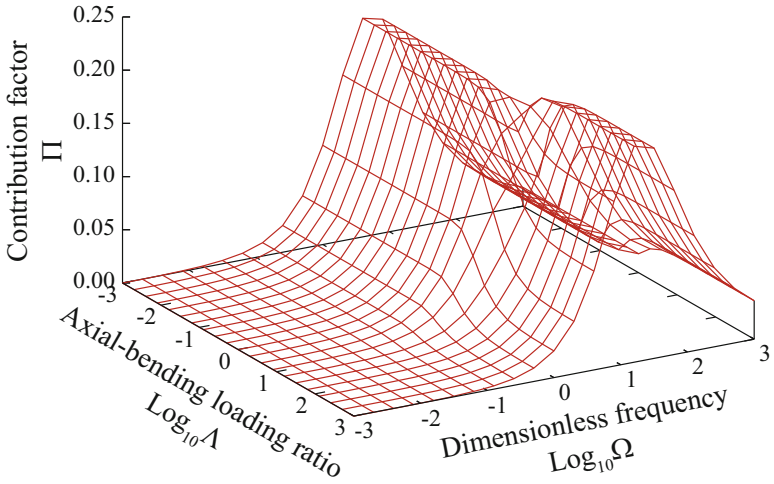

Fig. 3.6 The contribution factor of the transient response Π versus $\log_{10}\Lambda$ and $\log_{10}\Omega$ (This figure was adapted from Kameo et al. (2009) with permission from Elsevier)

3.4.2 Steady-State Response

As shown in Fig. 3.2a, the fluid pressure in a steady state is built up with an increase in the dimensionless frequency Ω because the excess fluid pressure has difficulty diffusing owing to the rapid change in applied loading. In addition, the fluid pressure profile along the x-direction transforms from a parabolic shape into a linear shape, leading to an increase in the fluid pressure gradient near the surface, particularly in the positive region of the x-coordinates. Figure 3.3 indicates that there was a remarkable phase shift between the applied cyclic loading and the corresponding fluid pressure evolution in a steady state at $x^* = 0$ at low frequency ($\Omega = 0.1$) owing to the interstitial fluid transport. On the other hand, when Ω is larger than 10, the profiles are nearly in phase because the interstitial fluid has difficulty moving at a high frequency.

Recalling that the fluid pressure p is normalized by the amplitude of axial load N_0, as shown in Eq. (3.19), the axial-bending loading ratio Λ can be regarded as the dimensionless bending moment when N_0 is constant. Figure 3.4a indicates that the fluid pressure increases with Λ owing to the additional bending moment. When the magnitude of axial load is much larger than that of the bending moment ($\Lambda = 0.1$), the fluid pressure profile has a symmetric shape about $x^* = 0$. However, the increase in Λ causes a sign inversion of the fluid pressure around both surfaces of the poroelastic material. When the bending moment is dominant compared to the axial load ($\Lambda = 100$), the fluid pressure profile exhibits an antisymmetric shape about $x^* = 0$. This transition of the fluid pressure profile with an increasing axial-bending loading ratio Λ induces a significant fluid pressure gradient, not only in the neighborhood of the material surfaces but also around the center of the material far from the surfaces.

3.4.3 Transient Response

The transient stage was observed after applying cyclic loading to the poroelastic material until the fluid pressure reached a steady state, but decayed within time $t^* = 1$. As shown in Fig. 3.3, the effect of the transient response is dominant when the phase shift between the fluid pressure evolution during the steady state and the applied cyclic loading is remarkable. The magnitude of the transient response is related to such a phase shift because the sum of the transient and steady-state fluid pressures at $t^* = 0$ must be zero to eliminate the phase shift from the initial conditions. As a result, the rate of change in the fluid pressure is enlarged during the transient stage. As mentioned in the previous section, the fluid pressure evolution and the applied cyclic loading are nearly in phase for a large dimensionless frequency Ω. Therefore, the effect of the transient response is limited to the region close to the surface of the poroelastic material when Ω is large, as shown in Fig. 3.2b.

Figure 3.5 shows that the half-value period of the transient stage $T_{1/2}$ reaches a plateau at 0.29 as Ω increases. This factor has a peak value of 0.36 when Λ is smaller than 1 ($\log_{10}\Lambda < 0$) and Ω is about 10 ($\log_{10}\Omega \sim 1$). These results suggest that the effect of the transient response is reduced by 50% during the first 0.4 period of the applied cyclic loading. For the contribution factor of the transient response Π, Fig. 3.6 shows that there is a spike of Π at around $\Omega = 10$ ($\log_{10}\Omega \sim 1$) with a peak value of 0.20, whereas the value of Ω that maximizes Π varies at around $\Lambda = 1$ ($\log_{10}\Lambda \sim 0$). This result indicates that the magnitude of the transient response is about 20% of that of the steady-state response under any loading conditions. In contrast to the behavior of $T_{1/2}$, Π gradually declines after the peak with an increase in Ω because the effect of the transient response becomes trivial when Ω increases, as shown in Fig. 3.2b.

3.5 Importance of Transient Fluid Pressure Response

There have been many studies conducted on the mechanical behavior of poroelastic materials under cyclic loading in a variety of fields, including geomechanics (Bredehoeft 1967; Jacob 1940; Quilty and Roeloffs 1991; Roeloffs 1996; Rojstaczer 1988) and biomechanics (Harrigan and Hamilton 1993; Swan et al. 2003; Weinbaum et al. 1994; Zhang and Cowin 1994; Zhang et al. 1998). Although a detailed understanding of the poroelastic behavior requires an investigation into the transient response observed immediately after loading, few reports have addressed this phenomenon.

The importance of the transient stage prior to the steady state was first acknowledged through a finite element analysis of a three-dimensional poroelastic beam under cyclic loading (Manfredini et al. 1999). In this study, the authors reported that the duration of the transient stage was nearly confined to the first cycle of the loading curve. For a free leakage at the surface of the poroelastic material, which corresponds to our boundary condition, the authors described the following characteristics of the fluid pressure evolution around the center far from the surface: (i) When the dimensionless frequency is low ($\Omega = 0.1$), there is an immediate sharp increase in the rate of change in fluid pressure during the transient stage, which leads to a 1/4 phase shift between the fluid pressure evolution and the applied cyclic loading during a steady state. (ii) When the dimensionless frequency is high ($\Omega = 100$), the influence of the transient response is nearly negligible, and the fluid pressure evolution and applied cyclic loading are in phase during a steady state. All of the fluid pressure behaviors above are in agreement with our results (see Fig. 3.3), thereby suggesting the validity of the analytical solution obtained in the present study.

For a quantitative evaluation of the transient properties of the fluid pressure, we introduced two factors: the half-value period $T_{1/2}$, defined by Eq. (3.41), and the contribution factor Π, defined by Eq. (3.42). As shown in Figs. 3.5 and 3.6, the behavior of both factors varies at around $\Lambda = 1$ with an increase in the

dimensionless frequency Ω because the stress distribution for $\Lambda > 1$ has specific characteristics, i.e., there is a region where the stress σ_{yy} in a poroelastic material is neutral. With the exception of such Λ-dependence, $T_{1/2}$ and Π depend almost solely on Ω and have peak values at around $\Omega = 10$. This suggests that the transient response has a magnitude comparable to the steady-state response and can significantly affect the mechanical behavior of poroelastic materials when the dimensionless frequency Ω is around 10.

3.6 Implications of Fluid Flow in Trabecular Bone Remodeling

When the applied cyclic loading can be regarded as quasi-static, the interstitial fluid pressure behavior described in this chapter is commonly observed in various poroelastic materials, including individual trabeculae within a living body. For a physiological range of activities excluding shock, living bone experiences only low frequencies of loading and exhibits a quasi-static mechanical behavior.

The mechanical behavior of trabeculae is influenced significantly by two factors: the material properties and the loading conditions. For two-dimensional poroelastic materials subjected to cyclic loading, the material properties are represented by the dimensionless stress coefficient H and the loading conditions are represented by the dimensionless frequency Ω and axial-bending loading ratio Λ. Using the material properties of trabeculae (Smit et al. 2002), the dimensionless stress coefficient H was derived as 82.6. This indicates that the H of trabeculae is sufficiently large, and thus the interstitial fluid behavior is nearly independent of H. Meanwhile, the dimensionless frequency Ω depends not only on the angular loading frequency ω but also on the model size a and the diffusion coefficient c, which is proportional to the permeability k. Considering the bone permeability at the lacuno-canalicular level, $k = 10^{-22}$–10^{-19} m^2 (Beno et al. 2006), under the assumption of the typical width of an individual trabecula, $a = 100$ μm, and the physiological loading frequency, 1–20 Hz, the dimensionless frequency Ω that trabeculae experience during daily activities is estimated to be 10^{-2}–10^{2}. Such a broad range for this estimated value, which is mainly due to the difficulty of determining the permeability, covers the range of dimensionless frequencies where the contribution of transient response is comparatively large ($\Omega \sim 10$). This suggests that considering the effects of the transient response is critical for an analysis of the interstitial fluid flow in trabeculae. The axial-bending loading ratio Λ depends on the location where the individual trabecula is placed in cancellous bone, and is expected to have a wide range of values from zero to infinity. It seems reasonable to assume that the variations in Ω and Λ in cancellous bone induce a variety of mechanical stimuli that the osteocytes sense through an interstitial fluid flow, and as a result, bone resorption and formation are appropriately regulated.

The seepage velocity in poroelastic materials is one of the mechanical properties quantifying the fluid flow at the macroscopic scale. In the context of bone poroelasticity, the seepage velocity represents the average velocity of interstitial fluid in a lacuno-canalicular porosity and is closely associated with the mechanical stimuli to the osteocytes during the bone remodeling process. This quantity is proportional to the fluid pressure gradient, which is the driving force of a fluid flow. Figure 3.2 shows that, as the dimensionless frequency Ω increases, the seepage velocity, and thus the mechanical stimuli to the osteocytes close to the trabecular surface increases. Furthermore, as shown in Fig. 3.4, an increase in the axial-bending loading ratio Λ produces a larger seepage velocity around the center of the trabecula, stimulating the osteocytes. Considering that the seepage velocity near the trabecular surface is always larger than that far from the surface regardless of the values of Ω and Λ, the results obtained in the current analytical study imply that osteocytes buried within the neighborhood of a trabecular surface operate primarily as mechanosensory cells during the bone remodeling process.

3.7 Conclusion

In this chapter, we developed an analytical solution for the interstitial fluid pressure in two-dimensional poroelastic materials subjected to cyclic axial and bending loads. The analytical solution contains steady-state and transient responses, both of which depend on three dimensionless parameters: the dimensionless stress coefficient H governing the solid-fluid coupling behavior in a poroelastic material; the dimensionless frequency Ω, which indicates the ratio of the characteristic time of the fluid pressure relaxation to that of the applied load; and the axial-bending loading ratio Λ, which represents the ratio of the magnitude of the bending moment to that of the axial load. Using the material properties of trabeculae, we investigated the behavior of an interstitial fluid flow in a single trabecula with a change in two dimensionless parameters Ω and Λ.

A poroelastic analysis showed that an increase in the dimensionless frequency Ω increases the seepage velocity, which is a characteristic of the mechanical stimuli to osteocytes, close to a trabecular surface. In addition, the increase in axial-bending loading ratio Λ induces an interstitial fluid flow around the center of the trabecula. Regardless of these two values, the seepage velocity close to the trabecular surfaces is consistently larger than that far from the surface. These results suggest that osteocytes embedded in the neighborhood of the trabecular surface play a primary role as mechanosensory cells during the bone remodeling process.

References

Beno T, Yoon YJ, Cowin SC, Fritton SP (2006) Estimation of bone permeability using accurate microstructural measurements. J Biomech 39(13):2378–2387. https://doi.org/10.1016/j.biomech.2005.08.005

Biot MA (1941) General theory of three-dimensional consolidation. J Appl Phys 12(2):155–164. https://doi.org/10.1063/1.1712886

Biot MA (1955) Theory of elasticity and consolidation for a porous anisotropic solid. J Appl Phys 26(2):182–185. https://doi.org/10.1063/1.1721956

Bredehoeft JD (1967) Response of well-aquifer systems to earth tides. J Geophys Res 72 (12):3075–3087. https://doi.org/10.1029/Jz072i012p03075

Burger EH, Klein-Nulend J (1999) Mechanotransduction in bone - role of the lacuno-canalicular network. FASEB J 13:S101–S112

Coussy O (2004) Poromechanics. Wiley, West Sussex

Cowin SC (1999) Bone poroelasticity. J Biomech 32(3):217–238

Detournay E, Cheng AH-D (1993) Fundamentals of poroelasticity. In: Fairhurst C (ed) Comprehensive rock engineering: principles, practice and projects, Analysis and design method, vol II. Pergamon Press, Oxford, pp 113–171

Harrigan TP, Hamilton JJ (1993) Bone strain sensation via transmembrane potential changes in surface osteoblasts - loading rate and microstructural implications. J Biomech 26(2):183–200

Jacob CE (1940) On the flow of water in an elastic artesian aquifer. Trans Am Geophys Union 21:574–586

Kameo Y, Adachi T, Hojo M (2008) Transient response of fluid pressure in a poroelastic material under uniaxial cyclic loading. J Mech Phys Solids 56(5):1794–1805. https://doi.org/10.1016/j.jmps.2007.11.008

Kameo Y, Adachi T, Hojo M (2009) Fluid pressure response in poroelastic materials subjected to cyclic loading. J Mech Phys Solids 57(11):1815–1827. https://doi.org/10.1016/j.jmps.2009.08.002

Manfredini P, Cocchetti G, Maier G, Redaelli A, Montevecchi FM (1999) Poroelastic finite element analysis of a bone specimen under cyclic loading. J Biomech 32(2):135–144

Pereira AF, Shefelbine SJ (2014) The influence of load repetition in bone mechanotransduction using poroelastic finite-element models: the impact of permeability. Biomech Model Mechanobiol 13(1):215–225. https://doi.org/10.1007/s10237-013-0498-8

Price C, Zhou X, Li W, Wang L (2011) Real-time measurement of solute transport within the lacunar-canalicular system of mechanically loaded bone: direct evidence for load-induced fluid flow. J Bone Miner Res 26(2):277–285. https://doi.org/10.1002/jbmr.211

Quilty EG, Roeloffs EA (1991) Removal of barometric pressure response from water level data. J Geophys Res 96(B6):10209–10218. https://doi.org/10.1029/91jb00429

Remond A, Naili S (2005) Transverse isotropic poroelastic osteon model under cyclic loading. Mech Res Commun 32(6):645–651. https://doi.org/10.1016/j.mechrescom.2004.10.003

Remond A, Naili S, Lemaire T (2008) Interstitial fluid flow in the osteon with spatial gradients of mechanical properties: a finite element study. Biomech Model Mechanobiol 7(6):487–495. https://doi.org/10.1007/s10237-007-0111-0

Roeloffs E (1996) Poroelastic techniques in the study of earthquake-related hydrologic phenomena. Adv Geophys 37:135–195. https://doi.org/10.1016/S0065-2687(08)60270-8

Rojstaczer S (1988) Determination of fluid-flow properties from the response of water levels in wells to atmospheric loading. Water Resour Res 24(11):1927–1938. https://doi.org/10.1029/Wr024i011p01927

Smit TH, Huyghe JM, Cowin SC (2002) Estimation of the poroelastic parameters of cortical bone. J Biomech 35(6):829–835

Swan CC, Lakes RS, Brand RA, Stewart KJ (2003) Micromechanically based poroelastic modeling of fluid flow in haversian bone. J Biomech Eng 125(1):25–37. https://doi.org/10.1115/1.1535191

Wang HF (2000) Theory of linear poroelasticity with applications to geomechanics and hydrogeology. Princeton University Press, Princeton

Weinbaum S, Cowin SC, Zeng Y (1994) A model for the excitation of osteocytes by mechanical loading-induced bone fluid shear stresses. J Biomech 27(3):339–360

Zeng Y, Cowin SC, Weinbaum S (1994) A fiber-matrix model for fluid-flow and streaming potentials in the canaliculi of an osteon. Ann Biomed Eng 22(3):280–292. https://doi.org/10.1007/bf02368235

Zhang DJ, Cowin SC (1994) Oscillatory bending of a poroelastic beam. J Mech Phys Solids 42 (10):1575–1599

Zhang DJ, Weinbaum S, Cowin SC (1998) On the calculation of bone pore water pressure due to mechanical loading. Int J Solids Struct 35(34–35):4981–4997

Chapter 4
Estimation of Bone Permeability for Poroelastic Analysis

Abstract Bone permeability is one of the most important material properties addressed in the investigations of interstitial fluid flow in lacuno-canalicular porosities based on poroelastic analysis. This chapter describes a method for estimating bone permeability by deriving the analytical relationship between the volume orientation fabric tensor, which characterizes the canalicular orientation, and the permeability tensor. By applying this method to a cross-sectional image of a cylindrical trabecula, it is shown that canaliculi are predominantly oriented in the radial direction of the trabecula, and the permeability depends largely on the canalicular morphology and dimension.

Keywords Bone permeability • Trabecula • Canalicular anisotropy • Cross-sectional image • Poroelastic Analysis

4.1 Introduction

The flow of the interstitial fluid in a lacuno-canalicular porosity is believed to initiate the mechanical response of osteocytes for bone remodeling, as well as transport cell signaling molecules, nutrients, and waste products (Bonewald and Johnson 2008; Burger and Klein-Nulend 1999; Fritton and Weinbaum 2009; Klein-Nulend et al. 2005; Riddle and Donahue 2009). Poroelastic theory has been widely used for determining the interstitial fluid flow caused by the bone matrix deformation (Cowin 1999; Kameo et al. 2008, 2009; Nowinski 1970), as shown in the Chap. 3. Among the material properties required for performing poroelastic analysis, the permeability, which measures the ability of a porous material to transmit fluids, can significantly influence the mechanical behavior of the interstitial fluid. Despite its importance, direct and exact experimental measurements of permeability are difficult because a typical lacuno-canalicular porosity has a complex three-dimensional structure with a diameter on the order of several hundred nanometers. Therefore, bone permeability is usually determined by combining experimental and theoretical approaches (Beno et al. 2006; Oyen 2008; Smit et al. 2002; Weinbaum et al. 1994).

This Chapter was adapted from Kameo et al. (2010) with permission from Elsevier.

Y. Kameo et al., *Bone Adaptation*, Frontiers of Biomechanics 2,
https://doi.org/10.1007/978-4-431-56514-7_4

In most studies aiming to determine the bone permeability, the bone tissue is regarded as an isotropic material (Oyen 2008; Smit et al. 2002; Weinbaum et al. 1994), even though the lacuno-canalicular porosity and the osteocyte network inside it both have anisotropic morphology. It follows that the interstitial fluid flow in the lacuno-canalicular porosity is strongly anisotropy-dependent. To accurately understand the mechanical behavior of the interstitial fluid, it is necessary to evaluate the orientation of a lacuno-canalicular porosity by using a fabric tensor (Cowin 1985, 1986), and to determine the anisotropic permeability tensor reflecting its characteristic morphology. Beno et al. (2006) focused on the canalicular anisotropy and successfully derived the anisotropic permeability in the three local principal directions around each osteocyte lacuna by considering the directional dependence of the number of canaliculi. However, as these authors mentioned, determining the orientation of each osteocyte lacuna is necessary for building anisotropic poroelastic finite element models that include lacuno-canalicular porosity.

In this chapter, we present a method for estimating the anisotropic bone permeability based on the images of lacuno-canalicular porosity. This method is applied to a two-dimensional cross-sectional image of a cylindrical trabecula acquired by using confocal laser scanning microscopy. First, the canalicular morphology is extracted from the original fluorescence images. Then, the orientation of canaliculi is quantitatively evaluated by using a fabric tensor. Finally, the anisotropic permeability tensor of a single trabecula can be estimated by deriving the analytical relationship between the fabric tensor and the permeability tensor.

4.2 Confocal Laser Scanning Imaging of Lacuno-Canalicular Porosity

A bone specimen for determining the permeability was excised from a swine proximal tibia (8 months old, about 300 kgf). Figure 4.1 shows a fragment of the obtained bone, containing both cancellous and cortical bone, with a cross-section of about 3 × 3 mm. After staining the specimen with RH414 (50 μM), a longitudinal cross-sectional image of a cylinder-like trabecula in the cancellous bone was acquired by using a confocal laser scanning microscope (LSM510, Carl Zeiss), as shown in Fig. 4.2. The obtained image is 256 pixels × 256 pixels, with a pixel size of 0.36 μm. This image reveals three regions with high fluorescence intensity; the slender regions correspond to canaliculi, the ellipsoid-like regions correspond to lacunae, and the region in the upper right corner corresponds to the outside of the trabecula. The typical diameter of the canaliculi (~0.1 μm) is much smaller than that of the lacunae (~10 μm) and the characteristic length of the outside region (~10 μm). Taking advantage of such differences in dimensionality, we extracted

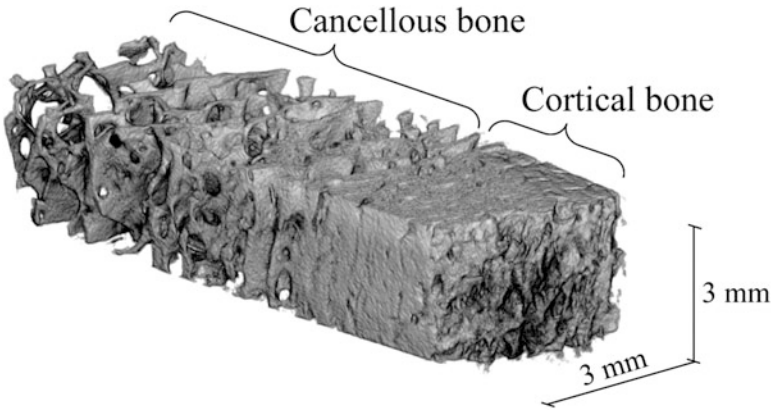

Fig. 4.1 A bone specimen containing cancellous bone and cortical bone excised from a swine proximal tibia. The cross-section dimensions are about 3 × 3 mm (This figure was adapted from Kameo et al. (2010) with permission from Elsevier)

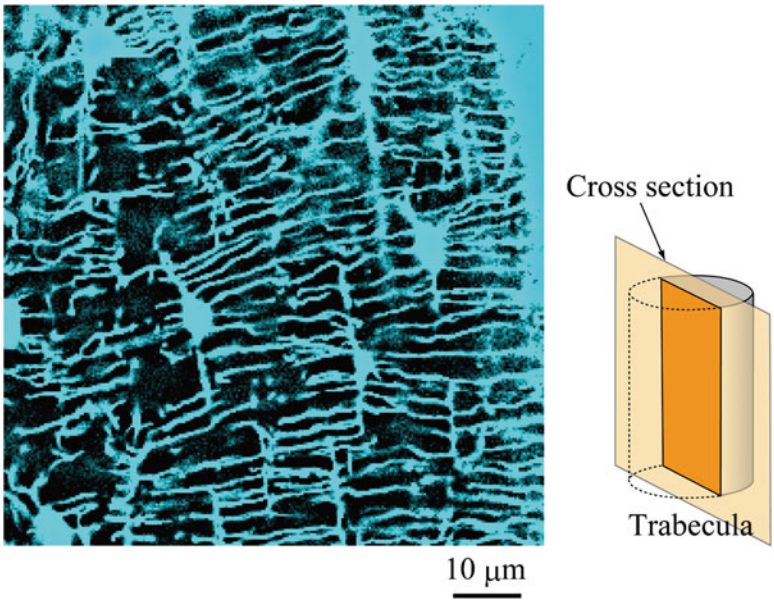

Fig. 4.2 Fluorescence image of the longitudinal cross-section of a cylindrical trabecula. This image was acquired by using a confocal laser scanning microscope. The slender regions correspond to canaliculi, the ellipsoid-like regions correspond to lacunae, and the region in the upper right corner corresponds to the outside of the trabecula (This figure was adapted from Kameo et al. (2010) with permission from Elsevier)

the canalicular morphology from the original image because the interstitial fluid flow in canaliculi is more important than that in lacunae for evaluating the permeability.

The process for extracting the canalicular morphology is schematically shown in Figs. 4.3a–d. First, we introduced the fluorescence intensity field $L(\boldsymbol{x})$ as a function of the position $\boldsymbol{x}$, based on the intensity of the original fluorescence image. By setting an appropriate intensity threshold L_t for binarizing the image, a domain D_1 can be defined as the regions satisfying $L(\boldsymbol{x}) > L_t$, which contain both the lacunae and the canaliculi (Fig. 4.3a). Second, the domain D_1 is contracted at the value of δ (>0), yielding a domain D_2 (Fig. 4.3b). In this process, δ is required to be larger than the maximal canalicular radius for eliminating the canalicular regions. Third, a domain D_3, which contains only the lacunae, is generated by expanding the domain D_2 at the same value of δ (Fig. 4.3c). Finally, by subtracting the domain D_3 from the domain D_1, the canaliculi can be extracted as a domain D_4 (Fig. 4.3d). The domain D_4 is used for estimating the trabecular bone permeability.

We applied the above method to the confocal laser scanning image of the lacuno-canalicular porosity, shown in Fig. 4.2. The obtained domains D_1–D_4 are shown in Figs. 4.4a–d, respectively. Considering that canalicular diameters range from 80 nm to 710 nm (You et al. 2004), we set the length of expansion or contraction δ as 900 nm, which is equivalent to the length of 2.5 pixels in the original image. The domain D_1 (Fig. 4.4a) includes the canaliculi, the lacunae, and the outside of the trabecula. By contracting and expanding the domain D_1, both the

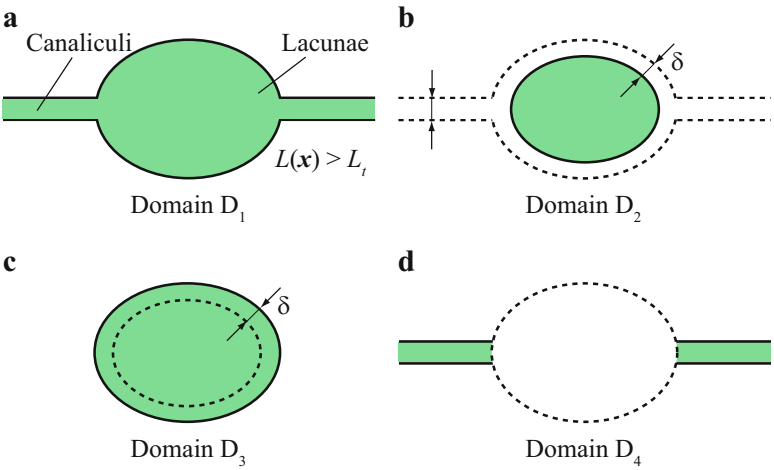

Fig. 4.3 The process for extracting canalicular morphology. (**a**) Domain D_1 corresponds to the regions containing both lacunae and canaliculi, which is defined based on the fluorescence intensity of the original image. (**b**) Contraction of domain D_1 at the value of δ yields domain D_2. Canalicular regions are eliminated through this process. (**c**) Expansion of domain D_2 at the value of δ produces domain D_3, which is regarded as the lacunae. (**d**) By subtracting the domain D_3 from the domain D_1, the canaliculi can be extracted as a domain D_4 (This figure was adapted from Kameo et al. (2010) with permission from Elsevier)

lacunae and the outside region were successfully extracted as the domain D_3 (Fig. 4.4c). The domain D_4, obtained by subtracting D_3 from D_1 (Fig. 4.4d), includes only slender regions, which can be regarded as canaliculi.

The level set method (Osher and Sethian 1988), which is one of the numerical algorithms for tracking interfaces and shapes of materials, was employed to expand

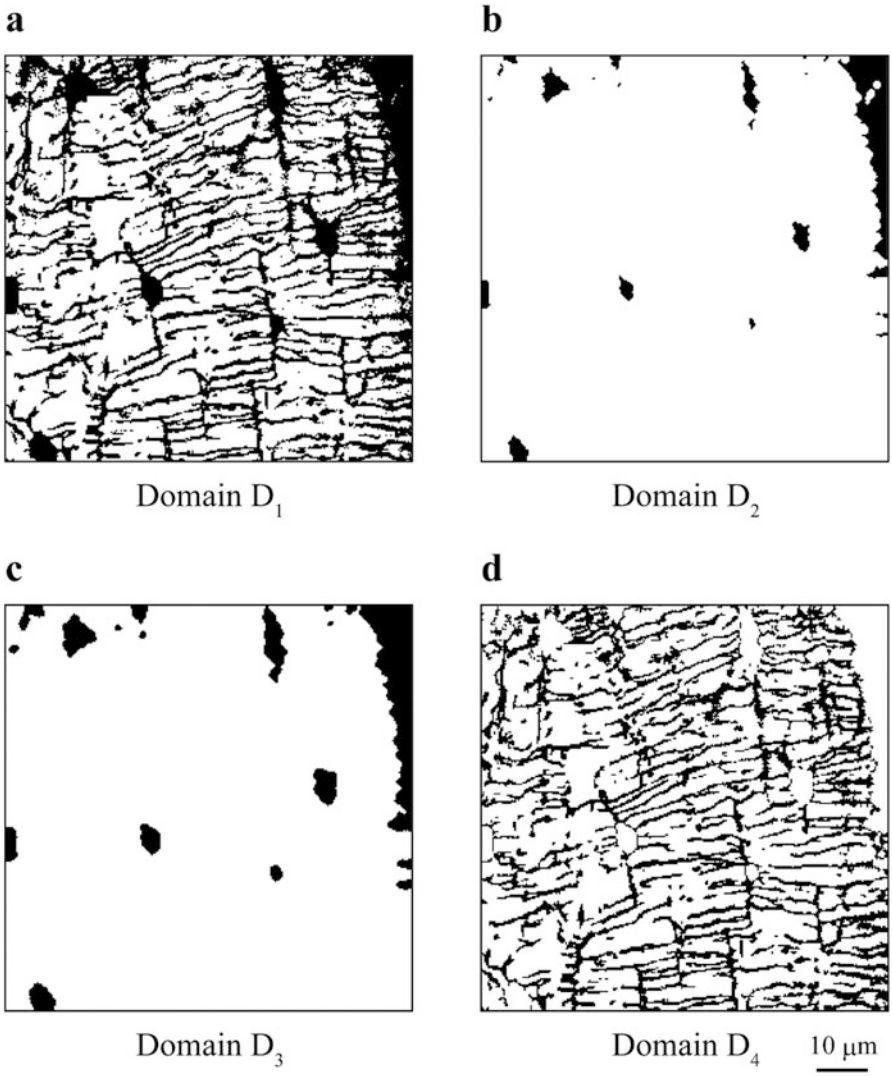

Fig. 4.4 Extraction of canalicular morphology from the fluorescence images through the process shown in Fig. 4.3. (**a**) Domain D_1 includes both lacunae and canaliculi. The region in the upper right corner is the outside of the trabecula. (**b**) Domain D_2 is the contracted domain of domain D_1. (**c**) Domain D_3 contains lacunae and the outside region. (**d**) Domain D_4 represents canaliculi (This figure was adapted from Kameo et al. (2010) with permission from Elsevier)

or contract the specified region. The boundaries of the object were represented by the iso-surface of the following level set function:

$$\left.\begin{array}{ll} \phi(\boldsymbol{x},t) < 0 & \boldsymbol{x} \in \Omega^{+} \\ \phi(\boldsymbol{x},t) = 0, & \boldsymbol{x} \in \partial\Omega \\ \phi(\boldsymbol{x},t) > 0, & \boldsymbol{x} \in \Omega^{-} \end{array}\right\}, \tag{4.1}$$

where Ω^{+}, $\partial\Omega$, and Ω^{-} are the inside, boundary, and outside of the object, respectively. The movement of the boundaries can be expressed by the evolution of the level set function $\phi(\boldsymbol{x}, t)$ according to the following equation:

$$\frac{\partial\phi(\boldsymbol{x},t)}{\partial t} + F(\boldsymbol{x})|\nabla\phi(\boldsymbol{x},t)| = 0, \tag{4.2}$$

where $F(\boldsymbol{x})$ is the speed function in the outward normal direction. By setting $F(\boldsymbol{x}) = \pm\delta$, we numerically calculated the level set function after a unit time $\phi(\boldsymbol{x}, 1)$, to obtain the object boundaries after expansion or contraction at the value of δ. The initial level set function, $\phi(\boldsymbol{x}, 0)$, was determined based on the fluorescence field intensity $L(\boldsymbol{x})$ of the original image, to satisfy Eq. (4.1).

4.3 Theoretical Method for Estimating Bone Permeability

This section describes the theoretical method for estimating anisotropic bone permeability. This method consists of two steps: (1) quantification of canalicular anisotropy (Sect. 4.3.1) and (2) derivation of the analytical relationship between the fabric tensor and the permeability tensor (Sect. 4.3.2).

4.3.1 Quantification of Canalicular Anisotropy

For the quantitative evaluation of the anisotropy of canalicular morphology extracted in Sect. 4.2, the volume orientation (VO) method (Odgaard et al. 1990) was utilized. This method makes it possible to characterize structural anisotropy by analyzing the statistical distribution of the local volume orientation, which describes the representative direction of the volume at an arbitrary position within an object. The local volume orientation is determined as shown in Fig. 4.5. Suppose that the entire domain with regular grid of points is composed of the canalicular domain D_c and the complementary bone matrix domain. The local volume orientation $\boldsymbol{n}$ $(\boldsymbol{x})$ can be defined for each point within D_c as the unit vector with the orientation of the longest intercept through the position $\boldsymbol{x}$, and written in the component form by using the orthogonal basis $\boldsymbol{e}_1$, $\boldsymbol{e}_2$, $\boldsymbol{e}_3$ as follows:

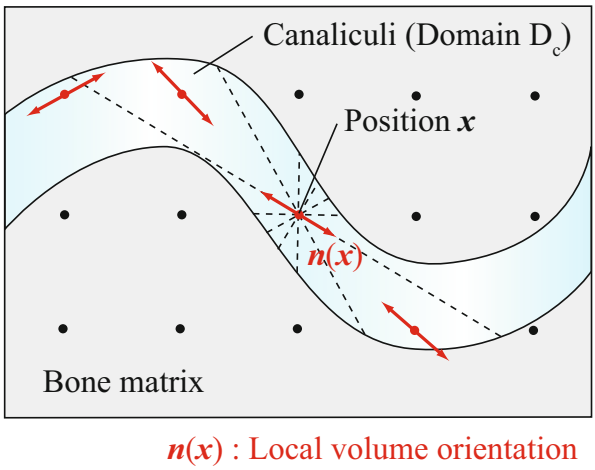

Fig. 4.5 Definition of the local volume orientation. The entire domain with the regular grid of points is composed of the canalicular domain D_c and the bone matrix domain. The local volume orientation $\boldsymbol{n}(\boldsymbol{x})$ is defined for each point within D_c as the unit vector with the orientation of the longest intercept through position $\boldsymbol{x}$. The local volume orientation at each point is indicated by double-headed arrows because the positive and negative directions are not distinguished in the VO method (This figure was adapted from Kameo et al. (2010) with permission from Elsevier)

$$\boldsymbol{n} = n_i \boldsymbol{e}_i = n_1 \boldsymbol{e}_1 + n_2 \boldsymbol{e}_2 + n_3 \boldsymbol{e}_3, \tag{4.3}$$

with the summation convention for the repeated subscript i, where the components n_1, n_2, n_3 are given by

$$n_1 = \sin\theta\cos\varphi, \qquad n_2 = \sin\theta\sin\varphi, \qquad n_3 = \cos\theta \tag{4.4}$$

In the above equation, θ is the angle between the x_3-axis in the Cartesian coordinate system (x_1, x_2, x_3) and the vector $\boldsymbol{n}$, and φ is the angle between the x_1-axis and the projection of $\boldsymbol{n}$ onto the $x_1\,x_2$-plane, measured anti-clockwise. Because the VO method assumes that the object is orthotropic, i.e., the local volume orientation has an unsigned direction, the angles are constrained according to

$$0 \le \theta \le \pi/2, \qquad 0 \le \varphi \le 2\pi \tag{4.5}$$

The statistical distribution of the local volume orientation can be expressed by using the VO fabric tensor (Odgaard et al. 1997), defined by

$$V_{ij} = \frac{1}{V_c}\int_{V_c} n_i n_j dV, \tag{4.6}$$

where V_c is the volume of the canalicular domain D_c. By introducing the local volume orientation frequency $\boldsymbol{\rho}_c(\boldsymbol{n})$, which indicates the volume fraction of canaliculi oriented toward $\boldsymbol{n}$, Eq. (4.6) is rewritten in the following form:

$$V_{ij} = \int_0^{2\pi} d\varphi \int_0^{\pi/2} n_i n_j \rho_c(\boldsymbol{n}) \sin\theta d\theta \tag{4.7}$$

4.3.2 Estimation of Trabecular Bone Permeability

The seepage flow of the interstitial fluid through porous trabeculae is significantly influenced by the dendritic morphology of a lacuno-canalicular porosity. Our method for estimating trabecular bone permeability is based on the derivation of the analytical relationship between the permeability tensor k_{ij} and the VO fabric tensor V_{ij}, describing the canalicular anisotropy. We considered two analytical models of lacuno-canalicular porosity with different levels of scale, as shown in Fig. 4.6 (Weinbaum et al. 1994). The larger-scale level model is a representative volume element (RVE) of a trabecula, containing several canaliculi (Fig. 4.6a). In this RVE, the seepage flow is assumed to be governed by Darcy's law; the fluid flux component q_i is related to the fluid pressure gradient $p_{,j}$ as

$$q_i = -\frac{k_{ij}}{\mu} p_{,j}, \tag{4.8}$$

where μ is the fluid viscosity. The smaller-scale level model represents a single canaliculus with the local volume orientation $\boldsymbol{n}$, in which a slender osteocytic process is housed (Fig. 4.6b).

For the smaller-scale level model of a single canaliculus, the microstructural model proposed by Weinbaum et al. (1994) was employed, as shown in Fig. 4.6b. This model can account for the interstitial fluid flow through a fiber matrix, such as proteoglycan, in a pericellular space between the wall of the canaliculus and the membrane of the osteocytic process. The canaliculus is idealistically modeled as a straight cylindrical tube with a smooth surface, and the osteocytic process is modeled as a coaxial cylinder. On this scale, the interstitial fluid flow in the pericellular space is considered to be governed by the Brinkman equation:

$$p_{,i} = -\frac{\mu}{k_p} u_{,i} + \mu u_{,kk}, \tag{4.9}$$

where k_p is the small-scale permeability of a pericellular matrix, approximated as $0.0572 a_0^2 (\Delta/a_0)^{2.377}$ by using the fiber radius a_0 and fiber spacing Δ (Tsay and Weinbaum 1991). Owing to this idealistic presentation, the average fluid velocity

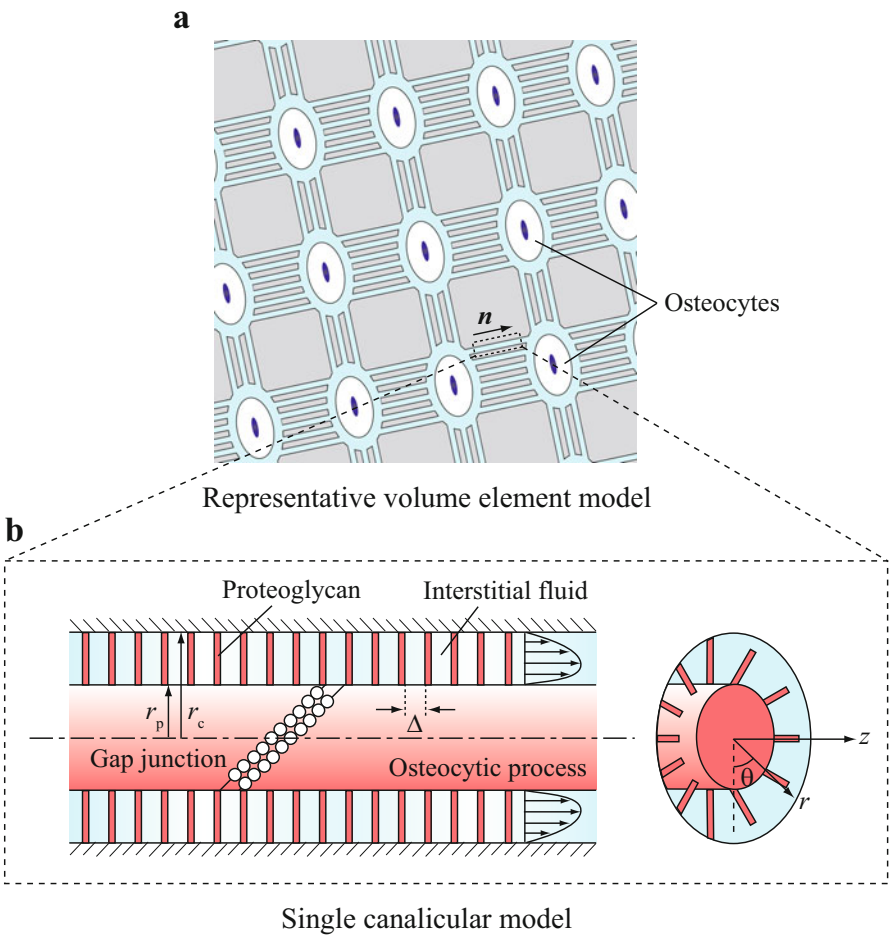

Fig. 4.6 Lacuno-canalicular porosity models with two different levels of scale: (**a**) The representative volume element (RVE) model on the larger-scale level, in which the seepage flow is governed by Darcy's law. (**b**) The model of an individual canaliculus on the smaller scale level, in which the interstitial fluid flow in the pericellular space is governed by the Brinkman equation (Weinbaum et al. 1994) (This figure was adapted from Kameo et al. (2010) with permission from Elsevier)

vector in the canaliculus $\boldsymbol{v}$ is parallel to the local volume orientation $\boldsymbol{n}$, and its magnitude is proportional to the fluid pressure gradient along the direction $\boldsymbol{n}$. Indeed, by analytically solving the Brinkman equation, Eq. (4.9), with no-slip boundary conditions on the surfaces of the canaliculus and the osteocytic process, the i-th component of the average fluid velocity vector in the canaliculi oriented toward $\boldsymbol{n}$, $v_i(\boldsymbol{n})$, is derived as

$$v_i(\boldsymbol{n}) = -W\left(p_{,j}n_j\right)n_i, \tag{4.10}$$

where $(p_{,j}n_j)n_i$ is the fluid pressure gradient in the direction $\boldsymbol{n}$, and the constant W is given by

$$W = -\frac{2r_p^2q^3}{\mu\gamma^3(q^2-1)}\left\{A_1\left[qI_1(\gamma) - I_1\left(\frac{\gamma}{q}\right)\right] - B_1\left[qK_1(\gamma) - K_1\left(\frac{\gamma}{q}\right)\right] - \frac{\gamma(q^2-1)}{2q}\right\} \tag{4.11}$$

In the above equation, r_p is the radius of the osteocytic process, q is the ratio of the radius of the canaliculus r_c to that of the osteocytic process r_p ($q = r_c/r_p$), and γ is the dimensionless parameter defined as $\gamma = r_c/\sqrt{k_p}$. The functions I_1 and K_1 are the modified Bessel functions of the first order. Using q and γ, the constants A_1 and B_1 are given by

$$\left.\begin{aligned} A_1 &= \frac{K_0(\gamma) - K_0(\gamma/q)}{I_0(\gamma/q)K_0(\gamma) - I_0(\gamma)K_0(\gamma/q)} \\ B_1 &= \frac{I_0(\gamma/q) - I_0(\gamma)}{I_0(\gamma/q)K_0(\gamma) - I_0(\gamma)K_0(\gamma/q)} \end{aligned}\right\}, \tag{4.12}$$

respectively, where I_0 and K_0 are the modified Bessel functions of the zeroth order (Weinbaum et al. 1994).

On the other hand, denoting by $v_i(\boldsymbol{x})$ the i-th component of the average fluid velocity vector at the position $\boldsymbol{x}$ in the RVE in Fig. 4.6a, the fluid flux component is obtained as follows:

$$q_i = \frac{1}{V_{\mathrm{RVE}}}\int_{V_f} v_i(\boldsymbol{x})dV, \tag{4.13}$$

where V_{RVE} is the RVE volume and V_f is the volume of the interstitial fluid in the RVE. Assuming that the geometry of the canaliculus and the osteocytic process inside it is invariant with respect to the position $\boldsymbol{x}$, the i-th component of the average fluid velocity vector, $v_i(\boldsymbol{x})$, depends only on the local volume orientation of canaliculi $\boldsymbol{n}$, i.e., $v_i(\boldsymbol{x}) = v_i(\boldsymbol{n})$. Under this assumption, Eq. (4.13) can be written by using the local volume orientation frequency $\rho_c(\boldsymbol{n})$ that was introduced in Sect. 4.3.1, in the following form:

$$q_i = \phi_f\int_0^{2\pi} d\varphi\int_0^{\pi/2} v_i(\boldsymbol{n})\rho_c(\boldsymbol{n})\sin\theta d\theta, \tag{4.14}$$

where ϕ_f is the volume fraction of the interstitial fluid, defined by V_f/V_{RVE}. By substituting Eq. (4.10) into Eq. (4.14) and by using Eq. (4.7), the fluid flux component q_i is given by

$$q_i = -W\phi_f V_{ij} p_{,j} \tag{4.15}$$

Comparing Eq. (4.15) with Darcy's law described in Eq. (4.8) yields the following relationship between the permeability tensor k_{ij} and the VO fabric tensor V_{ij}:

$$k_{ij} = \mu W \phi_f V_{ij} \tag{4.16}$$

By using this analytical relationship, we can estimate the components of the permeability tensor k_{ij}.

4.4 Application to Confocal Laser Scanning Imaging

The presented method was applied to a two-dimensional image of a cylindrical trabecular cross-section, acquired by using confocal laser scanning microscopy. This section explains the results related to (1) the quantification of canalicular anisotropy (Sect. 4.4.1), and (2) the estimation of canalicular bone permeability (Sect. 4.4.2).

4.4.1 Quantification of Canalicular Anisotropy

For quantifying the canalicular anisotropy, we applied the VO method to a 54 μm × 54 μm square region of the binarized confocal laser scanning image of canaliculi, obtained in Sect. 4.2, as shown in Fig. 4.7. The region of interest was divided into 150 × 150 square elements, with an edge size of 0.36 μm, based on the pixels of the fluorescence image, and the local volume orientation was determined at the center of each canalicular element. In two-dimensional analysis, the local volume orientation $\boldsymbol{n}$ depends only on the angle between the x_1-axis in the Cartesian coordinate system (x_1, x_2) and the vector $\boldsymbol{n}$, denoted by θ, and is given by $\boldsymbol{n}(\theta) = \cos\theta \boldsymbol{e}_1 + \sin\theta \boldsymbol{e}_2 \quad (0 \leq \theta \leq \pi)$. Figure 4.8 shows a polar-plotted histogram of the local volume orientation frequency $\rho_c(\boldsymbol{n})$ as a function of the angle θ. The profile of the histogram was symmetric with respect to the origin because the direction $-\boldsymbol{n}$ is equivalent to the direction $\boldsymbol{n}$ in the VO method. The canalicular orientation exhibited a principal peak in the direction in which θ was slightly larger than 0 or π, and a secondary peak in the direction perpendicular to the direction of the principal peak. The principal peak was attributed to the connections between the trabecular surface cells and osteocytes buried in the bone matrix. On the other hand, the secondary peak is likely caused by the intercellular connections between the trabecular surface cells in the process of bone formation.

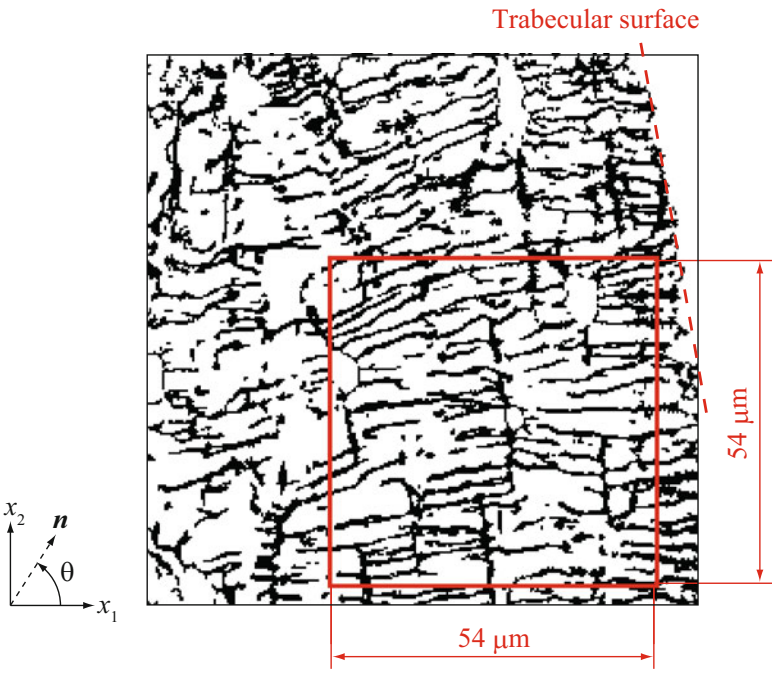

Fig. 4.7 Region of interest in the trabecular cross-section, for quantifying the canalicular anisotropy (This figure was adapted from Kameo et al. (2010) with permission from Elsevier)

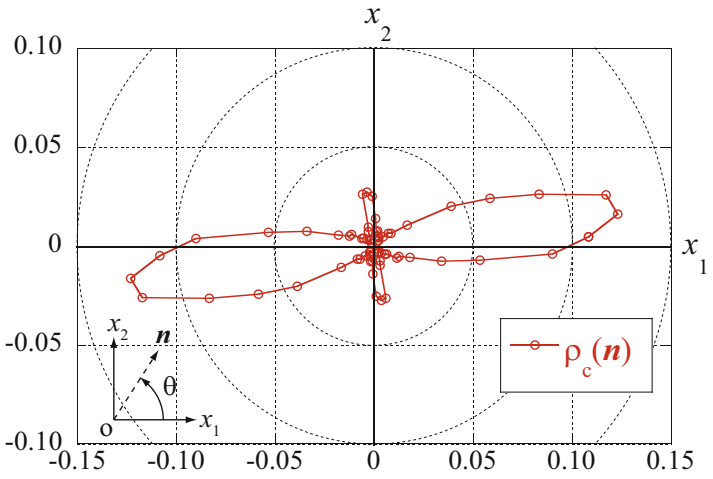

Fig. 4.8 Polar-plotted histogram of the local volume orientation frequency $\rho_c(\boldsymbol{n})$ as a function of the angle θ (This figure was adapted from Kameo et al. (2010) with permission from Elsevier)

Table 4.1 Canalicular anisotropy quantification by using the VO method

VO fabric tensor V_{ij}		$\begin{bmatrix} 0.782 & 0.0815 \\ 0.0815 & 0.218 \end{bmatrix}$	
Eigenvalues and eigenvectors	V_1	0.794	(0.990, 0.140)
	V_2	0.206	(–0.140, 0.990)
Deviation angle θ_1 (degrees)		8.05	

This table was adapted from Kameo et al. (2010) with permission from Elsevier

By substituting the measurements of the local volume orientation frequency $\rho_c(\boldsymbol{n})$ into Eq. (4.7), we calculated the VO fabric tensor for the canalicular orientation. Table 4.1 shows the VO fabric tensor, its eigenvalues, eigenvectors, and the deviation angle θ_1 of the eigenvector corresponding to the maximal eigenvalue. The eigenvalues and the eigenvectors of the VO fabric tensor represent the intensities and the principal directions of the canalicular orientation, respectively. The vectors of the primary direction (0.990, 0.140) and the secondary direction (−0.140, 0.990) were normal to each other owing to the orthotropic material assumption of the VO method. The primary direction of the canalicular orientation was almost parallel to the normal direction of the trabecular surface, as shown in the upper right corner of Fig. 4.7, while the secondary direction roughly coincided with the longitudinal direction of the trabecula. Recalling that individual trabeculae have a cylindrical morphology, these results indicate that the canaliculi are predominantly oriented in the radial direction of the trabecula. The canalicular anisotropy in the radial direction was ~3.85 times stronger than that in the longitudinal direction, based on the comparison of the two eigenvalues of the VO fabric tensor, shown in Table 4.1 ($V_1 = 0.794$ and $V_2 = 0.206$).

4.4.2 Estimation of Trabecular Bone Permeability

As indicated by Eq. (4.16), the trabecular permeability tensor k_{ij} is expressed as the product of four factors: the fluid viscosity μ, the constant W for determining the fluid velocity, the volume fraction of the interstitial fluid ϕ_f, and the VO fabric tensor V_{ij}. We regarded the square region in Fig. 4.7 as the RVE for estimating the trabecular bone permeability. It should be noted that in this study, the principal value of the permeability tensor in the x_3-axis direction was implicitly assumed to be zero because the canalicular orientation in this direction was not considered in our two-dimensional analysis.

The product of the fluid viscosity μ and the constant W does not in itself depend on μ, as indicated by Eq. (4.11). For calculating the product μW, four parameters associated with the dimensions of the canalicular microstructure are required: the radius of the osteocytic process r_p, the radius of the canaliculus r_c, the radius of the

fiber in the pericellular space a_0, and the spacing of the fiber matrix Δ. The radius of the osteocytic process r_p and the radius of the canaliculus r_c were determined as $r_p = 52$ nm, $r_c = 129.5$ nm, referring to the average values measured by You et al. (2004). The fiber radius a_0 and the fiber spacing Δ were set to $a_0 = 0.6$ nm and $\Delta = 7$ nm (Weinbaum et al. 1994). By using these four values, the other parameters appearing in Eq. (4.11) were calculated as follows: $q = 2.490$, $\gamma = 48.68$, $A_1 = 1.259 \times 10^{-20}$, and $B_1 = 1.095 \times 10^{9}$. Eventually, the product μW was derived as $\mu W = 6.591 \times 10^{-18}\ \mathrm{m}^2$.

The volume fraction of the interstitial fluid ϕ_f, defined as V_f/V_{RVE}, can be estimated from the binarized image in Fig. 4.7. Although osteocytic processes are not explicit in Fig. 4.7, by assuming their presence based on the model of a single canaliculus in Fig. 4.6b, the interstitial fluid volume V_f and the canalicular volume V_c in the RVE satisfy the following relation:

$$V_f = \frac{r_c^2 - r_p^2}{r_c^2} V_c = \left(1 - \frac{1}{q^2}\right) V_c \tag{4.17}$$

By using this relation, the volume fraction of the interstitial fluid ϕ_f can be rewritten as follows:

$$\phi_f = \frac{V_f}{V_{RVE}} = \left(1 - \frac{1}{q^2}\right) \phi_c, \tag{4.18}$$

where ϕ_c is the volume fraction of the canaliculi, defined as V_c/V_{RVE}. By using the value of ϕ_c obtained from Fig. 4.7, the volume fraction of the interstitial fluid ϕ_f was estimated from Eq. (4.18) as $\phi_f = 0.245$.

Substituting the values of μW and ϕ_f obtained in this section and the VO fabric tensor V_{ij} obtained in Sect. 4.4.1 into Eq. (4.16) yields the trabecular permeability tensor k_{ij}. The obtained permeability tensor and its eigenvalues are shown in Table 4.2. It should be noted that the principal value of the permeability in the primary direction, i.e., the trabecular radial direction, is larger than that in the secondary, i.e., the trabecular longitudinal, direction.

4.5 Validation of the Estimated Bone Permeability

Bone permeability on the scale of lacuno-canalicular porosity is one of the most important material properties for characterizing the interstitial fluid flow. Extensive theoretical and experimental research has been performed to determine the permeability. Smit et al. (2002) estimated the permeability of an osteon as $2.2 \times 10^{-22}\ \mathrm{m}^2$, by comparing the numerically calculated step response of the fluid pressure to the experimentally determined relaxation curve reported by Otter et al. (1992). Oyen (2008) estimated the permeability to be in the $10^{-26}\ \mathrm{m}^2$ to $10^{-24}\ \mathrm{m}^2$ range by

combining a nanoindentation technique with poroelastic analysis. Weinbaum et al. (1994) developed a theoretical method for estimating isotropic permeability by using a microstructural model of lacuno-canalicular porosity, in which the total number of canaliculi emanating from each osteocyte lacuna was considered. The reported value of permeability based on their method ranged from 10^{-20} m^2 to 10^{-19} m^2 (Wang et al. 1999; Zhang et al. 1998).

Beno et al. (2006) extended the method of Weinbaum et al. (1994) to estimate the anisotropic permeability by considering the difference between the number of canaliculi in the three local principal directions. Using accurate microstructural measurements of bones, they estimated the local lacuno-canalicular permeability to range from 10^{-22} m^2 to 10^{-19} m^2. These researchers pointed out that building anisotropic poroelastic finite element models that incorporate local permeability of lacuno-canalicular porosity would require determining the orientation of each osteocyte lacuna, and confocal microscopy could be used for achieving this goal. Following these suggestions, we developed an extended method for estimating the anisotropic permeability tensor based on the observed images of lacuno-canalicular porosity. Applying our presented method to the lacuno-canalicular model of these authors, which is a cuboidal periodic unit cell that surrounds the osteocyte lacuna, the analytical relationship described by Eq. (4.16), reduces to the formulation suggested by Beno et al. (2006). This result implies that our approach is more general and valid for estimating the anisotropic permeability.

The estimated permeability values in Table 4.2 are several orders of magnitude larger than those reported in the above-mentioned studies. Among the four parameters in Eq. (4.16), this discrepancy is most strongly associated with the volume fraction of the interstitial fluid ϕ_f. As was explained above, the volume fraction of the interstitial fluid used in this study, $\phi_f = 0.245$, was estimated from the binarized image in Fig. 4.7. This value is considerably larger compared with the previously reported lacuno-canalicular porosity of 0.042 (Morris et al. 1982) and 0.035 (in rats; Baylink and Wergedal 1971). The main reasons for the overestimation of ϕ_f are summarized as follows: (i) the image contains extra canaliculi in the out-of-focus plane; (ii) the pixel resolution of the image (0.36 μm) is too low to resolve the canaliculi; and (iii) the canaliculi appear larger owing to the image bleeding. Thus, the characteristics of the fluorescence images acquired by using confocal laser scanning microscopy could favor the overestimation of the permeability tensor. In spite of such limitations, the obtained principal directions and the ratio of the

Table 4.2 Estimated anisotropic trabecular permeability

Permeability tensor k_{ij} $[\times 10^{-18}\ m^2]$		$\begin{bmatrix} 1.26 & 0.131 \\ 0.131 & 0.351 \end{bmatrix}$
Eigenvalues $[\times 10^{-18}\ m^2]$	k_1	1.27
	k_2	0.332

This table was adapted from Kameo et al. (2010) with permission from Elsevier

principal values are considered to be sufficiently valid, because they are relatively immune to the influence of the above three factors. For more precise permeability estimation, it is indispensable to obtain more refined images of lacuno-canalicular porosity by using ultra-high voltage electron microscopy (Kamioka et al. 2009), as used in Chap. 2.

4.6 Characteristics of the Proposed Estimation Method

In our proposed method for estimating bone permeability, we assumed, for simplicity, ideal lacuno-canalicular morphology, despite the actually complex geometrical organization that is observed *in vivo* (Kamioka et al. 2001; Kamioka et al. 2009; McNamara et al. 2009). The interstitial fluid flow channels were regarded as smooth and straight annular tubes without tortuosity, and the presence of osteocyte lacunae was neglected. If the effects of the canalicular curvature and wall projections were taken into account, the fluid flow within the channels would be more complicated. In particular, the flow of the interstitial fluid close to the junctions between the canaliculi and osteocyte lacunae can be significantly influenced by the local change in the flow channel size and the flow direction. According to the theoretical formulation proposed by Cowin (2004), the relationship between the permeability tensor K_{ij} and the fabric tensor A_{ij} can be generally expressed as $K_{ij} = q_1\delta_{ij} + q_2A_{ij} + q_3A_{ik}A_{kj}$ when K_{ij} is an isotropic function of A_{ij}, where q_1, q_2, and q_3 are functions of the porosity and the three invariants of the fabric tensor. A comparison of the above relationship with Eq. (4.16) yields $q_2 = \mu W\phi_f$ and $q_1 = q_3 = 0$. This result suggests that the permeability tensor is proportional to the VO fabric tensor only in the special case in which the tortuosity and the wall projections of the canaliculi are neglected.

To investigate the interstitial fluid flow in a lacuno-canalicular porosity with complex geometry, computational fluid dynamics (CFD), as shown in Chap. 2, would be a powerful tool (Anderson et al. 2005). Indeed, by using CFD analysis it was determined that idealized pericellular flow channel geometry exerts a profound influence on the fluid flow prediction (Anderson and Tate 2008). If a three-dimensional morphology of a lacuno-canalicular porosity can be reconstructed *in silico* by using the observed images, performing CFD analysis aided by high performance computing would help in determining the anisotropic permeability tensor reflecting the microstructure.

The estimation method developed in this study makes it possible to derive the principal values and the principal directions of the anisotropic permeability tensor based on the observed images of lacuno-canalicular porosities. Therefore, our method would be useful for constructing poroelastic finite element models of bone considering the lacuno-canalicular anisotropy, because the region of interest for the permeability estimation can be arbitrarily chosen and the principal directions of the obtained anisotropic permeability tensor in the bone tissue can be easily determined. The poroelastic finite element analysis of bone tissue, incorporating the

anisotropic permeability, would enable us to investigate the interstitial fluid flow in response to external mechanical loading. Computational approaches, such as finite element analysis, are useful for understanding the interactions between mechanical and biochemical factors associated with bone remodeling (Adachi et al. 2001; Gerhard et al. 2009; Tsubota et al. 2009). Identifying the effect of the complex lacuno-canalicular morphology on the cellular mechanotransduction via the fluid flow through computational approaches will help clarify the mechanism of bone remodeling, as we shall see later in Chaps. 5, 6, and 7.

4.7 Conclusion

In this chapter, we developed a theoretical method for estimating trabecular bone permeability by using the images of lacuno-canalicular porosity in the trabecular cross-section. This method is based on the derivation of the analytical relationship between the VO fabric tensor, which characterizes the canalicular orientation, and the permeability tensor. Introducing idealized lacuno-canalicular models with different levels of scale, in which the microscopic flow is governed by the Brinkman equation and the macroscopic flow is governed by Darcy's law, the permeability tensor was shown to be proportional to the VO fabric tensor. We applied the proposed method to a binarized confocal laser scanning image of canaliculi, for evaluating the canalicular anisotropy and the trabecular permeability. The obtained results indicated that the canaliculi are predominantly oriented in the radial direction of the trabecula, and the permeability depends largely on the canalicular morphology and dimension. Our method is likely to be useful for deriving the anisotropic bone permeability referring to the actually observed canalicular morphology.

References

Adachi T, Tsubota K, Tomita Y, Hollister SJ (2001) Trabecular surface remodeling simulation for cancellous bone using microstructural voxel finite element models. J Biomech Eng 123 (5):403–409. https://doi.org/10.1115/1.1392315

Anderson EJ, Tate MLK (2008) Idealization of pericellular fluid space geometry and dimension results in a profound underprediction of nano-microscale stresses imparted by fluid drag on osteocytes. J Biomech 41(8):1736–1746. https://doi.org/10.1016/j.jbiomech.2008.02.035

Anderson EJ, Kaliyamoorthy S, Alexander JID, Tate MLK (2005) Nano-microscale models of periosteocytic flow show differences in stresses imparted to cell body and processes. Ann Biomed Eng 33(1):52–62. https://doi.org/10.1007/s10439-005-8962-y

Beno T, Yoon YJ, Cowin SC, Fritton SP (2006) Estimation of bone permeability using accurate microstructural measurements. J Biomech 39(13):2378–2387. https://doi.org/10.1016/j.biomech.2005.08.005

Bonewald LF, Johnson ML (2008) Osteocytes, mechanosensing and wnt signaling. Bone 42 (4):606–615. https://doi.org/10.1016/j.bone.2007.12.224

Burger EH, Klein-Nulend J (1999) Mechanotransduction in bone - role of the lacuno-canalicular network. FASEB J 13:S101–S112

Cowin SC (1985) The relationship between the elasticity tensor and the fabric tensor. Mech Mater 4(2):137–147. https://doi.org/10.1016/0167-6636(85)90012-2

Cowin SC (1986) Wolff's law of trabecular architecture at remodeling equilibrium. J Biomech Eng 108(1):83–88

Cowin SC (1999) Bone poroelasticity. J Biomech 32(3):217–238

Cowin SC (2004) Anisotropic poroelasticity: fabric tensor formulation. Mech Mater 36 (8):665–677. https://doi.org/10.1016/j.mechmat.2003.05.001

Fritton SP, Weinbaum S (2009) Fluid and solute transport in bone: flow-induced mechanotransduction. Annu Rev Fluid Mech 41:347–374. https://doi.org/10.1146/annurev.fluid.010908.165136

Gerhard FA, Webster DJ, van Lenthe GH, Muller R (2009) In silico biology of bone modelling and remodelling: adaptation. Philos Trans R Soc A 367(1895):2011–2030. https://doi.org/10.1098/rsta.2008.0297

Kameo Y, Adachi T, Hojo M (2008) Transient response of fluid pressure in a poroelastic material under uniaxial cyclic loading. J Mech Phys Solids 56(5):1794–1805. https://doi.org/10.1016/j.jmps.2007.11.008

Kameo Y, Adachi T, Hojo M (2009) Fluid pressure response in poroelastic materials subjected to cyclic loading. J Mech Phys Solids 57(11):1815–1827. https://doi.org/10.1016/j.jmps.2009.08.002

Kameo Y, Adachi T, Sato N, Hojo M (2010) Estimation of bone permeability considering the morphology of lacuno-canalicular porosity. J Mech Behav Biomed Mater 3(3):240–248. https://doi.org/10.1016/j.jmbbm.2009.10.005

Kamioka H, Honjo T, Takano-Yamamoto T (2001) A three-dimensional distribution of osteocyte processes revealed by the combination of confocal laser scanning microscopy and differential interference contrast microscopy. Bone 28(2):145–149. https://doi.org/10.1016/S8756-3282(00)00421-X

Kamioka H, Murshid SA, Ishihara Y, Kajimura N, Hasegawa T, Ando R, Sugawara Y, Yamashiro T, Takaoka A, Takano-Yamamoto T (2009) A method for observing silver-stained osteocytes in situ in 3-um sections using ultra-high voltage electron microscopy tomography. Microsc Microanal 15(5):377–383. https://doi.org/10.1017/s1431927609990420

Klein-Nulend J, Bacabac RG, Mullender MG (2005) Mechanobiology of bone tissue. Pathol Biol 53(10):576–580. https://doi.org/10.1016/j.patbio.2004.12.005

McNamara LM, Majeska RJ, Weinbaum S, Friedrich V, Schaffler MB (2009) Attachment of osteocyte cell processes to the bone matrix. Anat Rec 292(3):355–363. https://doi.org/10.1002/ar.20869

Morris MA, Lopezcurto JA, Hughes SPF, An KN, Bassingthwaighte JB, Kelly PJ (1982) Fluid spaces in canine bone and marrow. Microvasc Res 23(2):188–200

Nowinski JL (1970) A model of the human skull as a poroelastic spherical shell subjected to a quasistatic load. Math Biosci 8:397–416. https://doi.org/10.1016/0025-5564(70)90120-3

Odgaard A, Jensen EB, Gundersen HJG (1990) Estimation of structural anisotropy based on volume orientation - a new concept. J Microsc 157:149–162

Odgaard A, Kabel J, vanRietbergen B, Dalstra M, Huiskes R (1997) Fabric and elastic principal directions of cancellous bone are closely related. J Biomech 30(5):487–495

Osher S, Sethian JA (1988) Fronts propagating with curvature-dependent speed - algorithms based on hamilton-jacobi formulations. J Comput Phys 79(1):12–49

Otter MW, Palmieri VR, Wu DD, Seiz KG, MacGinitie LA, Cochran GV (1992) A comparative analysis of streaming potentials in vivo and in vitro. J Orthop Res 10(5):710–719

Oyen ML (2008) Poroelastic nanoindentation responses of hydrated bone. J Mater Res 23 (5):1307–1314. https://doi.org/10.1557/jmr.2008.0156

Riddle RC, Donahue HJ (2009) From streaming potentials to shear stress: 25 years of bone cell mechanotransduction. J Orthop Res 27(2):143–149. https://doi.org/10.1002/jor.20723

Smit TH, Huyghe JM, Cowin SC (2002) Estimation of the poroelastic parameters of cortical bone. J Biomech 35(6):829–835

Tsay RY, Weinbaum S (1991) Viscous flow in a channel with periodic cross-bridging fibers - exact solutions and brinkman approximation. J Fluid Mech 226:125–148

Tsubota K, Suzuki Y, Yamada T, Hojo M, Makinouchi A, Adachi T (2009) Computer simulation of trablecular remodeling in human proximal femur using large-scale voxel fe models: approach to understanding Wolff's law. J Biomech 42(8):1088–1094. https://doi.org/10.1016/j.jbiomech.2009.02.030

Wang LY, Fritton SP, Cowin SC, Weinbaum S (1999) Fluid pressure relaxation depends upon osteonal microstructure: modeling an oscillatory bending experiment. J Biomech 32 (7):663–672

Weinbaum S, Cowin SC, Zeng Y (1994) A model for the excitation of osteocytes by mechanical loading-induced bone fluid shear stresses. J Biomech 27(3):339–360

You LD, Weinbaum S, Cowin SC, Schaffler MB (2004) Ultrastructure of the osteocyte process and its pericellular matrix. Anat Rec A Discov Mol Cell Evol Biol 278A(2):505–513. https://doi.org/10.1002/ar.a.20050

Zhang D, Weinbaum S, Cowin SC (1998) Estimates of the peak pressures in bone pore water. J Biomech Eng 120(6):697–703

Chapter 5
Modeling Trabecular Bone Adaptation Induced by Flow Stimuli to Osteocytes

Abstract In this chapter, we provide a mathematical model for trabecular bone remodeling that incorporates the possible mechanisms of cellular mechanosensing and intercellular communication. This model postulates that osteocytes, as mechanosensory cells, are stimulated by interstitial fluid flow to regulate bone adaptation. The morphological changes in trabeculae, in response to the mechanical environment, are demonstrated with the help of a voxel finite element method. The validity of the proposed mathematical model is tested through a remodeling simulation for a single trabecula subjected to cyclic uniaxial loading at various frequencies.

Keywords Trabecular bone adaptation • Remodeling simulation • Mathematical model • Flow stimulus • Osteocyte

5.1 Introduction

Individual trabeculae that make up cancellous bones can change their morphology by remodeling to adapt to the mechanical environment (Wolff 2010). This trabecular bone remodeling is induced by the collaboration of bone-resorbing osteoclasts and bone-forming osteoblasts at the trabecular surface (Parfitt 1994). The metabolic activities of these effector cells are believed to be orchestrated by mechanosensory osteocytes embedded in the bone matrix through their intercellular network via slender cell processes (Adachi et al. 2009a, b, c; Bonewald 2011; Cowin et al. 1991; Tatsumi et al. 2007), as shown in Chap. 4. However, it is still unclear how bone tissue adaptation is appropriately regulated by numerous bone cells under the influence of an external load.

Computer simulations are useful for exploring the mechanism of bone adaptation. A number of mathematical models of bone remodeling that consider cellular mechanosensing have been developed to predict the evolution of bone microstructure (Gerhard et al. 2009). While the majority of previous remodeling models postulate that the change in bone mass is associated with the mechanical condition at the tissue level, it has been proposed that osteocytes, as mechanosensory cells, are activated by the interstitial fluid flow in a lacuno-canalicular porosity (Burger

This Chapter was adapted from Kameo et al. (2011) with permission from Elsevier.

Y. Kameo et al., *Bone Adaptation*, Frontiers of Biomechanics 2,
https://doi.org/10.1007/978-4-431-56514-7_5

and Klein-Nulend 1999; Fritton and Weinbaum 2009; Knothe Tate et al. 1998; Weinbaum et al. 1994), as explained in Chap. 3. Unfortunately, little is known about the relationship between the flow stimuli at the cellular level and bone adaptation at the tissue level.

In this chapter, we construct an original mathematical model for trabecular bone remodeling based on a theoretical framework that links the microscopic cellular activities to macroscopic bone tissue adaptation through mechanical hierarchy. The flow of interstitial fluid inside the lacuno-canalicular porosity is explicitly considered as the mechanical stimulus for the osteocytes that initiate bone remodeling. In addition, the process of intercellular signal transmission from osteocytes to effector cells, such as osteoclasts and osteoblasts, is incorporated. Combining this model with the voxel finite element method, we numerically simulate the morphological changes in a single trabecula under cyclic uniaxial loadings at various frequencies in order to test the validity of the proposed remodeling model.

5.2 Mathematical Model of Trabecular Bone Remodeling

A mathematical model of trabecular bone remodeling that incorporates the cellular response to interstitial fluid flow and intercellular communication is explained in this section. This model can provide a theoretical bridge between the microscopic cellular activities and macroscopic bone tissue adaptation.

5.2.1 Theoretical Framework

The mathematical model of trabecular bone remodeling was developed according to the theoretical framework shown in Fig. 5.1. This model is based on the assumption that the change in bone mass is caused by osteoclastic bone resorption and osteoblastic bone formation on the trabecular surface, which are regulated by mechanosensory osteocytes in response to interstitial fluid flow. The process of trabecular bone remodeling is postulated to consist of three parts: (i) cellular mechanosensing, (ii) intercellular signal transmission, and (iii) trabecular surface movement.

When the bone tissue is subjected to mechanical loading, bone matrix deformation induces interstitial fluid flow in canaliculi. The fluid flow can be characterized by the fluid pressure p and its gradient ∇p. The osteocytes buried in the mineralized bone matrix are activated by flow-induced shear stress on their dendritic processes, and transduce the mechanical stimulus into the biochemical signal S_{oc}. Then, the produced signal is transmitted from the osteocytes to the osteoclasts and osteoblasts on the trabecular surface through an intercellular network, and is integrated as the

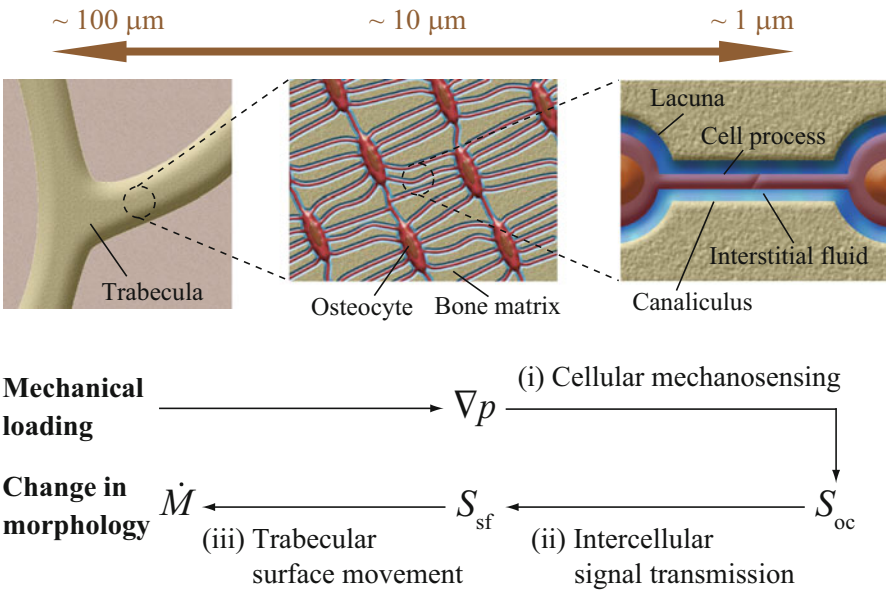

Fig. 5.1 Theoretical framework for trabecular bone remodeling considering the mechanical hierarchy from the microscopic activities of bone cells to the macroscopic changes in trabecular morphology. The process of trabecular bone remodeling consists of the following three parts: (*i*) cellular mechanosensing, (*ii*) intercellular signal transmission, and (*iii*) trabecular surface movement (This figure was adapted from Kameo and Adachi (2014) with permission from Springer)

total stimulus S_{sf}. Finally, the rate of trabecular surface remodeling $\dot{M}$, i.e. the rate of bone resorption and formation on the trabecular surface, is determined by the stimulus S_{sf}. The details of each remodeling process are explained in the following subsections.

5.2.2 *Cellular Mechanosensing*

Osteocytes are believed to be major mechanosensory cells and known to be sensitive to shear stress caused by interstitial fluid flow over their slender processes. The shear stress is evaluated based on the microstructure model of Weinbaum et al. (1994), shown in Fig. 5.2 and introduced in Sect. 4.3.2, where the interstitial fluid flow in the annular canaliculus is assumed to be governed by the Brinkman equation. The flow-induced shear stress $\tau_{\mathrm{p}}(\boldsymbol{n})$ acting on the osteocyte process aligned in direction $\boldsymbol{n}$ is derived, using the fluid pressure gradient at the trabecular level ∇p, as:

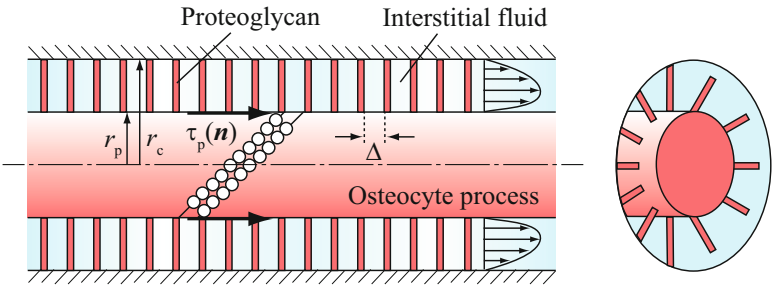

Fig. 5.2 Microstructure model of annular canaliculus, in which the interstitial fluid flow in the pericellular space is governed by the Brinkman equation (This figure is modified from Weinbaum et al. (1994). This figure was adapted from Kameo et al. (2011) with permission from Elsevier)

$$\tau_p(\boldsymbol{x},\boldsymbol{n}) = \frac{qr_p}{\gamma}\left[A_1 I_1\left(\frac{\gamma}{q}\right) - B_1 K_1\left(\frac{\gamma}{q}\right)\right]\nabla p(\boldsymbol{x})\cdot\boldsymbol{n}, \tag{5.1}$$

where all the constants are as defined in Sect. 4.3.2. The fluid pressure gradient is numerically calculated by poroelastic finite element analysis (Manfredini et al. 1999).

In the modeling of cellular mechanotransduction, we assumed that osteocytes are susceptible to the value of flow-induced shear stress averaged over a day, and the biochemical signal produced by them is proportional to the shear force on their dendritic processes. Using the local volume orientation frequency of canaliculi $\rho_c(\boldsymbol{n})$ introduced in Sect. 4.3.1, the signal $S_{oc}(\boldsymbol{x})$ produced by the osteocytes per unit bone volume at the spatial position $\boldsymbol{x}$ can be defined as:

$$S_{oc}(\boldsymbol{x}) = \int_0^{2\pi} d\varphi \int_0^{\pi/2} \alpha \frac{2r_p}{r_c^2}\rho_c(\boldsymbol{n})\overline{|\tau_p(\boldsymbol{x},\boldsymbol{n})|}\sin\theta d\theta, \tag{5.2}$$

where θ is the angle between the vector $\boldsymbol{n}$ and the x_3-axis in the arbitrarily assigned Cartesian coordinate system, φ the angle between the x_1-axis and the projection of $\boldsymbol{n}$ onto the x_1x_2-plane measured counterclockwise, α the mechanosensitivity of the osteocytes, and $\overline{|\tau_p(\boldsymbol{n})|}$ the time-averaged shear stress over a day. For simplicity, here we ignored individual variability in osteocyte mechanosensitivity by setting $\alpha = 1$ and assumed the isotropic orientation of canaliculi by setting $\rho_c(\boldsymbol{n}) = \phi/2\pi$, where ϕ is the porosity of the trabeculae.

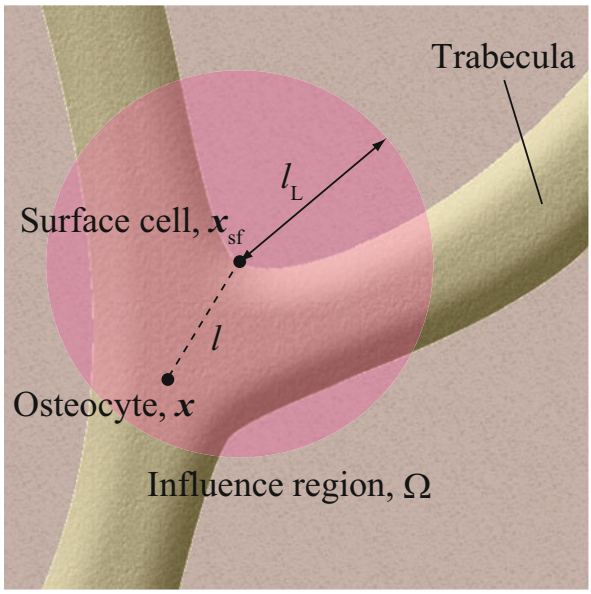

Fig. 5.3 Modeling of intercellular signal transmission. The surface cell receives mechanical signals from the osteocytes within the influence region. The signal intensity decays with increasing distance between the surface cell and the osteocyte (This figure was adapted from Kameo et al. (2011) with permission from Elsevier)

5.2.3 *Intercellular Signal Transmission*

The biochemical signals produced by the osteocytes are modeled to be transmitted to the osteoclasts and osteoblasts on the trabecular surface, through the intercellular network. The cell located on the surface position $\boldsymbol{x}_{sf}$ receives the signals from the osteocytes within a limited influence region Ω, as shown in Fig. 5.3. Assuming that the intercellular communication capability is dependent on the distance $l = |\boldsymbol{x}_{sf} - \boldsymbol{x}|$, the total stimulus S_{sf} located on the trabecular surface $\boldsymbol{x}_{sf}$ is expressed, using a weight function $w(l)$ that describes the decay in the signal intensity relative to the distance l, as the following integral form:

$$S_{sf}(\boldsymbol{x}_{sf}) = \int_{\Omega} w(l) S_{oc}(\boldsymbol{x})\, d\Omega, \quad w(l) = 1 - l/l_L (l \le l_L), \tag{5.3}$$

where l_L is the maximum distance for intercellular communication. The total stimulus S_{sf} is a positive scalar function that represents the activity of the surface cell.

5.2.4 *Trabecular Surface Movement*

The self-regulation of bone mass on the trabecular surface is achieved by the osteoclastic bone resorption and the following osteoblastic bone formation. For

modeling the time-averaged change of the trabecular surface as a result of remodeling, we introduced a piecewise sinusoidal function, as shown in Fig. 5.4, which describes the relationship between the rate of trabecular surface remodeling $\dot{M}$ and the total stimulus S_{sf}, as follows:

$$\dot{M}\left(S_{\mathrm{sf}}\right)=\begin{cases}\dot{M}_{\max} & \left(S_{\mathrm{sf}}^{\mathrm{U}}<S_{\mathrm{sf}}\right)\\ \dfrac{\dot{M}_{\max}}{2}\left[\sin\pi\left\{\dfrac{S_{\mathrm{sf}}-\left(S_{\mathrm{sf}}^{\mathrm{O}}+S_{\mathrm{sf}}^{\mathrm{Z}}/2\right)}{S_{\mathrm{sf}}^{\mathrm{U}}-\left(S_{\mathrm{sf}}^{\mathrm{O}}+S_{\mathrm{sf}}^{\mathrm{Z}}/2\right)}-\dfrac{1}{2}\right\}+1\right] & \left(S_{\mathrm{sf}}^{\mathrm{O}}+\dfrac{S_{\mathrm{sf}}^{\mathrm{Z}}}{2}<S_{\mathrm{sf}}\le S_{\mathrm{sf}}^{\mathrm{U}}\right)\\ 0 & \left(S_{\mathrm{sf}}^{\mathrm{O}}-\dfrac{S_{\mathrm{sf}}^{\mathrm{Z}}}{2}\le S_{\mathrm{sf}}\le S_{\mathrm{sf}}^{\mathrm{O}}+\dfrac{S_{\mathrm{sf}}^{\mathrm{Z}}}{2}\right),\\ -\dfrac{\dot{M}_{\max}}{2}\left[\sin\pi\left\{\dfrac{S_{\mathrm{sf}}-\left(S_{\mathrm{sf}}^{\mathrm{O}}-S_{\mathrm{sf}}^{\mathrm{Z}}/2\right)}{S_{\mathrm{sf}}^{\mathrm{L}}-\left(S_{\mathrm{sf}}^{\mathrm{O}}-S_{\mathrm{sf}}^{\mathrm{Z}}/2\right)}-\dfrac{1}{2}\right\}+1\right] & \left(S_{\mathrm{sf}}^{\mathrm{L}}\le S_{\mathrm{sf}}<S_{\mathrm{sf}}^{\mathrm{O}}-\dfrac{S_{\mathrm{sf}}^{\mathrm{Z}}}{2}\right)\\ -\dot{M}_{\max} & \left(S_{\mathrm{sf}}<S_{\mathrm{sf}}^{\mathrm{L}}\right)\end{cases}\tag{5.4}$$

where $S_{\mathrm{sf}}^{\mathrm{U}}$ is the upper threshold for bone formation, $S_{\mathrm{sf}}^{\mathrm{L}}$ the lower threshold for bone resorption, $S_{\mathrm{sf}}^{\mathrm{O}}$ a stimulus at the remodeling equilibrium, and $S_{\mathrm{sf}}^{\mathrm{Z}}$ the width of the lazy zone. The maximum resorption/formation rates in the direction along the outward normal to the trabecular surface are denoted by $-\dot{M}_{\max}$ and $\dot{M}_{\max}$, respectively. The physiological interpretation of $\dot{M}$ is discussed in detail in Chap. 8. This empirical function indicates that bone resorption is caused by stimuli below the remodeling equilibrium, while bone formation is caused by stimuli exceeding the equilibrium. As a numerical technique to represent trabecular surface movement, the level set method (Osher and Sethian 1988), which was used also in Sect. 4.2, was incorporated in the remodeling simulation.

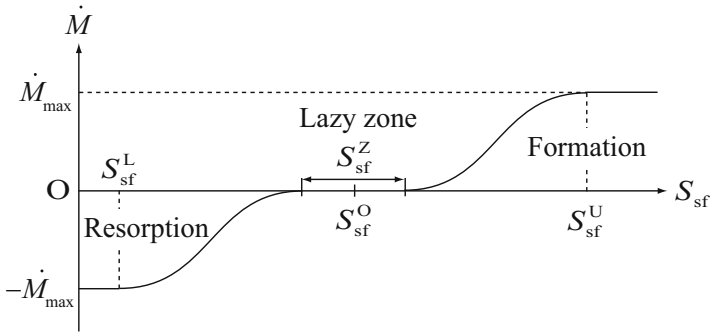

Fig. 5.4 Relationship between the rate of trabecular surface remodeling and the total stimulus received by the surface cell (This figure was adapted from Kameo et al. (2011) with permission from Elsevier)

5.3 Voxel Modeling of a Single Trabecula under Cyclic Uniaxial Load

A three-dimensional computational model of a single trabecula for the remodeling simulation was constructed as shown in Fig. 5.5. The whole region for analysis was $a_1 \times a_2 \times a_3 = 0.8 \times 1.6 \times 1.2\ \text{mm}^3$, discretized by $20 \times 40 \times 30$ cubic voxel finite elements with an edge size of 40 μm. A cylindrical trabecula with an initial diameter of 240 μm was set at the center of the region with a skew angle of 30°. The trabecula was assumed to be a homogeneous and isotropic poroelastic material (Cowin 1999; Kameo et al. 2008, 2009) with the material properties listed in Table 5.1 (Beno et al. 2006; Smit et al. 2002). To impose external loadings, two 40 μm-thick plates were placed at the upper and lower surfaces of the region. These plates have the same material properties as the trabecula, but they are not subjected to morphological changes throughout the remodeling simulation.

As mechanical and fluid boundary conditions, a shear-free condition was applied to the lower plane, and a drained condition on the trabecular surfaces was assumed by setting the fluid pressure as $p = 0$. A cyclic uniaxial load $\sigma(t) = \sigma_3 \sin 2\pi ft$. ($\sigma_3 = 0.07$ MPa) was imposed on the upper plate in the x_3-direction for 1.0 s per day, keeping the displacement along the x_3-direction u_3 uniform. To investigate the effect of the rate of the applied load, three different values of loading frequency were determined as $f = 1$, 5, and 10 Hz, which are within the physiological range.

The settings of the physiological parameters used in the proposed remodeling model are specified in Table 5.2. The values of four parameters required for the

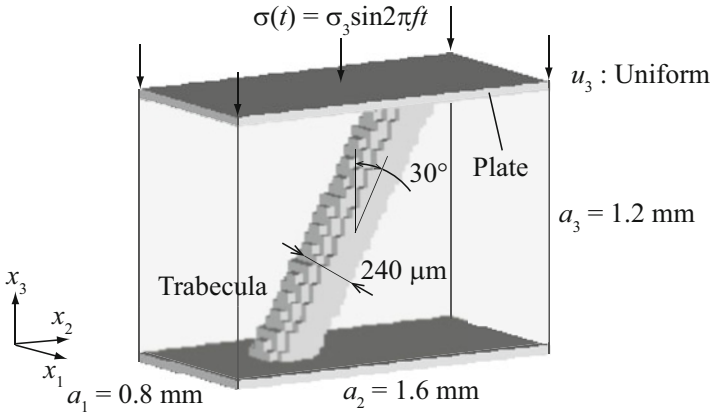

Fig. 5.5 Voxel finite element model of a cylindrical single trabecula with an initial diameter of 240 μm and a skew angle of 30°. A cyclic uniaxial load was imposed on the upper plate in the x_3-direction for 1.0 s per day, maintaining the uniform displacement u_3 along the x_3-direction (This figure was adapted from Kameo et al. (2011) with permission from Elsevier)

Table 5.1 Poroelastic material properties of the trabecula

Symbol (unit)	Description	Value
k (m^2)	Intrinsic permeability	1.1×10^{-21}
μ (Pa·s)	Fluid viscosity	1.0×10^{-3}
G (GPa)	Shear modulus	5.94
ν	Drained Poisson's ratio	0.325
K_s (GPa)	Solid bulk modulus	17.66
K_f (GPa)	Fluid bulk modulus	2.3
ϕ	Porosity	0.05

Permeability was estimated by the method presented in Beno et al. (2006), and other constants were taken from Smit et al. (2002)
This table was adapted from Kameo et al. (2011) with permission from Elsevier

Table 5.2 Parameter settings for the trabecular remodeling simulation

Symbol (unit)	Description	Value
r_p (nm)	Radius of osteocyte process	52[a]
r_c (nm)	Radius of canaliculus	129.5[a]
a_0 (nm)	Radius of fiber	0.6[b]
Δ (nm)	Spacing of fiber matrix	7[b]
l_L (μm)	Maximum distance for intercellular communication	200[c,d]
$\dot{M}_{max}$ (μm/day)	Maximum remodeling rate	40[e]
S_{sf}^{U} (μN)	Upper threshold for bone formation	1.5
S_{sf}^{L} (μN)	Lower threshold for bone resorption	0.5
S_{sf}^{O} (μN)	Stimulus at remodeling equilibrium	1.0
S_{sf}^{Z} (μN)	Width of lazy zone	0.2

[a]You et al. (2004)
[b]Weinbaum et al. (1994)
[c]Huo et al. (2008)
[d]Adachi et al. (2009b)
[e]Jaworski and Lok (1972)

derivation of the flow-induced shear stress Eq. (5.1), i.e., the radius of the osteocyte process r_p and the radius of the canaliculus r_c, the fiber radius a_0, and the fiber spacing Δ, were set as in Sect. 4.4.2 (Weinbaum et al. 1994; You et al. 2004). The maximum distance for intercellular communication l_L was determined in reference to the *in vitro* experiments on the propagation of calcium signaling between bone cells (Adachi et al. 2009b; Huo et al. 2008). The maximum remodeling rate $\dot{M}_{max}$ was determined from the resorption rate of osteoclasts (Jaworski and Lok 1972). The remaining four parameters associated with the mechanical stimulus, S_{sf}^{U}, S_{sf}^{L}, S_{sf}^{O}, and S_{sf}^{Z}, were arbitrarily set.

5.4 Adaptation of a Single Trabecula to Cyclic Uniaxial Load

This section explains simulation results regarding morphological changes in trabecula (Sect. 5.4.1), and quantitative evaluation of remodeling process (Sect. 5.4.2).

5.4.1 Morphological Changes in Trabecula

By incorporating the proposed mathematical model of trabecular bone remodeling into the voxel finite element method, we simulated the morphological changes in a single trabecula in response to an external cyclic uniaxial load. Figure 5.6a–c show the progress of the distribution of the 1-day average flow-induced shear stress acting on the osteocyte processes at the loading frequency $f = 1$, 5, and 10 Hz, respectively.

When the loading frequency $f = 1$ Hz, as shown in Fig. 5.6a, large flow-induced shear stress was observed at the inner surfaces near both ends of the trabecula in the initial state. This means that the trabecular surface cells received large mechanical stimuli from neighboring osteocytes. As a result, bone formation was promoted around both ends, while at the middle of the trabecula, the morphology was almost unchanged. During the period from 3 to 6 days, bone resorption occurred on the outer surfaces near both ends owing to small flow-induced shear stress. After 30 days, the concentration of flow-induced shear stress observed in the initial state was relaxed, and the single trabecula reoriented parallel to the loading direction, i.e. x_3-direction.

As the frequency of the applied cyclic loading increased, the flow-induced shear stress close to the trabecular surfaces became larger in the initial state, as shown in Fig. 5.6b, c. In both cases $f = 5$ Hz and $f = 10$ Hz, bone formation was induced on the entire trabecular surface for the first 3 days because the mechanical stimuli to the surface cells exceeded the physiological equilibrium value. As a result of this remodeling, the trabecular diameter was enlarged, while maintaining the original

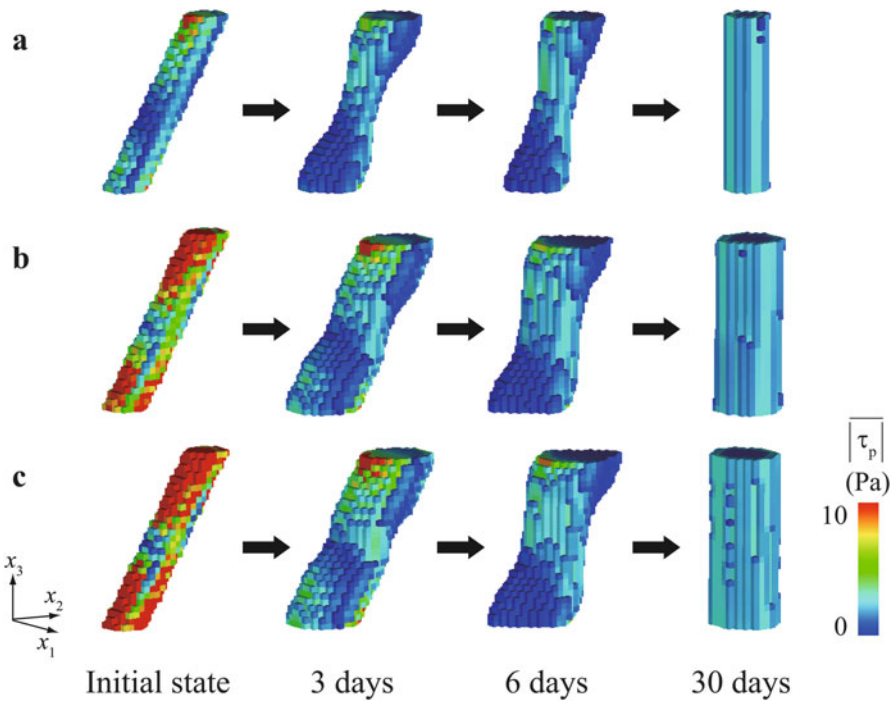

Fig. 5.6 Change in trabecular morphology and 1-day average flow-induced shear stresses under the loading frequencies (**a**) $f = 1$ Hz, (**b**) $f = 5$ Hz, and (**c**) $f = 10$ Hz (This figure was adapted from Kameo et al. (2011) with permission from Elsevier)

longitudinal direction. The subsequent remodeling process was similar to that in the case $f = 1$ Hz, and the single trabecula aligned along the loading direction after 30 days. The diameter of the trabecula in the equilibrium state increased with the increase in the loading frequency.

5.4.2 Quantitative Evaluation of Remodeling Process

For the quantitative evaluation of the morphological changes in the trabecula through the remodeling process, we investigated the temporal variation of the bone volume fraction and apparent stiffness. The bone volume fraction represents the ratio of the trabecular volume to the total volume of the region for analysis, and the apparent stiffness is defined as the ratio of the loading amplitude σ_3 to the apparent strain u_3/a_3. Figure 5.7a, b show the changes in the bone volume fraction and apparent stiffness, respectively. Regardless of the loading frequency, the bone volume fraction increased in an early stage, and then slightly decreased to converge to the specific value, as shown in Fig. 5.7a. On the other hand, the apparent stiffness

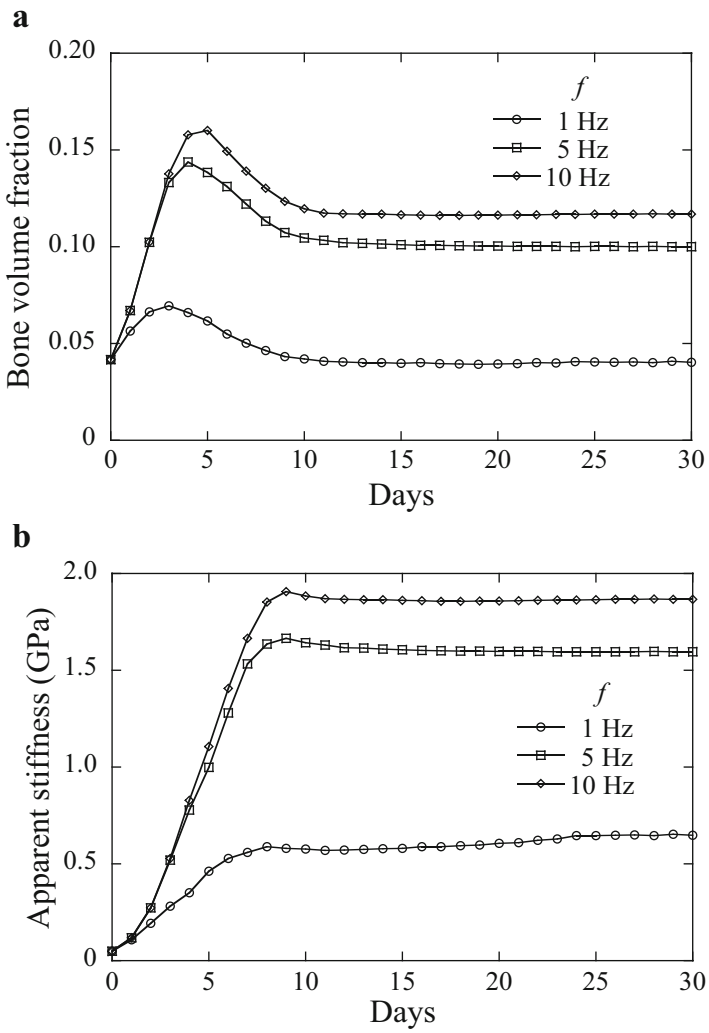

Fig. 5.7 Quantitative evaluation of morphological changes in trabeculae under various loading frequencies. (**a**) Change in bone volume fraction, (**b**) Change in apparent stiffness (This figure was adapted from Kameo et al. (2011) with permission from Elsevier)

increased monotonically for the first 10 days and reached a plateau value for all cases of the loading frequency, as shown in Fig. 5.7b. The convergence values of both the bone volume fraction and the apparent stiffness increased with an increase in the applied loading frequency. The relationship between the loading frequency and the bone volume fraction at 30 days is shown in Fig. 5.8. In this figure the

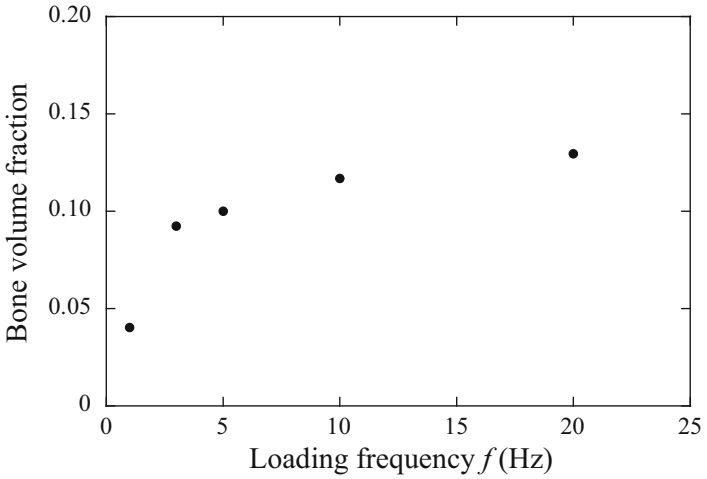

Fig. 5.8 Relationship between the applied loading frequency and the bone volume fraction at 30 days (This figure was adapted from Kameo et al. (2011) with permission from Elsevier)

results for $f = 3$ Hz and $f = 20$ Hz are additionally plotted. Figure 5.8 indicates that the bone volume fraction in the equilibrium state is not proportional to the loading frequency, and tends to converge to a certain value with increasing the loading frequency.

5.5 Characteristics of the Proposed Remodeling Model

The modeling approach for trabecular bone remodeling has progressed with the advancement in experimental studies at the organ, tissue, and cellular level. A variety of computational remodeling models considering cellular mechanosensing have been developed, in which the change in bone mass is assumed to be regulated by either the strain energy density (Huiskes et al. 2000; Mullender and Huiskes 1995; Mullender et al. 1994; Ruimerman et al. 2005), the accumulation of microdamage (McNamara and Prendergast 2007; Mulvihill and Prendergast 2008; Prendergast and Taylor 1994), or the nonuniformity of the local stress on the trabecular surface (Adachi et al. 1997, 2001; Tsubota and Adachi 2004, 2005, 2006; Tsubota et al. 2002, 2009). The common feature of these mathematical models is that they are based on the phenomenological hypothesis that bone remodeling is driven by the mechanical condition at the tissue level. While the previous models can successfully express bone adaptation to the external loading, investigating the mechanical state at the cellular level is essential for understanding

the mechanism of bone remodeling. The novelty of our mathematical model lies in the consideration of the mechanical hierarchy from the microscopic activities of bone cells to the macroscopic changes in trabecular morphology by quantifying the flow-mediated stimulus to the osteocytes.

The proposed remodeling model requires a total of ten parameters to describe the three processes of trabecular bone remodeling without considering the seven poroelastic material properties of the trabecula listed in Table 5.1: four parameters for (i) cellular mechanosensing (r_p, r_c, a_0, and Δ), one parameter for (ii) intercellular signal transmission (l_L), and five parameters for (iii) trabecular surface movement ($\dot{M}_{max}$, S_{sf}^U, S_{sf}^L, S_{sf}^O, and S_{sf}^Z). Of the above parameters, the setting of the last four associated with the mechanical stimulus, i.e. S_{sf}^U, S_{sf}^L, S_{sf}^O and S_{sf}^Z, is an important issue in the remodeling simulation because the change in bone mass on the trabecular surface is virtually governed by these empirical parameters. The stimulus at the remodeling equilibrium S_{sf}^O regulates the balance between bone resorption and formation. The increase in S_{sf}^O promotes bone resorption if the external loading condition is constant. The width of the lazy zone S_{sf}^Z is based on the remodeling rate sensitivity to the stimulus in the neighborhood of the point of remodeling equilibrium. As S_{sf}^Z increases, the change in bone mass becomes more insensitive to the variation in the stimulus. The morphological changes in a trabecula are more sensitive to the parameter set of S_{sf}^O and S_{sf}^Z than that of S_{sf}^U and S_{sf}^L, which is responsible for the remodeling rate sensitivity to the stimulus around the lazy zone. Although these parameters should be determined through a comparison with the experimental findings, there is as yet no way to conduct this because of the difficulty in observing a single trabecula under a controlled mechanical condition. In the present study, we set them arbitrarily in order to demonstrate trabecular bone remodeling under physiological conditions. By choosing the appropriate values of the parameters, this simulation has the potential to represent pathological bone remodeling, such as osteoporosis and osteopetrosis.

5.6 Validity of the Simulated Remodeling Process

To demonstrate the validity of the simulated remodeling process, we first focus on the results when the loading frequency $f = 1$ Hz. As shown in Fig. 5.7a, the bone volume fraction at 30 days was approximately equal to that at the initial state, despite the reorientation of the single trabecula. Although there is generally a positive correlation between the volume of material and the stiffness of the structure, the apparent stiffness of the trabecula increased initially and then converged to the constant value owing to bone remodeling, as shown in Fig. 5.7b. These results imply that the trabecula actively adapted its own morphology to the applied load in order to satisfy the mechanical demands. Figure 5.7b further indicates that the increase in the loading frequency derives the increase in the apparent stiffness of the single trabecula in the state of the remodeling equilibrium. Considering that a cyclic

loading with higher frequency increases the risk of fatigue fracture of the trabeculae, this behavior can also be regarded as a functional adaptation of the trabecula in order to avoid the risk of fracture. The results qualitatively agree with the experimental findings that a more significant bone ingrowth was induced under a higher loading rate condition (Goldstein et al. 1991). As shown in Fig. 5.8, in the high loading frequency range, the bone volume fraction in the equilibrium state is insensitive to the variation in the frequency. This is because the interstitial fluid around the center of trabecula cannot flow through easily under high-frequency conditions, and only the osteocytes embedded near the surfaces contribute to mechanosensing (Kameo et al. 2008, 2009). From a physiological point of view, this behavior seems reasonable for preventing excess bone deposition.

In our modeling, we idealized a single trabecula as a homogeneous and isotropic poroelastic material for simplicity. However, it is well known that the mechanical properties of the bone matrix depend on the degree of calcification and have anisotropy owing to the component mineral crystals and collagen fibers. In addition, the lacuno-canalicular porosity inside trabeculae also has a highly anisotropic structure, as shown in Chap. 4 (Kameo et al. 2010). To investigate such effects of microstructure of individual trabeculae, it will be necessary to extend our mathematical model by incorporating the contributions of the heterogeneity and anisotropy of material properties into the finite element models. In spite of the above limitations, we showed that the proposed mathematical model for trabecular bone remodeling can predict bone functional adaptation successfully at the single trabecular level. Here we investigated the fundamental characteristics of the mathematical model through the remodeling simulation of a single trabecula subjected to uniaxial loading. As a next step, it is important to identify the influence of the types of external loadings on the process of trabecular adaptation via remodeling.

5.7 Conclusion

In this chapter, we developed a mathematical model of trabecular bone remodeling that considers cellular mechanosensing and intercellular signal transmission. In the proposed model, osteocytes embedded in a bone matrix were assumed to be activated by the flow of interstitial fluid in a lacuno-canalicular porosity to regulate osteoclastic bone resorption and osteoblastic bone formation on the trabecular surface. To identify the fundamental characteristics of the mathematical model, we demonstrated morphological changes in a single trabecula in response to cyclic uniaxial loading with the help of a voxel finite element method. The simulation results showed that the single trabecula reoriented to the applied loading direction as a result of bone remodeling. Furthermore, the diameter of the trabecula in the remodeling equilibrium state increased with an increase in the loading frequency. These results imply that our remodeling model has the potential to represent the process of bone functional adaptation to the surrounding mechanical environment at the single trabecular level.

References

Adachi T, Tomita Y, Sakaue H, Tanaka M (1997) Simulation of trabecular surface remodeling based on local stress nonuniformity. JSME Int J Ser C 40(4):782–792. https://doi.org/10.1299/jsmec.40.782

Adachi T, Tsubota K, Tomita Y, Hollister SJ (2001) Trabecular surface remodeling simulation for cancellous bone using microstructural voxel finite element models. J Biomech Eng 123 (5):403–409. https://doi.org/10.1115/1.1392315

Adachi T, Aonuma Y, Ito S, Tanaka M, Hojo M, Takano-Yamamoto T, Kamioka H (2009a) Osteocyte calcium signaling response to bone matrix deformation. J Biomech 42 (15):2507–2512. https://doi.org/10.1016/j.jbiomech.2009.07.006

Adachi T, Aonuma Y, Taira K, Hojo M, Kamioka H (2009b) Asymmetric intercellular communication between bone cells: propagation of the calcium signaling. Biochem Biophys Res Commun 389(3):495–500. https://doi.org/10.1016/j.bbrc.2009.09.010

Adachi T, Aonuma Y, Tanaka M, Hojo M, Takano-Yamamoto T, Kamioka H (2009c) Calcium response in single osteocytes to locally applied mechanical stimulus: differences in cell process and cell body. J Biomech 42(12):1989–1995. https://doi.org/10.1016/j.jbiomech.2009.04.034

Beno T, Yoon YJ, Cowin SC, Fritton SP (2006) Estimation of bone permeability using accurate microstructural measurements. J Biomech 39(13):2378–2387. https://doi.org/10.1016/j.biomech.2005.08.005

Bonewald LF (2011) The amazing osteocyte. J Bone Miner Res 26(2):229–238. https://doi.org/10.1002/jbmr.320

Burger EH, Klein-Nulend J (1999) Mechanotransduction in bone – role of the lacuno-canalicular network. FASEB J 13:S101–S112

Cowin SC (1999) Bone poroelasticity. J Biomech 32(3):217–238

Cowin SC, Moss-Salentijn L, Moss ML (1991) Candidates for the mechanosensory system in bone. J Biomech Eng 113:191–197

Fritton SP, Weinbaum S (2009) Fluid and solute transport in bone: flow-induced mechanotransduction. Annu Rev Fluid Mech 41:347–374. https://doi.org/10.1146/annurev.fluid.010908.165136

Gerhard FA, Webster DJ, van Lenthe GH, Muller R (2009) In silico biology of bone modelling and remodelling: adaptation. Philos Trans R Soc A 367(1895):2011–2030. https://doi.org/10.1098/rsta.2008.0297

Goldstein SA, Matthews LS, Kuhn JL, Hollister SJ (1991) Trabecular bone remodeling: An experimental model. J Biomech 24:135–150

Huiskes R, Ruimerman R, van Lenthe GH, Janssen JD (2000) Effects of mechanical forces on maintenance and adaptation of form in trabecular bone. Nature 405(6787):704–706

Huo B, XL L, Hung CT, Costa KD, QB X, Whitesides GM, Guo XE (2008) Fluid flow induced calcium response in bone cell network. Cell Mol Bioeng 1(1):58–66. https://doi.org/10.1007/s12195-008-0011-0

Jaworski ZF, Lok E (1972) The rate of osteoclastic bone erosion in haversian remodeling sites of adult dogs rib. Calcif Tissue Res 10(2):103–112

Kameo Y, Adachi T (2014) Modeling trabecular bone adaptation to local bending load regulated by mechanosensing osteocytes. Acta Mech 225(10):2833–2840. https://doi.org/10.1007/s00707-014-1202-5

Kameo Y, Adachi T, Hojo M (2008) Transient response of fluid pressure in a poroelastic material under uniaxial cyclic loading. J Mech Phys Solids 56(5):1794–1805. https://doi.org/10.1016/j.jmps.2007.11.008

Kameo Y, Adachi T, Hojo M (2009) Fluid pressure response in poroelastic materials subjected to cyclic loading. J Mech Phys Solids 57(11):1815–1827. https://doi.org/10.1016/j.jmps.2009.08.002

Kameo Y, Adachi T, Sato N, Hojo M (2010) Estimation of bone permeability considering the morphology of lacuno-canalicular porosity. J Mech Behav Biomed Mater 3(3):240–248. https://doi.org/10.1016/j.jmbbm.2009.10.005

Kameo Y, Adachi T, Hojo M (2011) Effects of loading frequency on the functional adaptation of trabeculae predicted by bone remodeling simulation. J Mech Behav Biomed Mater 4 (6):900–908. https://doi.org/10.1016/j.jmbbm.2011.03.008

Knothe Tate ML, Knothe U, Niederer P (1998) Experimental elucidation of mechanical load-induced fluid flow and its potential role in bone metabolism and functional adaptation. Am J Med Sci 316(3):189–195

Manfredini P, Cocchetti G, Maier G, Redaelli A, Montevecchi FM (1999) Poroelastic finite element analysis of a bone specimen under cyclic loading. J Biomech 32(2):135–144

McNamara LM, Prendergast PJ (2007) Bone remodelling algorithms incorporating both strain and microdamage stimuli. J Biomech 40(6):1381–1391. https://doi.org/10.1016/j.jbiomech.2006.05.007

Mullender MG, Huiskes R (1995) Proposal for the regulatory mechanism of Wolffs law. J Orth Res 13(4):503–512

Mullender MG, Huiskes R, Weinans H (1994) A physiological approach to the simulation of bone remodeling as a self-organizational control process. J Biomech 27(11):1389–1394

Mulvihill BM, Prendergast PJ (2008) An algorithm for bone mechanoresponsiveness: implementation to study the effect of patient-specific cell mechanosensitivity on trabecular bone loss. Comput Methods Biomech Biomed Eng 11(5):443–451. https://doi.org/10.1080/10255840802136150

Osher S, Sethian JA (1988) Fronts propagating with curvature-dependent speed – algorithms based on hamilton-jacobi formulations. J Comput Phys 79(1):12–49

Parfitt AM (1994) Osteonal and hemi-osteonal remodeling: the spatial and temporal framework for signal traffic in adult human bone. J Cell Biochem 55(3):273–286

Prendergast PJ, Taylor D (1994) Prediction of bone adaptation using damage accumulation. J Biomech 27(8):1067–1076. https://doi.org/10.1016/0021-9290(94)90223-2

Ruimerman R, Hilbers P, van Rietbergen B, Huiskes R (2005) A theoretical framework for strain-related trabecular bone maintenance and adaptation. J Biomech 38(4):931–941. https://doi.org/10.1016/j.jbiomech.2004.03.037

Smit TH, Huyghe JM, Cowin SC (2002) Estimation of the poroelastic parameters of cortical bone. J Biomech 35(6):829–835

Tatsumi S, Ishii K, Amizuka N, Li MQ, Kobayashi T, Kohno K, Ito M, Takeshita S, Ikeda K (2007) Targeted ablation of osteocytes induces osteoporosis with defective mechanotransduction. Cell Metab 5(6):464–475. https://doi.org/10.1016/j.cmet.2007.05.001

Tsubota K, Adachi T (2004) Changes in the fabric and compliance tensors of cancellous bone due to trabecular surface remodeling, predicted by a digital image-based model. Comput Methods Biomech Biomed Engin 7(4):187–192. https://doi.org/10.1080/10255840410001729524

Tsubota K, Adachi T (2005) Spatial and temporal regulation of cancellous bone structure: characterization of a rate equation of trabecular surface remodeling. Med Eng Phys 27 (4):305–311. https://doi.org/10.1016/j.medengphy.2004.09.013

Tsubota K, Adachi T (2006) Computer simulation study on local and integral mechanical quantities at single trabecular level as candidates of remodeling stimuli. J Biomech Sci Eng 1(1):124–135. https://doi.org/10.1299/jbse.1.124

Tsubota K, Adachi T, Tomita Y (2002) Functional adaptation of cancellous bone in human proximal femur predicted by trabecular surface remodeling simulation toward uniform stress state. J Biomech 35(12):1541–1551. https://doi.org/10.1016/S0021-9290(02)00173-2

Tsubota K, Suzuki Y, Yamada T, Hojo M, Makinouchi A, Adachi T (2009) Computer simulation of trablecular remodeling in human proximal femur using large-scale voxel fe models: approach to understanding Wolff' law. J Biomech 42(8):1088–1094. https://doi.org/10.1016/j.jbiomech.2009.02.030

Weinbaum S, Cowin SC, Zeng Y (1994) A model for the excitation of osteocytes by mechanical loading-induced bone fluid shear stresses. J Biomech 27(3):339–360

Wolff J (2010) The classic on the inner architecture of bones and its importance for bone growth (reprinted from virchows arch pathol anat physiol, vol 50, pg 389–450, 1870). Clin Orthop Relat Res 468 (4):1056–1065. doi:https://doi.org/10.1007/s11999-010-1239-2

You LD, Weinbaum S, Cowin SC, Schaffler MB (2004) Ultrastructure of the osteocyte process and its pericellular matrix. Anat Rec A Discov Mol Cell Evol Biol 278A(2):505–513. https://doi.org/10.1002/ar.a.20050

Chapter 6
Effects of Local Bending Load on Trabecular Bone Adaptation

Abstract This chapter investigates the relationship between the individual trabecular morphology in cancellous bone and the types of load applied. In particular, to understand the effects of a bending load on trabecular bone adaptation, we conduct remodeling simulations for a single trabecula subjected to a cyclic bending load based on our original remodeling model. It is shown that the bending load influences not only the formation of the plate-like trabecula but also the changes in its topology. The results suggest the possibility that the characteristic morphology of an individual trabecula is determined by the local mechanical environment in the overall cancellous bone.

Keywords Trabecular bone adaptation • Remodeling simulation • Plate-like trabecula • Bending load • Topological change

6.1 Introduction

Trabecular architecture in the cancellous bone is dynamically reorganized via remodeling to satisfy the mechanical demands. Owing to the continual osteoclastic bone resorption and osteoblastic bone formation at the trabecular surface, cancellous bone maintains a three-dimensional network structure consisting of rod-like and plate-like trabeculae (Basaruddin et al. 2012; Carbonare et al. 2005). The characteristic morphologies of the individual trabeculae vary depending on their position within the cancellous bone. While it is widely accepted that trabecular morphology is related to the surrounding mechanical environment, the determinant remains elusive.

Trabeculae within a living body are usually subjected to low-frequency cyclic loading from daily activities, which consists of axial and bending components (Weinbaum et al. 1994). We hypothesized that the unique morphology of trabeculae is formed as a result of their functional adaptation to different types of loadings. To test this hypothesis, we used the mathematical model of trabecular bone remodeling developed in Chap. 5, which considers the osteocytic mechanical response to the interstitial fluid flow (Adachi et al. 2010). As we mentioned in Chap. 5, the application of a uniaxial load to a single trabecula produced a rod-like

This Chapter was adapted from Kameo and Adachi (2014) with permission from Springer.

Y. Kameo et al., *Bone Adaptation*, Frontiers of Biomechanics 2,
https://doi.org/10.1007/978-4-431-56514-7_6

form aligned along the loading direction (Kameo et al. 2011). In this chapter, we investigate the effects of a bending load on trabecular morphology. By applying our original remodeling model to the voxel finite element model of a trabecula, we performed a bone remodeling simulation for a single trabecula under a cyclic bending load.

6.2 Voxel Modeling of a Single Trabecula under a Cyclic Bending Load

For a computational investigation of the role of the local bending load on the trabecular bone adaptation, we prepared a voxel finite element model of a single upright trabecula as shown in Fig. 6.1. The region for analysis was $a_1 \times a_2 \times a_3 = 0.8 \times 1.6 \times 1.2$ mm^3 and the voxel element size was 40 μm; both the parameters are the same as in Sect. 5.3. A rod-like poroelastic trabecula with an initial diameter of 240 μm was set at the center of the region along the x_3-direction. Two parallel 40 μm-thick plates were placed at the top and bottom of the trabecula to impose external loading. The material properties of the trabecula and plate are shown in Table 5.1 (Beno et al. 2006; Smit et al. 2002).

The upright trabecula was subjected to a cyclic bending load, which was linearly distributed along the x_2-direction $\sigma(t) = (2\sigma_3 x_2/a_2)\sin 2\pi ft$. ($f = 1$ Hz), through the upper plate in the x_3-direction for 1.0 s per day. A shear-free condition on the lower plane and a drained condition on the trabecular surfaces were applied. To investigate the effects of the magnitude of the bending load, we set $\sigma_3 = -0.10$ and -0.15 MPa in reference to a previous remodeling simulation study (Tsubota and Adachi 2005). The physiological parameters used in the present simulations are specified in Table 6.1 (Adachi et al. 2009; Huo et al. 2008; Jaworski and Lok 1972; Weinbaum et al. 1994; You et al. 2004). These parameter values, other than $S_{\mathrm{sf}}^{\mathrm{Z}}$, are the same as used in Chap. 5 (see Table 5.2). As mentioned in Sect. 5.5, the changes in trabecular morphology are greatly influenced by the width of the lazy zone $S_{\mathrm{sf}}^{\mathrm{Z}}$ (see Fig. 5.4) that represents the remodeling rate sensitivity to the stimulus near the remodeling equilibrium. Hence, two different lazy zone width values were selected: $S_{\mathrm{sf}}^{\mathrm{Z}} = 0.6$ and 0.4 μN.

6.3 Adaptation of a Single Trabecula to a Cyclic Bending Load

Based on the mathematical bone remodeling model developed in Sect. 5.2, we investigated the functional adaptation of a single upright trabecula to a cyclic bending load through remodeling simulations. Figures 6.2 and 6.3 show the changes in the trabecular morphology and distribution of the 1-day average flow-

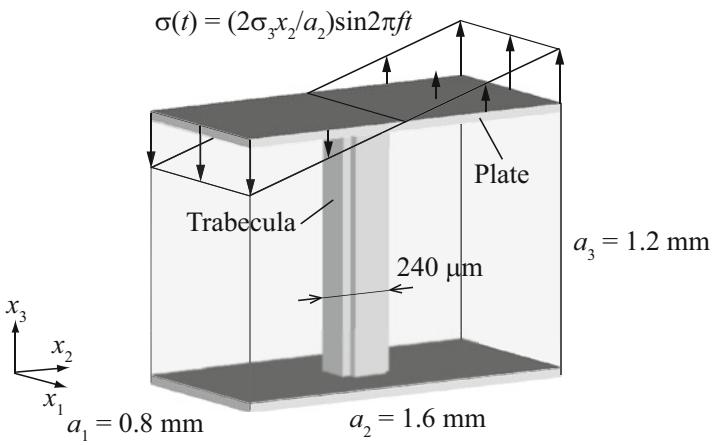

Fig. 6.1 Voxel finite element model of an upright single trabecula with an initial diameter of 240 μm. A cyclic bending load, which was linearly distributed along the x_2-direction, was applied on the upper plate in the x_3-direction for 1.0 s per day (This figure was adapted from Kameo and Adachi (2014) with permission from Springer)

Table 6.1 Parameter settings for the trabecular remodeling simulation. Two different values for the width of the lazy zone were chosen

Symbol (unit)	Description	Value
r_p (nm)	Radius of osteocyte process	52[a]
r_c (nm)	Radius of canaliculus	129.5[a]
a_0 (nm)	Radius of fiber	0.6[b]
Δ (nm)	Spacing of fiber matrix	7[b]
l_L (μm)	Maximum distance for intercellular communication	200[c,d]
$\dot{M}_{max}$ (μm/day)	Maximum remodeling rate	40[e]
S_{sf}^U (μN)	Upper threshold for bone formation	1.5
S_{sf}^L (μN)	Lower threshold for bone resorption	0.5
S_{sf}^O (μN)	Stimulus at remodeling equilibrium	1.0
S_{sf}^Z (μN)	Width of lazy zone	0.6 or 0.4

This table was adapted from Kameo and Adachi (2014) with permission from Springer
[a]You et al. (2004)
[b]Weinbaum et al. (1994)
[c]Huo et al. (2008)
[d]Adachi et al. (2009)
[e]Jaworski and Lok (1972)

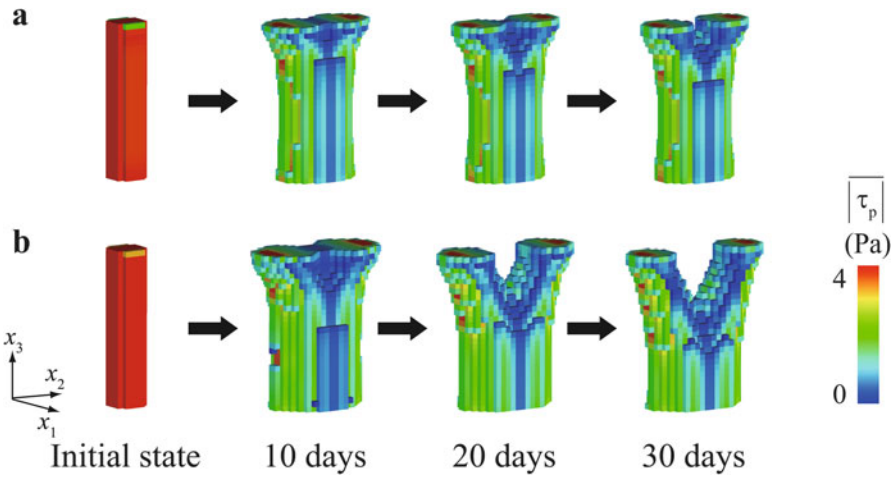

Fig. 6.2 Changes in the trabecular morphology and 1-day average flow-induced shear stresses when the width of the lazy zone $S_{sf}^{Z} = 0.6$ μN: (**a**) $\sigma_3 = -0.10$ MPa and (**b**) $\sigma_3 = -0.15$ MPa (This figure was adapted from Kameo and Adachi (2014) with permission from Springer)

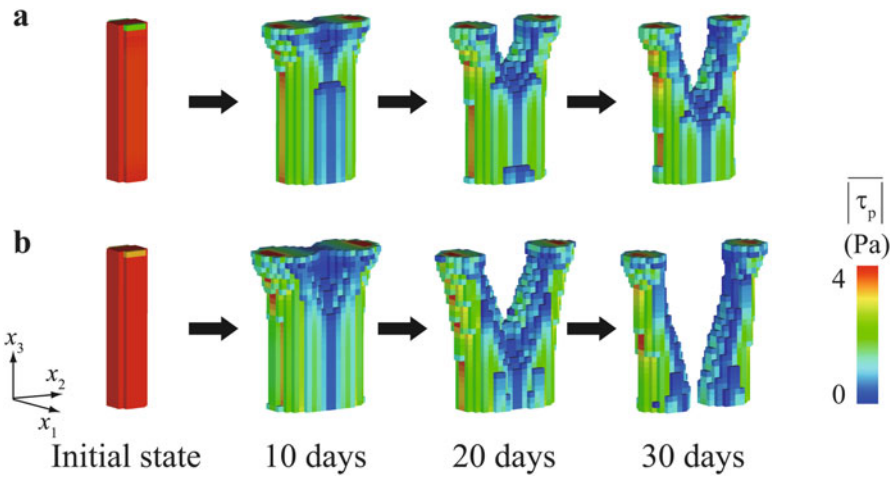

Fig. 6.3 Changes in the trabecular morphology and 1-day average flow-induced shear stresses when the width of the lazy zone $S_{sf}^{Z} = 0.4$ μN: (**a**) $\sigma_3 = -0.10$ MPa and (**b**) $\sigma_3 = -0.15$ MPa (This figure was adapted from Kameo and Adachi (2014) with permission from Springer)

induced shear stress acting on the osteocyte processes when the width of the lazy zone S_{sf}^{Z} is 0.6 and 0.4 μN, respectively. In these figures, part (a) corresponds to the results for the bending load $\sigma_3 = -0.10$ MPa and part (b) corresponds to the results for $\sigma_3 = -0.15$ MPa.

As shown in Fig. 6.2a, when the loading magnitude is $\sigma_3 = -0.10$ MPa, bone formation along the x_2-direction was triggered in the initial state because the applied bending load was linearly distributed along that direction. The bone deposition for 10 days formed a plate-like trabecula whose length in the x_2-direction is larger than that in the x_1-direction. Although the morphology of the trabecula was almost unchanged after this stage, the single trabecula was perforated close to the upper end owing to the local bone resorption. The obtained asymmetric trabecular morphology along the x_3-direction is due to the asymmetry of the imposed boundary conditions.

The increase in the magnitude of the applied bending load generated larger flow-induced shear stress on the trabecular surfaces. When $\sigma_3 = -0.15$ MPa, as shown in Fig. 6.2b, bone formation was promoted on the entire trabecular surface in the initial state owing to the increased flow-induced shear stress. The significant bone deposition formed a plate-like trabecula with an enlarged width and thickness. After 20 days, a local bone resorption was triggered around the upper end near the neutral axis of bending because the flow-induced shear stress in the region decreased owing to the prior bone formation along the x_2-direction. As a result of successive bone erosion, the Y-shaped trabecula with a bifurcation was formed.

As the width of the lazy zone $S_{\mathrm{sf}}^{\mathrm{Z}}$ decreases, the change in bone mass generally becomes more sensitive to the change in the total stimulus S_{sf} near the remodeling equilibrium, which will be discussed in Chap. 9. A comparison of the morphological changes in the trabeculae for the two different parameter settings of $S_{\mathrm{sf}}^{\mathrm{Z}}$, shown in Figs. 6.2 and 6.3, indicates that both the remodeling processes during the first 10 days are similar. However, when the lazy zone is comparatively small, large bone volume was lost owing to the subsequent bone resorption around the central region of the plate-like trabecula. In particular, under a large bending load, as shown in Fig. 6.3b, the plate-like trabecula separated towards double rod-like trabeculae.

6.4 Role of Local Bending Load in Bone Remodeling

Individual trabeculae that constitute cancellous bone *in vivo* are usually subjected to cyclic loading, consisting of both axial and bending components, due to locomotion and maintenance of posture (Weinbaum et al. 1994). Because the magnitude and ratio of each loading component depend on the region of interest in cancellous bone, we simulated the effects of uniaxial and bending loads on the trabecular bone adaptation separately to understand their fundamental roles. In Chap. 5, it was identified that a uniaxial load is responsible for the formation of a rod-like trabecula oriented toward the loading direction (Kameo et al. 2011). On the other hand, the present study showed that the application of the bending load is associated with not only the formation of the plate-like trabecula but also the change in trabecular

topology. These results suggest that the characteristic morphology of an individual trabecula can be determined by the local mechanical environment in an overall cancellous bone.

Whether the plate-like morphology is maintained or the bifurcation is formed depends on the magnitude of the applied bending load and the cellular activity on the trabecular surface. As shown in Figs. 6.2 and 6.3, the application of a larger bending load caused more significant bone erosion in the neighborhood of the neutral axis of bending, owing to an insufficient flow of stimuli to osteocytes. In addition, the decrease in the width of the remodeling lazy zone enhanced the motion of the bifurcation towards the lower edge. The lazy zone has been introduced in the Frost's mechanostat theory (Frost 1987, 2003) as the "adaptive window" and it represents the ability of the surface cells to detect changes in the local stimuli. Thus, the decrease in the lazy zone corresponds to the increase in the cellular sensitivity to the mechanical stimuli. Considering the biological implications of the lazy zone, the simulation results can be interpreted as indicating the plate-like trabecula to be maintained under the condition that the mechanical response of the surface effector cells is stable against the change in the local mechanical stimuli.

Through Chap. 5 and here, we have investigated the fundamental characteristics of our mathematical model of trabecular bone remodeling at the level of a single trabecula. Although not quantitatively validated, the remodeling simulations based on the proposed model could successfully express reasonable changes in trabecular morphology to adapt to various loading conditions. In the future, through a possible *in silico* reconstruction of the three-dimensional trabecular bone architecture for the entire bone with the aid of high-resolution scanners (Badilatti et al. 2016; Majumdar et al. 1998; Muller et al. 1994; Schulte et al. 2013), an image-based finite element analysis could help us investigate the state of stress in the arbitrary region and identify the relationship between the trabecular microstructure and the local mechanical environment. It will be essential for such future work to show the validity of our remodeling model at a more macroscopic level, such as a cancellous bone specimen comprising multiple trabeculae.

6.5 Conclusion

In this chapter, we applied our original remodeling model proposed in Sect. 5.2 to the voxel finite element model of a single upright trabecula and demonstrated its morphological adaptation to a cyclic bending load. The remodeling simulations showed that a plate-like trabecula was formed owing to the bone deposition that occurred in the early phase of the simulation. The width and thickness of the plate-like trabecula increased with the increase in the magnitude of the applied bending load. Furthermore, the subsequent bone resorption around the central region of the plate-like trabecula contributed to the bifurcation and separation of the single

trabecula. These simulation results suggest that the unique morphology of an individual trabecula, such as a rod-like or plate-like form, can be formed depending on the local mechanical environment in an overall cancellous bone.

References

Adachi T, Aonuma Y, Taira K, Hojo M, Kamioka H (2009) Asymmetric intercellular communication between bone cells: propagation of the calcium signaling. Biochem Biophys Res Commun 389(3):495–500. https://doi.org/10.1016/j.bbrc.2009.09.010

Adachi T, Kameo Y, Hojo M (2010) Trabecular bone remodelling simulation considering osteocytic response to fluid-induced shear stress. Philos Trans R Soc A 368 (1920):2669–2682. https://doi.org/10.1098/rsta.2010.0073

Badilatti SD, Christen P, Levchuk A, Marangalou JH, van Rietbergen B, Parkinson I, Muller R (2016) Large-scale microstructural simulation of load-adaptive bone remodeling in whole human vertebrae. Biomech Model Mechanobiol 15(1):83–95. https://doi.org/10.1007/s10237-015-0715-8

Basaruddin KS, Takano N, Yoshiwara Y, Nakano T (2012) Morphology analysis of vertebral trabecular bone under dynamic loading based on multi-scale theory. Med Biol Eng Comput 50 (10):1091–1103. https://doi.org/10.1007/s11517-012-0951-3

Beno T, Yoon YJ, Cowin SC, Fritton SP (2006) Estimation of bone permeability using accurate microstructural measurements. J Biomech 39(13):2378–2387. https://doi.org/10.1016/j.biomech.2005.08.005

Carbonare LD, Valenti MT, Bertoldo F, Zanatta M, Zenari S, Realdi G, Lo Cascio V, Giannini S (2005) Bone microarchitecture evaluated by histomorphometry. Micron 36(7–8):609–616. https://doi.org/10.1016/j.micron.2005.07.007

Frost HM (1987) Bone "mass" and the "mechanostat": a proposal. Anat Rec 219(1):1–9. https://doi.org/10.1002/ar.1092190104

Frost HM (2003) Bone's mechanostat: a 2003 update. Anat Rec A Discov Mol Cell Evol Biol 275A(2):1081–1101. https://doi.org/10.1002/ar.a.10119

Huo B, XL L, Hung CT, Costa KD, QB X, Whitesides GM, Guo XE (2008) Fluid flow induced calcium response in bone cell network. Cell Mol Bioeng 1(1):58–66. https://doi.org/10.1007/s12195-008-0011-0

Jaworski ZF, Lok E (1972) The rate of osteoclastic bone erosion in haversian remodeling sites of adult dogs rib. Calcif Tissue Res 10(2):103–112

Kameo Y, Adachi T (2014) Modeling trabecular bone adaptation to local bending load regulated by mechanosensing osteocytes. Acta Mech 225(10):2833–2840. https://doi.org/10.1007/s00707-014-1202-5

Kameo Y, Adachi T, Hojo M (2011) Effects of loading frequency on the functional adaptation of trabeculae predicted by bone remodeling simulation. J Mech Behav Biomed Mater 4 (6):900–908. https://doi.org/10.1016/j.jmbbm.2011.03.008

Majumdar S, Kothari M, Augat P, Newitt DC, Link TM, Lin JC, Lang T, Lu Y, Genant HK (1998) High-resolution magnetic resonance imaging: three-dimensional trabecular bone architecture and biomechanical properties. Bone 22(5):445–454. https://doi.org/10.1016/s8756-3282(98)00030-1

Muller R, Hildebrand T, Ruegsegger P (1994) Noninvasive bone-biopsy - a new method to analyze and display the 3-dimensional structure of trabecular bone. Phys Med Biol 39(1):145–164. https://doi.org/10.1088/0031-9155/39/1/009

Schulte FA, Ruffoni D, Lambers FM, Christen D, Webster DJ, Kuhn G, Mueller R (2013) Local mechanical stimuli regulate bone formation and resorption in mice at the tissue level. PLoS One 8(4). https://doi.org/10.1371/journal.pone.0062172

Smit TH, Huyghe JM, Cowin SC (2002) Estimation of the poroelastic parameters of cortical bone. J Biomech 35(6):829–835

Tsubota K, Adachi T (2005) Spatial and temporal regulation of cancellous bone structure: characterization of a rate equation of trabecular surface remodeling. Med Eng Phys 27 (4):305–311. https://doi.org/10.1016/j.medengphy.2004.09.013

Weinbaum S, Cowin SC, Zeng Y (1994) A model for the excitation of osteocytes by mechanical loading-induced bone fluid shear stresses. J Biomech 27(3):339–360

You LD, Weinbaum S, Cowin SC, Schaffler MB (2004) Ultrastructure of the osteocyte process and its pericellular matrix. Anat Rec A Discov Mol Cell Evol Biol 278A(2):505–513. https://doi.org/10.1002/ar.a.20050

Chapter 7
Cancellous Bone Adaptation Predicted by Remodeling Simulations

Abstract This chapter describes a functional adaptation of cancellous bone at the macroscopic level by considering the microscopic cellular activities through a computational approach. We simulate the morphological changes in a cancellous bone specimen consisting of multiple trabeculae in response to external loadings. The remodeling simulation predicts the reorientation of trabeculae parallel to the loading direction, leading to the uniformalization of the mechanical state in the cancellous bone. This result implies that our model of remodeling, in which flow stimuli to osteocytes are assumed to be a driving force of bone remodeling, can represent the phenomenological law of bone transformation toward a locally uniform state of stress or strain at the trabecular level.

Keywords Cancellous bone adaptation • Remodeling simulation • Mechanical hierarchy • Cellular activity • Stress uniformalization

7.1 Introduction

Cancellous bone is porous bone composed of rod-like and plate-like trabeculae, as shown in Chap. 6, forming a well-arranged three-dimensional network structure. The architecture of the trabeculae is continually reorganized via bone remodeling to functionally adapt to the mechanical environment, a phenomenon referred to as Wolff's law (Brand 2010; Duda et al. 2010; Wolff 1870, 2010). This process has a hierarchical structure from the microscopic cellular level to the macroscopic tissue level. The apparent changes in density and orientation of cancellous bone result from bone remodeling on the individual trabecular surfaces. Further the changes in a single trabecular morphology are caused by the coupling of cellular activities, including bone-resorbing osteoclasts and bone-forming osteoblasts, which is called the remodeling cycle (Parfitt 1994), under the regulation of mechanosensing osteocytes (Bonewald 2011; Knothe Tate et al. 2004). In order to understand the mechanical nature of bone remodeling, it is indispensable to focus on the hierarchy of bone structure and function in the multiscale analysis.

In this chapter, we investigate the functional adaptation of cancellous bone achieved by the collaboration of osteoclasts, osteoblasts, and osteocytes through a

This Chapter was adapted from Kameo and Adachi (2014) with permission from Springer.

Y. Kameo et al., *Bone Adaptation*, Frontiers of Biomechanics 2,
https://doi.org/10.1007/978-4-431-56514-7_7

computational approach. We applied the mathematical model for trabecular bone remodeling developed in Chap. 5, which enables the interconnection of the cellular activities at the microscopic scale and the trabecular morphological changes at the macroscopic scale through the mechanical hierarchy, to model a cancellous bone specimen comprising multiple trabeculae. Through the remodeling simulations, we demonstrated the changes in cancellous bone morphology in response to uniaxial and bending loads and compared the results obtained with experimental findings and the previous simulation results based on the phenomenological law of bone transformation.

7.2 Voxel Modeling of a Cancellous Bone Cube

A three-dimensional computational model of a cancellous bone cube consisting of multiple trabeculae was prepared, as shown in Fig. 7.1. The region for analysis was set to $a_1 \times a_2 \times a_3 = 3.2 \times 3.2 \times 3.2\ \text{mm}^3$ by reference to previous remodeling simulation studies (Adachi et al. 2001; Ruimerman et al. 2005), and was discretized by $80 \times 80 \times 80$ cubic voxel finite elements with an edge size of 40 μm. To produce a homogeneous and isotropic porous structure as the initial configuration of cancellous bone, many pieces of torus-like trabeculae, with an outer diameter of 0.36 mm and inner diameter of 0.28 mm, were scattered at random throughout the entire analysis region (Jang and Kim 2008; Tsubota et al. 2002, 2009). As a result of this procedure, a bone volume fraction BV/TV in the initial state was given as 0.4, which is within the physiological range. Two 0.2 mm-thick plates were added to the upper and lower surfaces of the region to apply external loadings. The individual trabeculae and the plate have the same poroelastic properties, as shown in Table 5.1 (Beno et al. 2006; Smit et al. 2002).

To investigate the effects of different loading scenarios on cancellous bone adaptation, two types of monotonously increasing loads $\sigma(t) = \sigma_3(x_1, x_2)t$ were imposed through the upper plate in the x_3-direction for 0.25 s per day: (i) a uniaxial load $\sigma_3 = -8$ MPa/sec and (ii) a bending load linearly distributed along the x_2-direction from -12 to 12 MPa/sec, i.e., $\sigma_3 = -24x_2/a_2$ (MPa/sec). A shear-free condition on the lower plane and free leakage of interstitial fluid on all trabecular surfaces were applied. The settings of the physiological parameters for the present remodeling simulation are listed in Table 7.1 (Adachi et al. 2009; Huo et al. 2008; Jaworski and Lok 1972; Weinbaum et al. 1994; You et al. 2004). All parameter values except S_{sf}^{U}, S_{sf}^{L}, S_{sf}^{O}, and S_{sf}^{Z} were the same as in Chaps. 5 and 6; these four parameters associated with the mechanical stimulus were adjusted with the enlargement of the model scale.

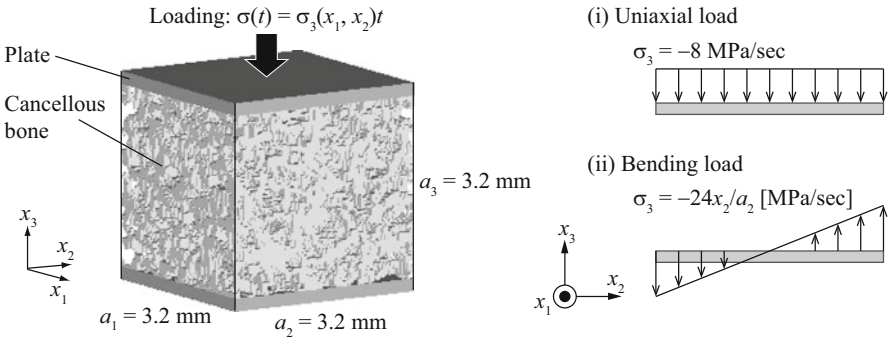

Fig. 7.1 Voxel finite element model of a cancellous bone cube, where all of the trabeculae are randomly oriented in the initial configuration. The sample was subjected to two different types of monotonously increasing loading through the upper plate: (*i*) uniaxial loading and (*ii*) bending loading (This figure was adapted from Kameo and Adachi (2014) with permission from Springer)

Table 7.1 Parameter settings for the trabecular remodeling simulation

Symbol (unit)	Description	Value
r_p (nm)	Radius of osteocyte process	52[a]
r_c (nm)	Radius of canaliculus	129.5[a]
a_0 (nm)	Radius of fiber	0.6[b]
Δ (nm)	Spacing of fiber matrix	7[b]
l_L (μm)	Maximum distance for intercellular communication	200[c,d]
$\dot{M}_{max}$ (μm/day)	Maximum remodeling rate	40[e]
S_{sf}^{U} (μN)	Upper threshold for bone formation	13
S_{sf}^{L} (μN)	Lower threshold for bone resorption	1.0
S_{sf}^{O} (μN)	Stimulus at remodeling equilibrium	7.0
S_{sf}^{Z} (μN)	Width of lazy zone	10

This table was adapted from Kameo and Adachi (2014) with permission from Springer
[a]You et al. (2004)
[b]Weinbaum et al. (1994)
[c]Huo et al. (2008)
[d]Adachi et al. (2009)
[e]Jaworski and Lok (1972)

7.3 Adaptation of a Cancellous Bone Cube to External Loads

This section explains simulation results regarding (1) morphological changes in cancellous bone (Sect. 7.3.1), and (2) spatial distribution of mechanical quantities (Sect. 7.3.2).

7.3.1 Morphological Changes in Cancellous Bone

According to the bone remodeling algorithm developed in Sect. 5.2, we simulated the mechanical adaptation of a cancellous bone cube to uniaxial and bending loads. Figure 7.2 shows the morphological changes in cancellous bone (a) under uniaxial loading and (b) under bending loading. The color contour indicates the one-day average of the flow-induced shear stress acting on the osteocyte processes, which is regarded as a driving force of bone remodeling.

As shown in Fig. 7.2a, the application of a uniaxial load triggered bone resorption on all trabecular surfaces in the initial state, owing to the small flow-induced shear stress, which resulted in a decrease in the *BV*/*TV*. After 3 days, despite the ongoing loss of the horizontal trabeculae, bone formation was promoted on the surfaces of the vertically oriented trabeculae, where the flow-induced shear stress was comparatively large. Successive bone remodeling gradually reduced the degree of trabecular connectivity, and the trabeculae consisting of cancellous bone reoriented in the loading direction.

When the cancellous bone cube was subjected to a bending load, as shown in Fig. 7.2b, for the first 3 days, significant bone volume was lost around the central

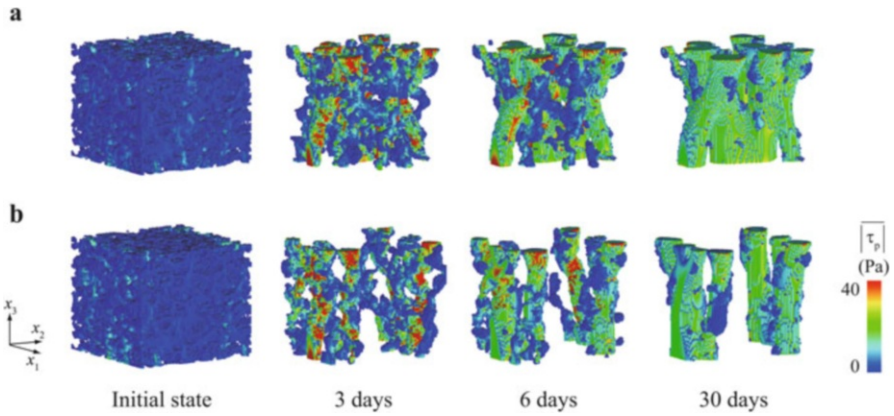

Fig. 7.2 Change in cancellous bone morphology and one-day average flow-induced shear stresses: (**a**) under uniaxial loading and (**b**) under bending loading (This figure was adapted from Kameo and Adachi (2014) with permission from Springer)

region for analysis, which is close to the neutral axis of bending, owing to insufficient mechanical stimuli to osteocytes. During the period from 3 to 6 days, bone erosion in the central region and bone deposition near the sides of the cuboidal region proceeded simultaneously. After this stage, the trabeculae around the central region were completely absorbed, and the remaining trabeculae aligned along the loading direction.

In both loading scenarios, the cancellous bone architecture reached a state of remodeling equilibrium by the end of 30 days. It should be noted that individual trabeculae in the remodeling equilibrium state had approximately circular cross-sections even though the cancellous bone cube at the starting point was composed of random-shaped trabeculae.

7.3.2 *Spatial Distribution of Mechanical Quantities*

It is widely accepted that the spatial distribution of the mechanical quantities of the trabeculae is one of the most important structural determinants of cancellous bone. In the previously published mathematical model for bone remodeling, several mechanical quantities were assumed as mechanical factors that drive bone resorption and formation (Gerhard et al. 2009). In order to understand the relationship between the trabecular architecture in cancellous bone and the mechanical state of individual trabeculae, we investigated the distribution of von Mises equivalent stress σ_{eq} and strain energy density (SED) U under the maximum load during one day and considered these as representative mechanical quantities. Here we introduced the deviation of both mechanical quantities defined as

$$\bar{Q} = Q - \mathrm{Mean}(Q), \tag{7.1}$$

where Q is either an equivalent stress, $Q = \sigma_{\mathrm{eq}}$, or a SED, $Q = U$. Mean(Q) denotes the mean value of Q in the cancellous bone cube at a specific stage of remodeling.

The distributions of the volume fractions corresponding to the deviation of equivalent stress $\overline{\sigma}_{\mathrm{eq}}$ are shown in Fig. 7.3, where the bin width of the plots is $\Delta\overline{\sigma}_{\mathrm{eq}} = 0.8$ (MPa). Figure 7.3a is the result for uniaxial loading and Fig. 7.3b is the result for bending loading. The mean value and standard deviation (s.d.) of the equivalent stress at different stages of remodeling are shown in Table 7.2 in the form: mean $\pm$ s.d. Regardless of the loading scenarios, the initial distributions were asymmetric with respect to $\overline{\sigma}_{\mathrm{eq}} = 0$, although differing in kurtosis values slightly. Their distribution profiles shifted to almost symmetrical curves by the end of 30 days. As shown in Table 7.2, the standard deviation of the equivalent stress decreased by 32% through the 30-day remodeling in both loading cases.

As for the deviation of SED $\bar{U}$, Fig. 7.4 shows the distributions of the volume fractions under uniaxial loading (Fig. 7.4a) and bending loading (Fig. 7.4b), where the bin width of the plots is $\Delta\bar{U} = 0.8$ (kJ/m^3). The mean value and standard

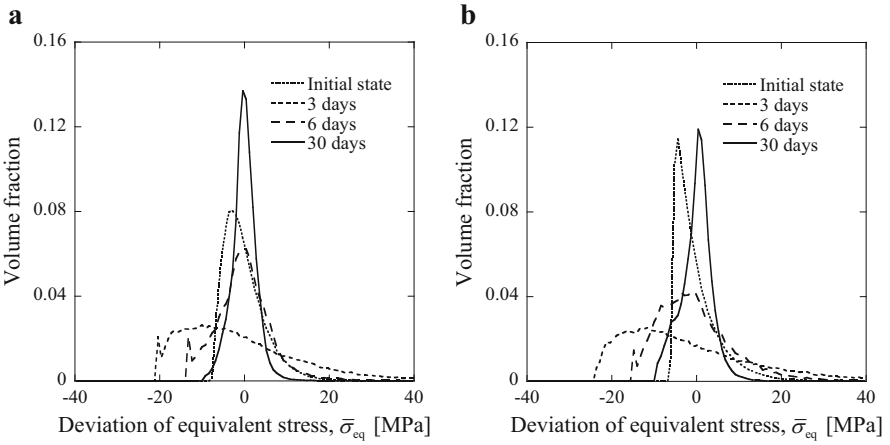

Fig. 7.3 Distributions of the volume fraction corresponding to the deviation of equivalent stress: (**a**) under uniaxial loading and (**b**) under bending loading. The bin width of the plots is $\Delta\bar{\sigma}_{eq} = 0.8$ (MPa) (This figure was adapted from Kameo and Adachi (2014) with permission from Springer)

Table 7.2 Mean value and standard deviation (s.d.) of von Mises equivalent stress during the process of bone remodeling

	von Mises equivalent stress, σ_{eq} [MPa]	
	Uniaxial load	Bending load
Initial state	7.24 ± 4.93	5.89 ± 5.46
3 days	20.4 ± 16.9	24.0 ± 20.7
6 days	13.1 ± 7.15	14.5 ± 9.62
30 days	9.80 ± 3.36	9.94 ± 3.72

(mean ± s.d.)

This table was adapted from Kameo and Adachi (2014) with permission from Springer

deviation of the SED during the process of bone remodeling are shown in Table 7.3. The initial distribution profiles in both loading cases exhibited similar characteristics, e.g., strong asymmetry with respect to $\bar{U} = 0$, and sharp peaks and fat tails in the positive direction. As a result of bone adaptation to external loadings, the kurtosis decreased and the peak position shifted toward the mean value. In contrast to the result for the equivalent stress, as shown in Table 7.2, the standard deviation of the SED increased by 47% under uniaxial loading even though it decreased by 43% under bending loading.

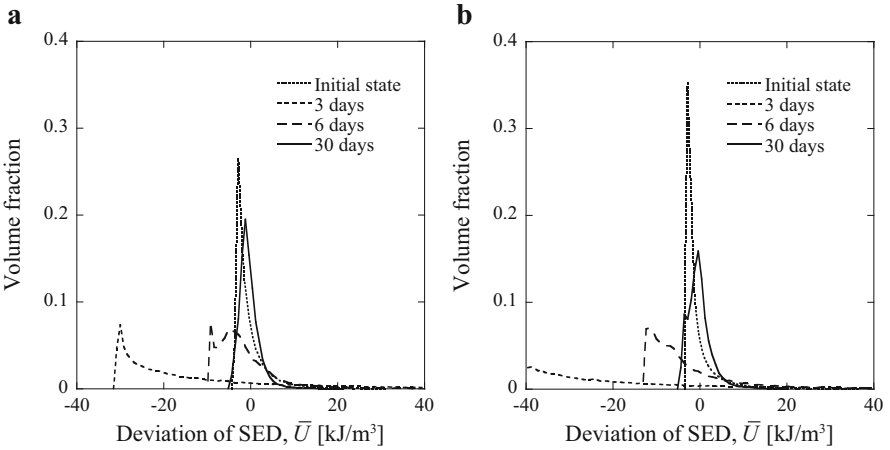

Fig. 7.4 Distributions of the volume fraction corresponding to the deviation of strain energy density (SED): (**a**) under uniaxial loading and (**b**) under bending loading. The bin width of the plots is $\Delta\bar{U} = 0.8$ (kJ/m^3) (This figure was adapted from Kameo and Adachi (2014) with permission from Springer)

Table 7.3 Mean value and standard deviation (s.d.) of strain energy density (SED) during the process of bone remodeling

	SED, U [kJ/m^3]	
	Uniaxial load	Bending load
Initial state	3.30 ± 4.92	2.77 ± 6.05
3 days	30.6 ± 78.4	44.4 ± 130
6 days	9.43 ± 15.5	12.5 ± 23.7
30 days	4.35 ± 7.25	4.19 ± 3.46

(mean ± s.d.)

This table was adapted from Kameo and Adachi (2014) with permission from Springer

7.4 Validity of the Simulated Remodeling Process

As shown in Fig. 7.2, the remodeling simulations indicated that imposing external loads on cancellous bone with randomly arranged trabeculae resulted in the alignment of multiple trabeculae along the loading direction, leading to a well-organized architecture specific to the type of external loads. Such trabecular reorientation can be regarded as a functional adaptation to satisfy mechanical demands and agrees qualitatively with the *in vivo* experimental studies where the remodeling process of

cancellous bone was observed under controlled mechanical conditions (Goldstein et al. 1991; Guldberg et al. 1997a, 1997b). When the cancellous bone cube was subjected to a bending load, the *BV/TV* decreased, owing to erosion of trabeculae around the central region for analysis, which corresponds to the neutral axis of bending. Although this phenomenon has not yet been experimentally validated, a trabecular remodeling simulation based on the phenomenological rule that remodeling progresses toward a locally uniform state of equivalent stress produced a similar pattern (Tsubota and Adachi 2005), as shown in Chap. 9.

Under both uniaxial and bending loading conditions, after 30 days, the individual trabecula in cancellous bone had approximately circular cross-sections. This is because the interstitial fluid velocity and, thus, the flow stimulus to osteocytes are uniform in the neighborhood of the cylindrical trabecula surfaces. These results indicate that our mathematical model for trabecular bone remodeling developed in Chap. 5 can successfully predict the changes in cancellous bone architecture at the macroscopic level by considering the cellular response to flow stimuli at the microscopic level.

7.5 Fluid Flow as a Candidate of Remodeling Stimulus

We identified the characteristics of interstitial fluid flow as a mechanical stimulus for bone remodeling by investigating the spatial distributions of von Mises equivalent stress and SED, both of which are representative remodeling stimuli in the previous mathematical simulations (Adachi et al. 1997; Huiskes et al. 1987). The distributions of these mechanical quantities at the trabecular level are, in general, non-uniform, owing to the complexity of cancellous bone architecture (Tsubota and Adachi 2006). As shown in Table 7.2, the standard deviation of the equivalent stress decreased as a result of the 30-day remodeling regardless of the loading types. This implies that our model of remodeling that considers the flow stimuli to osteocytes can represent the phenomenological law of bone transformation toward a locally uniform state of stress or strain at the trabecular level. On the other hand, comparing the distribution profiles for equivalent stress and SED, as shown in Figs. 7.3 and 7.4, reveals that the distribution of SED is more sensitive to the slight changes in cancellous bone morphology because SED is expressed as the quadratic form of stress or strain. Consequently, the standard deviation of the SED decreased under bending loading, but increased under uniaxial loading at the end of the 30-day simulation, as shown in Table 7.3. This suggests that the uniformalization of the local SED may not be indispensable for trabecular bone remodeling.

The physical characteristic of our mathematical model lies in the fact that bone remodeling is triggered not by the hydrostatic pressure, but by the gradient of interstitial fluid pressure. This means that the balance of bone resorption and formation on the trabecular surfaces is assumed to be governed by the local variation in the specific mechanical quantity. In this sense, our model of remodeling has a similar property to the model of remodeling driven by the local nonuniformity

of equivalent stress (Adachi et al. 2001), which is discussed in the following chapters, rather than the previous models in which remodeling was designed to reach the global reference value of the specific mechanical quantity (Huiskes et al. 2000; McNamara and Prendergast 2007). Considering that the former model, despite its basis on the phenomenological rule, can successfully reproduce a trabecular network pattern similar to that in the human proximal femur (Tsubota et al. 2009), as shown in Chap. 12, it is possible that bone remodeling is regulated not by the magnitude of mechanical quantities, but by their local variation in the trabeculae.

7.6 Conclusion

In this chapter, we simulated the morphological changes in a cancellous bone specimen under uniaxial and bending loads based on a model of remodeling that incorporates the possible mechanisms of cellular mechanosensing and intercellular communication. The remodeling simulation showed that multiple trabeculae in a cancellous bone cube reoriented in the external loading direction and exhibited a unique trabecular pattern depending on the type of applied loads. These behaviors are qualitatively in agreement with the remodeling process of cancellous bone observed *in vivo* under controlled mechanical conditions, indicating that our mathematical model for trabecular bone remodeling can successfully predict the functional adaptation of cancellous bone architecture. Regardless of the loading scenarios, the progress of bone remodeling reduced the standard deviation of the von Mises equivalent stress in cancellous bone, in contrast to that of the strain energy density. This result suggests that our model of remodeling developed in Chap. 5, in which flow stimuli to osteocytes are assumed to trigger bone remodeling, has the potential to represent the phenomenological law of bone transformation toward a locally uniform state of stress or strain at the trabecular level.

References

Adachi T, Tomita Y, Sakaue H, Tanaka M (1997) Simulation of trabecular surface remodeling based on local stress nonuniformity. JSME Int J Ser C 40(4):782–792. https://doi.org/10.1299/jsmec.40.782

Adachi T, Tsubota K, Tomita Y, Hollister SJ (2001) Trabecular surface remodeling simulation for cancellous bone using microstructural voxel finite element models. J Biomech Eng 123 (5):403–409. https://doi.org/10.1115/1.1392315

Adachi T, Aonuma Y, Taira K, Hojo M, Kamioka H (2009) Asymmetric intercellular communication between bone cells: propagation of the calcium signaling. Biochem Biophys Res Commun 389(3):495–500. https://doi.org/10.1016/j.bbrc.2009.09.010

Beno T, Yoon YJ, Cowin SC, Fritton SP (2006) Estimation of bone permeability using accurate microstructural measurements. J Biomech 39(13):2378–2387. https://doi.org/10.1016/j.biomech.2005.08.005

Bonewald LF (2011) The amazing osteocyte. J Bone Miner Res 26(2):229–238. https://doi.org/10.1002/jbmr.320

Brand RA (2010) Biographical sketch Julius Wolff, 1836-1902. Clin Orthop Relat Res 468(4):1047–1049. https://doi.org/10.1007/s11999-010-1258-z

Duda GN, Haas NP, Bergmann G (2010) Founding of the Julius Wolff Institut Charite – Universitatsmedizin Berlin. Clin Orthop Relat Res 468(4):1050–1051. https://doi.org/10.1007/s11999-010-1238-3

Gerhard FA, Webster DJ, van Lenthe GH, Muller R (2009) In silico biology of bone modelling and remodelling: adaptation. Philos Trans R Soc A 367(1895):2011–2030. https://doi.org/10.1098/rsta.2008.0297

Goldstein SA, Matthews LS, Kuhn JL, Hollister SJ (1991) Trabecular bone remodeling: An experimental model. J Biomech 24:135–150

Guldberg RE, Caldwell NJ, Guo XE, Goulet RW, Hollister SJ, Goldstein SA (1997a) Mechanical stimulation of tissue repair in the hydraulic bone chamber. J Bone Miner Res 12(8):1295–1302. https://doi.org/10.1359/jbmr.1997.12.8.1295

Guldberg RE, Richards M, Caldwell NJ, Kuelske CL, Goldstein SA (1997b) Trabecular bone adaptation to variations in porous-coated implant topology. J Biomech 30(2):147–153

Huiskes R, Weinans H, Grootenboer HJ, Dalstra M, Fudala B, Slooff TJ (1987) Adaptive bone-remodeling theory applied to prosthetic-design analysis. J Biomech 20(11–12):1135–1150. https://doi.org/10.1016/0021-9290(87)90030-3

Huiskes R, Ruimerman R, van Lenthe GH, Janssen JD (2000) Effects of mechanical forces on maintenance and adaptation of form in trabecular bone. Nature 405(6787):704–706

Huo B, XL L, Hung CT, Costa KD, QB X, Whitesides GM, Guo XE (2008) Fluid flow induced calcium response in bone cell network. Cell Mol Bioeng 1(1):58–66. https://doi.org/10.1007/s12195-008-0011-0

Jang IG, Kim IY (2008) Computational study of Wolff's law with trabecular architecture in the human proximal femur using topology optimization. J Biomech 41(11):2353–2361. https://doi.org/10.1016/j.jbiomech.2008.05.037

Jaworski ZF, Lok E (1972) The rate of osteoclastic bone erosion in haversian remodeling sites of adult dogs rib. Calcif Tissue Res 10(1):103–112

Kameo Y, Adachi T (2014) Interstitial fluid flow in canaliculi as a mechanical stimulus for cancellous bone remodeling: in silico validation. Biomech Model Mechanobiol 13(4):851–860. https://doi.org/10.1007/s10237-013-0539-3

Knothe Tate ML, Adamson JR, Tami AE, Bauer TW (2004) The osteocyte. Int J Biochem Cell Biol 36(1):1–8. https://doi.org/10.1016/s1357-2725(03)00241-3

McNamara LM, Prendergast PJ (2007) Bone remodelling algorithms incorporating both strain and microdamage stimuli. J Biomech 40(6):1381–1391. https://doi.org/10.1016/j.jbiomech.2006.05.007

Parfitt AM (1994) Osteonal and hemi-osteonal remodeling: the spatial and temporal framework for signal traffic in adult human bone. J Cell Biochem 55(3):273–286

Ruimerman R, Hilbers P, van Rietbergen B, Huiskes R (2005) A theoretical framework for strain-related trabecular bone maintenance and adaptation. J Biomech 38(4):931–941. https://doi.org/10.1016/j.jbiomech.2004.03.037

Smit TH, Huyghe JM, Cowin SC (2002) Estimation of the poroelastic parameters of cortical bone. J Biomech 35(6):829–835

Tsubota K, Adachi T (2005) Spatial and temporal regulation of cancellous bone structure: characterization of a rate equation of trabecular surface remodeling. Med Eng Phys 27(4):305–311. https://doi.org/10.1016/j.medengphy.2004.09.013

Tsubota K, Adachi T (2006) Computer simulation study on local and integral mechanical quantities at single trabecular level as candidates of remodeling stimuli. J Biomech Sci Eng 1(1):124–135. https://doi.org/10.1299/jbse.1.124

Tsubota K, Adachi T, Tomita Y (2002) Functional adaptation of cancellous bone in human proximal femur predicted by trabecular surface remodeling simulation toward uniform stress state. J Biomech 35(12):1541–1551. https://doi.org/10.1016/S0021-9290(02)00173-2

Tsubota K, Suzuki Y, Yamada T, Hojo M, Makinouchi A, Adachi T (2009) Computer simulation of trablecular remodeling in human proximal femur using large-scale voxel fe models: approach to understanding Wolff's law. J Biomech 42(8):1088–1094. https://doi.org/10.1016/j.jbiomech.2009.02.030

Weinbaum S, Cowin SC, Zeng Y (1994) A model for the excitation of osteocytes by mechanical loading-induced bone fluid shear stresses. J Biomech 27(3):339–360

Wolff J (1870) Ueber die innere Architectur der Knochen und ihre Bedeutung für die Frage vom Knochenwachstum. Virchows Arch Pathol Anat Physiol 50:389–450

Wolff J (2010) The classic on the inner architecture of bones and its importance for bone growth (reprinted from virchows arch pathol anat physiol, vol 50:389–450, 1870). Clin Orthop Relat Res 468 (4):1056–1065. doi:https://doi.org/10.1007/s11999-010-1239-2

You LD, Weinbaum S, Cowin SC, Schaffler MB (2004) Ultrastructure of the osteocyte process and its pericellular matrix. Anat Rec A Discov Mol Cell Evol Biol 278A(2):505–513. https://doi.org/10.1002/ar.a.20050

Chapter 8
Trabecular Surface Remodeling Toward Uniform Local Stress State

Abstract This chapter describes a rate equation of trabecular surface remodeling and its two-dimensional computer simulation to investigate changes in trabecular structure due to bone remodeling toward uniform local stress state. Nonuniformity in the local stress distribution on the trabecular surface is assumed to be the driving force of the remodeling. The trabecular structure is computationally modeled with an assemblage of pixel finite elements, and their morphological changes are simulated by removal/addition of the elements from/to the trabecular surface. The basic features of the proposed rate equation are investigated through remodeling simulations for trabecular-level and cancellous-bone-level structures. Simulated changes in the trabecular structure, represented by orientation, thickness, and connectivity, demonstrate the capability of the proposed rate equation to computationally predict the mechanical adaptation of the cancellous bone structure.

Keywords Cancellous bone • Trabecular surface remodeling • Adaptation • Uniform stress

8.1 Introduction

Mathematical modeling and computational simulation of bone functional adaptation by remodeling started with modeling its rate equations using macroscopic mechanical quantities such as stress/strain and strain energy density based on phenomenological hypotheses (Carter 1984; Carter et al. 1987; Cowin and Hegedus 1976; Huiskes et al. 1987; Ruimerman et al. 2005). *In vivo* and *in vitro* experiments contributed to the significant advancement in our understanding of the bone adaptation mechanism from tissue level down to the cellular and molecular levels. As discussed in Chaps. 5, 6, and 7, microscopic mechanical phenomena such as interstitial fluid flow in the lacuna-canalicular system (Han et al. 2004; Weinbaum et al. 1994) and responses from osteocytic mechanosensory network were involved in the rate equations of bone adaptation (Adachi et al. 2010; Kameo and Adachi 2014a, b; Kameo et al. 2011).

This Chapter was adapted from Adachi et al. (1997) with permission from The Japan Society of Mechanical Engineers.

Y. Kameo et al., *Bone Adaptation*, Frontiers of Biomechanics 2,
https://doi.org/10.1007/978-4-431-56514-7_8

The approach to understanding bone adaptation breaks down the phenomena—in this book volume, the correspondence of trabecular orientation to the local loading direction—into its key players, which include the mechanosensing osteocytes, the bone resorbing osteoclasts, and the bone forming osteoblasts. We conducted a series of *in vitro* experiments to characterize the osteocyte calcium signaling response to mechanical stimuli and their communication. The results showed that (1) osteocytes embedded in the bone matrix can respond to the matrix deformation (Adachi et al. 2009a), (2) osteocytic dendritic processes are sensitive to the mechanical stimuli (Adachi et al. 2009c), and (3) the calcium signaling response significantly propagates asymmetrically from the osteocytes to the osteoblasts (Adachi et al. 2009b). Therefore, the mechanical signals sensed by osteocytic cellular processes occupying the canaliculae are transmitted to the osteoblasts on the bone surfaces. Based on these experimental evidences, microscopic interstitial fluid flow and cellular communication among osteocyte networks were mathematically modeled, and computational simulation demonstrated that a single trabecula under uniaxial loading changes its morphology to align with the loading direction as shown in Chap. 5, resulting in a uniform stress distribution on the trabecular surface.

Similar to the experiment, the more detailed mechanism have been clarified, the more complexity as a system is recognized in modeling and simulation. Thus, this reminds us again an importance of the contraction in mathematical modeling with reduction of the model parameters to extract and capture the essential features of the complex system. In this chapter, we will propose a simple remodeling rate equation for trabecular surface remodeling that contains only two model parameters: one for spatial and one for temporal regulation, based on the phenomenological hypothesis that the cellular-level mechanical stimuli are related to the trabecular surface remodeling to achieve local uniform stress condition at the remodeling equilibrium. In addition, the proposed rate equation is applied to a two-dimensional finite element simulation to investigate morphological changes in the trabecular structure, and the correspondence of their principal direction to the principal stress direction is discussed. Finally, we notice that the local uniform stress distribution on the trabecular surface attained in Chap. 5, which considers a microscopic lacuna-canalicular network of osteocytes, is consistent with the phenomenological hypothesis proposed in this chapter.

8.2 Model of Trabecular Surface Remodeling

At a local point on the trabecular surface, the surface movement by bone remodeling is related to the local mechanical stimulus based on the uniform stress hypothesis.

8.2.1 Morphological Change of Trabecula by Surface Movement

On the trabecular surfaces in cancellous bone, a cycle of five successive stages of quiescence, activation, resorption by the osteoclasts, reversal, and formation by the osteoblasts (Parfitt 1994), as illustrated in Fig. 8.1, results in trabecular surface remodeling. The relative difference between downward erosion by resorption and upward refilling of a cavity by formation in a single cycle determines the local movement of the trabecular surface in the direction perpendicular to the surface. After repetitive cycles, macroscopic changes in the trabecular architecture in cancellous bone are observed, which correspond to cancellous bone remodeling.

Because of the cyclical nature of this process, a trabecular surface remodeling rate equation was expressed at two different hierarchical time scales, t and T, as shown in Fig. 8.1, where t denotes the time on the cellular activity scale and T denotes a time longer enough than ΔT of the characteristic period of one remodeling turnover cycle. Let $\dot{m}\ (= \partial m/\partial t)$ denote the rate of the surface movement by remodeling in the outer direction perpendicular to the surface; i.e., $\dot{m} = 0$: quiescence, $\dot{m} < 0$: resorption, and $\dot{m} > 0$: formation. Averaging $\dot{m}$ over the period ΔT for one remodeling cycle, the trabecular surface remodeling rate in the outer direction perpendicular to the surface $\dot{M}\ (= \partial M/\partial t)$ is defined as

$$\dot{M} = \frac{1}{\Delta T}\int_{\Delta T} \dot{m}\, dt \tag{8.1}$$

In the following sections, the expression of $\dot{M}$ is discussed for trabecular surface remodeling as a local stress regulation process.

8.2.2 Local Stress Nonuniformity

Osteoclastic bone resorption and osteoblastic bone formation at local sites are regulated by two different-scale mechanisms; systematic regulation by hormones and local regulation by signaling molecules. We assume that the former mechanism is related to the volumetric and/or mass changes in the bone, whereas the latter is associated with local morphological changes in the trabecular architecture. To discuss how the microscopic mechanical conditions relate to the trabecular surface remodeling and how the macroscopic trabecular architecture emerges from the local surface remodeling, we employ local mechanical conditions as stimuli regulating the trabecular surface remodeling based on the fact that a cell-to-cell network and communication exist (Cowin et al. 1991). Thus, we consider that the positive scalar function a as a mechanical stimulus that bone cells (i.e., the osteocytes embedded in the bone matrix and/or the osteoblasts on the trabecular surface) can sense, and assume that local nonuniformity is a driving force for remodeling.

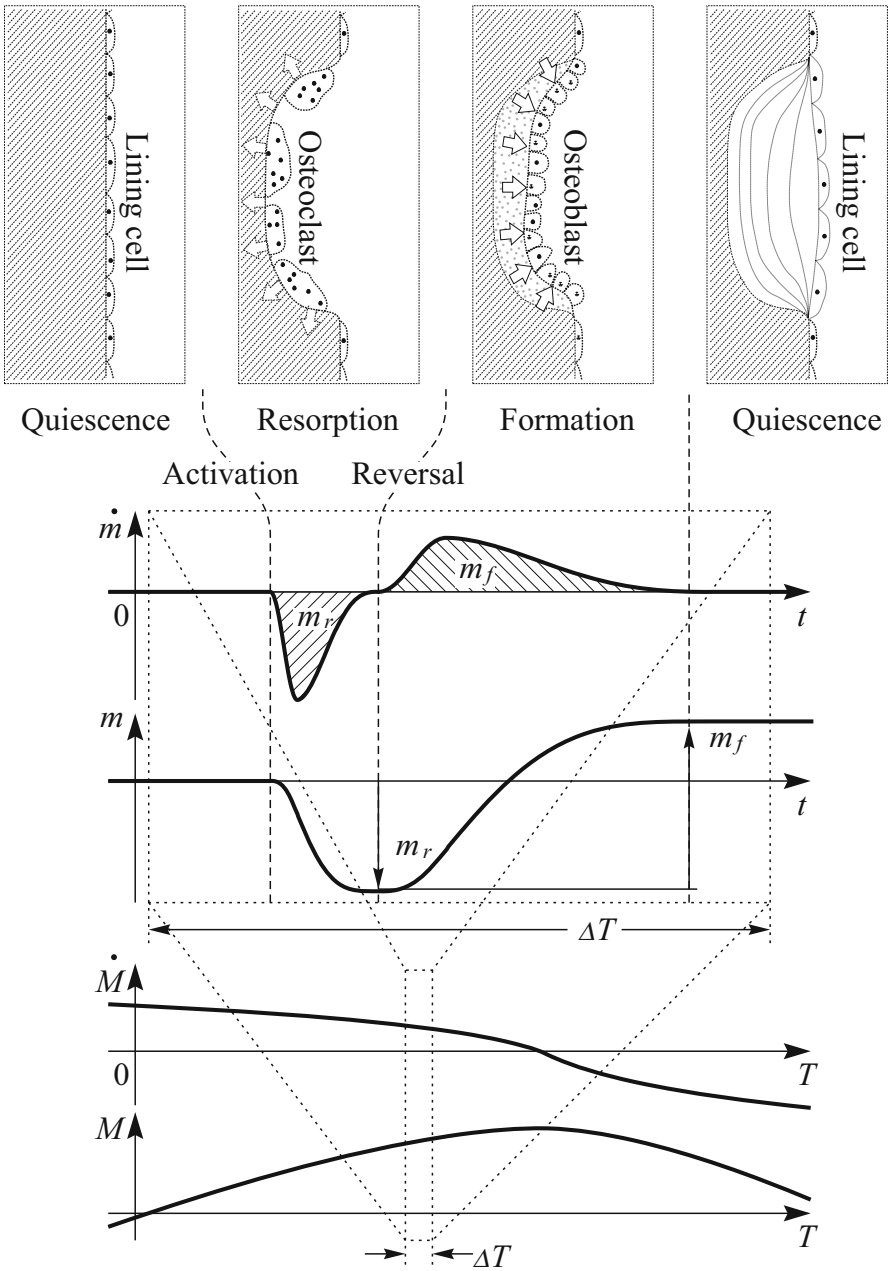

Fig. 8.1 Surface movement of trabecula in hierarchical time scale due to remodeling cellular activities (This figure was adapted from Adachi et al. (1997) with permission from The Japan Society of Mechanical Engineers)

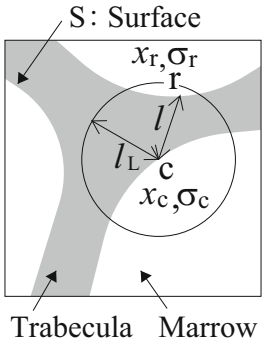

Fig. 8.2 Stress nonuniformity at point c on trabecular surface (This figure was adapted from Adachi et al. (2001) with permission from The American Society of Mechanical Engineers)

To express the nonuniformity of the scalar function in space, the differential form using the Laplacian operator or the integral form with suitable weight functions may be used. In this study, we use the latter integral form considering the stresses $\sigma_c(\boldsymbol{x}_c)$ and $\sigma_r(\boldsymbol{x}_r)$ at point $\boldsymbol{x}_c$ and at its neighbor point $\boldsymbol{x}_r$ (Fig. 8.2). Averaging σ_r with the weight function $w(l)$, the representative stress σ_d is determined as

$$\sigma_d = \int_S w(l)\sigma_r dS \Big/ \int_S w(l) dS, \tag{8.2}$$

where S denotes the trabecular surface, $l = |\boldsymbol{x}_r - \boldsymbol{x}_c|$, and the weight function $w(l)$ takes a non-zero value at the neighbor point ($l < l_L$). When the mechanosensory osteocytes in bone matrix are considered, the integrated area S can be replaced by volume V. As the driving force of the local trabecular remodeling, we use the relative value of σ_c to σ_d, that is defined as

$$\Gamma = \ln(\sigma_c/\sigma_d) \tag{8.3}$$

This function Γ, which expresses the nonuniformity of the stress distribution, takes a positive value for a convex stress distribution and a negative value for a concave distribution. Therefore, the function Γ allows expressing the nonuniformity of the stress distribution with a small number of parameter. In Eq. 8.3, only one model parameter l_L is introduced that has a spatial unit. The characteristics of the function Γ will be discussed in detail in Chap 10.

8.2.3 Rate Equation of Trabecular Remodeling

For a mechanical load-bearing structure, the uniform stress condition on the trabecular surface is the optimal criterion that leads to the uniform strength.

Based on the uniform stress hypothesis in the remodeling equilibrium, we propose a new rate equation for trabecular surface remodeling as a stress regulation process toward its uniform distribution on the surface. Using the stress nonuniformity function Γ in Eq. (8.3), the remodeling rate equation is written as

$$\dot{M}(\Gamma) = F(\Gamma) = \begin{cases} \geq 0 \ (\Gamma \geq 0): & \text{Formation} \\ < 0 \ (\Gamma < 0): & \text{Resorption} \end{cases}, \tag{8.4}$$

by which the formation at the site with a convex stress distribution and the resorption with a concave distribution are expressed. In this equation, the local remodeling rate is determined using only local mechanical conditions evaluated by Γ without considering the prescribed systematic global stresses such as the goal or the optimal stress. In this sense, the proposed remodeling rate Eq. (8.4) is different from the equation in the optimization problem that seeks the global minimum/maximum conditions and provides a history-dependent process of the bone adaptation by remodeling.

8.3 Computer Simulation Method with Pixel FE Models

This section describes a two-dimensional simulation method of trabecular surface remodeling based on the mathematical model of Sect. 2 combined with pixel finite element (FE) models.

8.3.1 Pixel FE Model of Trabecular Structure

The trabecular architecture is discretized by two-dimensional pixel FE elements, as shown in Fig. 8.3. The trabecular surface movement by remodeling is expressed by adding and removing the square (pixel) elements on the surface, as shown in Fig. 8.4, in response to the mechanical conditions determined through finite element analysis. The element size should be smaller than the dimension of the basic multicellular unit. In the remodeling simulation, the trabecular thickness is discretized with at least three elements as an initial shape. The trabecular bone part is assumed to be a homogeneous and isotropic elastic material with Young's modulus $E_t = 20$ GPa and Poisson's ratio $n_t = 0.3$. The marrow is considered to be a cavity, and thus neglected in the finite element analysis.

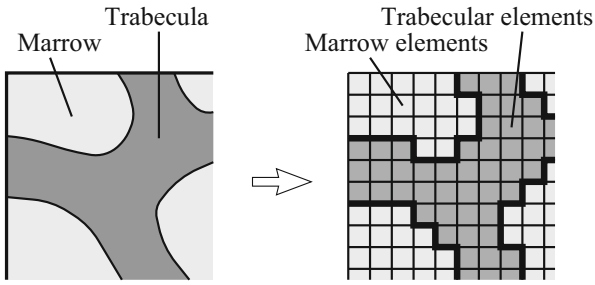

Fig. 8.3 Discretization of trabecula with pixel elements in two dimensional problem (This figure was adapted from Adachi et al. (1997) with permission from The Japan Society of Mechanical Engineers)

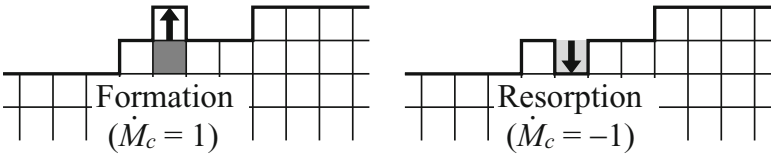

Fig. 8.4 Trabecular surface movement due to bone formation and resorption expressed by addition and removal, respectively, of bone pixel element

8.3.2 *Calculation of Stress Nonuniformity on Trabecular Surface*

The stress nonuniformity Γ on the trabecular surface in Eq. (8.3) is determined for the trabecular pixel FE elements, as follows. For the surface element c,

$$\Gamma_c = \ln\left(\sigma_c \sum_i^N w\left(l_i^c\right) \Big/ \sum_i^N w\left(l_i^c\right)\sigma_i\right) \tag{8.5}$$

is determined where N is the total number of trabecular surface elements, and σ_i is the stress at the surface element i at the distance l_i^c, as illustrated in Fig. 8.5. In a simple case, the weight function $w(l)$ is assumed to be

$$w(l) = \begin{cases} 1 - \dfrac{l}{l_L} & (0 \le l < l_L), \\ 0 & (l_L \le l) \end{cases} \tag{8.6}$$

representing a monotonic linear decrease with l to zero at $l = l_L$ as shown in Fig. 8.5. Thus, the cell at $\boldsymbol{x}_c$ is assumed to be able to sense the mechanical conditions in the neighboring region of $l \le l_L$.

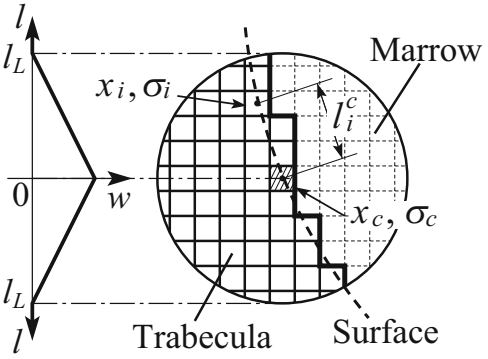

Fig. 8.5 Calculation of stress nonuniformity Γ_c at element c of trabecular surface (This figure was adapted from Adachi et al. (1997) with permission from The Japan Society of Mechanical Engineers)

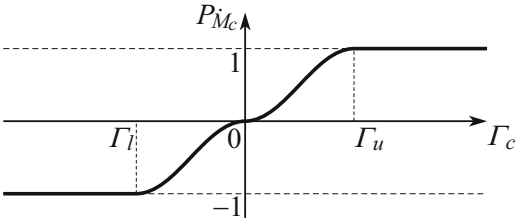

Fig. 8.6 Probability function of remodeling rate (This figure was adapted from Adachi et al. (1997) with permission from The Japan Society of Mechanical Engineers)

8.3.3 *Rate of Surface Movement for Pixel FE Model*

The trabecular surface movement is discretely expressed by adding and removing the finite element on the trabecular surface, as illustrated in Fig. 8.4. Therefore, the rate of the surface movement for each simulation step assumes the value $\dot{M}_c = 1, 0, -1$ (elem./step). However, because $\dot{M}$ is naturally continuous in time, as illustrated in Fig. 8.1, we introduce the continuous probability function $P_{\dot{M}_c}$ in the range $\Gamma_l \le \Gamma_c \le \Gamma_u$, as is shown in Fig. 8.6, where Γ_l and Γ_u denote the lower and upper threshold values, respectively. The ranges $\Gamma_l \le \Gamma_c \le 0$ and $0 \le \Gamma_c \le \Gamma_u$ are interpolated by sine functions. As the remodeling progresses, the nonuniformity of the surface stress becomes smaller, i.e., $|\Gamma_c|$ approaches zero. The remodeling probability $|P_{\dot{M}_c}|$ also approaches zero, which represents the lazy zone (dead zone) of remodeling (Carter 1984; Huiskes et al. 1987) around the equilibrium state ($\dot{M}_c = 0$).

8.3.4 *Remodeling Simulation Procedure*

The trabecular surface remodeling simulation is conducted through the following procedures:

1. The initial shape of the trabecular architecture and the model parameters are defined.

2. The stress of the trabecular surface elements is analyzed by a pixel FEM under the given boundary conditions.
3. The surface stress nonuniformity Γ_c in Eq. (8.5) is calculated for all surface elements.
4. The rate of the surface movement $\dot{M}_c$ is determined by the calculated Γ_c based on the relationship expressed in Fig. 8.6, and a surface element is added or removed, as shown in Fig. 8.4.
5. If a remodeling equilibrium is not attained, the process is repeated from procedure (2).

Procedures (2)–(5) form a single step of the simulation. Moreover, the equivalent stress is used as the scalar function σ of the stress, as discussed in Chap.10. The two-dimensional pixel FE analysis assumes a plane-strain condition. The volumetric change of cancellous bone because of remodeling may be maintained constant at every step by shifting the equilibrium point of Γ_c in Fig. 8.6, assuming that the volumetric change is caused by global systematic regulation and not by local regulation.

8.4 Remodeling at Trabecular Level

The primary features of the trabecular structural changes predicted by the proposed remodeling rate equation were investigated with a model of a single trabecula under compressive loading.

8.4.1 Model of Single Trabecula Under Compressive Loading

Referring to the basic trabecular structures as introduced by Frost (1988), the simulation of trabecular surface remodeling was performed for a single trabeculae with characteristic shapes Z, Y, and X under compressive loading, as shown in Figs. 8.7 and 8.8. Rigid plates were attached to the upper and lower surfaces. A uniform compressive stress of 2.0 MPa was applied to the upper plate, while the lower plate remained fixed. The entire area, including the rigid plates, was discretized by 40 × 40 pixel FEs, as shown in Fig. 8.7; each element was 12.5 μm in length and the whole region was 500 × 500 μm. The parameter l_L in the weight function $w(l)$ of Eq. (8.6) was set to 200 μm, equal to the length of 16 elements. The remodeling threshold values (Fig. 8.6) were set to $\Gamma_u, \Gamma_l = \pm 0.05$. The effects of these model parameters on the trabecular remodeling process of cancellous bone will be discussed in Chap. 9.

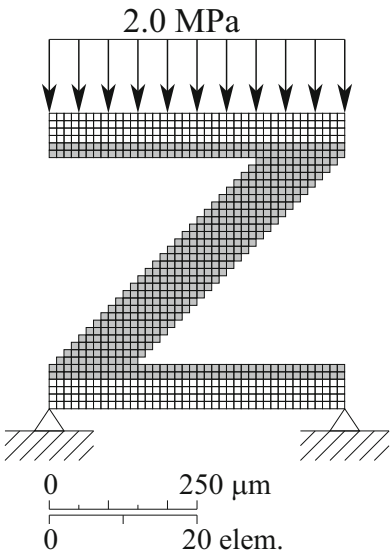

Fig. 8.7 Model of single trabecula under compressive loading condition (This figure was adapted from Adachi et al. (1997) with permission from The Japan Society of Mechanical Engineers)

8.4.2 Morphological Changes of a Single Trabecula

The morphological changes of a single trabeculae and the regulation of the distribution of equivalent stress by surface remodeling under compressive loading are shown in Fig. 8.8, where each column shows the progress from the original shape (left) to the final equilibrium shape (right). For an initially Z-shaped trabecula (Fig. 8.8a), the center of trabecula was subject to bending. The trabecula grew near the rigid plates, where the equivalent stress σ was higher than that in the neighbors, while the bone resorbed in the middle in a few initial steps due to the low σ. At the 4th step, the trabecular surface at the compression side still had higher stress, whereas on the tensed surface, the equivalent stress σ decreased and the surface remodeling turned to resorption by approximately the 20th step. Gradually, the stress distribution on the trabecular surface was regulated and became uniform; the trabecula was reoriented to the loading direction and reached its equilibrium shape at the 40th step.

For an initially X-shaped trabecula (Fig. 8.8b), the upper and lower corners of the crossing region exhibited low σ, and the right and left corners had high σ. The original X shape changed to an H shape by remodeling at the 4th step. The horizontal trabecula between two vertical trabeculae became thinner at the 8th step, and then, disappears. Finally, it changed to two parallel trabeculae at the remodeling equilibrium by the 20th step.

For an initially Y-shaped trabecula (Fig. 8.8c), the trabecula grew at the lower corners of the branch, whereas it resorbed at the upper corner because of its

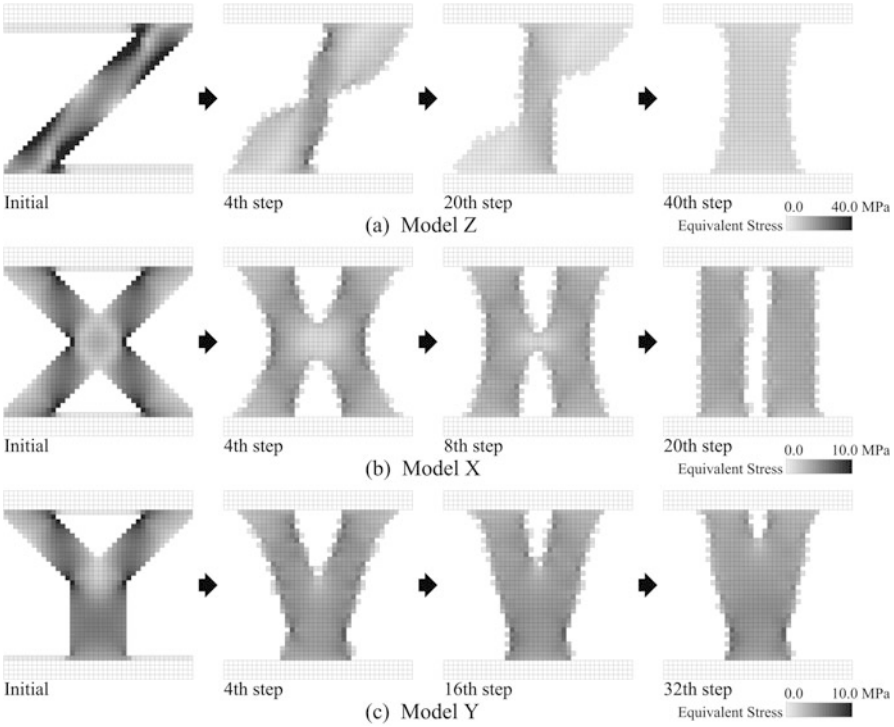

Fig. 8.8 Results of remodeling simulation for single trabecula under compressive loading: (**a**) Model Z; (**b**) Model X; (**c**) Model Y (This figure was adapted from Adachi et al. (1997) with permission from The Japan Society of Mechanical Engineers)

nonuniform stress distribution. The original Y shape changed to a V shape at the 4th step. These two trabeculae moved closer to each other by remodeling at the 16th step. Finally, the remodeling reached an equilibrium state at the 32th step, the two trabeculae did not fuse together because of the existence of the lazy zone around the remodeling equilibrium.

In all models, a trabecula changed its shape in order to orientate in the loading direction, which successfully expresses the bone structure adaptation by remodeling to support the mechanical loading. Even if the same boundary conditions and model parameters were applied to the simple compressed trabecular structure, a simulated trabecular structure at an equilibrium depends on the initial trabecular shape. If there was no lazy zone in the remodeling equilibrium, the trabecular structure with a Y shape (Fig. 8.8c) would become a single trabecula (Fig. 8.8a) by fusion of two trabeculae in the upper half region, and or a parallel trabecular structure (Fig. 8.8b) by separation into two trabeculae in the lower half region.

8.5 Remodeling at Cancellous Bone Level

The primary features of cancellous-bone-level structural changes by remodeling were investigated using a square cancellous bone model under biaxial stress.

8.5.1 Model of Square Cancellous Bone

A two-dimensional square region of cancellous bone under a uniform stress field was considered. This region was assumed as an infinitesimal area of the cancellous bone but with a sufficient number of the trabeculae.

In order to construct the initial morphology of cancellous bone model, circular trabeculae were randomly pasted in the square region (Fig. 8.9a). This initial cancellous bone has an isotropic trabecular structure that can be quantitatively evaluated from the measurement of the fabric ellipse (Harrigan and Mann 1984), as shown in Fig. 8.9b, that was determined by the mean intercept length. The square region of the cancellous bone was surrounded by three-layered dummy elements with Young's modulus E_d ($= E/10$) $= 2.0$ GPa and Poisson's ratio $\nu_d = 0.3$ to apply uniformly distributed external loads as a boundary condition in the uniform stress field with the corresponding normal and shearing stresses. The entire square region was discretized using 150×150 pixel elements. The side of an element was 60 μm long, and, thus, the side of the square region was 9 mm long. The sensing distance l_L was set to 600 μm ($=$ 10 elements), and the threshold values for the remodeling were set to Γ_u, $\Gamma_l = \pm 0.5$.

As a boundary condition, two cases of uniform stress field with principal stresses σ_1 and σ_2 were assumed (Fig. 8.10): (a) $\sigma_1 = -1.0$, $\sigma_2 = -2.0$ MPa (compression-compression) and (b) $\sigma_1 = 1.0$, $\sigma_2 = -2.0$ MPa (tension-compression). The principal stresses σ_1 and σ_2 in the two cases had the same magnitudes with (a) the same signs and (b) opposite signs. The angle θ_p between the principal direction of σ_1 and the horizontal axis was varied.

8.5.2 Morphological Changes of Cancellous Bone

The remodeling process in the cancellous square region and its fabric ellipses, which were caused by the rotation of the principal direction of the stress from $\theta_p = 0°$ to 45° at intervals of 15°, are shown in Fig. 8.11, in which a and b denote the principal radii of the fabric ellipses. For each direction of θ_p, the changes in the trabecular architecture for eight remodeling steps were calculated. It was thus confirmed that 15 simulation steps were enough to reach an equilibrium state.

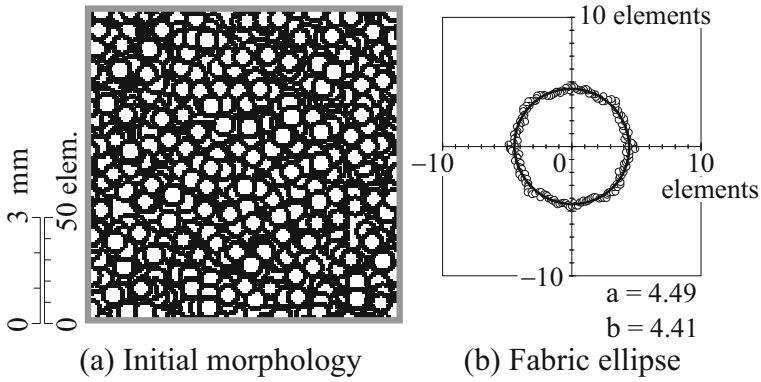

Fig. 8.9 Model of square cancellous bone: (**a**) Initial morphology; (**b**) Fabric ellipse (This figure was adapted from Adachi et al. (1997) with permission from The Japan Society of Mechanical Engineers)

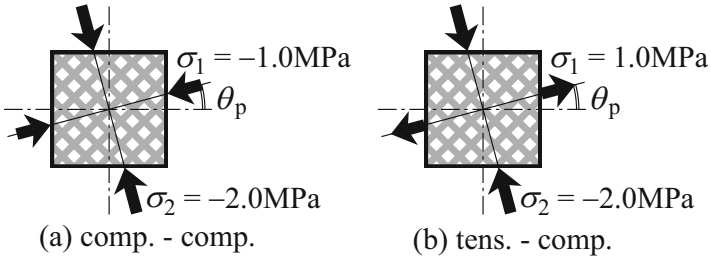

Fig. 8.10 Boundary conditions of biaxial stress for model of square cancellous bone: (**a**) compression-compression; (**b**) tension-compression (This figure was adapted from Adachi et al. (1997) with permission from The Japan Society of Mechanical Engineers)

In the case of the same signs for the compression-compression principal stresses at $\theta_p = 0°$, the originally isotropic trabecular architecture changed its morphology to an anisotropic architecture aligned to the direction of the principal stress σ_2, which is indicated by the principal direction of the fabric ellipse (Fig. 8.11a). The thickness of the trabeculae aligning along the direction of σ_2 increased, whereas that along the direction of σ_1 decreased. Following the rotation of the principal stress direction from $\theta_p = 0°$ to 15°, 30°, and 45°, the trabeculae were gradually reoriented, resulting in the rotation of the principal direction of the fabric ellipse, as shown in the lower column of Fig. 8.11a. The disappearance of the trabeculae aligned to the principal direction of σ_1 caused the principal radius a to become longer, whereas b did not changed significantly. Accordingly, the aspect ratio of the fabric principal radii a/b increased from 1.02 to 1.46.

In the case of the opposite signs for the tension-compression principal stresses at $\theta_p = 0°$, the morphology of the originally isotropic trabecular architecture also changed to anisotropic architecture aligned to the directions of the principal stresses σ_1 and σ_2, as shown in Fig. 8.11b. However, the trabecular architecture became obviously different from that for the case with the same signs for the principal stress in Fig. 8.11a. When the principal stresses had the same signs, as shown in Fig. 8.11a, the trabeculae were interconnected at rounded corners. However, when they had opposite signs, the trabeculae were interconnected at right angles (Fig. 8.11b). As a result, the trabeculae in the direction of σ_1 did not disappear as much in Fig. 8.11b, and the ratio of the trabecular thicknesses became approximately 1: 2, corresponding to $|\sigma_1|$: $|\sigma_2|$. Following the rotation of the principal stress direction from $\theta_p = 0°$ to 15°, 30°, and 45°, the trabeculae were gradually reoriented in the same manner as in the case with the same signs. The aspect ratio of the fabric principal radii changes from 1.02 to 1.30.

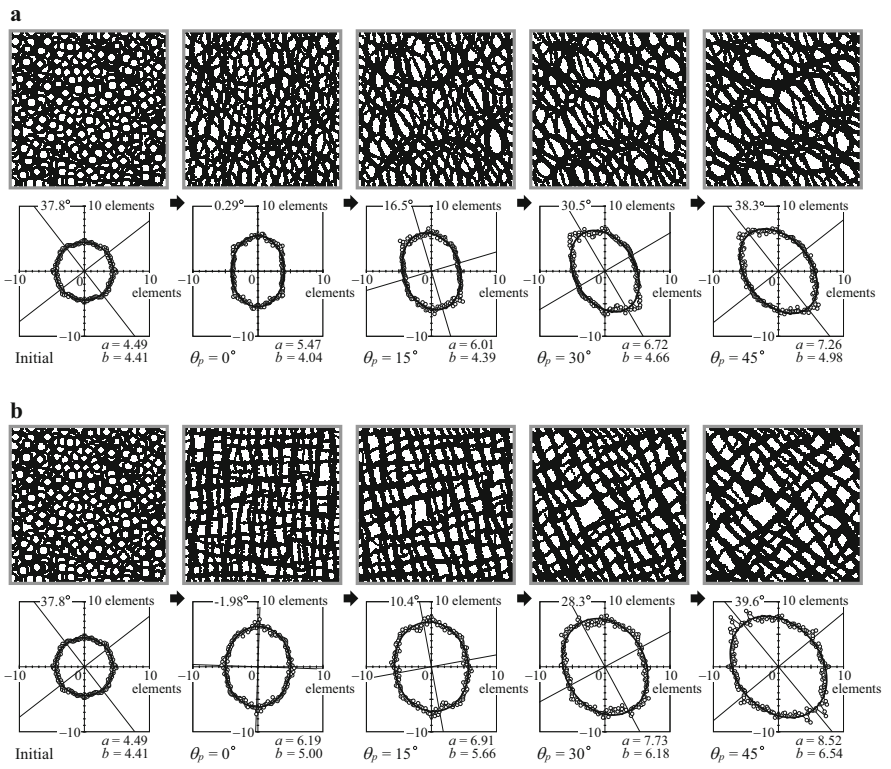

Fig. 8.11 Simulated morphological changes of trabecular structure in square cancellous bone under biaxial stress: (**a**) compression-compression ($\sigma_1 = -1.0$, $\sigma_2 = -2.0$ MPa); (**b**) tension-compression ($\sigma_1 = 1.0$, $\sigma_2 = -2.0$ MPa) (This figure was adapted from Adachi et al. (1997) with permission from The Japan Society of Mechanical Engineers)

8.5.3 *Relationships Between Cancellous Bone Structure and Apparent Stress*

The change of the trabecular architecture as predicted by the simulation can be characterized by the fact that individual trabeculae were reoriented into the loading direction. That is, the trabeculae changed their morphology to align to the direction of the principal stress. This reorientation of the trabecular architecture is reasonable for the bone tissue structure as a load bearing system. The evolution equation proposed by Cowin (1992) (Cowin et al. 1992) also leads to a reorientation of the trabecular architecture that supports the hypothesis by Wolff (1892, 1986) (Wolff 1892, 1986), according to which the principal stress axes coincide with the principal trabecular direction at the remodeling equilibrium.

Depending on the signs of the principal stresses σ_1 and σ_2, the corresponding trabecular architecture patterns at the remodeling equilibrium differed as shown in Figs. 8.11a, b. The difference between the architecture with rounded corners in Fig. 8.11a and that with right-angled corners in Fig. 8.11b is because the remodeling rate equation employed the equivalent stress σ as a mechanical stimulus that always has a positive value. When the principal stresses σ_1 and σ_2 have the same signs (Fig. 8.12a), the stress in the direction of σ_2 became convex, and that in the direction of σ_1 became concave, leading to growth and resorption, respectively, and resulting in the rounded corners of the trabecular architecture. In contrast, if the principal stresses assumed opposite signs (Fig. 8.12b), the stress σ in both the directions of σ_1 and σ_2 became convex, leading to growth that resulted in the

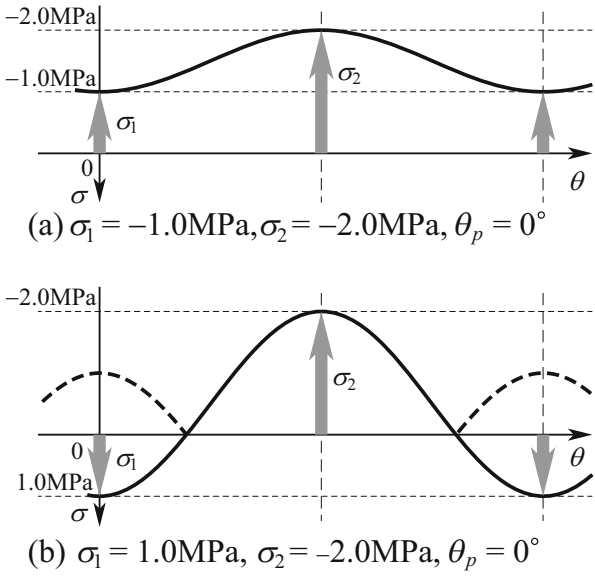

Fig. 8.12 Schematic drawings of normal stress distribution in square cancellous bone model ($\theta_p = 0°$): (**a**) compression-compression ($\sigma_1 = -1.0$, $\sigma_2 = -2.0$ MPa); (**b**) tension-compression ($\sigma_1 = 1.0$, $\sigma_2 = -2.0$ MPa) (This figure was adapted from Adachi et al. (1997) with permission from The Japan Society of Mechanical Engineers)

interconnection of the trabeculae at right angles. This result was due to the evaluation of the mechanical stimulus as a positive definite value, so the same results can be expected if other positive values, such as strain energy density, were used as mechanical stimuli for the rate equation in trabecular surface remodeling. In actual cancellous bone, orthogonality of the trabecular architecture is observed in the frontal section of the proximal femur (Wolff 1892, 1986) and in the sagittal plane of patella (Hayes and Snyder 1981), where the principal stresses have opposite signs.

8.6 Conclusion

In this chapter, we proposed a rate equation for trabecular surface remodeling as a regulation process of the nonuniform stress distribution on the trabecular surface to a uniform distribution. In this rate equation, the local stress nonuniformity was employed as the driving force of the remodeling, which did not employ any prescribed goal or optimal stress as a global constraint of the systematic regulation. Using a pixel finite element method for the discretized trabecular architecture, two-dimensional simulations of trabecular surface remodeling were conducted for trabecular-level and cancellous-bone-level structures. In these simulations, the morphologies of the trabeculae were changed in response to the mechanical conditions by changing the trabecular orientation, thickness, and connectivity. The results indicated that the proposed model of trabecular surface remodeling is capable of predicting trabecular structural adaptation by cellular activities driven by cellular-level mechanical stimuli.

References

Adachi T, Tomita Y, Sakaue H, Tanaka M (1997) Simulation of trabecular surface remodeling based on local stress nonuniformity. JSME Int J C 40(4):782–792. https://doi.org/10.1299/jsmec.40.782

Adachi T, Tsubota K, Tomita Y, Hollister SJ (2001) Trabecular surface remodeling simulation for cancellous bone using microstructural voxel finite element models. J Biomech Eng-T Asme 123(5):403–409. https://doi.org/10.1115/1.1392315

Adachi T, Aonuma Y, Ito S, Tanaka M, Hojo M, Takano-Yamamoto T, Kamioka H (2009a) Osteocyte calcium signaling response to bone matrix deformation. J Biomech 42 (15):2507–2512. https://doi.org/10.1016/j.jbiomech.2009.07.006

Adachi T, Aonuma Y, Taira K, Hojo M, Kamioka H (2009b) Asymmetric intercellular communication between bone cells: propagation of the calcium signaling. Biochem Biophys Res Commun 389(3):495–500. https://doi.org/10.1016/j.bbrc.2009.09.010

Adachi T, Aonuma Y, Tanaka M, Hojo M, Takano-Yamamoto T, Kamioka H (2009c) Calcium response in single osteocytes to locally applied mechanical stimulus: differences in cell process and cell body. J Biomech 42(12):1989–1995. https://doi.org/10.1016/j.jbiomech.2009.04.034

Adachi T, Kameo Y, Hojo M (2010) Trabecular bone remodelling simulation considering osteocytic response to fluid-induced shear stress. Philos Transact A Math Phys Eng Sci 368 (1920):2669–2682. https://doi.org/10.1098/rsta.2010.0073

Carter DR (1984) Mechanical loading histories and cortical bone remodeling. Calcif Tissue Int 36: S19–S24

Carter DR, Fyhrie DP, Whalen RT (1987) Trabecular bone density and loading history: regulation of connective tissue biology by mechanical energy. J Biomech 20(8):785–794

Cowin SC, Hegedus DH (1976) Bone remodeling I: theory of adaptive elasticity. J Elast 6 (3):313–326

Cowin SC, Moss-Salentijn L, Moss ML (1991) Candidates for the mechanosensory system in bone. J Biomech Eng 113(2):191–197

Cowin SC, Sadegh AM, Luo GM (1992) An evolutionary Wolff's law for trabecular architecture. J Biomech Eng 114(1):129–136

Frost H (1988) Structural adaptations to mechanical usage. A proposed "Three-Way Rule" for bone modeling, part I. Vet Comp Orthop Traumatol 1(1):13–23

Han Y, Cowin SC, Schaffler MB, Weinbaum S (2004) Mechanotransduction and strain amplification in osteocyte cell processes. Proc Natl Acad Sci U S A 101(47):16689–16694. https://doi.org/10.1073/pnas.0407429101

Harrigan TP, Mann RW (1984) Characterization of microstructural anisotropy in orthotropic materials using a 2nd rank tensor. J Mater Sci 19(3):761–767

Hayes WC, Snyder B (1981) Toward a quantitative formulation of Wolff's law in trabecular bone, vol AMD-45. Mechanical properties of bone

Huiskes R, Weinans H, Grootenboer HJ, Dalstra M, Fudala B, Slooff TJ (1987) Adaptive bone-remodeling theory applied to prosthetic-design analysis. J Biomech 20(11–12):1135–1150

Kameo Y, Adachi T (2014a) Interstitial fluid flow in canaliculi as a mechanical stimulus for cancellous bone remodeling: in silico validation. Biomech Model Mechanobiol 13 (4):851–860. https://doi.org/10.1007/s10237-013-0539-3

Kameo Y, Adachi T (2014b) Modeling trabecular bone adaptation to local bending load regulated by mechanosensing osteocytes. Acta Mech 225(10):2833–2840. https://doi.org/10.1007/s00707-014-1202-5

Kameo Y, Adachi T, Hojo M (2011) Effects of loading frequency on the functional adaptation of trabeculae predicted by bone remodeling simulation. J Mech Behav Biomed Mater 4 (6):900–908. https://doi.org/10.1016/j.jmbbm.2011.03.008

Parfitt AM (1994) Osteonal and hemi-osteonal remodeling: the spatial and temporal framework for signal traffic in adult human bone. J Cell Biochem 55(3):273–286. https://doi.org/10.1002/jcb.240550303

Ruimerman R, Hilbers P, van Rietbergen B, Huiskes R (2005) A theoretical framework for strain-related trabecular bone maintenance and adaptation. J Biomech 38(4):931–941. https://doi.org/10.1016/j.jbiomech.2004.03.037

Weinbaum S, Cowin SC, Zeng Y (1994) A model for the excitation of osteocytes by mechanical loading-induced bone fluid shear stresses. J Biomech 27(3):339–360

Wolff J (1892) Das Gesetz Der Transformation Der Knochen. Hirschwald, Berlin

Wolff J (1986) The law of bone remodeling (trans: Maquet P, Furlong R). Springer, New York

Chapter 9
Spatial and Temporal Regulation of Cancellous Bone Structure by Trabecular Surface Remodeling

Abstract This chapter describes the application of a computer simulation of trabecular surface remodeling (proposed in Chap. 8) for investigating the spatial and temporal changes in the trabecular structure caused by remodeling. Two model parameters, the threshold value of the lazy zone and the sensing distance of the mechanical environment, are introduced into the remodeling rate equation to express the sensitivity of bone cells to mechanical stimuli. A two-dimensional rectangular cancellous bone model under non-uniform compressive loads is constructed using pixel finite elements. A simulation result revealed that the trabecular structure underwent temporal and spatial changes depending on the loading condition. Sensing distance regulates the spatial distribution of the trabecular structure, while the threshold value of the lazy zone regulates the rate of structural changes in time. The results indicate that these model parameters are important in controlling the spatial and temporal regulation of the trabecular structure that depends on the sensitivities of bone cells to mechanical stimuli.

Keywords Cancellous bone • Trabecular surface remodeling • Adaptation • Uniform stress

9.1 Introduction

In a bone remodeling computer simulation, model parameters in a remodeling rate equation are keys to determining the spatial and temporal changes in bone structure (Cowin et al. 1985), as well as the trabecular mechanical environment determined by external loading condition, cortical bone shape, and internal trabecular structure, as described in Chaps. 11, 12, and 13. In a surface remodeling rate equation described in Chap. 8, we introduced two model parameters in the model for trabecular surface remodeling in order to express the sensitivity of bone cells to mechanical stimuli. Therefore, these model parameters are important not only for the accurate prediction of the actual trabecular structure (Adachi et al. 2001;

This Chapter was adapted from Tsubota and Adachi (2005) with permission from Institute of Physics and Engineering in Medicine.

Y. Kameo et al., *Bone Adaptation*, Frontiers of Biomechanics 2,
https://doi.org/10.1007/978-4-431-56514-7_9

Tsubota et al. 2002, 2009), but also for giving an insight into the regulation mechanism of the trabecular structure caused by cellular response to the mechanical stimuli.

In this chapter, we clarify the effects of the model parameters on trabecular structural changes in both space and time. 2D simulations of trabecular surface remodeling are conducted with a large-scale pixel finite element model of rectangular cancellous bone under simple and nonuniform compressive loads. In addition, the spatial and temporal regulation processes of cancellous bone are discussed on the basis of the simulation results, in terms of the mechanical adaptations resulting from cellular responses to local mechanical stimuli.

9.2 Simulation Model of Cancellous Bone

A rectangular cancellous bone model was created using a large number of pixel finite elements (Sect. 9.2.1). Simple and non-uniform compressive loads were applied to the model (Sect. 9.2.2), and it was used to simulate trabecular structural changes by a trabecular surface remodeling model described in Chap. 8.

9.2.1 Rectangular Cancellous Bone Model

A rectangular cancellous bone model was constructed using pixel finite elements, as shown in Fig. 9.1. The initial morphology of the cancellous bone was created by randomly pasting circular trabeculae with outer and inner diameters of 500 μm and 300 μm, respectively. The dimensions of the model were $W = 10$ mm in the X_1 direction and $W/2 = 5$ mm in the X_2 direction. The pixel elements numbered 800 in the X_1 direction and 400 in the X_2 direction, and size of each pixel was 12.5 μm. The structural parameters of the cancellous bone (Parfitt et al. 1987) were: bone volume fraction $BVF = 0.57$, trabecular bone thickness $Tb.Th = 73$ μm and

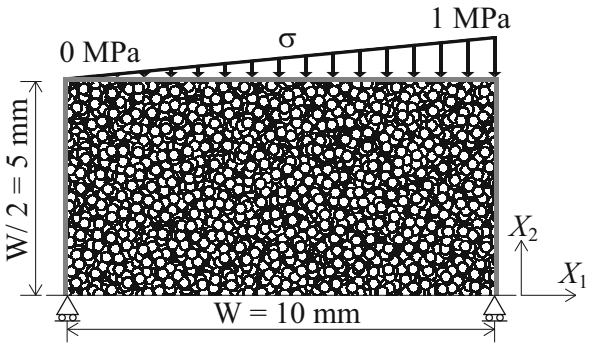

Fig. 9.1 Simulation model of a cancellous bone under non-uniform compressive loads (This figure was adapted from Tsubota and Adachi (2005) with permission from Institute of Physics and Engineering in Medicine)

connectivity $CON = 27.9\ \text{mm}^{-2}$. In this simulation method, the time scale of each simulation step was not explicitly considered, although it can be determined by comparing the simulation results with the experimental ones (Adachi et al. 2001, 1997). Stress was analyzed by the finite element method with the element-by-element preconditioned conjugate gradients (EBE/PCG) method (Hughes et al. 1987; van Rietbergen et al. 1995). Trabeculae were assumed to be a homogeneous, isotropic material with Young's modulus of $E_t = 20$ GPa and Poisson's ratio of $\nu_t = 0.3$, while the marrow was regarded as a cavity, and was neglected in the finite element analysis.

9.2.2 *Boundary Condition for Nonuniform Compressive Loads*

As a boundary condition, compressive load in the X_2 direction, which was linearly distributed along the X_1 direction from 0 to 1 MPa, was applied through a thin bone layer that was placed around the cancellous part to smoothly distribute the force applied to the cancellous part (Fig. 9.1). The bone layer was 8 elements thick and its Young's modulus was one-hundredth that of the trabeculae.

9.3 Regulation of Cancellous Bone Structure

This section describes the effects of model parameters threshold values of lazy zone (Sect. 9.3.1) and sensing distance of mechanical stimuli (Sect. 9.3.2) on cancellous bone structure. It also discusses that the spatial and temporal regulation of the trabecular structure is determined by the sensitivities of bone cells to mechanical stimuli (Sect. 9.3.3).

9.3.1 *Effects of Threshold Values of Lazy Zone*

Threshold values Γ_u and Γ_l are the parameters that relate remodeling driving force Γ to the rate of surface movement $\dot{M}$ in Fig. 8.6, and affect the activation of the remodeling. To clarify the effects of threshold values Γ_u and Γ_l on trabecular structural changes, remodeling simulation was conducted for different values of $|\Gamma|$ $(=\Gamma_u = -\Gamma_l)$ from 0 to 10, where sensing distance l_L (Eq. (8.6)) was set constant at 2.0 mm.

The trabecular structures at the 10th and 20th steps for $|\Gamma| = 2.0$, 3.0, 5.0, and 10.0 are shown in Fig. 9.2. Trabeculae reorganized and aligned along the compressive loading direction, which expressed the functional adaptation as is observed in

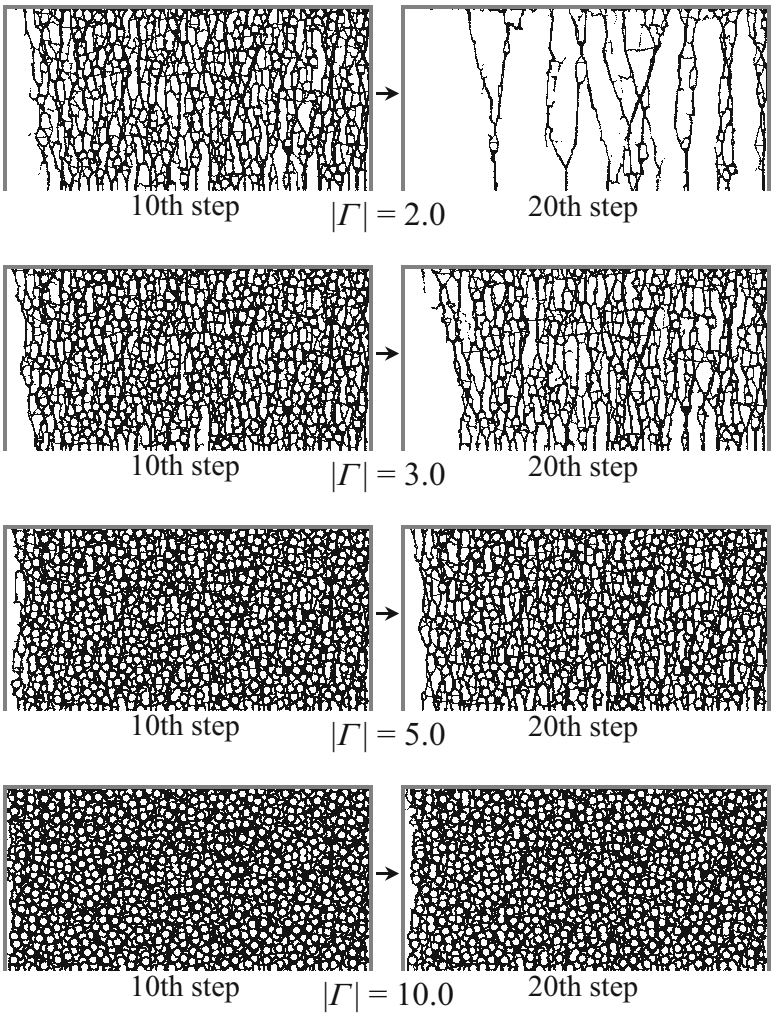

Fig. 9.2 Trabecular structures obtained by the remodeling simulation at the 10th and 20th steps for different threshold values of $|\Gamma| = 2.0$, 3.0, 5.0, and 10.0 (This figure was adapted from Tsubota and Adachi (2005) with permission from Institute of Physics and Engineering in Medicine)

the actual bone. The smaller threshold value $|\Gamma|$ led to a faster alignment of the trabeculae. To evaluate the effect of the threshold value $|\Gamma|$ on the structural changes quantitatively, changes in structural parameters BVF, $Tb.Th$ and CON were calculated as shown in Fig. 9.3a–c. BVF was decreased by remodeling because the number of trabecular surface elements activated to form new bone

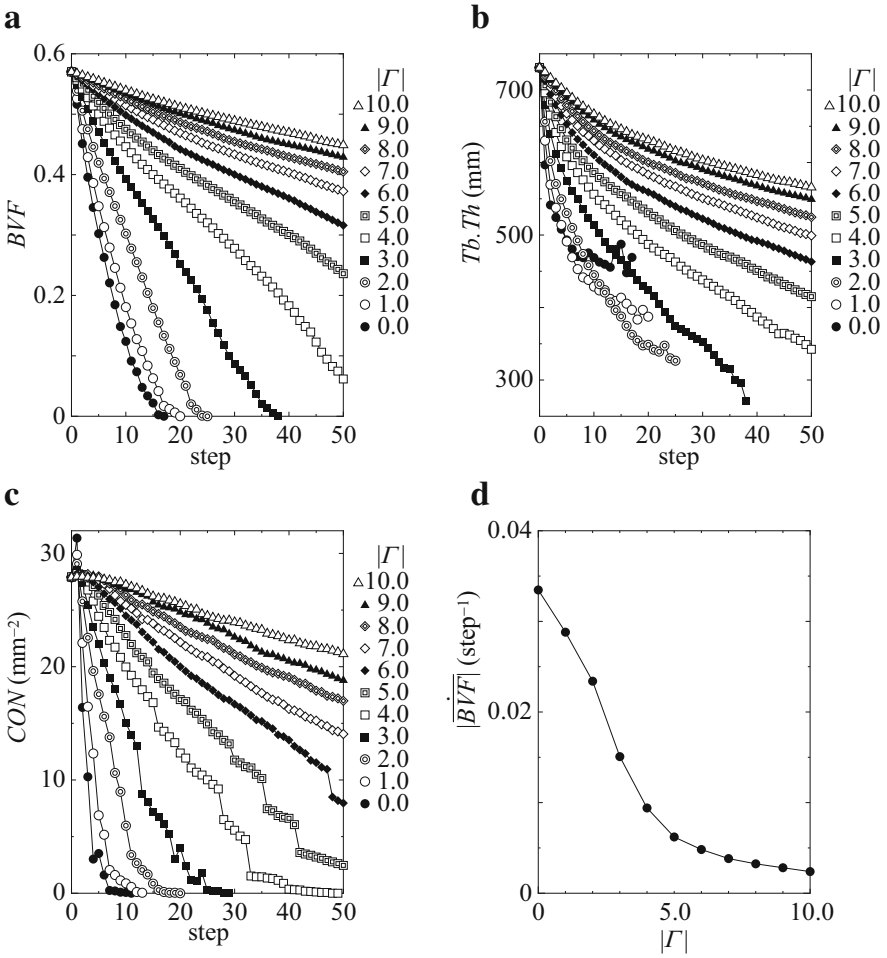

Fig. 9.3 Temporal changes in structural parameters depending on the threshold value $|\Gamma|$: (**a**) Bone volume fraction *BVF*, (**b**) Trabecular bone thickness *Tb*.*Th*, and (**c**) Connectivity *CON*. (**d**) Rate of volumetric change $|\dot{\overline{BVF}}|$ as a function of threshold value $|\Gamma|$ (This figure was adapted from Tsubota and Adachi (2005) with permission from Institute of Physics and Engineering in Medicine)

was less than that activated for resorption. *Tb*.*Th* and *CON* also decreased corresponding to the decrease in *BVF*. The calculations of the curve slopes in Fig. 9.3a by linear fitting showed the magnitude of the rate in volumetric changes $|\dot{\overline{BVF}}|$ decreases with increasing threshold value $|\Gamma|$, as shown in Fig. 9.3d.

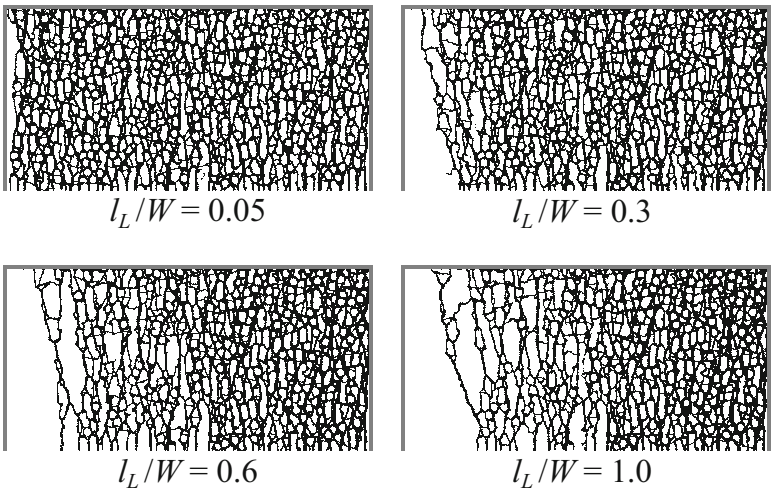

Fig. 9.4 Trabecular structures obtained by remodeling simulation at the 30th step for different normalized sensing distances of l_L/W=0.05, 0.3, 0.6, and 1.0 (This figure was adapted from Tsubota and Adachi (2005) with permission from Institute of Physics and Engineering in Medicine)

9.3.2 *Effects of Sensing Distance of Mechanical Stimuli*

Sensing distance l_L in Eq. (8.6) represents the area where cells can sense mechanical stimuli. To clarify the effects of sensing distance l_L on trabecular structural changes, remodeling simulation was conducted for different values of l_L normalized by the width of the cancellous bone model W from 0.05 to 1.0, where the threshold value $|\Gamma|$ was set constant at 5.0.

Trabecular structures at the 30th step for $l_L/W = 0.05$, 0.3, 0.6, and 1.0 are shown in Fig. 9.4. The larger sensing distance l_L caused a more distributed trabecular structure in accordance with the spatial distribution of the compressive loads. As a result, the largest loss of trabeculae occurred on the left side of the cancellous bone with less compressive loads for $l_L/W = 1.0$. To evaluate the effect of sensing distance l_L on the spatial distribution of the bone structure quantitatively, the distributions of BVF with respect to the normalized coordinate ξ $(=X_1/W)$ and its linear fitting line were calculated as shown in Fig. 9.5a. The gradients ΔBVF of the fitting lines, which represented the spatial distribution of BVF, were 0.03 for $l_L/W = 0.05$ and 0.52 for $l_L/W = 1.0$. ΔBVF for other l_L/W values at the 30th step were further calculated, and it was shown that ΔBVF increased with l_L/W, as shown in Fig. 9.5b.

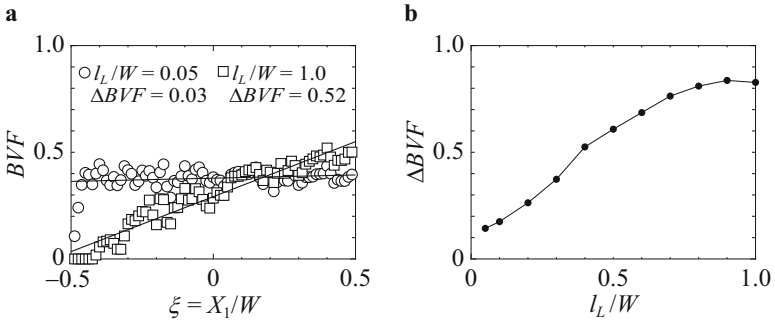

Fig. 9.5 Spatial distribution of bone volume fraction at the 30th step depending on the sensing distance l_L. (**a**) Bone volume fraction BVF to normalized coordinate ξ ($=X_1/W$). (**b**) Spatial gradient of bone volume fraction ΔBVF to normalized sensing distance l_L/W (This figure was adapted from Tsubota and Adachi (2005) with permission from Institute of Physics and Engineering in Medicine)

9.3.3 Structural Changes According to Sensing Mechanical State

A temporal and spatial change in the trabecular structure was obtained by the remodeling simulation. By studying the model parameters, it was found that the threshold value of the lazy zone $|\Gamma|$ regulated the rate of structural changes with time, and that the sensing distance l_L regulated the spatial distribution of the bone structure. The findings indicate that these parameters regulate the sensitivities of remodeling to mechanical stimuli in time and space. Therefore, the results demonstrate the possibility that the sensitivity of bone cells to mechanical stimuli is one of the critical factors in determining the spatial and temporal regulation of a trabecular structure.

Threshold value $|\Gamma|$ played a role similar to that of the rate coefficient used in a linear remodeling rate equation (Cowin et al. 1985). When the threshold value $|\Gamma|$ was small, a decrease in trabecular connectivity occurred in the less compressive region (on the left side of the cancellous bone region shown in Fig. 9.2). Subsequently, trabeculae were isolated due to the loss of connectivity and lack of loading, and the isolated trabeculae were resorbed because they were no longer loaded, as predicted in stochastic simulations of bone remodeling (Langton et al. 1998; Tabor and Rokita 2002). Finally, the trabeculae were completely lost. That is, the small threshold value $|\Gamma|$ led to a large loss of trabeculae in the less compressive region. This result can be regarded as an "over-adaptation" of the trabecular structure, as suggested by Weinans (1998), and thus indicates that excessive sensitivity of bone cells to mechanical stimuli is one of the candidate causes of osteoporosis.

Sensing distance l_L was shown to affect the spatial distribution of the trabecular structure. A large sensing distance led to the trabecular structure becoming more adapted to the spatial distribution of compressive loads, and to a large loss of trabeculae in the less compressive region. This can also be regarded as an over-adaptation of the trabecular structure, as in the case of the threshold value $|\Gamma|$. The parameter l_L corresponds to the distance in the cellular communication such as observed in calcium propagation (Xia and Ferrier 1992) and is thus expected to be a few hundred micrometers. On the basis of the characteristics of the model parameters clarified in this study, the appropriate values of the model parameters should be investigated by comparing the trabecular structures between the simulations and the experiments, as will be shown in Chap. 11. The identified model parameters will represent the cellular activities *in vivo*, and will thus provide an insight into the mechanism of bone remodeling at the cellular level.

9.4 Conclusion

In this chapter, the spatial and temporal regulation of the cancellous bone structure caused by bone cellular activities in response to a local mechanical environment were investigated by computer simulations of trabecular surface remodeling. In simulations, two model parameters, the threshold value of the lazy zone and the sensing distance of the mechanical environment, were used to express the sensitivity of bone cells to mechanical stimuli in time and space. 2D simulation using a rectangular cancellous bone model under simple and nonuniform compressive loads revealed that the trabecular structure underwent a temporal and spatial change depending on the loading condition. It was found that the threshold value of the lazy zone regulates the rate of structural changes in time, and that sensing distance regulates the spatial distribution of the trabecular structure. The results demonstrate the possibility that the spatial and temporal regulation of the trabecular structure is determined by the sensitivities of bone cells to mechanical stimuli.

References

Adachi T, Tomita Y, Sakaue H, Tanaka M (1997) Simulation of trabecular surface remodeling based on local stress nonuniformity. Jsme Int J Ser C-Mech Syst Mach Elem Manuf 40 (4):782–792. https://doi.org/10.1299/jsmec.40.782

Adachi T, Tsubota K, Tomita Y, Hollister SJ (2001) Trabecular surface remodeling simulation for cancellous bone using microstructural voxel finite element models. J Biomech Eng-T ASME 123(5):403–409. https://doi.org/10.1115/1.1392315

Cowin SC, Hart RT, Balser JR, Kohn DH (1985) Functional adaptation in long bones: establishing in vivo values for surface remodeling rate coefficients. J Biomech 18(9):665–684

Hughes TJR, Ferencz RM, Hallquist JO (1987) Large-scale Vectorized implicit calculations in solid mechanics on a Cray X-Mp/48 utilizing Ebe preconditioned conjugate gradients. Comput Method Appl M 61(2):215–248

Langton CM, Haire TJ, Ganney PS, Dobson CA, Fagan MJ (1998) Dynamic stochastic simulation of cancellous bone resorption. Bone 22(4):375–380. https://doi.org/10.1016/S8756-3282(97)00290-1

Parfitt AM, Drezner MK, Glorieux FH, Kanis JA, Malluche H, Meunier PJ, Ott SM, Recker RR (1987) Bone histomorphometry: standardization of nomenclature, symbols, and units. Report of the ASBMR histomorphometry nomenclature committee. J Bone Miner Res 2(6):595–610. https://doi.org/10.1002/jbmr.5650020617

Tabor Z, Rokita E (2002) Stochastic simulations of remodeling applied to a two-dimensional trabecular bone structure. Bone 31(3):413–417. https://doi.org/10.1016/S8756-3282(02)00837-2

Tsubota K, Adachi T (2005) Spatial and temporal regulation of cancellous bone structure: characterization of a rate equation of trabecular surface remodeling. Med Eng Phys 27(4):305–311. https://doi.org/10.1016/j.medengphy.2004.09.013

Tsubota K, Adachi T, Tomita Y (2002) Functional adaptation of cancellous bone in human proximal femur predicted by trabecular surface remodeling simulation toward uniform stress state. J Biomech 35(12):1541–1551. https://doi.org/10.1016/S0021-9290(02)00173-2

Tsubota K, Suzuki Y, Yamada T, Hojo M, Makinouchi A, Adachi T (2009) Computer simulation of trabecular remodeling in human proximal femur using large-scale voxel FE models: approach to understanding Wolff's law. J Biomech 42(8):1088–1094. https://doi.org/10.1016/j.jbiomech.2009.02.030

van Rietbergen B, Weinans H, Huiskes R, Odgaard A (1995) A new method to determine trabecular bone elastic properties and loading using micromechanical finite-element models. J Biomech 28(1):69–81

Weinans H (1998) Is osteoporosis a matter of over-adaptation? Technol Health Care 6(5-6):299–306

Xia SL, Ferrier J (1992) Propagation of a calcium pulse between osteoblastic cells. Biochem Biophys Res Commun 186(3):1212–1219

Chapter 10
Comparison of Mechanical Quantities as Bone Remodeling Stimuli

Abstract In this chapter, different trabecular-level mechanical quantities are compared for determining their appropriateness as bone remodeling stimuli. Distribution functions of the mechanical quantities were evaluated by using digital image-based finite element models of rat vertebral bodies subject to physiological loading conditions. Strain energy density (SED) and von Mises equivalent stress were considered as local mechanical quantities, while SED integration and stress non-uniformity were considered as integral mechanical quantities. The analysis demonstrated that the mechanical quantities were non-uniformly distributed over the trabecular surface owing to the three-dimensionally complex trabecular structure. The distribution patterns of the four mechanical quantities were compared in terms of the skewness of their distribution functions. The results support the notion that the integral formalism, proposed for bone remodeling stimuli on the basis of the process of bone cells to sense mechanical stimuli, corresponds to trabecular structural adaptation to its mechanical environment.

Keywords Cancellous bone • Trabecular surface remodeling • Adaptation • Uniform stress

10.1 Introduction

One of the key issues in computer simulation of trabecular remodeling is quantifying the mechanical stimuli, to account for the biological response to mechanical factors during remodeling (Burr 2002). On the basis of the experimental and clinical observations, the mechanical stimulus of bone remodeling has been formulated using the intensity of the mechanical quantity in the macroscopic mathematical models for bone remodeling in which the trabecular bone is regarded as a continuum. Developing the theory of adaptive elasticity (Cowin and Hegedus 1976), which is one of the first bone remodeling models based on macroscopic continuum mechanics, Sadegh et al. (1993) have related surface remodeling-induced trabecular structural changes to the local strain intensity on the trabecular surface. They showed that a trabecular structural change occurs as the trabecular-

This Chapter was adapted from Tsubota and Adachi (2006) with permission from The Japan Society of Mechanical Engineers.

Y. Kameo et al., *Bone Adaptation*, Frontiers of Biomechanics 2,
https://doi.org/10.1007/978-4-431-56514-7_10

level adaptation to the trabecular mechanical environment. In an extension of their work (Luo et al. 1995), the authors considered mechanical stimuli at different strain rate, and demonstrated that the strain rate affects the rate of trabecular structural change but not the final shape of the trabeculae in the remodeling equilibrium. These studies suggest that in determining the trabecular structure in the remodeling equilibrium, the spatial distributions of the mechanical quantities are more important than the temporal changes in the mechanical quantities.

The spatial distributions of the mechanical quantities have been investigated in detail to explain the actual biological systems, such as intercellular communication networks. Mullender et al. (1994) and Mullender and Huiskes (1995) have accounted for the role of osteocytes as mechanosensors and formulated the remodeling stimulus as the integral of the strain energy density over the bone volume around the remodeling site. In Chap. 8, we have proposed a stress nonuniformity for determining the spatial sensitivity of the bone cells to mechanical stimuli, assuming a uniform stress hypothesis in the remodeling equilibrium (Adachi et al. 1997, 1998). These spatially integrated mechanical quantities can explain the physiological mechanism of bone remodeling, and, therefore, are expected to be key parameters governing bone remodeling from cellular responses up to trabecular structural changes (Huiskes et al. 2000; Mullender et al. 1998).

In this chapter, we demonstrate the spatial distributions of mechanical quantities in the trabecular bone as remodeling stimuli around the remodeling equilibrium state. We then consider the more appropriate quantities as remodeling stimuli among the quantities at the remodeling site (namely, local mechanical quantities) and those integrated over the space around the remodeling site (namely, integral mechanical quantities). Considering the three-dimensionally complex structure of the trabecular bone, the mechanical quantities on the trabecular surface were estimated by using digital image-based finite element models of five specimens of normal rat vertebral bodies, subject to physiological loading conditions. The difference between the distribution functions was evaluated for the local mechanical quantities and for the integral ones, for which the strain energy density (SED) (Huiskes et al. 1987) and the von Mises equivalent stress (Carter et al. 1987) were examined as representative local mechanical quantities, while spatial integration of SED with a decay function (Mullender and Huiskes 1995) and spatial non-uniformity of the von Mises equivalent stress (Chaps. 8 and 9) were examined as representative integral mechanical quantities.

10.2 Methods for Comparison of Mechanical Quantities

A digital image-based voxel FE model was created for the vertebral bodies of normal rats (Sect. 10.2.1). The use of mechanical quantities as remodeling stimuli is explained in Sect. 10.2.2. A method for evaluating the distributions of mechanical quantities in a cancellous bone is described (Sect. 10.2.3).

10.2.1 Digital Image-Based Finite Element Models of Rat Vertebral Bodies

Serial images of the cross-section of a vertebral body were measured for five specimens of normal L1 vertebral bodies harvested from healthy Wistar rats (female, 10 weeks) using X-ray micro-computed tomography. Based on these images, a digital image-based finite element model of each specimen was constructed to describe the central part of a vertebral body, as shown in Fig. 10.1a. The model size was approximately 4.3 mm in the bilateral direction, 2.7 mm in the anteroposterior direction, and 2.6 mm in the axial direction. Each

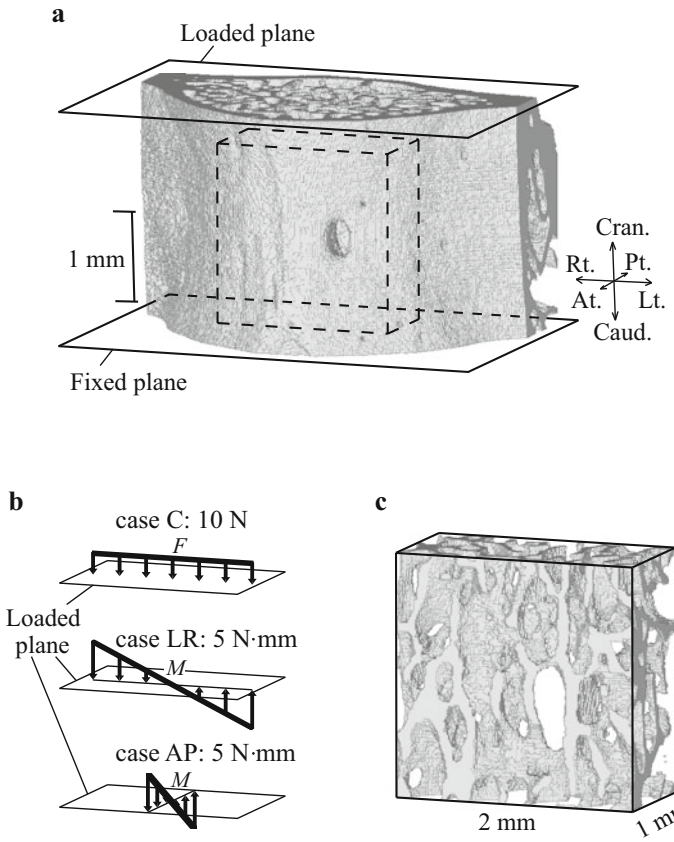

Fig. 10.1 Digital image-based finite element model of a L1 vertebral body of a normal rat. (**a**) Overview of the model. The load was applied to the upper plane, while the lower plane was fixed. (**b**) Three loading scenarios of axial compression (*C*) and lateral (*LR*) and anteroposterior (*AP*) bending. (**c**) The central hexahedral region of $2 \times 1 \times 2$ mm^3 in the cancellous bone (This figure was adapted from Tsubota and Adachi (2006) with permission from The Japan Society of Mechanical Engineers)

voxel had the volume of $12.8 \times 12.8 \times 12.8\ \mu m^3$, corresponding to the pixel area of $12.8 \times 12.8\ \mu m^2$ and to the inter-slice distance of 12.8 μm. There were approximately 4.6 million bone elements. The X_1 axis corresponded to the bilateral direction, the X_2 axis to the anteroposterior direction, and the X_3 axis to the axial direction, as shown in Fig. 10.1a. The bone was assumed to be homogeneous and isotropic, with Young's modulus $E_t = 20$ GPa and Poisson's ratio $\nu_t = 0.3$. The marrow was regarded as a cavity, and was neglected in the finite element analysis. The element-by-element preconditioned conjugate gradients (EBE/PCG) method (Hughes et al. 1987; van Rietbergen et al. 1995) was used for the finite element analysis.

Considering the mechanical function of a vertebral body as a load-bearing structure, three loading scenarios with axial compression (C) of $F_c = 10$ N and lateral (LR) and anteroposterior (AP) bending of $M_{LR} = M_{AP} = 5\ N \cdot m$ were assumed as the physiological loading conditions of a normal rat, as shown in Fig. 10.1b. These loads were applied to the upper plane of the vertebral model via a one-voxel-thick dummy bone layer that was placed for uniformly transferring the loads to the vertebral body. The lower plane of the model was fixed.

10.2.2 Mechanical Quantities on the Trabecular Surface as Remodeling Stimuli

Local mechanical quantities at a specific point on the trabecular surface were defined as the corresponding mechanical quantities at that point, while integral mechanical quantities were defined as the spatial integrals or averages of the corresponding mechanical quantities over the bone volume around the considered point. SED U [J/m^3] and von Mises equivalent stress σ [MPa], which have been used since introducing the pioneering mathematical and computational models of bone remodeling (Carter et al. 1987; Cowin and Hegedus 1976; Huiskes et al. 1987), were considered as representative local mechanical quantities. Two types of integral mechanical quantities, in which the cellular network system in bone remodeling is considered, were considered, and are summarized in what follows.

One of the integral mechanical quantities considered here was SED integration with a decay function (Huiskes et al. 2000; Mullender and Huiskes 1995):

$$P = \sum_{i=1}^{n} f_i(\boldsymbol{x}) \mu_i U_i \quad \left[\mathrm{J/m^3}\right], \tag{10.1}$$

which accounts for the role of osteocytes as mechano-sensors. In Eq. (10.1), U_i is the SED at the location of an osteocyte i, μ_i is the mechano-sensitivity of the osteocyte i, $f_i(\boldsymbol{x})$ is an exponentially decaying function describing the strength of the effect of the osteocyte i on a point $\boldsymbol{x}$ on the surface, and n is the number of

osteocytes around the point $\boldsymbol{x}$ on the surface. The exponentially decaying function $f_i(\boldsymbol{x})$ is given by:

$$f_i(\boldsymbol{x}) = e^{-(d_i(\boldsymbol{x})/D)}, \tag{10.2}$$

where d_i(x) is the distance between the osteocyte i and the surface location $\boldsymbol{x}$, and D is the spatial decay constant (Mullender et al. 1994).

Another integral mechanical quantity is the spatial non-uniformity of equivalent stress, described in Sect. 8.2:

$$\Gamma = \ln(\sigma_c/\sigma_d), \tag{10.3}$$

in which surface remodeling is assumed to yield a state with uniformly distributed mechanical stimulus in the remodeling equilibrium. In Eq. (10.3), σ_c is the stress at a point $\boldsymbol{x}_c$ on the trabecular surface, and σ_d is the representative stress around the point $\boldsymbol{x}_c$, defined as:

$$\sigma_d = \int w(l)\sigma_r dV / \int w(l) dV, \tag{10.4}$$

where σ_r is the stress at a point $\boldsymbol{x}_r$, l is the distance between the points $\boldsymbol{x}_c$ and $\boldsymbol{x}_r$, and dV is the trabecular volume. In this chapter, spatial integration was performed over the trabecular volume in Eq. (10.4) for considering osteocytes as mechano-sensors, instead of the trabecular surface in Eq. (8.2). The weighting function $w(l)$ $[w(l) > 0 \ (0 \leq l < l_L)]$ decreases linearly with the distance l, similar to what is described in Eq. (10.2) for the SED integration model. The sensing distance l_L, which indicates the area in which osteocytes can sense mechanical stimuli, determines the area for evaluating the stress non-uniformity Γ (Sect. 8.2).

The model parameters included in the integral mechanical quantities were set as the number of osteocytes $n = 10{,}000$ mm^{-3} in Eq. (10.1) and the spatial decay constant $D = 100$ μm in Eq. (10.2) for the SED integration P (Mullender et al. 1996), and the sensing distance $l_L = 200$ μm in Eq. (10.4) for the stress non-uniformity Γ (Donahue 1998; Xia and Ferrier 1992).

10.2.3 Evaluation of the Spatial Distributions of Mechanical Quantities

The four mechanical quantities U, σ, P, and Γ were considered as remodeling stimuli S and their spatial distributions were evaluated under the following assumptions. First, in a normal rat subject to physiological loadings (that is, the bone is in the remodeling equilibrium), the extent of the trabecular bone formation was assumed to be equal to that of the bone resorption. Second, the rate of the trabecular surface movement $\dot{M}$, which determines the structural changes in the trabeculae,

was assumed to be a function of the mechanical stimulus S (Cowin 1993). Third, since we focused on the bone in and around the remodeling equilibrium, the rate of the trabecular surface movement $\dot{M}(S)$ was approximated by a simple linear rate equation (first order Taylor expansion of the function $\dot{M}(S)$):

$$\dot{M}(S) = C\left(S - S^{\mathrm{ref}}\right), \tag{10.5}$$

where C was the rate coefficient of trabecular surface remodeling, and S^{ref} was the reference stimulus in the remodeling equilibrium (Cowin 1993). With C and S^{ref} being constant in time and non-site specific (constant in space), the third assumption implies that the distribution function of the mechanical stimulus is symmetric with respect to the reference stimulus S^{ref} (if not, the ammount of the bone formation would no longer be equal to that of the bone resorption). Considering these assumptions, the magnitudes of the distribution functions' skewness were calculated for the four mechanical quantities U, σ, P, and Γ for evaluating the distribution function symmetry. Because a more symmetric distribution of a certain mechanical quantity increases the likelihood of using this quantity as a stimulus for remodeling, mechanical quantities with lower skewness were considered to be more likely candidates to serve as stimuli for remodeling.

In summary, the spatial distributions of the mechanical quantities were evaluated by employing the following procedures:

1. For the five specimens of the rat vertebral bodies, the mechanical quantities U, σ, P, and Γ on the trabecular surface were calculated for each of the three loading scenarios by using digital image-based models, as shown in Fig. 10.1. To neglect the artificial effects associated with the boundary conditions, we discuss only the simulation results for the central hexahedral region of $2 \times 1 \times 2$ mm^3 in the cancllous bone, as shown in Fig. 10.1c. In the stress/strain calculation for the trabecular structure, a finite element analysis was conducted by using an element-by-element preconditioned conjugate gradients approach (Hughes et al. 1987; van Rietbergen et al. 1995).
2. To compare the distribution functions of the four mechanical quantities U, σ, P, and Γ that have different scales of magnitude, the mechanical quantities, regarded as bone remodeling stimuli S, were normalized as

$$\hat{S} = \frac{S - S^{\mathrm{ref}}}{\sigma_S}, \tag{10.6}$$

where σ_S is the standard deviation of a stimulus S in the center hexahedral region of the cancellous bone. The mean value $\bar{S}$ of the stimulus S in the center hexahedral region was used as the reference stimulus S^{ref}, considering that the trabecular bone volume was the same in the remodeling equilibrium (see Appendix. 10.A for details).

3. The trabecular surface area A was calculated as a function of the normalized stimulus $\hat{S}$ and normalized by the total trabecular surface area, A^{total}. The normalized area $\hat{A}(\hat{S}) = A(\hat{S})/A^{\text{total}}$ was defined as the distribution function of the stimulus $\hat{S}$.
4. The magnitude of the skewness $|\widehat{\beta}|$ of the distribution function $\hat{A}(\hat{S})$ was calculated as:

$$|\widehat{\beta}| = \left| \frac{\int \hat{A}^3(\hat{S})\, d\hat{S}}{\sigma_{\hat{A}}^3 \int d\hat{S}} \right|, \tag{10.7}$$

and compared among the four mechanical quantities. In Eq. (10.7), $\sigma_{\hat{A}}$ is the standard deviation of the distribution function $\hat{A}(\hat{S})$.

10.3 Comparison of Mechanical Quantities

In this section, we describe the distributions of the mechanical quantities and compare the quantities (Sect. 10.3.1). Limitations of the employed simulation model are discussed as well (Sect. 10.3.2), along with the appropriateness of the analyzed mechanical quantities as remodeling stimuli.

10.3.1 Spatial Distributions of Mechanical Quantities in Cancellous Bone

The values of the SED U, the equivalent stress σ, the SED integration P, and the stress non-uniformity Γ on the trabecular surface in the central hexahedral region of the cancellous bone were obtained for the five specimens, for each of the three loading scenarios of axial compression (C) and lateral (LR) and anteroposterior (AP) bending. The three-dimensionally complex structure of the trabeculae yielded non-uniform distributions of the mechanical quantities on the trabecular surface, even though the vertebral body was only subjected to a simple external loading, as shown in Fig. 10.2, in which the mechanical quantities of one of the five specimens for the loading scenario C are shown as examples.

The distribution function $\hat{A}(\hat{S})$ of the normalized mechanical stimulus $\hat{S}$ on the trabecular surface was calculated for the four mechanical quantities, as shown in Fig. 10.3, in which the result obtained for one of the five specimens is shown as an example. In the case of SED U, equivalent stress σ, and SED integration P, the corresponding distribution functions $\hat{A}(\hat{S})$, characterized by the distribution's

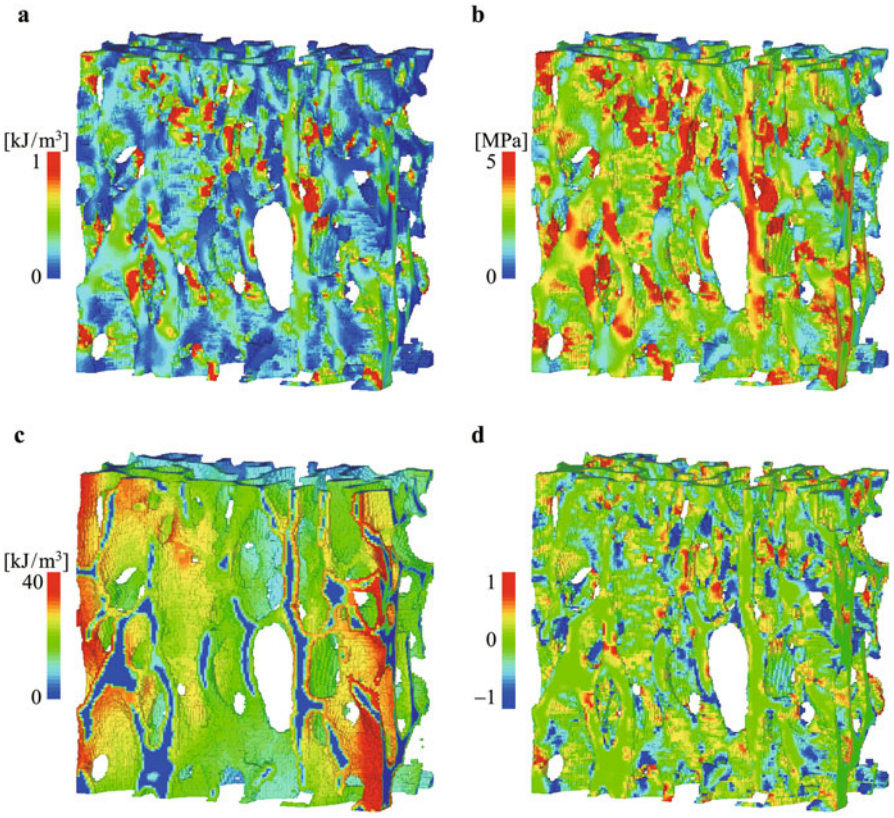

Fig. 10.2 Mechanical quantities on the trabecular surface in the central hexahedral region of the cancellous bone, for the loading scenario C of axial compression. (**a**) Strain energy density (SED) U, (**b**) von Mises equivalent stress σ, (**c**) SED integration P, and (**d**) stress non-uniformity Γ (This figure was adapted from Tsubota and Adachi (2006) with permission from The Japan Society of Mechanical Engineers)

mode, kurtosis, and skewness, were affected by the loading conditions, whereas no such dependence was observed in the case of stress non-uniformity Γ.

The magnitude of the skewness $|\widehat{\beta}|$ of the distribution function $\hat{A}(\hat{S})$ was different for the different mechanical quantities and loading conditions, as shown in Fig. 10.4. Among the four mechanical quantities, the skewness $|\widehat{\beta}| = 0.23 \pm 0.15$ (mean $\pm$ s.d.) of the SED integration P was the smallest in the compressive loading scenario C, and the skewness magnitude $|\widehat{\beta}|$ of the stress non-uniformity was the smallest in the bending loading scenarios of LR ($|\widehat{\beta}| = 1.19 \pm 0.14$) and AP ($|\widehat{\beta}| = 1.20 \pm 0.13$). The skewness magnitude values $|\widehat{\beta}|$ of the SED U and equivalent stress σ in all of the loading scenarios were smaller than those of the SED

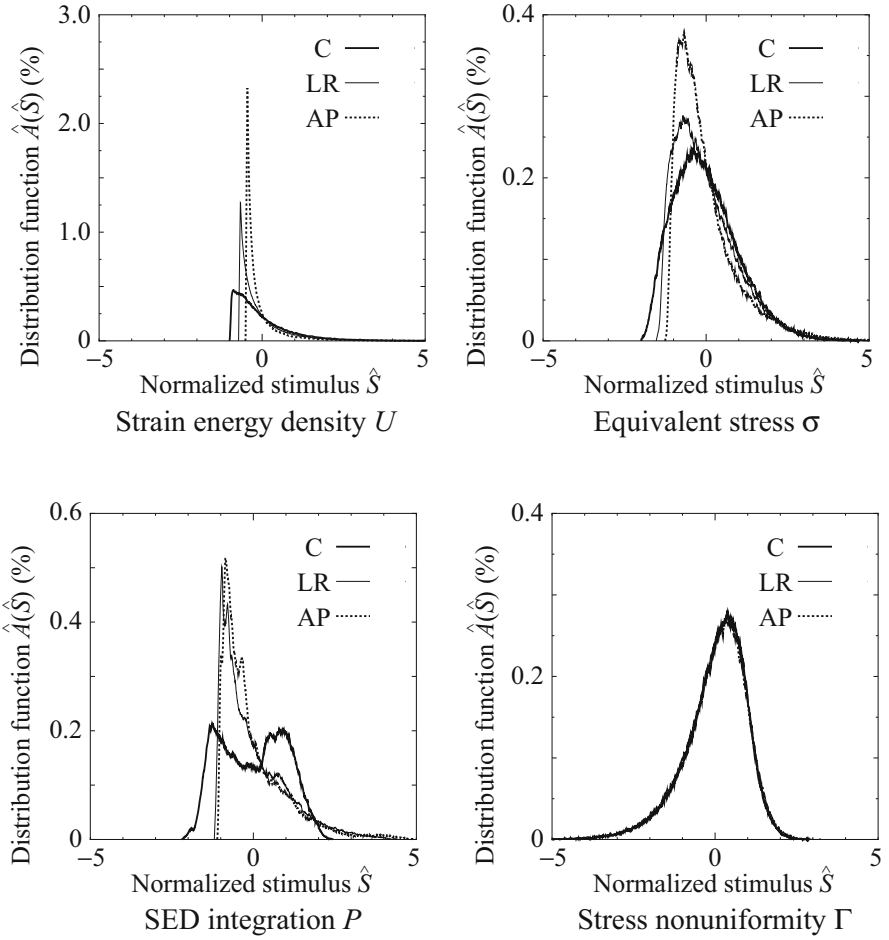

Fig. 10.3 Distribution function $\hat{A}(\hat{S})$ of the normalized mechanical stimulus $\hat{S}$ for the strain energy density (SED) U, equivalent stress σ, SED integration P, and stress non-uniformity Γ in the three loading scenarios of axial compression (C) and lateral (LR) and anteroposterior (AP) bending (This figure was adapted from Tsubota and Adachi (2006) with permission from The Japan Society of Mechanical Engineers)

integration P and stress non-uniformity Γ, respectively, except for the loading scenario C, in which the skewness of the equivalent stress σ was smaller than that of the stress non-uniformity Γ. It was also revealed that the skewness magnitude $|\widehat{\beta}|$ varied with external loading conditions, as shown in Table 10.1. In all of the loading scenarios, the changes in the skewness mean and standard deviation for the SED integration P and stress non-uniformity Γ were smaller than those for the SED U and equivalent stress σ.

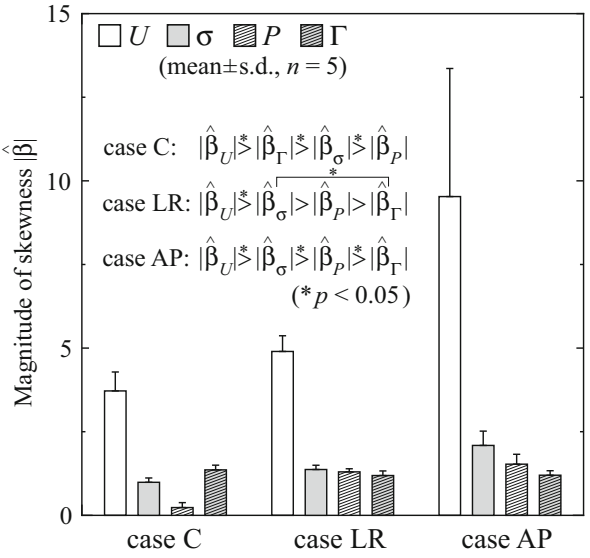

Fig. 10.4 Skewness magnitude $|\hat{\beta}|$ of the distribution function $\hat{A}(\hat{S})$, for the distributions of strain energy density (SED) U, equivalent stress σ, SED integration P, and stress non-uniformity Γ, the three loading scenarios of axial compression (C) and lateral (LR) and anteroposterior (AP) bending (This figure was adapted from Tsubota and Adachi (2006) with permission from The Japan Society of Mechanical Engineers)

Table 10.1 Changes in the magnitude of skewness $|\hat{\beta}|$ of the distribution function $\hat{A}(\hat{S})$ of different quantities, for the changes in external loading conditions

Quantity type	Change in mean value of $\lvert\hat{\beta}\rvert$	Change in s.d. of $\lvert\hat{\beta}\rvert$
SED U	5.81	3.36
Equivalent stress σ	1.10	0.30
SED integration P	1.30	0.20
Stress nonuniformity Γ	0.17	0.01

This table was adapted from Tsubota and Adachi (2006) with permission from The Japan Society of Mechanical Engineers

10.3.2 Candidate Mechanical Quantities to Serve as Remodeling Stimuli

10.3.2.1 Model Assumptions

Digital image-based models combined with large-scale finite element analysis were used for determining the distributions of mechanical quantities in a rat vertebral body subject to physiological loading conditions. Considering the spinal structure function and the arrangement of the tissue surrounding vertebra, the loading condition of the spinal structure is likely to be similar to the human one, consisting of compression and bending. Therefore, three loading scenarios, corresponding to axial compression and anteroposterior and lateral bending, were assumed as the physiological loading scenarios of the rat vertebral body. In addition, we assumed that mechanical quantities with more symmetric distributions are better candidates to serve as remodeling stimulus, based on the linear rate equation of bone

remodeling with a non-site specific rate coefficient (Cowin 1993). In this study, a non-site specific model was adopted based on the fact that non-site specific remodeling models successfully predicted realistic changes in bone structure resulting from the distribution of mechanical quantities such as that denoted by the function of stress/strain (Cowin 1993).

10.3.2.2 Dependence of the Distribution of Mechanical Quantities on the Quantity Type

Comparison of the skewness values of the distribution functions of the mechanical quantities has revealed that the distribution characteristics are quantity type-dependent, as shown in Fig. 10.4. Spatial distributions of mechanical quantities have been suggested to play an important role in maintenance and adaptation by bone remodeling. Fyhrie et al. (2000) suggested that the average value of shear stress in a cancellous bone region is related to the stress standard deviation: these studies also suggested that such dependence might be related to the structural adaptation of trabeculae. In the present study, the distributions of the considered mechanical quantities were estimated from the viewpoint of the balance between bone amount during the bone formation and bone resorption in the remodeling equilibrium. In all of the three loading scenarios, the skewness of the SED distribution function (indicating a highly asymmetric distribution because SED is expressed in a quadratic form) decreased when the SED was integrated. This result reflects the fact that the distribution functions of the considered mechanical quantities became more symmetric when the quantities were integrated over larger volumes (i.e., imagine that the integral quantities become closer to their corresponding spatial mean values with increasing the integration volume).

10.3.2.3 Local vs. Integral Mechanical Quantities as Remodeling Stimuli

The distribution functions of equivalent stress and SED became more symmetric when integrated in the two bending loading scenarios; however, this did not occur in the compressive loading scenario. Spatial integration of mechanical quantities is likely to affect the distributions of the mechanical quantities in two ways. One effect would be to symmetrize the distribution pattern, as noted in the previous paragraph on SED and its integration. Another tendency would be reduce the distribution pattern symmetry, which would result from amplifying local fluctuations of mechanical quantities on the trabecular length scale. The latter effect would yield specific relationships between global and local distributions of mechanical quantities, such as the observed relationships between spatially averaged shear stress and its standard deviation (Fyhrie et al. 2000; Yeni et al. 2003); these relationships may determine the morphological properties of a trabecular structure,

such as trabecular thickness and separation (Mullender and Huiskes 1995; Yeni et al. 2003). In the case of equivalent stress, the degree of the distribution function symmetry is so high in the scenario of compressive loading that the net effect of spatial integration would be to make the corresponding distribution function asymmetric rather than symmetric. On the other hand, the skewness of the stress non-uniformity is more consistent with the changes in the loading conditions than the equivalent stress, as shown in Table 10.1. This result suggests that the stress non-uniformity may be more appropriate as a mechanical stimulus than the equivalent stress, with respect to homeostasis when subject to physiological loading conditions.

The results obtained in this study may indicate that integral mechanical quantities are stronger candidates for stimuli than local mechanical quantities, with respect to the following two points: (1) the balance between bone amount during the bone formation and bone resorption, for maintaining the bone mass in the remodeling equilibrium, and (2) the homeostasis in the presence of varying external loading conditions. This supports the integral formalism proposed for the bone remodeling stimuli (Mullender and Huiskes 1995; Mullender et al. 1994), corresponding not only to cellular communication in actual biological systems (Ruimerman et al. 2005), but also to the observed phenomenon of trabecular structural adaptation to its mechanical environment. On the other hand, equivalent stress but not SED, as a local mechanical quantity, still appears to be the leading candidate stimulus with respect to (1) a satisfactory balance between bone formation and resorption, but not with respect to (2) homeostasis in the presence of varying loading conditions.

10.4 Conclusion

In this chapter, distribution functions of mechanical quantities on trabecular surfaces were estimated by using digital image-based finite element models of five specimens of rat vertebral bodies subject to physiological loading conditions. As the representative quantities that have been used as mechanical stimuli in the remodeling rate equation, strain energy density (SED) and von Mises equivalent stress were considered as local mechanical quantities, and SED integration and stress non-uniformity were considered as integral mechanical quantities. These mechanical quantities were demonstrated to be non-uniformly distributed over the trabecular surface owing to the three-dimensionally complex trabecular structure, even though only simple external loading was applied to the vertebral body. The skewness values of the distribution functions of these quantities were calculated for comparing the distribution patterns of the four mechanical quantities. For all of the considered loading scenarios, excluding the axial compression scenario, the skewness values for the SED integration and stress non-uniformity were smaller than those for the SED and equivalent stress. In the case of axial compression, the skewness for the equivalent stress was smaller than that for the stress

non-uniformity. It was also revealed that the skewness varied with changes in the external loading conditions, and that changes in the skewness mean and standard deviation for the SED integration and stress non-uniformity were smaller than those for the SED and equivalent stress. The results support the understanding that the integral formalism proposed for the bone remodeling stimuli corresponds not only to the actual biological system but also to the observed phenomenon of trabecular structural adaptation to its mechanical environment.

Appendix: A Remodeling Equilibrium Around Mean Stimulus

The rate of the trabecular surface movement $\dot{M}$ was assumed to be a simple linear function of the mechanical stimulus S, as shown in Eq. (10.5). If C and S^{ref} do not depend on time and are non-site specific, the extent of the net change in the total bone mass $\dot{M}^{\mathrm{total}}$ is expressed by the rate coefficient C, the reference stimulus S^{ref}, the mean stimulus $\bar{S}$ in the trabecular bone region, and the total trabecular surface area $\int \mathrm{d}A$, as:

$$\begin{aligned} \dot{M}^{\mathrm{total}} &= \int \dot{M}\,\mathrm{d}A \\ &= \int C\left(S - S^{\mathrm{ref}}\right)\mathrm{d}A \\ &= C\left(\int S\mathrm{d}A - \int S^{\mathrm{ref}}\mathrm{d}A\right) \\ &= C\left(\bar{S} - S^{\mathrm{ref}}\right)\int \mathrm{d}A \quad \left(\because \int S\mathrm{d}A = \bar{S}\int \mathrm{d}A\right) \end{aligned} \tag{10.8}$$

Because $\dot{M}^{\mathrm{total}}$ should be zero in a normal trabecular bone in the remodeling equilibrium, Eq. (10.8) indicates that the reference stimulus S^{ref} is equivalent to the mean stimulus $\bar{S}$ of a normal trabecular bone.

References

Adachi T, Tomita Y, Sakaue H, Tanaka M (1997) Simulation of trabecular surface remodeling based on local stress nonuniformity. JSME Int J C 40(4):782–792. https://doi.org/10.1299/jsmec.40.782

Adachi T, Tanaka M, Tomita Y (1998) Uniform stress state in bone structure with residual stress. J Biomech Eng 120(3):342–347. https://doi.org/10.1115/1.2798000

Burr DB (2002) Targeted and nontargeted remodeling. Bone 30(1):2–4

Carter DR, Fyhrie DP, Whalen RT (1987) Trabecular bone density and loading history: regulation of connective tissue biology by mechanical energy. J Biomech 20(8):785–794

Cowin SC (1993) Bone stress adaptation models. J Biomech Eng 115(4B):528–533

Cowin SC, Hegedus DH (1976) Bone remodeling I: theory of adaptive elasticity. J Elast 6 (3):313–326

Donahue HJ (1998) Gap junctional intercellular communication in bone: a cellular basis for the mechanostat set point. Calcif Tissue Int 62(2):85–88

Fyhrie DP, Hoshaw SJ, Hamid MS, Hou FJ (2000) Shear stress distribution in the trabeculae of human vertebral bone. Ann Biomed Eng 28(10):1194–1199

Hughes TJR, Ferencz RM, Hallquist JO (1987) Large-scale Vectorized implicit calculations in solid mechanics on a Cray X-Mp/48 utilizing Ebe preconditioned conjugate gradients. Comput Method Appl M 61(2):215–248

Huiskes R, Weinans H, Grootenboer HJ, Dalstra M, Fudala B, Slooff TJ (1987) Adaptive bone-remodeling theory applied to prosthetic-design analysis. J Biomech 20(11-12):1135–1150

Huiskes R, Ruimerman R, van Lenthe GH, Janssen JD (2000) Effects of mechanical forces on maintenance and adaptation of form in trabecular bone. Nature 405(6787):704–706. https://doi.org/10.1038/35015116

Luo G, Cowin SC, Sadegh AM, Arramon YP (1995) Implementation of strain rate as a bone remodeling stimulus. J Biomech Eng 117(3):329–338

Mullender MG, Huiskes R (1995) Proposal for the regulatory mechanism of Wolff's law. J Orthop Res 13(4):503–512. https://doi.org/10.1002/jor.1100130405

Mullender MG, Huiskes R, Weinans H (1994) A physiological approach to the simulation of bone remodeling as a self-organizational control process. J Biomech 27(11):1389–1394

Mullender MG, van der Meer DD, Huiskes R, Lips P (1996) Osteocyte density changes in aging and osteoporosis. Bone 18(2):109–113

Mullender M, van Rietbergen B, Ruegsegger P, Huiskes R (1998) Effect of mechanical set point of bone cells on mechanical control of trabecular bone architecture. Bone 22(2):125–131

Ruimerman R, van Rietbergen B, Hilbers P, Huiskes R (2005) The effects of trabecular-bone loading variables on the surface signaling potential for bone remodeling and adaptation. Ann Biomed Eng 33(1):71–78

Sadegh AM, Luo GM, Cowin SC (1993) Bone ingrowth: an application of the boundary element method to bone remodeling at the implant interface. J Biomech 26(2):167–182

Tsuota K, Adachi T (2006) Simulation study on local and integral mechanical quantities at single trabecular level as candidates of remodeling stimuli. J Biomech Sci Eng 1(1):124–135. https://doi.org/10.1299/jbse.1.124

van Rietbergen B, Weinans H, Huiskes R, Odgaard A (1995) A new method to determine trabecular bone elastic properties and loading using micromechanical finite-element models. J Biomech 28(1):69–81

Xia SL, Ferrier J (1992) Propagation of a calcium pulse between osteoblastic cells. Biochem Biophys Res Commun 186(3):1212–1219

Yeni YN, Hou FJ, Ciarelli T, Vashishth D, Fyhrie DP (2003) Trabecular shear stresses predict in vivo linear microcrack density but not diffuse damage in human vertebral cancellous bone. Ann Biomed Eng 31(6):726–732

Chapter 11
Trabecular Surface Remodeling Simulation of Cancellous Bone Using Image-Based Voxel Finite Element Models

Abstract This chapter describes a three-dimensional computer simulation of trabecular surface remodeling using voxel finite element models. The rate equation and the simulation method for the trabecular surface remodeling described in Chap. 8 are extended to the three-dimensional problems of trabecular-level and cancellous-bone-level structures under compressive loading. While Z, X, and Y shaped trabeculae are constructed as models of simplified trabecular-level structure, a cancellous-bone-level structure is modeled on the basis of digital images obtained from X-ray microcomputed tomography (μCT). Remodeling simulations predict the increasing apparent stiffness against the applied load by the trabecular reorientation to the loading direction, in both models of trabecular-level and cancellous-bone-level structures. This demonstrates functional adaptation to the applied load. Simulated structural changes in cancellous bone are anisotropic, although the loading condition is that of simple compression, and thus, changes in the structural and mechanical properties of cancellous-bone-level structures are essentially anisotropic and should be expressed by tensorial quantities. Changes in the structural indices of the trabecular architecture coincide well with reported experimental data.

Keywords Image-based model • Voxel finite element model • Cancellous bone • Trabecular surface remodeling • Functional adaptation

11.1 Introduction

Anisotropic modeling and simulations (Adachi et al. 1997; Cowin et al. 1992; Huiskes et al. 2000; Jacobs et al. 1997; Luo et al. 1995; Mullender et al. 1994; Sadegh et al. 1993; Tsubota and Adachi 2005; Tsubota et al. 2002, 2009) are essential to relate local mechanical stimuli at the trabecular level with bone remodeling by cellular activities (Cowin et al. 1991; Guldberg et al. 1997b). Therefore, the detailed modeling of complex trabecular microstructures is essential. Digital-image-based high resolution voxel models of cancellous bone, which can be

This Chapter was adapted from Adachi et al. (2001) and Tsubota and Adachi (2004) with permission from The American Society of Mechanical Engineers and Taylor & Francis Ltd., respectively.

Y. Kameo et al., *Bone Adaptation*, Frontiers of Biomechanics 2,
https://doi.org/10.1007/978-4-431-56514-7_11

obtained by X-ray μCT scanning (Feldkamp et al. 1989), as shown in Chap. 10, enable modeling and stress analysis (Hollister et al. 1994; van Rietbergen et al. 1995; Badilatti et al. 2016) of the trabecular microstructure. In addition, this voxel finite element modeling technique is a useful tool for predicting microstructural changes in cancellous bone caused by remodeling; for example, structural changes in the case of osteoporosis were predicted by solving the evolution of bone relative density as a continuum (Mullender et al. 1998). However, since trabecular remodeling is due to cellular activities on the trabecular surface (Parfitt 1994), the morphological changes due to surface movement should be directly modeled and simulated at the trabecular level.

In this chapter, we present a three-dimensional computer simulation of trabecular surface remodeling by using image-based voxel finite element models. Here, the trabecular structure of a cancellous bone cube is created on the basis of digital images obtained by X-ray μCT scanning, and compressive loading is applied. A remodeling simulation predicts adaptive changes of the trabecular structure in response to the compressive loading, and successfully reproduces trabecular structural changes in reported experiments (Guldberg et al. 1997b).

11.2 Remodeling at the Single Trabecular Level

The primary features of trabecular structural changes by three-dimensional remodeling simulation are investigated by using models of single trabecula under compressive loading. The simulation model (Sect. 11.2.1) and results (Sect. 11.2.2) are described in this section.

11.2.1 Model of Single Trabecula Under Compressive Loading

Referring to the basic trabecular structures as introduced by Frost (1988), the simulation of trabecular surface remodeling was conducted for single trabeculae with characteristic shapes Z, X, and Y under a compressive load, as shown in Figs. 11.1 and 11.2. The initial diameter of the trabecula was set to 100 μm, considering that the trabecular thickness (*Tb.Th*) measured by μCT scanning of cancellous bone was approximately 100 μm (Guldberg et al. 1997b). The total volume for the analysis was $a_1 \times a_2 \times a_3 = 700 \times 700 \times 500\ \mu m^3$. This region was discretized into voxel elements at a resolution of 10 μm, and represented by $70 \times 70 \times 50 = 245{,}000$ voxel elements of which 11,664 (Model Z), 10,984 (Model X), and 7492 (Model Y) represented the trabecular bone.

A uniform displacement $U_3(<0)$ was controlled at every simulation step on the upper plane at 500 μm to apply the apparent stress $\sigma_3 = F_3/(a_1 a_2) = -1.0$ MPa,

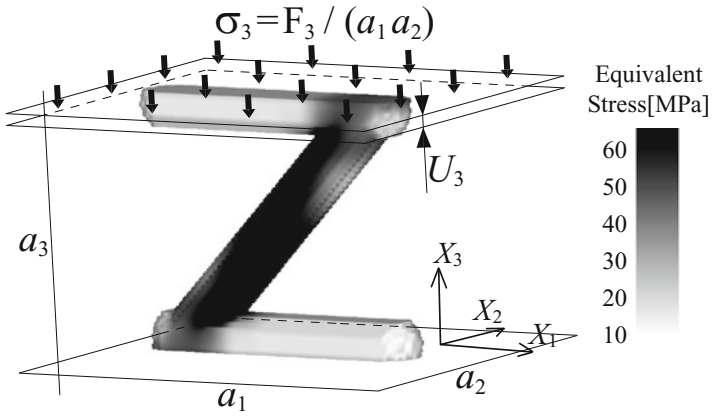

Fig. 11.1 Voxel finite element model of single trabecula under compressive loading, $\sigma_3 = F_3/(a_1 a_2)$ (This figure was adapted from Adachi et al. (2001) with permission from The American Society of Mechanical Engineers)

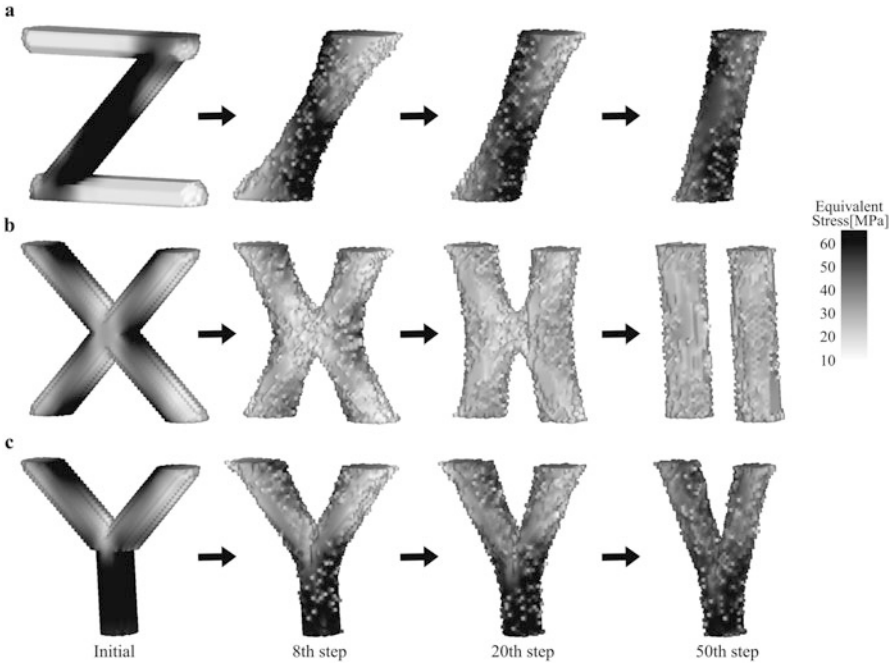

Fig. 11.2 Simulated structural changes of single trabecula under compressive loading: (**a**) Model Z; (**b**) Model X; (**c**) Model Y (This figure was adapted from Adachi et al. (2001) with permission from The American Society of Mechanical Engineers)

where $F_3(<0)$ is the total force applied on the plane, and the lower plane was fixed at $X_3 = 0$. The apparent strain in this direction was defined as $\varepsilon_3 = U_3/a_3$. The trabeculae were assumed to be a homogeneous, isotropic material with Young's modulus of $E_t = 5.33$ GPa and Poisson's ratio of $\nu_t = 0.3$. The marrow was regarded as a cavity, and was neglected in the finite element analysis. The element-by-element preconditioned conjugate gradients (EBE/PCG) method (Hughes et al. 1987; van Rietbergen et al. 1995) was used for the finite element analysis. The sensing distance l_L (Chap. 9) was set to 250 μm, equal to the length of 25 voxel elements, and the threshold values of remodeling (Chap. 9) were set to $\Gamma_u = 0.1$ and $\Gamma_l = -0.2$.

11.2.2 Structural Changes of Single Trabecula

The progress in morphological changes of trabeculae and regulation of the equivalent stress distribution on the trabecular surface, caused by remodeling under compressive load, are shown in Fig. 11.2 for Models Z, Y and X at the initial, 8th, 20th and 50th steps, respectively.

For Model Z, as shown in Fig. 11.2a, the stress concentrated on the inner surface of the acute angles in the middle trabecula, subject to bending in the initial step. The surface near both ends of the middle trabecula with higher equivalent stress was activated to form new bone, while that with the lower stress started resorbing. The stress distribution on the trabecular surface was gradually regulated to become uniform. Then, the trabecula reoriented to align along the loading direction, and reached its equilibrium shape at approximately the 50th step. The trabeculae at the top and bottom of the model were subject to low stress, and therefore these trabeculae disappear in the initial steps.

For Model X, as shown in Fig. 11.2b, the upper and lower corners of the intersection region had lower stress, and both the right- and left-hand corners had higher stress. As the remodeling progressed, the original X-shape became an H-shape, and the horizontal trabecula between the two vertical trabeculae became thinner. Finally, the H-shaped trabecula became two parallel trabeculae at the remodeling equilibrium at approximately the 50th step.

For Model Y, as shown in Fig. 11.2c, the stress in the lower single trabecula was higher than that in the upper two trabeculae, such that the lower trabecula increased in diameter through formation. The surface at the upper corners of the branches resorbed, whereas that at the lower corners grew due to the nonuniformity of the stress. The remodeling around the branching region was less active than that observed in the intersection region of Model X due to the lower degree of nonuniformity of the stress. The two upper trabeculae remodeled and grew closer to each other. The original Y-shape became a V-shape, and finally the remodeling reached an equilibrium state at approximately the 50th step, before the upper trabeculae fused due to the existence of the lazy zone around the remodeling equilibrium.

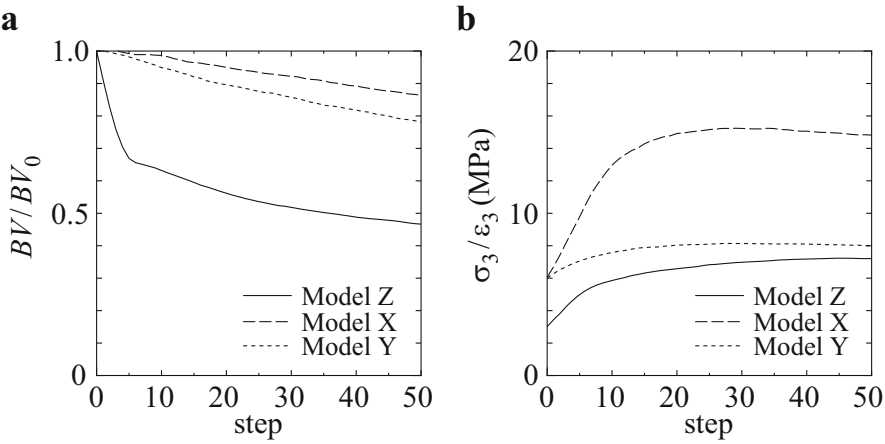

Fig. 11.3 Changes in (**a**) bone volume fraction BV/BV_0, and (**b**) apparent stiffness σ_3/ε_3 of single trabecula under compressive loading due to trabecular surface remodeling

In all models, the stress nonuniformity was reduced on the trabecular surface, and the trabeculae changed their morphology to align along the loading direction. Moreover, the trabecular bone volume decreased as a result of remodeling under compressive load, as shown in Fig. 11.3a, however, the apparent stiffness, defined as σ_3/ε_3, increased through the early stages of remodeling, and then became a constant, as shown in Fig. 11.3b.

11.3 Model of Cancellous Bone Cube

A voxel finite element model of the trabeculae (Hollister et al. 1994; Hollister and Kikuchi 1994; Ulrich et al. 1998; van Rietbergen et al. 1995) enables the direct estimation of the stress and strain at the trabecular level, as shown in Chap. 10. Here, the simulation model of trabecular surface remodeling in Chap. 8 is applied to the three-dimensional microstructural voxel finite element models reconstructed from digital images obtained by microcomputed tomography (μCT).

11.3.1 Digital-Image-Based Model

The experimental observation of the trabecular bone adaptation adjacent to porous-coated platen implants embedded within canine distal femoral metaphyses has been reported (Goldstein et al. 1991; Guldberg et al. 1997b). In the present study, adaptive changes of the trabecular bone architecture underneath the 6 mm diameter platen were simulated, and compared with the experimental results. A digital-

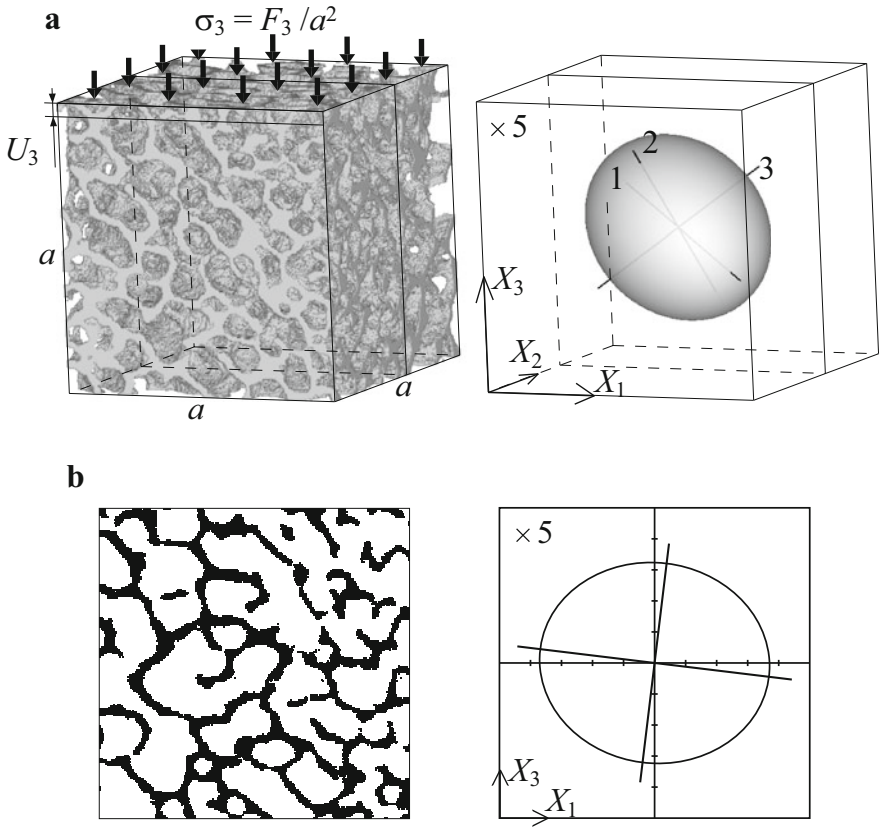

Fig. 11.4 Image-based voxel finite element model of cancellous bone cube, constructed from X-Ray μCT images obtained from a canine distal femur. (**a**) 3D trabecular structure ($200 \times 200 \times 200$ voxel elements) and its fabric ellipsoid and (**b**) $X_1 - X_3$ cross-section and its fabric ellipse (This figure was adapted from Adachi et al. (2001) with permission from The American Society of Mechanical Engineers)

image-based model of a 5 mm cancellous bone cube was obtained from canine distal femoral metaphyses based on three-dimensionally reconstructed CT data, as shown in Fig. 11.4. The voxel element size was 25 μm, the same as the resolution of the μCT data, and thus the total volume contained 8 million voxel elements, of which approximately 2.3 million elements were trabecular bone elements. The structural indices (Feldkamp et al. 1989) and the fabric ellipsoid (Cowin 1985) of the trabecular architecture can be directly calculated from the binarized three-dimensional data.

The trabeculae were assumed to be a homogeneous, isotropic material with Young's modulus of $E_t = 5.33$ GPa and Poisson's ratio of $\nu_t = 0.3$. The marrow was regarded as a cavity, and was neglected in the finite element analysis with EBE/PCG (Hughes et al. 1987; van Rietbergen et al. 1995).

11.3.2 Boundary Condition

The uniform displacement U_3 was controlled at every simulation step on the upper plane at $X_3 = 5.0$ mm to apply the experimental value of apparent stress $\sigma_3 = F_3/a^2 = 1.24$ MPa (Guldberg et al. 1997b), as shown in Fig. 11.4, where $F_3(<0)$ is the total force applied on the plane, and $\varepsilon_3 = U_3/a$ is defined as the apparent strain in the X_3 direction. On the other five planes, shear-free boundary conditions were applied, that is, the displacements perpendicular to the plane were fixed. The sensing distance l_L (Chap. 9) was set to 500 μm, equal to the length of 20 voxel elements, and the threshold values of remodeling (Chap. 9) were set to $\Gamma_u = 4.0$ and $\Gamma_l = -5.0$.

11.3.3 Calculation of Fabric and Compliance Tensors of Cancellous Bone

To clarify the anisotropic mechanical properties of cancellous bone, the fabric and compliance tensors were determined for the trabecular structures obtained by remodeling simulations. At each simulation step, the fabric tensor and orthotropic compliance tensor of the resulting trabecular structure were determined for the core cube. The fabric tensor was determined from the mean intercept length (Harrigan and Mann 1984), in which the principal values H_i ($i = 1, 2, 3$) of the fabric tensor were sorted such that $H_1 \geq H_2 \geq H_3$. A compliance tensor with 21 independent components was obtained by the homogenization method (Guedes and Kikuchi 1990; Hollister et al. 1994; Hollister and Kikuchi 1994; van Rietbergen et al. 1996), in which the marrow was considered to be a homogeneous, isotropic material with Young's modulus of $E_m = E_t/1000 = 5.33$ MPa and Poisson's ratio of $\nu_m = 0$. Therefore, a finite element analysis for $160^3 = 4,096,000$ elements was performed 1200 times (six analyses per simulation step for 200 steps) to obtain the compliance tensor. The best orthotropic elastic symmetries were found using an optimization procedure (van Rietbergen et al. 1996) to determine the nine constants of the orthotropic compliance matrix: $1/E_1$, $1/E_2$, $1/E_3$, ν_{12}/E_1, ν_{23}/E_2, ν_{13}/E_1, $1/G_{23}$, $1/G_{13}$ and $1/G_{12}$, where E_i is Young's modulus, G_{ij} is shear modulus, and ν_{ij} is Poisson's ratio ($i, j = 1, 2, 3$). Young's modulus E_i was sorted such that $E_1 \geq E_2 \geq E_3$.

The difference angle α_i ($i = 1, 2, 3$) between the principal direction of the fabric tensor with principal value H_i and the orthotropic principal direction of the compliance tensor with Young's modulus E_i, was calculated to investigate the relationship between the fabric and compliance tensors (Cowin 1986; Odgaard et al. 1997; van Rietbergen et al. 1998). In addition, the correlations between the structural parameters (the normalized principal value of the fabric tensor $H_i/(H_1 + H_2 + H_3)$ and the bone volume fraction BV/TV) and the mechanical parameters (the nine constants of the orthotropic compliance tensor: $1/E_i$, ν_{ij}/E_i and $1/G_{ij}$)

during the trabecular structural changes were calculated using the equations proposed by Cowin (1986; van Rietbergen et al. 1998). The number of observations was set at 1800 (9 equations for 200 remodeling simulation steps) when calculating a goodness of fit criteria R^2_{adj} (van Rietbergen et al. 1998), assuming the joint dependence of all nine orthotropic constants for 200 simulation steps.

11.4 Remodeling at Cancellous Bone Level

This section explains the simulation results regarding trabecular structural changes (Sect. 11.4.1), functional adaptation (Sect. 11.4.2), fabric and compliance tensors of cancellous bone (Sect. 11.4.3), as well as the comparison to the *in vivo* experiment (Sect. 11.4.4).

11.4.1 Trabecular Structural Changes

Morphological changes in the trabecular architecture of a cancellous bone cube due to remodeling under compressive loading at the 10th, 20th, and 50th steps are represented in Fig. 11.5, in which fabric ellipsoids of the three-dimensional architecture and fabric ellipses of the $X_1 - X_3$ cross-section show the development of the trabecular anisotropy. The initial morphology, shown in Fig. 11.4, adapted to the applied compressive load by resorption and formation on the trabecular surface to reduce the nonuniformity of the stress. The degrees of anisotropy, defined as H_1/H_3 where H_i $(H_1 \geq H_2 \geq H_3)$ is the principal value of the fabric ellipsoid, increased from 1.33 (initial) to 1.39 (50th step) upon alignment of the trabecular architecture along the compressive loading axis; this can be observed in the rotation of the principal direction of the fabric ellipsoid from Fig. 11.4 to Fig. 11.5. The preferential loss of horizontal trabeculae, indicated by open rectangles in the cross-sectional image in Fig. 11.5, and the preservation and increase in thickness of vertically oriented trabeculae directed along the compressive loading axis, indicated by open circles, contribute to the development of trabecular anisotropy.

Changes in structural indices are plotted in Fig. 11.6. The indices were measured using voxel finite elements at every simulation step for the center core cube of $4.0 \times 4.0 \times 4.0$ mm^3 from the whole volume of $5.0 \times 5.0 \times 5.0$ mm^3 to eliminate numerical errors adjacent to the boundary. As a result of remodeling, a decrease of 21.2% in the bone volume fraction (*BV/TV*), 19.3% in the trabecular thickness (*Tb.Th*), and 2.2% in the trabecular number (*Tb.N*) were found at the 50th step compared with the initial values, which resulted in a 10.0% increase in the trabecular separation (*Tb.Sp*). The increase in *Tb.Sp* is because the resorption of the

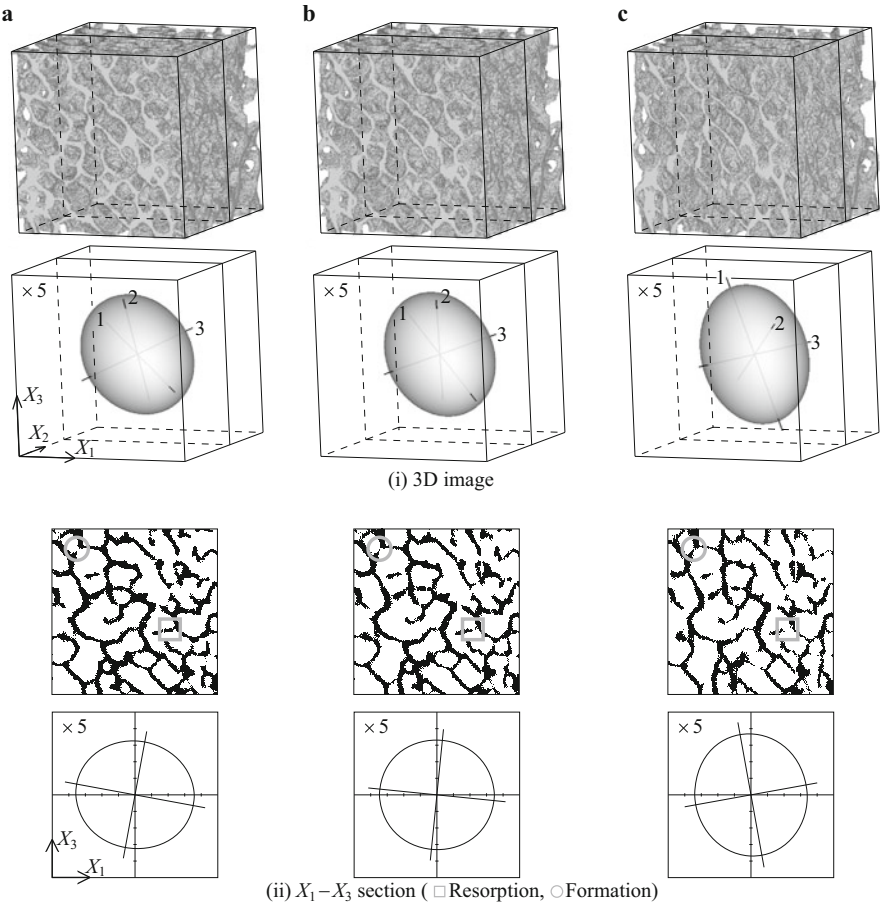

Fig. 11.5 Changes in three-dimensional architecture of a cancellous bone cube and fabric ellipsoid; $X_1 - X_3$ cross-section and fabric ellipse, due to trabecular surface remodeling under compressive loading: (**a**) 10th step, (**b**) 20th step, and (**c**) 50th step (This figure was adapted from Adachi et al. (2001) with permission from The American Society of Mechanical Engineers)

horizontal trabeculae is more remarkable than the formation of the vertical trabeculae. The angle Θ_{i3} between the i-th principal direction of the fabric ellipsoid and the loading axis X_3 changed upon the reorientation of the trabecular architecture. The angle Θ_{13} monotonically decreased from 73.6° toward zero; in contrast, Θ_{23} and Θ_{33} increased toward 90°. These changes in the structural indices and angles indicate that the trabecular orientation changes to align along the compressive axis X_3, which exhibits adaptive remodeling to support uniaxial compressive load.

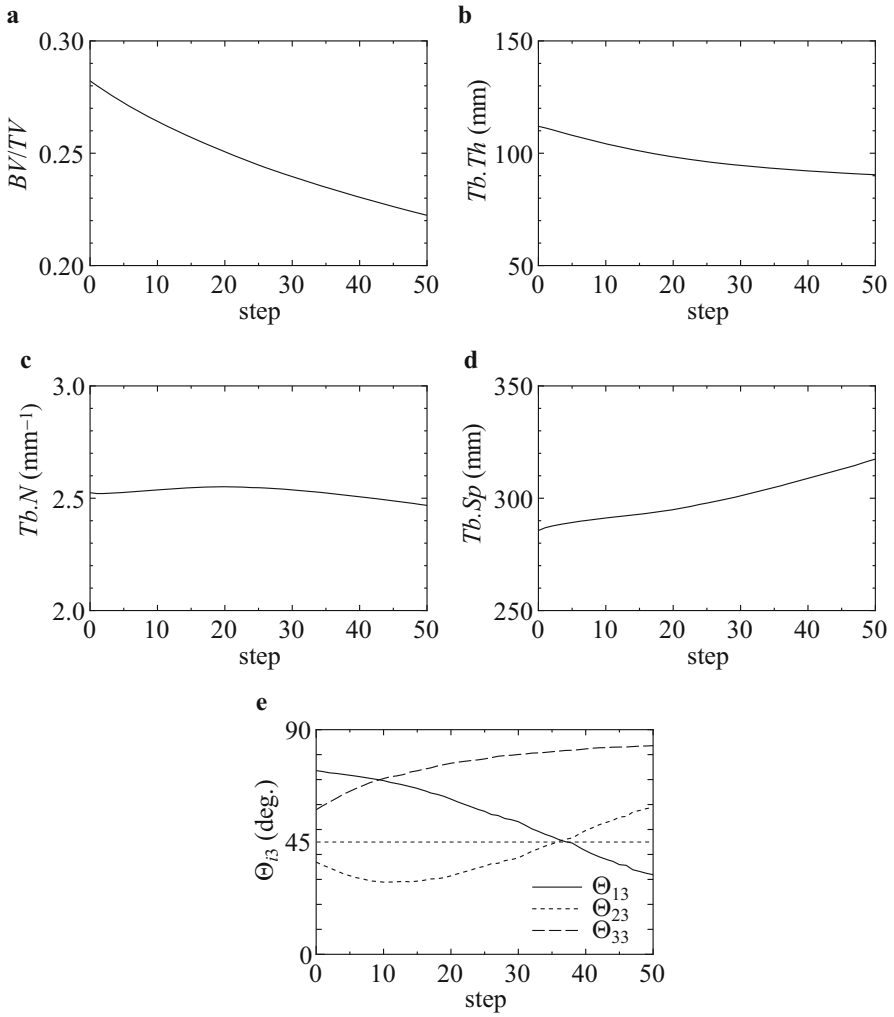

Fig. 11.6 Changes in structural indices of trabecular architecture of cancellous bone cube due to remodeling under compressive loading: (**a**) bone volume fraction (*BV/TV*); (**b**) trabecular bone thickness (*Tb.Th*); (**c**) trabecular bone number (*Tb.N*); (**d**) trabecular bone separation (*Tb.Sp*); and (**e**) angle Θ_{i3} between principal direction of H_i and loading axis X_3 (This figure was adapted from Adachi et al. (2001) with permission from The American Society of Mechanical Engineers)

11.4.2 Functional Adaptation

The apparent stiffness of the core cube of $4.0 \times 4.0 \times 4.0\,\text{mm}^3$ in the direction of the three orthogonal axes X_1, X_2, and X_3 were numerically measured by uniaxial compression testing at each simulation step. The applied boundary conditions were similar to those in the remodeling simulation, that is, uniform displacement

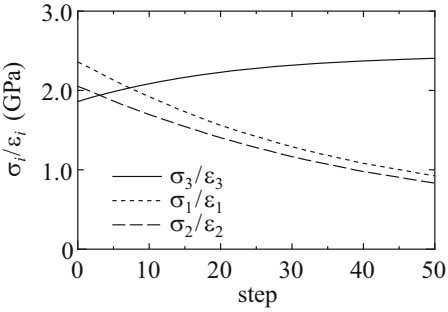

Fig. 11.7 Changes in apparent stiffness σ_i/ε_i in X_i direction of cancellous bone cube (This figure was adapted from Adachi et al. (2001) with permission from The American Society of Mechanical Engineers)

was applied to the upper surface, while the remaining surfaces were fixed under share-free conditions. Changes in the apparent stiffness σ_i/ε_i in the direction of coordinate axes X_i are plotted in Fig. 11.7. In the compressive loading direction, X_3, in the remodeling simulation, the apparent stiffness σ_3/ε_3 gradually increased by 29.4%; however, both σ_1/ε_1 and σ_2/ε_2, in the direction perpendicular to the loading axis, decreased by approximately 60% due to remodeling. Thus, remodeling resulted in functional changes in the trabecular architecture and increases in the degree of anisotropy in the mechanical properties. Although the average bone volume fraction decreased by remodeling, as shown in Fig. 11.6a, the stiffness as a structure increased, demonstrating the adaptive response in order to support the compressive load through the reorganization of the trabecular architecture.

In general, a reduction in bone mass is responsible for the decrease in the stiffness as a structure; however, although the trabecular bone volume decreased, the apparent stiffness as a structure increased, through the reorganization of the trabeculae aligned along the compressive loading axis. These results, obtained under the assumption of the uniform stress hypothesis, can be understood as a functional adaptation, by remodeling, to the applied mechanical load.

11.4.3 Fabric and Compliance Tensors of Cancellous Bone

Details of the fabric tensor of cancellous bone and compliance tensors are illustrated in Figs. 11.8 and 11.9 up to the 200th simulation step, at which the anisotropy of the trabecular structure further increased from that at the 50th step (Fig. 11.5). The diameter of the fabric ellipsoid, which is a graphical representation of the fabric tensor (Cowin 1986), increased, and its first principal direction changed to the direction of compressive loading, as shown in Fig. 11.8. The principal values of H_i ($i = 1, 2, 3$) changed from $H_1 = 387$ μm to 556 μm, $H_2 = 311$ μm to 413 μm, and $H_3 = 291$ μm to 321 μm between the initial and 200th simulation steps. The degree of structural anisotropy increased from $H_1/H_2 = 1.24$ to 1.34 for the first and second axes, and from $H_1/H_3 = 1.33$ to 1.73 for the first and third axes. As denoted in Sect. 11.4.1 and in Fig. 11.6, angle Θ_{i3} ($i = 1, 2, 3$) approached zero, while

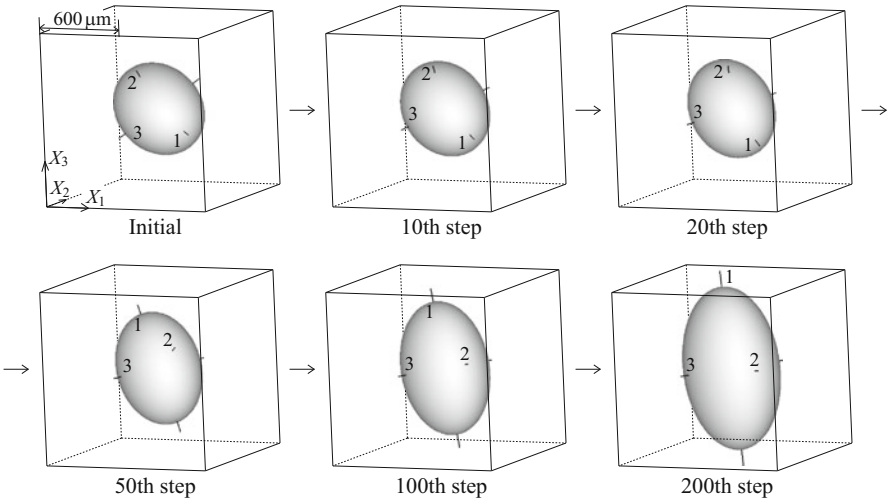

Fig. 11.8 Changes in fabric ellipsoid of cancellous bone due to trabecular structural changes. Plotted is the fabric ellipsoid with its principal axes (This figure was adapted from Tsubota and Adachi (2004) with permission from Taylor & Francis Ltd)

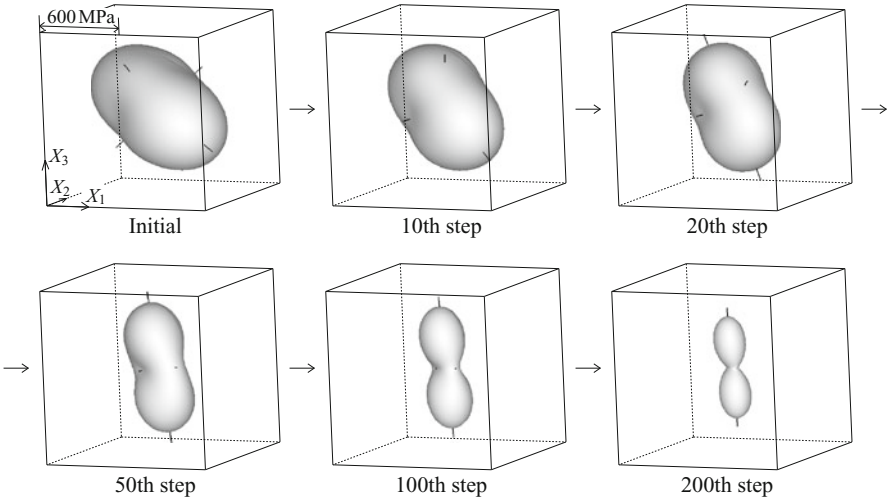

Fig. 11.9 Changes in stiffness of cancellous bone caused by trabecular structural changes. Stiffness is plotted in polar coordinates with the orthotropic principal axes (This figure was adapted from Tsubota and Adachi (2004) with permission from Taylor & Francis Ltd)

angles Θ_{23} and Θ_{33} approached 90°, and bone volume fraction *BV/TV* decreased from 0.28 to 0.15.

The changes in the component of the compliance tensor that relates nominal stress to nominal strain are shown in Fig. 11.9, in which the inverse of the

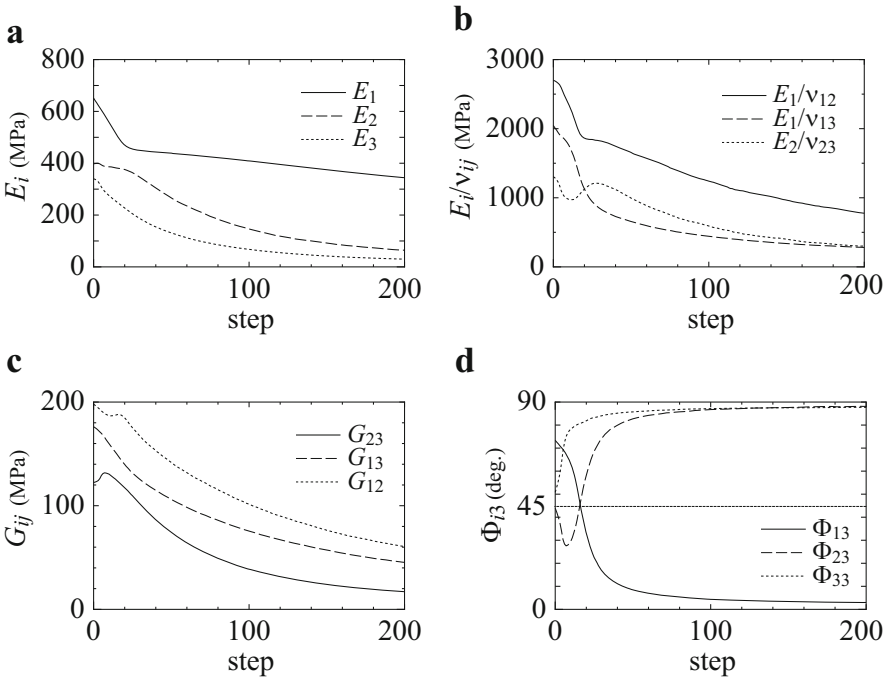

Fig. 11.10 Changes in the stiffness of cancellous bone: (**a**) Young's modulus E_i ($i = 1, 2, 3$); (**b**) Ratio of Young's modulus to Poisson's ratio E_i/ν_{ij} ($j = 1, 2, 3$); (**c**) Shear modulus G_{ij}; (**d**) Angle Φ_{i3} between the principal directions of the compliance tensor and the compressive loading direction (This figure was adapted from Tsubota and Adachi (2004) with permission from Taylor & Francis Ltd)

component is plotted in polar coordinates with the orthotropic principal directions. The radius of the plot, which expresses stiffness in the corresponding direction, decreased as a result of the decrease in the bone volume fraction *BV/TV*. The inverses of the nine constants of the orthotropic compliance tensor (E_i, E_i/ν_{ij} and G_{ij}) also decreased, as shown in Figs. 11.10a–c. If we assume that cancellous bone is isotropic with Young's modulus E_{iso} subjected to the square power law of the bone volume fraction ($E_{iso} = E_t(BV/TV)^2$), the modulus E_{iso} would decrease by 71% (from $E_{iso} = 418$ MPa with $BV/TV = 0.28$ to $E_{iso} = 210$ MPa with $BV/TV = 0.15$). The decrease in the stiffness, however, was different for each direction due to the anisotropic changes in trabecular structure. The decreases in E_1 (47%), E_1/ν_{12} (71%) and G_{12} (69%) were smaller than that of the isotropic assumption, while they were greater for the remaining directions (84% for E_2, 91% for E_3, 77% for E_2/ν_{23}, 86% for E_1/ν_{13}, 86% for G_{23} and 74% for G_{13}). The first principal direction changed to the direction of the compressive load, as shown in Fig. 11.9, as is the case of the fabric tensor shown in Fig. 11.8. That is, angle Φ_{13} between the principal direction with Young's modulus E_1 and loading axis X_3 decreased

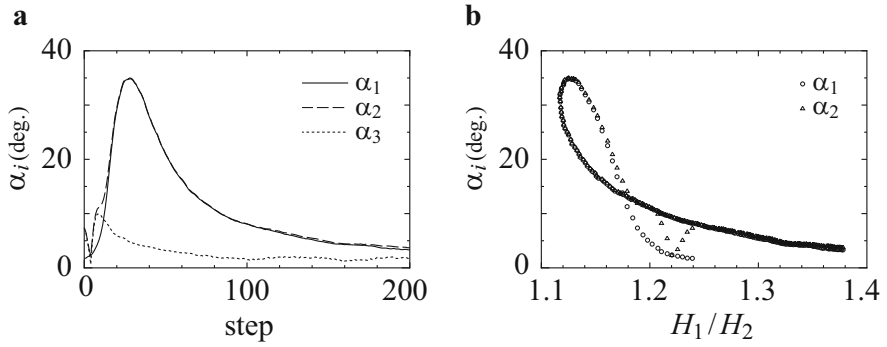

Fig. 11.11 Differences in the principal directions of the fabric and compliance tensors: (**a**) Changes in the difference angle α_i ($i = 1,\ 2,\ 3$) between the fabric and compliance tensors for first ($i = 1$), second ($i = 2$), and third ($i = 3$) principal directions; (**b**) Difference angles α_1 and α_2 versus the degree of structural anisotropy H_1/H_2 (This figure was adapted from Tsubota and Adachi (2004) with permission from Taylor & Francis Ltd)

monotonously toward zero, while angles Φ_{23} and Φ_{33} for the E_2 and E_3 directions, respectively, increased toward 90°, as shown in Fig. 11.10d.

The difference angle α_i ($i = 1, 2, 3$), shown in Fig. 11.11a, indicates that the principal directions of the fabric and compliance tensors did not always correspond. The difference angle α_i is larger for the first and second principal directions than for the third. Angles α_1 and α_2 decreased with increasing structural anisotropy H_1/H_2, as shown in Fig. 11.11b. The nine constants of the orthotropic compliance tensor $1/E_i$, ν_{ij}/E_i and $1/G_{ij}$ were well correlated with structural parameters H_i and *BV/TV* during the trabecular structural changes with goodness of fit criteria $R^2_{adj} = 0.998$.

11.4.4 Comparison to Experimental Data

In the simulation, the initial digital-image-based model was produced based on the control trabecular bone cube from the contralateral side in the experiment (Guldberg et al. 1997b), and the simulation results were compared with the experimental, within the same animal. The structural indices for the control and experimental canine bones, and the simulation results are listed in Table 11.1. In the simulation, the trabecular bone volume fraction (*BV/TV*) and the angle Θ_{13} of the principal axis of the trabecular architecture decreased, and the trabecular separation (*Tb.Sp*) increased by remodeling under compressive load. These results qualitatively coincide with experimental observations, in which changes in *BV/TV*, Θ_{13}, and *Tb.Sp* were statistically significant compared with the control data in the experiment. The trabecular number (*Tb.N*) decreased slightly, while that in the experiment significantly decreased. For the trabecular thickness (*Tb.Th*), the

Table 11.1 Structural indices of trabecular architecture for control, experiment, and simulation: The control cancellous bone cube is sourced from the contralateral side in the experiment, and used as the initial model in the simulation

	BV/TV	*Tb.Th* (μm)	*Tb.N* (mm^{-1})	*Tb.Sp* (μm)	Θ_{13} (deg.)
Control	0.282	112	2.52	286	73.6
Experiment	0.230	121	1.88	421	47.9
Simulation	0.222	90	2.47	317	31.9

This table was adapted from Adachi et al. (2001) with permission from The American Society of Mechanical Engineers

simulation result showed a decrease by remodeling; however, in the experiment, *Tb.Th* did not show a significant change.

The discrepancy between the experiment and simulation results in Table 11.1 is because the comparison is made for only one set of canine data, and another simulation with a different initial trabecular structure is expected to yield qualitatively the same results. To develop models that can predict the details of the remodeling phenomenon, the model parameters Γ_u, Γ_l, and l_L have to be quantitatively determined through comparison with experimental observations for multiple specimens. However, to date, because of the difficulty in observing the changes in trabecular architecture under a controlled mechanical environment *in vivo*, only a small number of remodeling experiments (Goldstein et al. 1991; Guldberg et al. 1997a, 1997b; Schulte et al. 2011, 2013) have been performed to obtain quantitative results regarding bone remodeling controlled by the mechanical environment.

11.5 Conclusion

In this chapter, the potential of the simulation method using image-based finite element model is demonstrated as a technique for representing the morphological changes in trabeculae due to trabecular surface remodeling. The remodeling to achieve a uniform stress state brings about the functional adaptive response of the bone as a load-bearing structure. The changes in mechanical properties of cancellous bone under the loading conditions applied in this study are essentially anisotropic, and thus should be expressed by tensorial quantities. The simulated structural indices coincide with reported experimental data.

Quantitative comparison of the changes in the trabecular structure, demonstrated by the computer simulation with the experimental observations obtained under a controlled mechanical environment, would enable us to develop more detailed models. In addition, one of the noteworthy features of the proposed simulation method is the capability to handle a large-scale three-dimensional voxel model with a regular finite element mesh for complex trabecular architecture. This offers many practical advantages, such as enabling us to create voxel finite element models based on digital images, such as those obtained by μCT scanning, and allowing us to analyze a variety of cancellous using images obtained from *in vivo* experiments.

References

Adachi T, Tomita Y, Sakaue H, Tanaka M (1997) Simulation of trabecular surface remodeling based on local stress nonuniformity. JSME Int J C 40(4):782–792. https://doi.org/10.1299/jsmec.40.782

Adachi T, Tsubota K, Tomita Y, Hollister SJ (2001) Trabecular surface remodeling simulation for cancellous bone using microstructural voxel finite element models. J Biomech Eng-T Asme 123(5):403–409. https://doi.org/10.1115/1.1392315

Badilatti SD, Christen P, Levchuk A, Marangalou JH, van Rietbergen B, Parkinson I, Muller R (2016) Large-scale microstructural simulation of load-adaptive bone remodeling in whole human vertebrae. Biomech Model Mechanobiol 15(1):83–95. https://doi.org/10.1007/s10237-015-0715-8

Cowin SC (1985) The relationship between the elasticity tensor and the fabric tensor. Mech Mater 4(2):137–147. https://doi.org/10.1016/0167-6636(85)90012-2

Cowin SC (1986) Wolff's law of trabecular architecture at remodeling equilibrium. J Biomech Eng 108(1):83–88

Cowin SC, Moss-Salentijn L, Moss ML (1991) Candidates for the mechanosensory system in bone. J Biomech Eng 113(2):191–197

Cowin SC, Sadegh AM, Luo GM (1992) An evolutionary Wolff's law for trabecular architecture. J Biomech Eng 114(1):129–136

Feldkamp LA, Goldstein SA, Parfitt AM, Jesion G, Kleerekoper M (1989) The direct examination of three-dimensional bone architecture in vitro by computed tomography. J Bone Miner Res 4(1):3–11. https://doi.org/10.1002/jbmr.5650040103

Frost H (1988) Structural adaptations to mechanical usage. A proposed "Three-Way Rule" for bone modeling, part I. Vet Comp Orthop Traumatol 1(1):13–23

Goldstein SA, Matthews LS, Kuhn JL, Hollister SJ (1991) Trabecular bone remodeling: an experimental model. J Biomech 24(Suppl 1):135–150

Guedes JM, Kikuchi N (1990) Preprocessing and Postprocessing for materials based on the homogenization method with adaptive finite-element methods. Comput Method Appl M 83(2):143–198

Guldberg RE, Caldwell NJ, Guo XE, Goulet RW, Hollister SJ, Goldstein SA (1997a) Mechanical stimulation of tissue repair in the hydraulic bone chamber. J Bone Miner Res 12(8):1295–1302. https://doi.org/10.1359/jbmr.1997.12.8.1295

Guldberg RE, Richards M, Caldwell NJ, Kuelske CL, Goldstein SA (1997b) Trabecular bone adaptation to variations in porous-coated implant topology. J Biomech 30(2):147–153

Harrigan TP, Mann RW (1984) Characterization of microstructural anisotropy in orthotropic materials using a 2nd rank tensor. J Mater Sci 19(3):761–767

Hollister SJ, Kikuchi N (1994) Homogenization theory and digital imaging: a basis for studying the mechanics and design principles of bone tissue. Biotechnol Bioeng 43(7):586–596. https://doi.org/10.1002/bit.260430708

Hollister SJ, Brennan JM, Kikuchi N (1994) A homogenization sampling procedure for calculating trabecular bone effective stiffness and tissue level stress. J Biomech 27(4):433–444

Hughes TJR, Ferencz RM, Hallquist JO (1987) Large-scale vectorized implicit calculations in solid mechanics on a Cray X-Mp/48 utilizing Ebe preconditioned conjugate gradients. Comput Method Appl M 61(2):215–248

Huiskes R, Ruimerman R, van Lenthe GH, Janssen JD (2000) Effects of mechanical forces on maintenance and adaptation of form in trabecular bone. Nature 405(6787):704–706. https://doi.org/10.1038/35015116

Jacobs CR, Simo JC, Beaupre GS, Carter DR (1997) Adaptive bone remodeling incorporating simultaneous density and anisotropy considerations. J Biomech 30(6):603–613

Luo G, Cowin SC, Sadegh AM, Arramon YP (1995) Implementation of strain rate as a bone remodeling stimulus. J Biomech Eng 117(3):329–338

Mullender MG, Huiskes R, Weinans H (1994) A physiological approach to the simulation of bone remodeling as a self-organizational control process. J Biomech 27(11):1389–1394

Mullender M, van Rietbergen B, Ruegsegger P, Huiskes R (1998) Effect of mechanical set point of bone cells on mechanical control of trabecular bone architecture. Bone 22(2):125–131

Odgaard A, Kabel J, van Rietbergen B, Dalstra M, Huiskes R (1997) Fabric and elastic principal directions of cancellous bone are closely related. J Biomech 30(5):487–495

Parfitt AM (1994) Osteonal and hemi-osteonal remodeling: the spatial and temporal framework for signal traffic in adult human bone. J Cell Biochem 55(3):273–286. https://doi.org/10.1002/jcb.240550303

Sadegh AM, Luo GM, Cowin SC (1993) Bone ingrowth: an application of the boundary element method to bone remodeling at the implant interface. J Biomech 26(2):167–182

Schulte FA, Lambers FM, Kuhn G, Muller R (2011) In vivo micro-computed tomography allows direct three-dimensional quantification of both bone formation and bone resorption parameters using time-lapsed imaging. Bone 48(3):433–442. https://doi.org/10.1016/j.bone.2010.10.007

Schulte FA, Ruffoni D, Lambers FM, Christen D, Webster DJ, Kuhn G, Muller R (2013) Local mechanical stimuli regulate bone formation and resorption in mice at the tissue level. PLoS One 8(4):e62172. https://doi.org/10.1371/journal.pone.0062172

Tsubota K, Adachi T (2004) Changes in the fabric and compliance tensors of cancellous bone due to trabecular surface remodeling, predicted by a digital image-based model. Comput Methods Biomech Biomed Engin 7(4):187–192. https://doi.org/10.1080/10255840410001729524

Tsubota K, Adachi T (2005) Spatial and temporal regulation of cancellous bone structure: characterization of a rate equation of trabecular surface remodeling. Med Eng Phys 27(4):305–311. https://doi.org/10.1016/j.medengphy.2004.09.013

Tsubota K, Adachi T, Tomita Y (2002) Functional adaptation of cancellous bone in human proximal femur predicted by trabecular surface remodeling simulation toward uniform stress state. J Biomech 35(12):1541–1551. https://doi.org/10.1016/S0021-9290(02)00173-2

Tsubota K, Suzuki Y, Yamada T, Hojo M, Makinouchi A, Adachi T (2009) Computer simulation of trabecular remodeling in human proximal femur using large-scale voxel FE models: approach to understanding Wolff's law. J Biomech 42(8):1088–1094. https://doi.org/10.1016/j.jbiomech.2009.02.030

Ulrich D, van Rietbergen B, Weinans H, Ruegsegger P (1998) Finite element analysis of trabecular bone structure: a comparison of image-based meshing techniques. J Biomech 31(12):1187–1192

van Rietbergen B, Weinans H, Huiskes R, Odgaard A (1995) A new method to determine trabecular bone elastic properties and loading using micromechanical finite-element models. J Biomech 28(1):69–81

van Rietbergen B, Odgaard A, Kabel J, Huiskes R (1996) Direct mechanics assessment of elastic symmetries and properties of trabecular bone architecture. J Biomech 29(12):1653–1657

van Rietbergen B, Odgaard A, Kabel J, Huiskes R (1998) Relationships between bone morphology and bone elastic properties can be accurately quantified using high-resolution computer reconstructions. J Orthop Res 16(1):23–28. https://doi.org/10.1002/jor.1100160105

Chapter 12
Functional Adaptation of Cancellous Bone in Human Proximal Femur

Abstract This chapter describes a two-dimensional computer simulation of trabecular structural changes in a human proximal femur. As described in Chap. 8, local stress nonuniformity is assumed to drive trabecular structural change by surface remodeling to seek a uniform stress state. A large-scale pixel finite element model is constructed for simulating structural changes of individual trabeculae over the entire bone. In the simulation, the initial structure of trabeculae changes from isotropic to anisotropic because of the trabecular microstructural changes according to the mechanical environment in the proximal femur. The apparent structural properties evaluated by fabric ellipses correspond to the apparent stress state in cancellous bone. As observed in the actual bone, a distributed trabecular structure is obtained under a multiple-loading condition. These results demonstrate that trabecular surface remodeling leading towards a local uniform stress state at the trabecular level results in a functional adaptation phenomenon at the apparent tissue level. The proposed simulation model is capable of providing insight into the hierarchical mechanism of trabecular surface remodeling from the microstructural level up to the apparent tissue level.

Keywords Human proximal femur • Cancellous bone • Surface remodeling • Functional adaptation • Pixel FE model

12.1 Introduction

The characteristic anisotropic trabecular structure of the human proximal femur has been extensively investigated in the computer simulation of bony structure adaptation by remodeling (Adachi et al. 1997; Bagge 2000; Beaupré et al. 1990; Carter et al. 1987, 1989; Doblare and Garcia 2001, 2002; Garcia-Aznar et al. 2005; Huiskes et al. 1987; Jacobs et al. 1997; McNamara and Prendergast 2007; Skedros and Baucom 2007; Turner et al. 1997; Wolff 1892, 1986). In the human proximal femur, the mechanical environment is complex due to the trabecular architecture, the external shape of cortical bone, and various external-loading conditions (van Rietbergen et al. 1999). At the apparent tissue level, relationships between bone structure, such as bone density, and stress/strain have been identified in previously

This Chapter was adapted from Tsubota et al. (2002) with permission from Elsevier.

Y. Kameo et al., *Bone Adaptation*, Frontiers of Biomechanics 2,
https://doi.org/10.1007/978-4-431-56514-7_12

reported simulation studies (Beaupré et al. 1990; Carter et al. 1987, 1989; Huiskes et al. 1987; Jacobs et al. 1997); however, multi-scale structure adaptation by remodeling over the entire size range, from bone cells (~10 μm) to entire bone (~10 cm) has not been sufficiently researched.

In this chapter, we present a two-dimensional computer simulation of trabecular surface remodeling in a human proximal femur. To evaluate the mechanical environment at the trabecular level over the entire bone, the architecture of each trabecula is directly modeled using a large number of pixel finite elements (FEs). The pixel FE model is combined with a trabecular surface remodeling model (presented in Chap. 8) in which local stress nonuniformity is assumed to drive trabecular structural change by surface remodeling to seek a uniform stress state. Trabecular structural changes are simulated under both single and multiple external-loading conditions to clarify the relationships between the local regulation process at the trabecular level, and the functional adaptation phenomenon at the apparent tissue level.

12.2 Pixel FE Model of Human Proximal Femur

A two-dimensional FE model was created with a large number of pixel elements to simulate trabecular remodeling in a human proximal femur. This model was combined with the simulation model shown in Chap. 8 to express the structural changes of the individual trabeculae over the entire proximal femur.

12.2.1 Pixel FE Model

A computational model of a human proximal femur was created using approximately 0.67 million pixel FEs, as shown in Fig. 12.1a. Assuming an isotropic trabecular structure at the initial stage, the cancellous bone part was filled with a random pattern of circular trabeculae, as shown in Fig. 12.1b. The external and internal diameters of each trabecula were 1680 and 1120 μm, respectively. The principal values of the fabric ellipse of the trabecular structure (Cowin 1985), $H_i\,(i=1, 2, H_1>H_2)$, were $H_1=714$ μm and $H_2=713$ μm, resulting in a degree of structural anisotropy H_1/H_2 nearly equal to unity. The bone was assumed to be a homogeneous, isotropic material with Young's modulus of $E_t=20$ GPa and Poisson's ratio of $\nu_t=0.3$. The marrow was regarded as a cavity, and was neglected in the finite element analysis. The element-by-element preconditioned conjugate gradients (EBE/PCG) method (Hughes et al. 1987; van Rietbergen et al. 1995) was used for the finite element analysis.

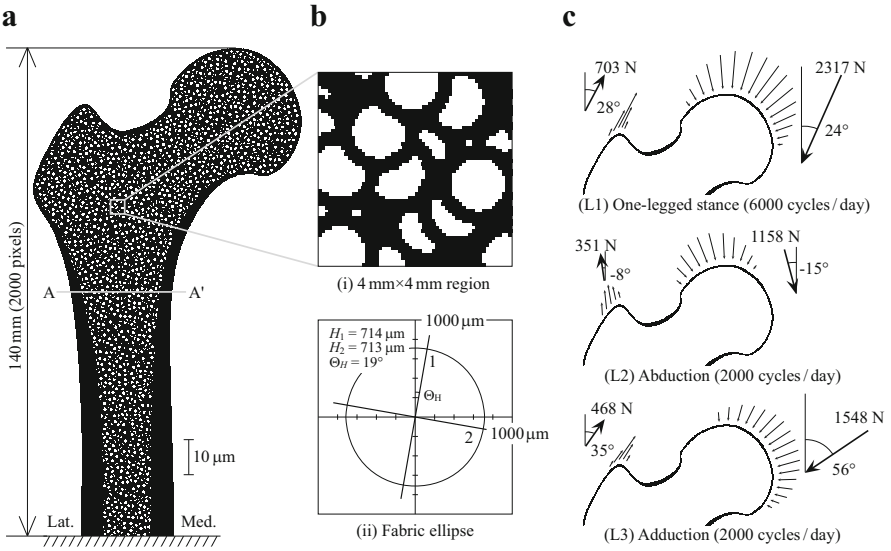

Fig. 12.1 Simulation model for trabecular surface remodeling in a human proximal femur using large-scale pixel finite elements: (**a**) Overview of the finite element model; (**b**) Initial trabecular structure and its fabric ellipse; (**c**) Boundary condition considering daily loading history (Beaupré et al. 1990) (This figure was adapted from Tsubota et al. (2002) with permission from Elsevier)

12.2.2 Loading Condition

As a representative daily loading condition, three loading cases, namely one-legged stance (L1), extreme ranges of motion of abduction (L2), and adduction (L3) were assumed (Beaupré et al. 1990), as shown in Fig. 12.1c. These external loadings were modeled as distributed forces generated using a sine function to the joint surface and the greater trochanter. The lower boundary corresponding to the diaphysis was fixed. Simulation results are discussed only for the proximal region of the finite element model, above the line A-A′ shown in Fig. 12.1a, to neglect the artificial influence of the fixed boundary condition. The sensing distance l_L (Chap. 9) in the weight function $w(l)$ was set to 1 mm, equal to the length of 20 voxel elements, and the threshold values of remodeling (Chap. 9) were set to $\Gamma_u = 1.0$ and $\Gamma_l = -2.0$.

Simulations were conducted for both single-loading and multiple-loading conditions. For multiple-loading conditions, remodeling driving force Γ_i for a single loading case Li was averaged over three single-loading cases with weighting depending on the loading frequency n_i:

$$\Gamma_{\mathrm{mlt}} = \sum_{i=1}^{3} w_i \Gamma_i, \quad \text{where } w_i = \frac{n_i}{n_1 + n_2 + n_3}, \tag{12.1}$$

and the averaged driving force Γ_{mlt} was used as Γ in Eq. (8.3) (Beaupré et al. 1990).

12.3 Trabecular Structural Changes in a Human Proximal Femur

This section explains the simulation results regarding trabecular structural changes under the single-loading (Sect. 3.1) and multiple-loading (Sect. 3.2) conditions.

12.3.1 Structural Change Under Single-Loading Condition

The trabecular structural change under single loading at the 16th simulation step was obtained for each loading case, as shown in Fig. 12.2. In the one-legged stance loading case (L1), shown in Fig. 12.2a, the trabeculae are aligned with the compressive joint reaction force in the femoral head, represented by region 1, and with the tensile abductor force in the greater trochanter, represented by region 2. On the other hand, an orthogonal trabecular pattern emerged in the lateral side of the femoral neck, represented by region 3. This orthogonal pattern consists of compressive trabeculae from the medial to the lateral side near the greater trochanter, and tensile trabeculae from the lateral side to the neck of the femoral head.

In the abduction loading case (L2), the joint reaction force caused bending loads at the femoral neck, resulting in an arcuate trabecular structure from the lateral cortical diaphysis to the femoral head, as shown in Fig. 12.2b. These arcuate trabeculae configured orthogonal trabecular patterns in the femoral head, represented by region 1, combined with the compressive trabeculae along the joint reaction force. An orthogonal trabecular pattern also emerged in the lateral side of the femoral neck, represented by region 3. In the greater trochanter, represented by region 2, trabeculae are aligned with the tensile abductor force. The structural changes in regions 2 and 3 are similar to those obtained in the L1 case.

In the adduction loading case (L3), shown in Fig. 12.2c, unidirectional trabeculae can be identified in the femoral head, represented by region 1, because the compressive joint reaction force did not cause bending loads at the femoral neck. This compressive trabecular pattern spread to the lateral side of the femoral neck, represented by region 3, and to the greater trochanter, represented by region 2. An orthogonal trabecular pattern appeared in region 2 because the trabeculae were also formed along the tensile abductor force direction.

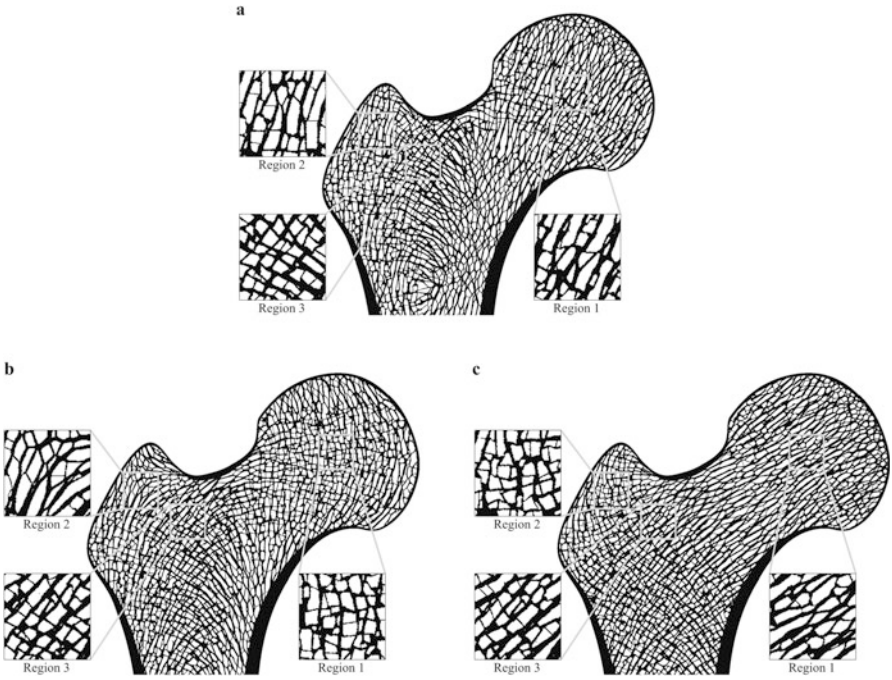

Fig. 12.2 Trabecular structural change in the proximal femur due to remodeling under single loading, at the 16th step: (**a**) One-legged stance (L1); (**b**) Abduction (L2); (**c**) Adduction (L3) (This figure was adapted from Tsubota et al. (2002) with permission from Elsevier)

The distribution of apparent bone density was obtained over the entire cancellous region. In loading cases L1 and L2, a higher density emerged in the center of the femoral head, represented by region 1, and in the lateral side of the femoral neck, represented by region 3. The regions with lower densities are the greater trochanter, represented by region 2, and the femoral neck. Compared to these two loading cases, the density distribution was not significant in loading case L3.

A structural property at the apparent tissue level, quantified by fabric ellipses, corresponds to the apparent stress state, as shown in Fig. 12.3. In loading case L1, the degree of structural anisotropy is $H_1/H_2 = 1.44$ and the principal direction of the fabric ellipse is $\Theta_H = 30^\circ$ in region 1, $H_1/H_2 = 1.60$ and $\Theta_H = 11^\circ$ in region 2, and $H_1/H_2 = 1.06$ and $\Theta_H = -66^\circ$ in region 3, as shown in Fig. 12.3a. Calculating the apparent principal stresses $|\sigma_1|$ and $|\sigma_2|$ ($|\sigma_1| > |\sigma_2|$) by averaging the stress components over the cancellous area, the ratio of magnitude of two principal stresses is $|\sigma_1|/|\sigma_2| = 14.6$ and the principal direction of the stresses is $\Theta_\sigma = 24^\circ$ in region 1, $|\sigma_1|/|\sigma_2| = 10.6$ and $\Theta_\sigma = 12^\circ$ in region 2, and $|\sigma_1|/|\sigma_2| = 1.4$ and $\Theta_\sigma = -56^\circ$ in region 3, as shown in Fig. 12.3b. Comparing the fabric ellipses to the apparent principal stresses, it was shown that a unidirectional trabecular pattern emerged in the regions of a uniaxial compressive stress state (region 1) or a tensile stress state (region 2), and that an orthogonal trabecular pattern emerged in the

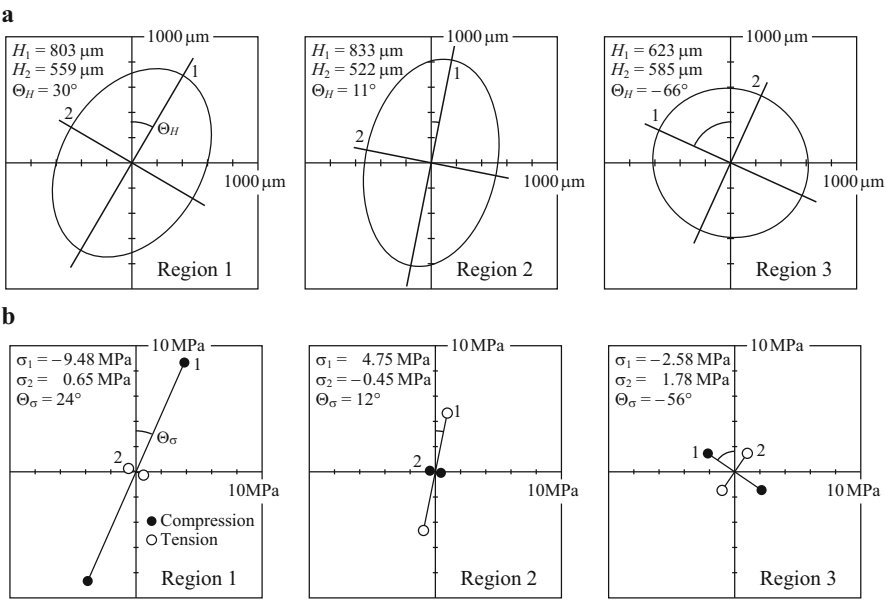

Fig. 12.3 Correspondence between structural property and mechanical environment at the apparent tissue level in regions 1, 2, and 3 at the 16th step under the single-loading condition of one-legged stance (L1): (**a**) Fabric ellipses; (**b**) Apparent principal stresses (This figure was adapted from Tsubota et al. (2002) with permission from Elsevier)

regions of a biaxial compressive-tensile stress state (region 3). This point was also confirmed by the fabric ellipses and the apparent principal stresses in loading cases L2 and L3 (data not shown).

12.3.2 Structural Change Under Multiple-Loading Condition

An anisotropic trabecular architecture was obtained under multiple loading at the 16th step, as shown in Fig. 12.4. Because the one-legged stance loading (L1) was the most frequent (60%) of the three loading cases, the apparent trabecular orientation and density distribution are similar to those obtained under the single-loading condition of case L1 (Fig. 12.2a). Functional adaptation at the apparent tissue level was also exhibited, as in the case of the single-loading condition. That is, the fabric ellipses, as shown in Fig. 12.5a, correspond to the apparent principal stress state, as shown in Fig. 12.5b. The degree of structural anisotropy is $H_1/H_2 = 1.32$ and the principal direction of the fabric ellipse is $\Theta_H = 33^\circ$ in region 1, $H_1/H_2 = 1.51$ and $\Theta_H = 11^\circ$ in region 2, and $H_1/H_2 = 1.06$ and $\Theta_H = 75^\circ$ in region 3. In evaluating the apparent principal stresses under multiple loading, the stresses

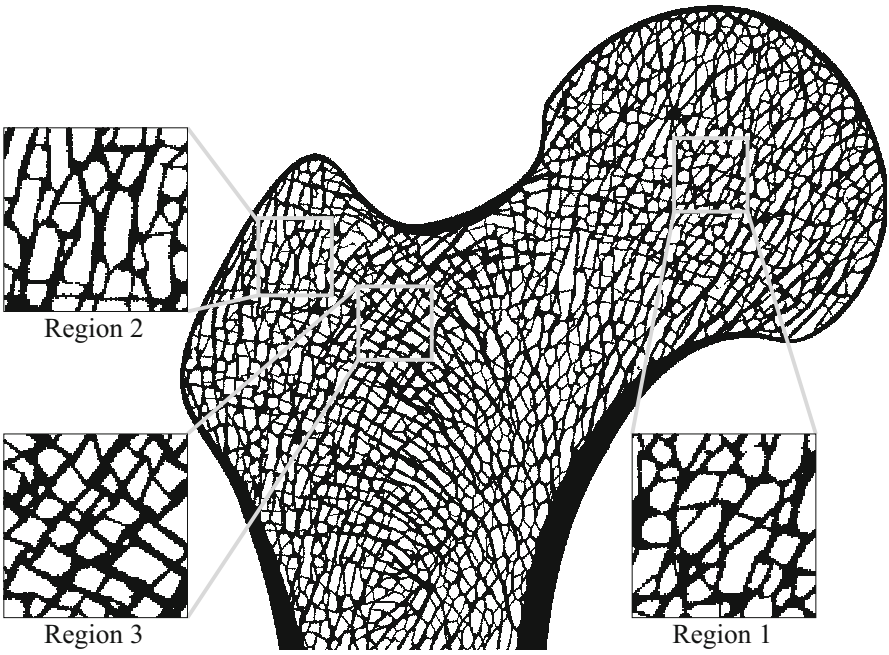

Fig. 12.4 Trabecular structural change in the proximal femur due to remodeling under multiple loading, at the 16th step (This figure was adapted from Tsubota et al. (2002) with permission from Elsevier)

for the three loading cases were averaged with weight factors, depending on the loading frequency, in the same manner as calculating the driving force Γ_{mlt} in Eq. (12.1). The ratio of the two principal stresses is $|\sigma_1|/|\sigma_2| = 27.5$ and the principal direction is $\Theta_\sigma = 21^\circ$ in region 1, $|\sigma_1|/|\sigma_2| = 13.2$ and $\Theta_\sigma = 10^\circ$ in region 2, and $|\sigma_1|/|\sigma_2| = 1.39$ and $\Theta_\sigma = -57^\circ$ in region 3. These characteristic parameters for the structure and mechanical environment are similar to those obtained under the single-loading condition of case L1.

As a result of adaptation to the multiple external loading, the orientation of the trabeculae has a greater distribution than that obtained under the single-loading condition. For instance, the trabecular structure and distribution of the von Mises equivalent stress are illustrated for the center of region 1 in Fig. 12.6. The equivalent stress of the trabeculae was variable up to a value of 10 MPa, and is dependent on the loading case. Driven by the various mechanical stimuli at the trabecular level, the surface remodeling resulted in a distributed trabecular orientation corresponding to each loading direction. The trabeculae mainly supporting the loadings varied according to the external-loading cases, as indicated by arrows in Fig. 12.6. Thus, multi-directional trabeculae were formed to support the multiple loadings.

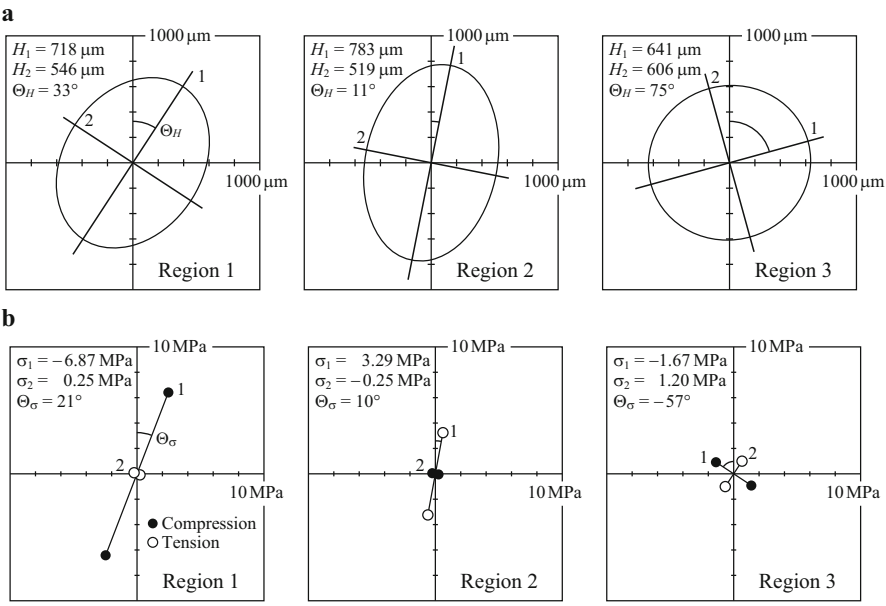

Fig. 12.5 Correspondence between structural property and mechanical environment at the apparent tissue level in regions 1, 2, and 3 at the 16th step under the multiple-loading condition: (**a**) Fabric ellipses; (**b**) Apparent principal stresses (This figure was adapted from Tsubota et al. (2002) with permission from Elsevier)

12.4 Validity of Simulation Model

12.4.1 Changes in Trabecular Structure to Seek Uniform Stress State

Under the single-loading condition, surface remodeling driven by local stress nonuniformity caused the structural changes of trabeculae, resulting in an anisotropic trabecular structure dependent on the applied loadings. Because the structural changes at the trabecular level resulted in the apparent structural properties that corresponded to the apparent mechanical environment, it was suggested that the surface remodeling model based on the uniform stress hypothesis could explain the functional adaptation in cancellous bone under a realistic mechanical environment. For example, the correspondence of the principal directions of the fabric ellipses to those of the apparent stresses agrees with the mathematical expression of Wolff's law denoted by Cowin (1986). Moreover, the predicted density pattern and trabecular orientation at the apparent tissue level are consistent with those predicted by the remodeling model that described the evolution of bone density and structural anisotropy (Jacobs et al. 1997). These results demonstrate the capability of the

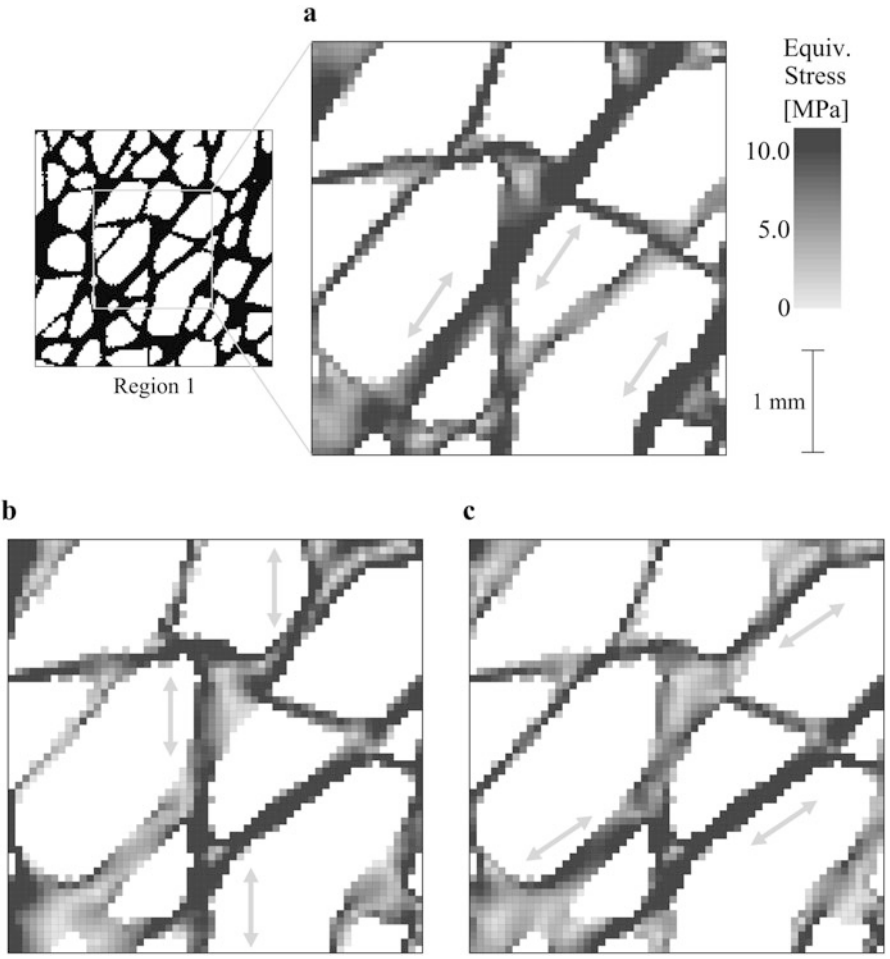

Fig. 12.6 Trabecular structure and distribution of von Mises equivalent stress at the centre of region 1 under multiple loadings at the 16th step: (**a**) One-legged stance (L1); (**b**) Abduction (L2); (**c**) Adduction (L3) (This figure was adapted from Tsubota et al. (2002) with permission from Elsevier)

surface remodeling model investigated in this study to predict the adaptive change in cancellous bone at both the trabecular and the apparent tissue levels.

Under the multiple-loading condition, the trabeculae adapted to the various mechanical environments in the three cases of external loadings. The obtained trabecular structure is distributed as predicted by the remodeling simulation that focused on the evolution of apparent bone density under multiple loading conditions (Carter et al. 1989). One of the novel developments of this study was that the distributed structure of each trabecula was predicted simultaneously with the apparent structural properties corresponding to the apparent principal stresses.

These results successfully predicted the trabecular structure observed in the actual bone, indicating the validity of the surface remodeling simulation based on the uniform stress hypothesis using a large-scale pixel finite element model.

12.4.2 Changes in Trabecular Structure by Sensing Mechanical Stress in Space

The obtained principal values of the fabric ellipses were larger than those of actual bone (Ciarelli et al. 2000) due to the trabecular size used in the simulation at the initial stage. This larger size of the trabeculae was the reason why the sensing distance l_L was chosen to be 1.0 mm, which might be significantly larger than the physiological range of a few hundred micrometers (Mullender et al. 1994; Xia and Ferrier 1992). To discuss an appropriate value of the sensing distance, the characteristic size of the initial trabecular structure should be refined to be of the same size as that in the actual bone. In addition, quantitative comparison of the trabecular structure obtained by three-dimensional remodeling simulation to experimental observation is necessary to determine the sensing distance.

Considering that the cellular activities are influenced by local mechanical stimuli, the local stress nonuniformity, which was equivalent to the convexity and concavity of the scalar function of stress/strain, was used as a remodeling driving force, as shown in Eqs. (8.2) and (8.3). In terms of the uniform stress hypothesis, the difference from the reference value of stress/strain (Turner et al. 1997) or the first-order gradient could be responsible for the fluid flow that would activate bone cells. Because the distribution of apparent bone density obtained in this study did not emerge clearly compared to the remodeling models that seek a reference value of the stress/strain, the model using local stress nonuniformity as a remodeling driving force is less sensitive to the global distribution of the mechanical stimulus. A clearer density distribution is expected to be obtained by choosing the larger sensing distance, as shown in Chap. 9. However, if the determined parameter l_L is out of the physiological range, it might be better to explicitly introduce the sensitivity to the global distribution of the mechanical stimulus into the surface remodeling model in addition to the local mechanical stimulus.

12.4.3 Large-Scale FE Models for Bone Remodeling Simulation

To clarify the mechanism of bone remodeling driven by a local mechanical stimulus at the microstructural level, it is necessary to consider a heterogeneously distributed trabecular structure under complicated external loadings. In investigating the functional adaptation of cancellous bone as a result of trabecular structural

changes under such a complicated mechanical environment, a direct simulation method with a large-scale computation is advantageous compared to the models using a unit cell trabecular structure, as was used in the lattice continuum model proposed by Adachi et al. (1999) or in the homogenization method introduced by Fernandes et al. (1999) and Bagge (2000). In this respect, it was found that the external-loading condition affected the stress distribution of each trabecula, as shown in Fig. 12.6. These figures illustrate the ability of a large-scale pixel finite element model to predict the micro-macro relationships in cancellous bone with a hierarchical structure. Exploring the mechanical stimulus at the cellular level might be possible by considering the internal structure of each trabecula. Therefore, it should be noted that the large-scale computational simulation of bone remodeling is an effective tool not only for clarifying the relationships between the functional adaptation at the apparent tissue level and the local regulation process at the trabecular level, but also for providing insight into cellular response to the mechanical stimuli *in vivo*.

12.4.4 Limitations of 2D Study

Following prior computational studies on bone remodeling (Carter et al. 1987, 1989; Huiskes et al. 1987; Jacobs et al. 1997; Turner et al. 1997), a two-dimensional model of human proximal femur was used in this study. This was based on the fact that two-dimensional models can represent the characteristic mechanical environment and trabecular structure of the proximal femur. This model was sufficient for investigating basic and qualitative relationships between trabecular structural changes and the mechanical environment. However, the simulation results obtained using the two-dimensional model do not quantitatively express the three-dimensional structure and the mechanical environment in actual bone. The fabric ellipse and apparent bone density predicted in this study, which are characteristic quantities of the trabecular structure, might be different from those obtained in the three-dimensional simulation, although the trabecular structural orientation would correspond to the mechanical environment, as was predicted in this study. Thus, in the next Chap. 13, we will extend this work to three dimensions for quantitative evaluation of trabecular structural changes in the proximal femur.

12.5 Conclusion

In this chapter, a mechanism of a trabecular structure adaptation in a human proximal femur is illustrated by a two-dimensional simulation model of trabecular surface remodeling (Chap. 8) combined with a large-scale pixel finite element model. As a result of the simulation, the anisotropic trabecular structure was obtained by surface remodeling of trabeculae according to the mechanical

environment in the proximal femur. Under a single-loading condition, the apparent structural properties evaluated by fabric ellipses corresponded to the apparent stress state in cancellous bone. A distributed trabecular structure was obtained under a multiple-loading condition. Through these studies, it was concluded that trabecular surface remodeling leading towards a local uniform stress state at the trabecular level could naturally bring about a functional adaptation phenomenon at the apparent tissue level. The proposed simulation model is capable of providing insight into the hierarchical mechanism of trabecular surface remodeling from the microstructural level up to the apparent tissue level.

References

Adachi T, Tomita Y, Sakaue H, Tanaka M (1997) Simulation of trabecular surface remodeling based on local stress nonuniformity. JSME Int J Ser C-Mech Syst Mach Elem Manuf 40 (4):782–792. https://doi.org/10.1299/jsmec.40.782

Adachi T, Tomita Y, Tanaka M (1999) Three-dimensional lattice continuum model of cancellous bone for structural and remodeling simulation. Jsme Int J Ser C-Mech Syst Mach Elem Manuf 42(3):470–480. https://doi.org/10.1299/jsmec.42.470

Bagge M (2000) A model of bone adaptation as an optimization process. J Biomech 33 (11):1349–1357

Beaupré GS, Orr TE, Carter DR (1990) An approach for time-dependent bone modeling and remodeling-application: a preliminary remodeling simulation. J Orthop Res 8(5):662–670. https://doi.org/10.1002/jor.1100080507

Carter DR, Fyhrie DP, Whalen RT (1987) Trabecular bone density and loading history: regulation of connective tissue biology by mechanical energy. J Biomech 20(8):785–794

Carter DR, Orr TE, Fyhrie DP (1989) Relationships between loading history and femoral cancellous bone architecture. J Biomech 22(3):231–244

Ciarelli TE, Fyhrie DP, Schaffler MB, Goldstein SA (2000) Variations in three-dimensional cancellous bone architecture of the proximal femur in female hip fractures and in controls. J Bone Miner Res 15(1):32–40. https://doi.org/10.1359/jbmr.2000.15.1.32

Cowin SC (1985) The relationship between the elasticity tensor and the fabric tensor. Mech Mater 4(2):137–147. https://doi.org/10.1016/0167-6636(85)90012-2

Cowin SC (1986) Wolff's law of trabecular architecture at remodeling equilibrium. J Biomech Eng 108(1):83–88

Doblare M, Garcia JM (2001) Application of an anisotropic bone-remodelling model based on a damage-repair theory to the analysis of the proximal femur before and after total hip replacement. J Biomech 34(9):1157–1170

Doblare M, Garcia JM (2002) Anisotropic bone remodelling model based on a continuum damage-repair theory. J Biomech 35(1):1–17

Fernandes P, Rodrigues H, Jacobs C (1999) A model of bone adaptation using a global optimisation criterion based on the trajectorial theory of Wolff. Comput Methods Biomech Biomed Eng 2(2):125–138. https://doi.org/10.1080/10255849908907982

Garcia-Aznar JM, Rueberg T, Doblare M (2005) A bone remodelling model coupling microdamage growth and repair by 3D BMU-activity. Biomech Model Mechanobiol 4 (2–3):147–167

Hughes TJR, Ferencz RM, Hallquist JO (1987) Large-scale Vectorized implicit calculations in solid mechanics on a Cray X-Mp/48 utilizing Ebe preconditioned conjugate gradients. Comput Method Appl M 61(2):215–248

Huiskes R, Weinans H, Grootenboer HJ, Dalstra M, Fudala B, Slooff TJ (1987) Adaptive bone-remodeling theory applied to prosthetic-design analysis. J Biomech 20(11–12):1135–1150

Jacobs CR, Simo JC, Beaupre GS, Carter DR (1997) Adaptive bone remodeling incorporating simultaneous density and anisotropy considerations. J Biomech 30(6):603–613

McNamara LM, Prendergast PJ (2007) Bone remodelling algorithms incorporating both strain and microdamage stimuli. J Biomech 40(6):1381–1391. https://doi.org/10.1016/j.jbiomech.2006.05.007

Mullender MG, Huiskes R, Weinans H (1994) A physiological approach to the simulation of bone remodeling as a self-organizational control process. J Biomech 27(11):1389–1394

Skedros JG, Baucom SL (2007) Mathematical analysis of trabecular 'trajectories' in apparent trajectorial structures: the unfortunate historical emphasis on the human proximal femur. J Theor Biol 244(1):15–45. https://doi.org/10.1016/j.jtbi.2006.06.029

Tsubota K, Adachi T, Tomita Y (2002) Functional adaptation of cancellous bone in human proximal femur predicted by trabecular surface remodeling simulation toward uniform stress state. J Biomech 35(12):1541–1551. https://doi.org/10.1016/S0021-9290(02)00173-2

Turner CH, Anne V, Pidaparti RM (1997) A uniform strain criterion for trabecular bone adaptation: do continuum-level strain gradients drive adaptation? J Biomech 30(6):555–563

van Rietbergen B, Muller R, Ulrich D, Ruegsegger P, Huiskes R (1999) Tissue stresses and strain in trabeculae of a canine proximal femur can be quantified from computer reconstructions. J Biomech 32(4):443–451

van Rietbergen B, Weinans H, Huiskes R, Odgaard A (1995) A new method to determine trabecular bone elastic properties and loading using micromechanical finite-element models. J Biomech 28(1):69–81

Wolff J (1892) Das Gesetz Der Transformation Der Knochen. Hirschwald, Berlin

Wolff J (1986) The law of bone remodeling (trans: Maquet P, Furlong R). Springer, New York

Xia SL, Ferrier J (1992) Propagation of a calcium pulse between osteoblastic cells. Biochem Biophys Res Commun 186(3):1212–1219

Chapter 13
3D Trabecular Remodeling in Human Proximal Femur: Approach to Understanding Wolff's Law

Abstract This chapter describes a large-scale three-dimensional (3D) computer simulation of trabecular remodeling in a human proximal femur in order to understand the mechanism of the Law of Bone Transformation, proposed by Wolff in the nineteenth century. A large-scale voxel finite element model is constructed to simulate the 3D structural changes of individual trabeculae over a cancellous bone. As a simple remodeling model that considers bone cellular activities regulated by the local mechanical environment, the nonuniformity of local stress is assumed to drive the trabecular surface remodeling to seek a uniform stress state (Chap. 8). In the simulation, cell-scale (10 μm) remodeling in response to mechanical stimulation creates complex 3D trabecular structures at the entire bone-scale (10 cm), as observed by Wolff in an actual femur. It is indicated that in a complex mechanical environment of a hierarchical bone structure with a length scale of greater than 10^4 (from 10 μm to 10 cm), a simple remodeling at the cellular/trabecular levels creates a highly complex and functional trabecular structure, as characterized by bone density and orientation.

Keywords Human proximal femur • Cancellous bone • Surface remodeling • Functional adaptation • Voxel FE model

13.1 Introduction

A trabecular structural adaptation to a mechanical environment (Wolff 1892, 1986) can be traced back to the bone formation and resorption process called remodeling (Parfitt 1994); however, little is known regarding the manner in which this cellular-level process is linked to the mechanism of the three-dimensional (3D) structural adaptation of the entire bone. This is because, while the mechanical environment of the trabecular structure and corresponding functions are of concern to the overall bone scale (centimeter scale), the mechanism determining structural adaptation changes the functions at considerably smaller cell levels (micrometer scale).

In Chap. 12, a two-dimensional (2D) computer simulation study demonstrated that the trabecular surface remodeling, in response to local mechanical stimuli, can produce the characteristic anisotropic trabecular structure in the human proximal

This Chapter was adapted from Tsubota et al. (2009) with permission from Elsevier.

Y. Kameo et al., *Bone Adaptation*, Frontiers of Biomechanics 2,
https://doi.org/10.1007/978-4-431-56514-7_13

femur. However, the mechanical conditions of the proximal femur are 3D due to its complex external shape and loading conditions (van Rietbergen et al. 1999). In this chapter, we extend the 2D computer simulations to 3D in order to investigate the functional adaptations caused by trabecular remodeling under the influence of the complex mechanical environment of the hierarchical bone structure of the femur. The simulation results demonstrate how simple remodeling at the cellular and trabecular levels creates a highly complex and functional trabecular structure of the entire human proximal femur in 3D.

13.2 Model of Human Proximal Femur

A voxel finite element (FE) model was created to simulate trabecular remodeling in a human proximal femur with a large number of elements. This model was combined with a simulation model, shown in Chap. 8, to express structural changes of individual trabeculae over the entire proximal femur.

13.2.1 Voxel FE Model

A 3D computational model of a human proximal femur was created using approximately 93 million voxel finite elements with a resolution of 87.5 μm, as shown in Figs. 13.1a–c. An isotropic and uniform initial structure was useful in explaining the effects of the mechanical environment on the trabecular structural changes that emerge from adaptive remodeling (Beaupré et al. 1990; Huiskes et al. 1987; Jacobs et al. 1997; Jang and Kim 2008; Tsubota et al. 2002). Thus, the cancellous bone of the femur model is filled with an isotropic and uniform porous bone structure with a degree of anisotropy $H_1/H_3 = 1.04$, where H_1 and H_3 are the first and third principal values of the fabric ellipsoid $\boldsymbol{H}$ of the trabecular structure (Cowin 1985, 1986). The bone volume fraction $(BV/TV) = 0.37$ is within the physiological range of the cancellous bone. This initial structure is generated by laying many pieces of torus-shaped trabeculae in random positions, in a manner similar to that in the 2D study of Chap. 12. The bone was assumed to be a homogeneous, isotropic material with Young's modulus of $E_t = 20$ GPa and Poisson's ratio of $\nu_t = 0.3$. The marrow was regarded as a cavity, and was neglected in the finite element analysis. The element-by-element preconditioned conjugate gradients (EBE/PCG) method (Hughes et al. 1987; van Rietbergen et al. 1995) was used for the finite element analysis.

13.2.2 Simulation Conditions

For typical daily loading conditions, three loading cases (a one-legged stance, and extreme ranges of motion for both abduction and adduction) were assumed (Beaupré et al. 1990), as shown in Fig. 13.1d, as with the two-dimensional study in Chap. 12. The lower boundary that corresponded to the diaphysis was fixed. The simulation results were discussed only for the proximal region to neglect the artificial influence of the fixed boundary condition.

In simulations based on single loading conditions, the model was coarse-grained and calculated at a resolution of 175 μm/voxel in order to qualitatively determine

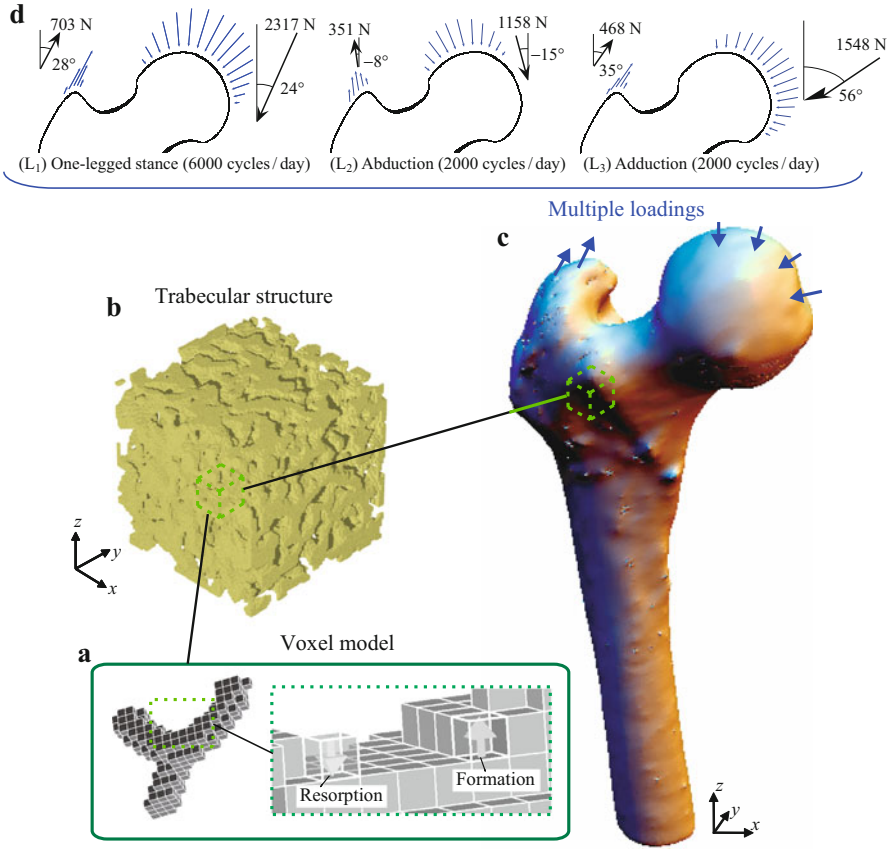

Fig. 13.1 3D simulation model of trabecular structural adaptation in human proximal femur with large-scale voxel FEs. (**a**) The assembly of voxel elements at a resolution that can express the morphologies of individual trabeculae demonstrates the overall morphology of the femur from (**b**) the cancellous bone, to (**c**) the entire femur, discretely. (**d**) External loading conditions applied to the hip joint considering the daily loading history (Beaupré et al. 1990) (This figure was adapted from Tsubota et al. (2009) with permission from Elsevier)

the effects of the loading conditions on the trabecular structure that was formed. In simulations based on multiple loading conditions, the calculations were performed at a resolution of 87.5 μm/voxel with the aim of accurately reproducing the actual trabecular structures in the model; the three loads were applied at a ratio of 3:1:1 (Beaupré et al. 1990), as shown in Fig. 13.1d.

The parameters of the remodeling model (Chap. 9) were set to be constant, with threshold values $\Gamma_u = 0.6$ and $\Gamma_l = -0.4$, and the sensing distance $l_L = 1$ mm, to provide reasonable trabecular structures, which best fit the figures of Wolff (Carter et al. 1987; Wolff 1892, 1986). In simulations of multiple loadings, the stimulus Γ_{mlt} (Eq. 12.1) weighted by the loading frequency (Beaupré et al. 1990) was used for remodeling.

13.3 Trabecular Structures Obtained by Remodeling in a Human Proximal Femur

This section explains the simulation results regarding 3D anisotropic trabecular structure in human proximal femur (Sect. 13.3.1), and functional adaptation of the trabecular structure (Sect. 13.3.2).

13.3.1 Trabecular Structure with 3D Anisotropy

The various trabecular structures of the femoral head under the three single-loading conditions were oriented in the direction of the load applied to the articular surface (Fig. 13.2). The trabecular orientations in the femoral head depended on the loading direction applied to the articular surfaces (white arrows in Fig. 13.2). An orthogonal trabecular pattern appeared in the femoral neck (white circles in Fig. 13.2) in

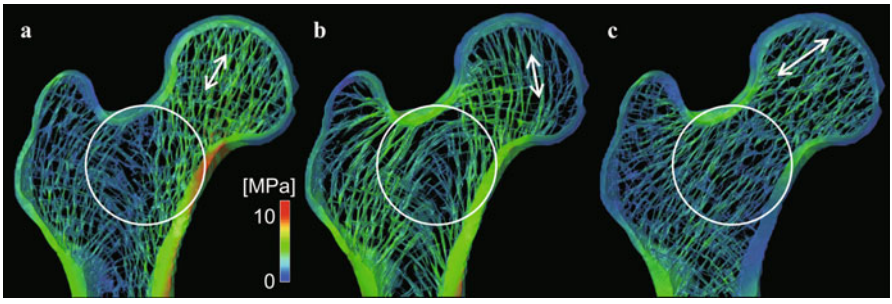

Fig. 13.2 Trabecular structures in the coronal section under loading conditions of (**a**) one-legged stance, (**b**) abduction, and (**c**) adduction, predicted by the remodeling simulation. The color indicates the equivalent stress value of the bone part (This figure was adapted from Tsubota et al. (2009) with permission from Elsevier)

loading cases (a) and (b), because the loading of articular surface causes a bending load in the clockwise direction around the neck. This pattern did not emerge in loading case (c) because the loading of the articular surface oriented to the femoral neck and did not generate bending loads in this region. These results are attributed to the hip joint load determining the cellular-level mechanical stimulus, which changed the trabecular structure accordingly.

In the simulation based on multiple-loading conditions similar to actual loading conditions, the trabecular structure appeared similar to that observed in the cross-sectional photograph of the human proximal femur (Beaupré et al. 1990; Wolff 1892, 1986), as shown in Fig. 13.3. As shown in the coronal section (Fig. 13.3a), the

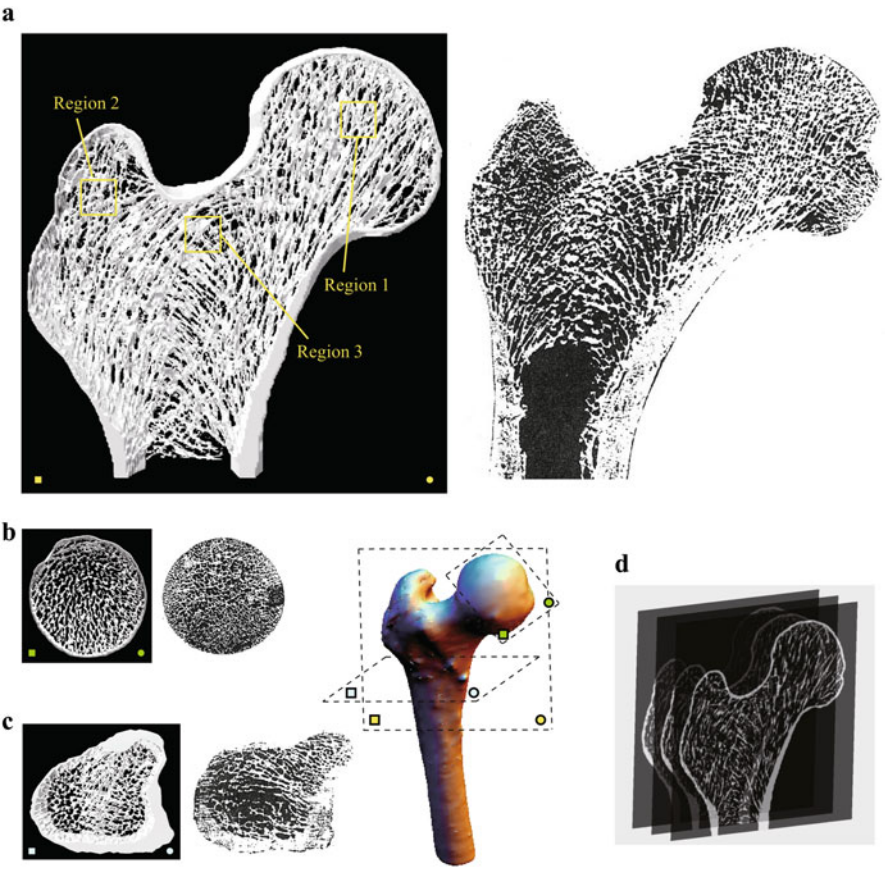

Fig. 13.3 The trabecular structure reproduced by computer simulation (*left*) and a photograph of an actual femur (*right*) from Wolff (1892, 1986). (**a**) The coronal cross-section, (**b**) the cross-section through the middle of the femoral head, and (**c**) the transverse section around the lesser trochanter. (**d**) A series of 2D slices to illustrate the 3D distributed trabecular structure (The proximal femur photograph is used from Wolff (1986) with the kind permission of Prof. Paul Maquet and of Springer Science and Business Media) (This figure was adapted from Tsubota et al. (2009) with permission from Elsevier)

trabecular bone was orientated in the direction of the compressive load applied to the articular surface in the femoral head (region 1), and orientated in the direction of the abduction tensile load in the greater trochanter (region 2). On the other hand, in the area of the femoral neck (region 3), an orthogonal pattern of the trabecular bone formed in the biaxial compression and tension load state in accordance with the bending load. In the cross-section through the middle of the femoral head, (Fig. 13.3b), as well as in the transverse section near the lesser trochanter (Fig. 13.3c), the trabecular structures were more isotropic than those in the coronal section, where an anisotropic structure clearly emerged. These trabecular structures correspond to the mechanical environment of the cross-section, i.e. the mechanical environments in the planes shown in Figs. 13.3b, c are more isotropic than those shown in Fig. 13.3a.

13.3.2 Functional Adaptation of Trabecular Structure

To investigate the functional adaptation of the trabecular structure, which differs by a region of the femur, the trabecular structure and the mechanical state were quantified and compared. The spatial averaged trabecular bone structural characteristics $\boldsymbol{H}$, fabric ellipsoid (Cowin 1985, 1986), and mechanical stress $\boldsymbol{\sigma}$ were calculated for the femoral head region (region 1) and the greater trochanter (region 2), in which a one-directional trabecular pattern was formed, and for the area near the femoral neck, in which an orthogonal pattern was formed (region 3), as shown in Fig. 13.4a–c. These results showed good correspondence between $\boldsymbol{H}$ and $\boldsymbol{\sigma}$, i.e., the principal directions of the trabecular structure $\boldsymbol{H}$ matched those of the principal stress $\boldsymbol{\sigma}$. In the entire proximal femur, the anisotropy of the structural characteristics H_1/H_3 increased with the principal stress ratio $|\sigma_1/\sigma_3|$ (Fig. 13.4d). H_1/H_3 also increased with the anisotropy of the stiffness, indicating that the mechanical characteristics were such that the trabecular bone deforms uniformly (Chap. 11). In this way, bone remodeling based on mechanical stimulus at the cellular level resulted in functional adaptive changes in load support, and quantitatively created a trabecular structure corresponding to the direction and magnitude of $\boldsymbol{H}$ and $\boldsymbol{\sigma}$ (Cowin 1986) in three dimesions. In addition, the relationship between the anisotropy of the structural characteristics H_1/H_3 and the principal stress ratio $|\sigma_1/\sigma_3|$ exhibited a dispersion (Fig. 13.4e). This was due to a lazy zone (dead zone) in which a small mechanical stimulus did not produce a significant remodeling response (Carter 1984), indicating that cellular-level remodeling creates various trabecular structures in a variety of responses to the mechanical environment.

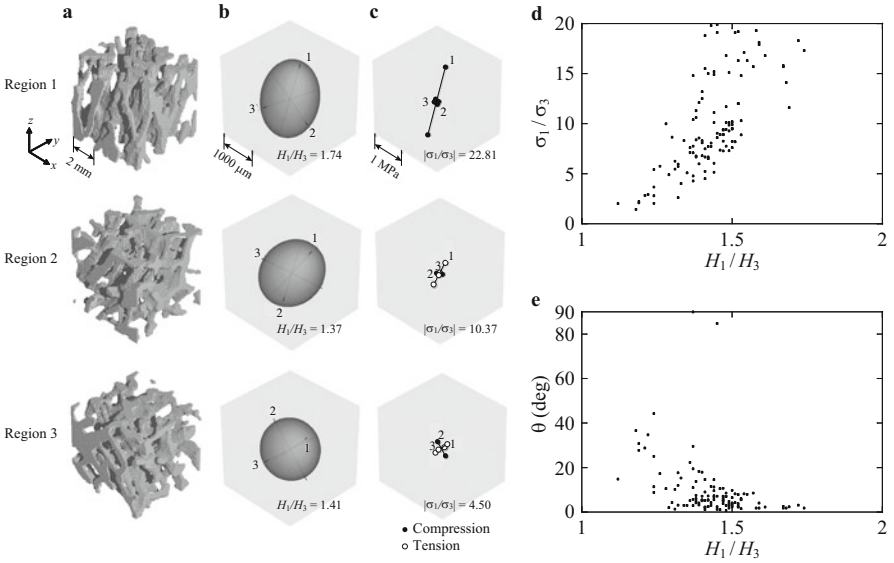

Fig. 13.4 The apparent structural and mechanical properties of cancellous bone. (**a**) The trabecular structure, (**b**) fabric ellipsoid and (**c**) principal stress of the cancellous bone cube in the femoral head (*region 1* of Fig. 13.3a), greater trochanter (*region 2*) and femoral neck (*region 3*). The size of the cancellous bone cube is 6.6 mm on each side. (**d**) The ratio of the maximum principal stress value to the minimum, $|\sigma_1/\sigma_3|$, and (**e**) the difference angle, θ, of the principal directions between the fabric ellipsoid and principal stress as a function of the structural anisotropy H_1/H_3. These plots correspond to 122 sampling bone cubes in the entire proximal femur (This figure was adapted from Tsubota et al. (2009) with permission from Elsevier)

13.3.3 Bone Remodeling in 3D Structural Hierarchy

The simulation results revealed that complex 3D trabecular structures form to adapt to the mechanical environment in accordance with the cellular-level simple remodeling law, which aims to achieve a uniform mechanical stimulus state. This quantifies the series of relations linking cellular-level mechanical stimulus Γ, determined by the mechanical stress $\boldsymbol{\sigma}$ of the trabecular structure, the rate of trabecular surface movement according to the stimulus $\dot{M}(\Gamma)$, and the overall trabecular structure $\boldsymbol{H}$, constructed according to $\dot{M}(\Gamma)$, in three dimensions. These factors are affected by mechanical conditions determined by the trabecular structure, cortical bone structure, loading conditions etc., and the 3D characteristics are essential conditions in each case (Ulrich et al. 1999; van Rietbergen et al. 1999).

The bone structures in the coronal cross-sections predicted by the 3D simulation depend on the loading conditions. The basic characteristics of the structures are

similar to those obtained in the 2D study in Chap. 12. In the remaining cross-sections, the trabecular structure is relatively isotropic, corresponding to the actual femur photograph by Wolff (1892, 1986). Thus, the 3D femur shape, as characterized by the anteversion angle (approximately 10° in this study), would not cause anisotropy of the trabecular structure in the normal state. On the other hand, degrees of anisotropy in the mechanical stress $\boldsymbol{\sigma}$ and trabecular structure $\boldsymbol{H}$ are different from those obtained in the 2D simulation of Chap. 12. For example, in regions 1 and 3, the H_1/H_3 values of the 3D results are larger than those of the 2D, and vice versa in region 2. This demonstrates that in trabecular bone remodeling, the mechanical and structural quantities of 3D differ from those of 2D, suggesting that consideration of the 3D is essential in characterizing of trabecular structural adaptation in a human proximal femur with a hierarchical 3D structure (Lakes 1993).

13.4 Conclusion

In this chapter, trabecular structure adaptation in a human proximal femur was simulated by a large-scale voxel FE model. The simulation results revealed that complex 3D trabecular structures form to adapt to the mechanical environment in accordance with the cellular-level simple remodeling law, which aims to achieve a uniform mechanical stimulus state. This quantifies the series of relations linking cellular-level mechanical stimulus Γ determined by mechanical stress $\boldsymbol{\sigma}$ of the trabecular structure (~10 μm), the rate of trabecular surface movement according to the stimulus $\dot{M}(\Gamma)$, and the overall trabecular structure $\boldsymbol{H}$ (~10 cm), constructed according to $\dot{M}(\Gamma)$, in three dimensions with a length scale greater than 10^4. These factors are affected by mechanical conditions determined by the trabecular structure, cortical bone structure, loading conditions etc., and the 3D characteristics are essential conditions in each case. As a result of contemporary computer simulation, we can quantify and understand the trabecular structure adaptation in a human proximal femur with a hierarchical 3D structure (Boyle and Kim 2011).

References

Beaupré GS, Orr TE, Carter DR (1990) An approach for time-dependent bone modeling and remodeling-application: a preliminary remodeling simulation. J Orthop Res 8(5):662–670. https://doi.org/10.1002/jor.1100080507

Boyle C, Kim IY (2011) Three-dimensional micro-level computational study of Wolff's law via trabecular bone remodeling in the human proximal femur using design space topology optimization. J Biomech 44(5):935–942. https://doi.org/10.1016/j.jbiomech.2010.11.029

Carter DR (1984) Mechanical loading histories and cortical bone remodeling. Calcif Tissue Int 36: S19–S24

Carter DR, Fyhrie DP, Whalen RT (1987) Trabecular bone density and loading history: regulation of connective tissue biology by mechanical energy. J Biomech 20(8):785–794

Cowin SC (1985) The relationship between the elasticity tensor and the fabric tensor. Mech Mater 4(2):137–147. https://doi.org/10.1016/0167-6636(85)90012-2

Cowin SC (1986) Wolff's law of trabecular architecture at remodeling equilibrium. J Biomech Eng 108(1):83–88

Hughes TJR, Ferencz RM, Hallquist JO (1987) Large-scale vectorized implicit calculations in solid mechanics on a Cray X-Mp/48 utilizing Ebe preconditioned conjugate gradients. Comput Method Appl M 61(2):215–248

Huiskes R, Weinans H, Grootenboer HJ, Dalstra M, Fudala B, Slooff TJ (1987) Adaptive bone-remodeling theory applied to prosthetic-design analysis. J Biomech 20(11–12):1135–1150

Jacobs CR, Simo JC, Beaupre GS, Carter DR (1997) Adaptive bone remodeling incorporating simultaneous density and anisotropy considerations. J Biomech 30(6):603–613

Jang IG, Kim IY (2008) Computational study of Wolff's law with trabecular architecture in the human proximal femur using topology optimization. J Biomech 41(11):2353–2361. https://doi.org/10.1016/j.jbiomech.2008.05.037

Lakes R (1993) Materials with structural hierarchy. Nature 361(6412):511–515

Parfitt AM (1994) Osteonal and hemi-osteonal remodeling: the spatial and temporal framework for signal traffic in adult human bone. J Cell Biochem 55(3):273–286. https://doi.org/10.1002/jcb.240550303

Tsubota K, Adachi T, Tomita Y (2002) Functional adaptation of cancellous bone in human proximal femur predicted by trabecular surface remodeling simulation toward uniform stress state. J Biomech 35(12):1541–1551. https://doi.org/10.1016/S0021-9290(02)00173-2

Tsubota K, Suzuki Y, Yamada T, Hojo M, Makinouchi A, Adachi T (2009) Computer simulation of trabecular remodeling in human proximal femur using large-scale voxel FE models: approach to understanding Wolff's law. J Biomech 42(8):1088–1094. https://doi.org/10.1016/j.jbiomech.2009.02.030

Ulrich D, van Rietbergen B, Laib A, Ruegsegger P (1999) The ability of three-dimensional structural indices to reflect mechanical aspects of trabecular bone. Bone 25(1):55–60

van Rietbergen B, Weinans H, Huiskes R, Odgaard A (1995) A new method to determine trabecular bone elastic properties and loading using micromechanical finite-element models. J Biomech 28(1):69–81

van Rietbergen B, Muller R, Ulrich D, Ruegsegger P, Huiskes R (1999) Tissue stresses and strain in trabeculae of a canine proximal femur can be quantified from computer reconstructions. J Biomech 32(4):443–451

Wolff J (1892) Das Gesetz Der Transformation Der Knochen. Hirschwald, Berlin

Wolff J (1986) The law of bone remodeling (trans: Maquet P, Furlong R). Springer, New York

Chapter 14
Trabecular Structural Changes in a Vertebral Body with a Fixation Screw

Abstract This chapter describes the effects of a spinal fixation screw on trabecular structural changes in a vertebral body, predicted by a three-dimensional simulation of trabecular remodeling. The entire vertebral body with a fixation screw and bone-screw interface were modeled using voxel finite elements. In the vertebral body, the implantation of the fixation screw caused a change in the mechanical environment of the cancellous bone, leading to trabecular structural changes at the cancellous bone level. The effects of the screw on the trabecular orientation were stronger in the regions above and below the screw compared to those in front of the screw. In the proximity of the bone-screw interface, the trabecular structural changes depended on the direction of the load applied to the screw. The bone resorption, predicted in the pull-out loading, is a candidate cause of screw loosening. The results indicate that the effects of implanted screws on trabecular structural changes are more important for long-term fixation.

Keywords Bone structural adaptation • Trabecular surface remodeling • Spinal fixation • Bone implant • Voxel FE model

14.1 Introduction

To predict and evaluate the trabecular structural changes by bone remodeling, computational simulation methods have been used as a powerful tool in the orthopaedic and orthodontics fields (Huiskes and Hollister 1993; Prendergast 1997; Hasegawa et al. 2016). To date, simulations of remodeling, based on the macroscopic continuum model, have predicted changes in the apparent bone density around the hip joint stem (Doblare and Garcia 2001; Huiskes et al. 1987; van Rietbergen et al. 1993) and knee prosthesis (Orr et al. 1990). Furthermore, surface remodeling simulations have been used for predicting trabecular microstructural changes at screw threads and on porous coated surfaces of bone implants (Luo et al. 1999; Sadegh et al. 1993). These computational methods are also applicable to the design of bone implants with desired shapes, where remodeling-induced bone structural changes are taken into consideration (Kuiper and Huiskes 1997).

This Chapter was adapted from Tsubota et al. (2003) with permission from Springer.

Y. Kameo et al., *Bone Adaptation*, Frontiers of Biomechanics 2,
https://doi.org/10.1007/978-4-431-56514-7_14

For spinal fixation with a screw, the biomechanical viewpoint is important in order to avoid loosening of a fixation screw and to attain mechanical stability of the reconstructed spinal structure (McCullen and Garfin 2000; Vaccaro and Garfin 1995). As a candidate mechanism underlying screw loosening, fatigue fracture of the bone at the bone-screw interface has been investigated using a quantitative experimental technique. On the contrary, mechanical remodeling-induced bone structural changes have been suggested to play an important role in the loosening phenomenon (Dalenberg et al. 1993; Lu et al. 2000).

In this chapter, the effects of a fixation screw on three-dimensional trabecular structural changes in a vertebral body were investigated using computer simulations of the trabecular surface remodeling. First, a remodeling simulation was conducted for a vertebral body, for examining the effects of the implanted screw on structural changes occurring on level of the cancellous bone. Second, trabecular microstructural changes in the proximity of the bone-screw interface were simulated for investigating the relationships between the screw loosening and the loads applied to the screw. Third, referring to the simulation results, important mechanical factors related to the screw implantation are discussed from the viewpoint of mechanical bone remodeling.

14.2 Model of a Vertebral Body with a Fixation Screw

The entire vertebral body and bone-screw interface were modeled using voxel finite elements (FEs) to simulate trabecular remodeling of the cancellous bone. Simulation models (Sects. 14.2.1 and 14.2.2), simulation conditions (Sect. 14.2.3), and data analysis methods (Sect. 14.2.4) are described below.

14.2.1 Model of an Entire Vertebral Body with a Fixation Screw

Spinal fixation screws, such as those used in internal fixation for fusion (McCullen and Garfin 2000; Vaccaro and Garfin 1995) and in total *en bloc* spondylectomy for vertebral tumors (Tomita et al. 1997), play an important role in maintaining the mechanical integrity of the reconstructed spinal structure. In this study, a half-model of a human L3 vertebral body with a fixation screw (model S) was created using approximately 0.79 million voxels as finite elements, as shown in Fig. 14.1, by assuming structural symmetry with respect to the central sagittal plane. The model consisted of the cortical bone, the cancellous bone, and a fixation screw. The cortical and cancellous bone parts were taken from the model of a normal vertebral body (model N), described in Appendix. The model vertebral body had a diameter of 50 mm in the bilateral and anteroposterior directions, and a height of 25 mm in

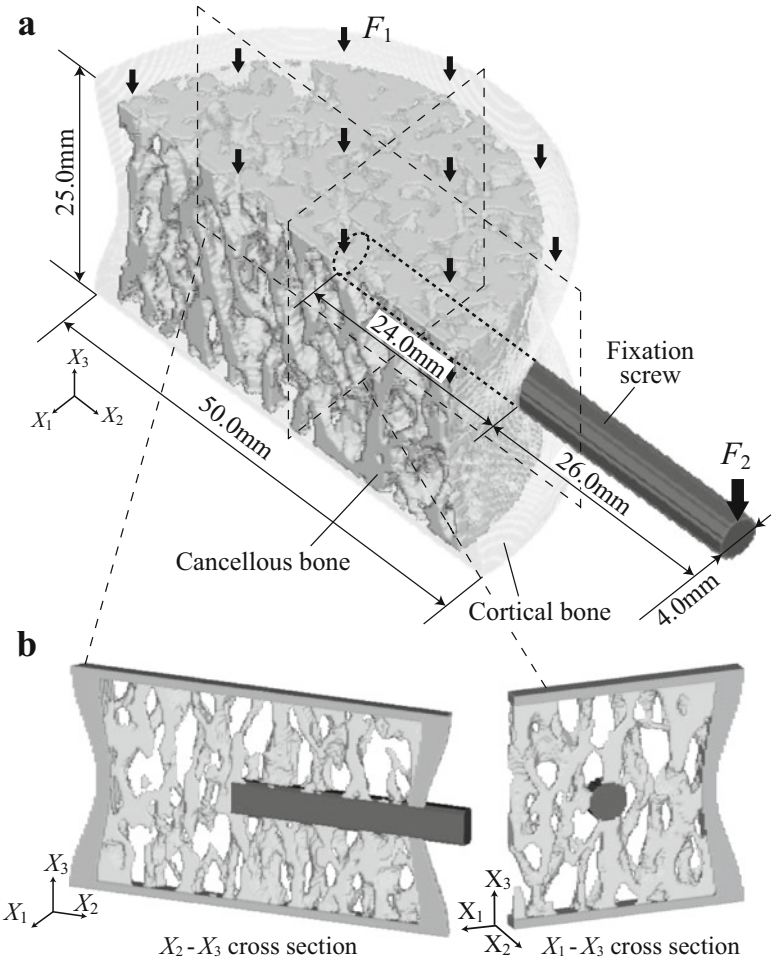

Fig. 14.1 Voxel finite element model of half of the vertebral body with a fixation screw (model S), assumed to be symmetric with respect to the central sagittal plane. (**a**) An overview of the model and the loading condition and (**b**) the $X_2 - X_3$ and $X_1 - X_3$ cross-sections (This figure was adapted from Tsubota et al. (2003) with permission from Springer)

the axial direction, as shown in Fig. 14.1a. The X_1 axis corresponded to the bilateral direction, the X_2 axis to the anteroposterior direction, and the X_3 axis to the axial direction. The initial trabecular structure was taken from the trabecular remodeling simulation of a normal vertebra, described in Appendix. The trabeculae were aligned along the axial direction based on the compressive load of the body weight, as shown in the images of $X_2 - X_3$ and $X_1 - X_3$ cross-sections in Fig. 14.1b. The screw diameter was 4 mm, and the screw length was 50 mm, of which 24 mm was implanted into the vertebral body. The volume of each element was 250 μm × 250 μm × 250 μm.

As a boundary condition of the vertebral body under the compressive load of the body weight, a uniform compressive displacement U_3 was applied to the upper plane at $X_3 = 25$ mm to apply the total load $F_1 = 588$ N, as shown in Fig. 14.1a. The lower plane at $X_3 = 0$ mm was fixed. When a compressive load is applied to the vertebral body, the displacement constraint U_3 is equivalent to the force constraint F_1, which is advantageous for computational efficiency, especially when performing large-scale finite element simulations (Hughes et al. 1987; van Rietbergen et al. 1995). As the load transferred from the fixation device, the bending load $F_2 = 58.8$ N was applied to the end of the screw. The bone and the screw were assumed to be homogeneous and isotropic materials, and Young's modulus E and Poisson's ratio ν were set to $E_t = 20$ GPa and $\nu_t = 0.3$ for the bone, and $E_s = 200$ GPa and $\nu_s = 0.29$ for the screw, which was assumed to be made of stainless steel (An 1999; Zioupos et al. 1999).

14.2.2 Model of the Bone-Screw Interface

The trabecular structure adjacent to the bone-screw interface is important for the proper fixation of a screw to the cancellous bone (Orr et al. 1990). As a model of the bone-screw interface, a $7 \times 7 \times 14$ mm^3 cancellous bone hexahedron was created (model I) using approximately 0.91 million voxels, as shown in Fig. 14.2a, in which the volume of each voxel was 70 μm×70 μm×70 μm. The cancellous bone part of model I was filled with toroidal trabeculae by assuming that the initial trabecular structure was isotropic. The external and root diameters of the screw were 4.9 mm and 3 mm, respectively, and the pitch was 1.8 mm. The coordinate axes were set as shown in Fig. 14.2a, in which the X_2 axis corresponded to the screw axis.

Assuming the screw was subjected to the body weight and pull-out load, two cases of simple loading, namely, compressive loading (Ic) and shear loading (Is), were considered in the remodeling simulations, as shown in Fig. 14.2b. As a boundary condition, uniform compressive displacement along the X_3 axis was applied to the upper surface of the screw in case Ic, while uniform shear displacement along the X_2 axis was applied in case Is, as shown in Fig. 14.2b. The displacements were controlled for applying an apparent stress of 1 MPa to the upper plane of the screw. The displacement constraint was advantageous for saving computational efficiency of the finite element analysis. On the bottom and side planes of the cancellous bone, shear-free boundary conditions were applied; in other words, the displacements normal to the plane were fixed. In what follows, we disregard the artefacts associated with the model boundary conditions and only discuss the simulation results for the internal region of the finite element model, delineated by the white box in Fig. 14.2a.

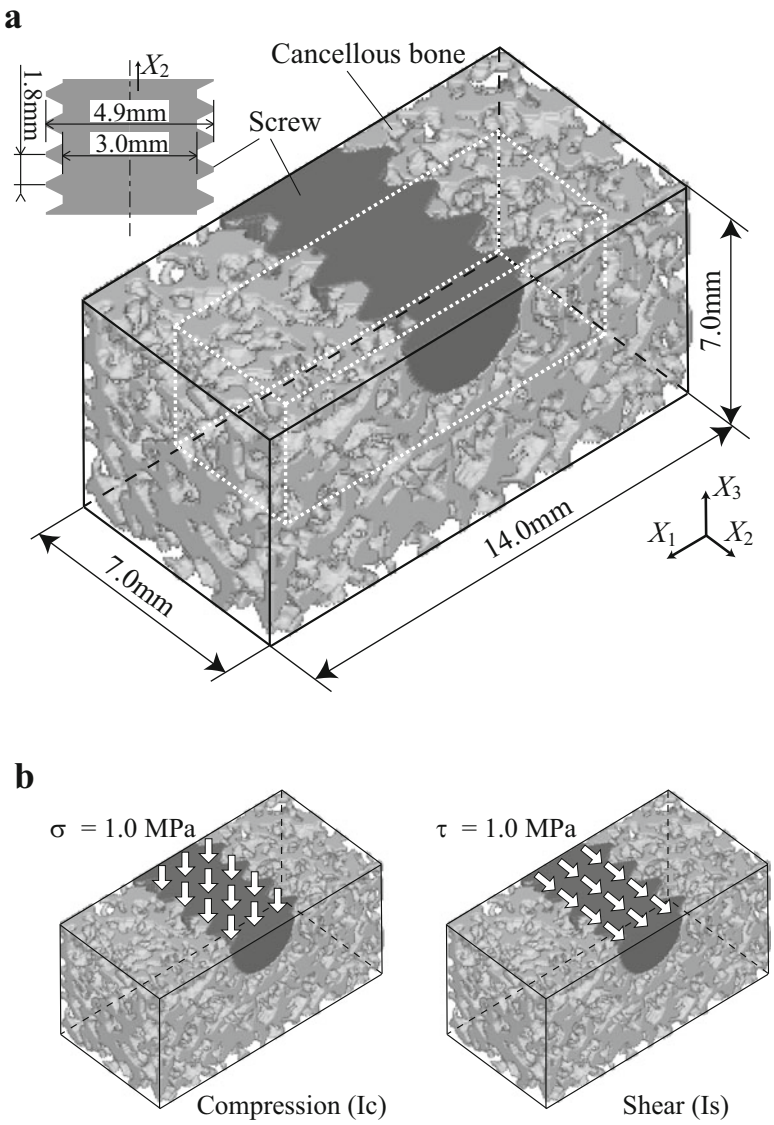

Fig. 14.2 Voxel finite element model of cancellous bone adjacent to the bone-screw interface (model I). (**a**) An overview of the model and (**b**) the two cases of simple loading, compression (Ic) and shear (Is), applied to the screw (This figure was adapted from Tsubota et al. (2003) with permission from Springer)

14.2.3 Simulation Conditions

For models S and I, trabecular structural changes were simulated using the surface remodeling simulation method in Chaps. 8 and 11. The model parameters in the remodeling model (Chaps. 8 and 9) were set constant as threshold values $\Gamma_u = 1.0$ and $\Gamma_l = -1.25$, and sensing distance $l_L = 2.5$ mm for model S, and $\Gamma_u = 1.5$, $\Gamma_l = -1.88$, and $l_L = 700$ μm for model I. With regard to the bone-screw interface in the stress analysis, it was assumed that the tensile load normal to the interface was not transferred from the screw to the bone.

14.2.4 Data Analysis

The simulation results were evaluated for regions F (in front of the screw tip), A (above the screw), and B (below the screw) for model S (Fig. 14.3), and regions C (below the screw), S1 (on the negative side on the X_1 axis), and S2 (on the positive side) for model I (Figs. 14.4 and 14.5). In these regions, a fabric ellipsoid (Cowin 1985) was measured as an anisotropic structural parameter. The degree of structural anisotropy was defined as the ratio of the maximum principal value of the fabric ellipsoid H_1 to the minimum value H_3. The trabecular orientation angle Θ_i $(i = 1, 2, 3)$ was defined as the angle between the maximum principal direction of the fabric ellipsoid $\boldsymbol{n}^{H_1}$ and the coordinate axis X_i. For model I, the contact area between the bone and the screw threads S, normalized by the initial contact area S_0, was measured for determining the structural changes in the trabeculae adjacent to the screw threads (Fig. 14.6).

14.3 Trabecular Structural Changes Induced by the Screw Implantation

This section describes the simulation results related to the trabecular structural changes (1) on the cancellous bone level, induced by the screw implantation (Sect. 14.3.1) and (2) on the trabecular level, at the bone-screw interface (Sect. 14.3.2).

14.3.1 Structural Changes on the Cancellous Bone Level

In the case of a vertebral body with a fixation screw (model S), the trabeculae adapted their structure to the mechanical environment that was changed by the implanted screw, as shown in Fig. 14.3. The load applied to the end of the screw

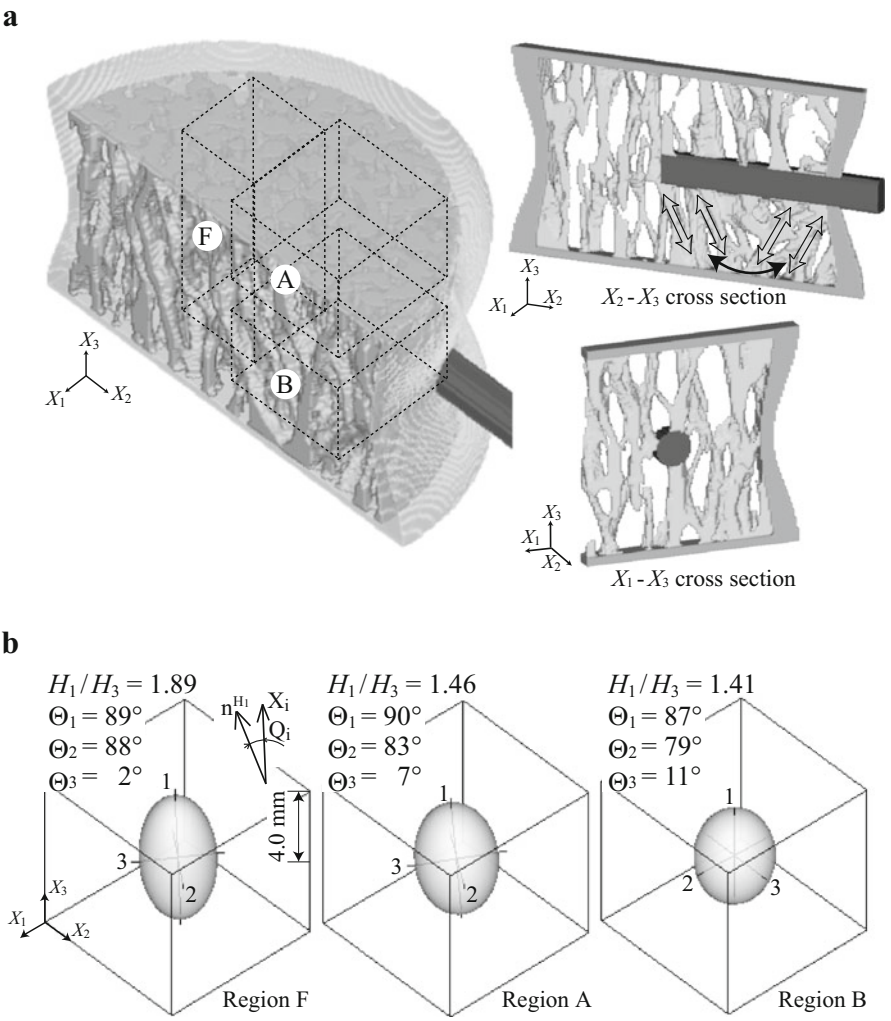

Fig. 14.3 Trabecular structural changes in a vertebral body with a fixation screw (model S) obtained from the simulation. (**a**) A three-dimensional image and the $X_2 - X_3$ and $X_1 - X_3$ cross-sections. (**b**) The fabric ellipsoids of the trabecular structure in regions F, A, and B (This figure was adapted from Tsubota et al. (2003) with permission from Springer)

induced larger trabecular structural changes in regions A and B than in region F, where the effect of the screw on the mechanical environment was smaller.

In region F, the trabeculae grew thick in the axial direction and were resorbed in the transverse direction owing to the compressive load of the body weight, as shown in the image of the $X_2 - X_3$ cross-section in Fig. 14.3a. The degree of structural anisotropy H_1/H_3 and the trabecular orientation angle Θ_i $(i = 1, 2, 3)$ were $H_1/H_3 = 1.89$ and $(\Theta_1, \Theta_2, \Theta_3) = (89^\circ, 88^\circ, 2^\circ)$, respectively. The structural

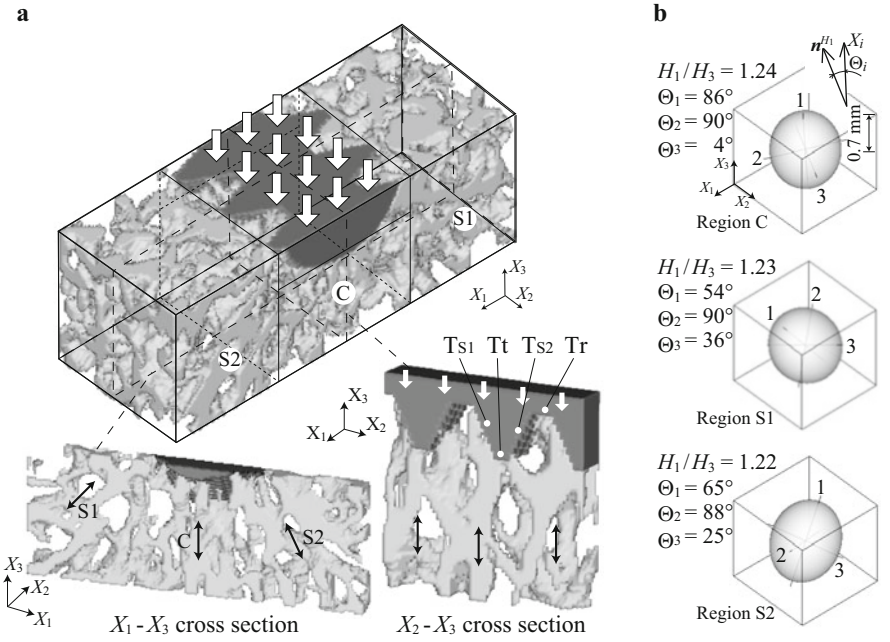

Fig. 14.4 Trabecular structural changes adjacent to the bone-screw interface under compressive load (case Ic). (**a**) A three-dimensional image and the $X_1 - X_3$ and $X_2 - X_3$ cross-sections. (**b**) The fabric ellipsoids of the trabecular structure in regions C (below the screw), S1 (on the negative side on the X_1 axis), and S2 (on the positive side) (This figure was adapted from Tsubota et al. (2003) with permission from Springer)

parameters and the fabric ellipsoid in Fig. 14.3b indicates that the trabeculae in region F are oriented along the axial direction.

The degree of structural anisotropy H_1/H_3 and the trabecular orientation angle Θ_i were, respectively, $H_1/H_3 = 1.46$ and $(\Theta_1, \Theta_2, \Theta_3) = (90^\circ, 83^\circ, 7^\circ)$ in region A, and $H_1/H_3 = 1.41$ and $(\Theta_1, \Theta_2, \Theta_3) = (87^\circ, 79^\circ, 11^\circ)$ in region B. In these two regions, the structural parameter H_1/H_3 was smaller and Θ_3 was larger than the corresponding parameter values in region F. This result shows that the trabecular structure is more distributed in regions A and B than in region F. For example, the trabeculae in region B were formed both from the screw tip and from the pedicle to the lower cortical shell, as indicated by the open arrows in the image of the $X_2 - X_3$ cross-section in Fig. 14.3a. Part of these trabeculae connected with each other and formed an arcuate structure, as indicated by the closed arrow in the image of the $X_2 - X_3$ cross-section in Fig. 14.3a.

Because changes in the trabecular orientation affect the mechanical integrity of the vertebral body, the simulation method is likely to be useful for evaluating trabecular bone remodeling-induced temporal changes in the mechanical integrity of a vertebral body with an implanted screw.

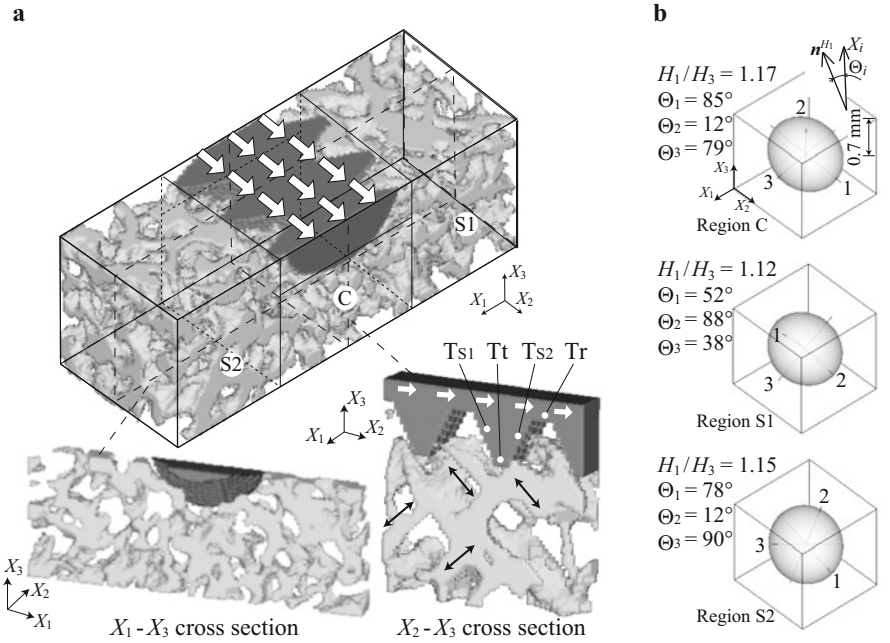

Fig. 14.5 Trabecular structural changes adjacent to the bone-screw interface in the case of shear loading (case Is). (**a**) A three-dimensional image and the $X_1 - X_3$ and $X_2 - X_3$ cross-sections. (**b**) The fabric ellipsoids of the trabecular structure in regions C, S1, and S2 (This figure was adapted from Tsubota et al. (2003) with permission from Springer)

14.3.2 Trabecular Level Structural Changes at the Bone-Screw Interface

In the case of the bone-screw interface (model I), the isotropic trabecular structure shown in Fig. 14.2a changed to the anisotropic one shown in Figs. 14.4 and 14.5. The extent of surface remodeling of the trabecular structure depended on the loads applied to the screw.

In the case of compressive loading (Ic), the trabeculae were aligned along the direction of compressive load below the screw, as indicated by the arrows in the image of the $X_2 - X_3$ cross-section in Fig. 14.4a, and were formed radially from the screw, as indicated by the arrows in the $X_1 - X_3$ cross-section image. The degree of structural anisotropy H_1/H_3 and trabecular orientation angle Θ_i $(i = 1, 2, 3)$ were $H_1/H_3 = 1.24$ and $(\Theta_1, \Theta_2, \Theta_3) = (86^\circ, 90^\circ, 4^\circ)$ in region C, $H_1/H_3 = 1.23$ and $(\Theta_1, \Theta_2, \Theta_3) = (54^\circ, 90^\circ, 36^\circ)$ in region S1, and $H_1/H_3 = 1.22$ and $(\Theta_1, \Theta_2, \Theta_3) = (65^\circ, 88^\circ, 25^\circ)$ in region S2, as shown in Fig. 14.4b. This result shows that different regions have the same degree of structural anisotropy but different structural orientation.

In the case of shear loading (Is), some of the trabeculae below the screw were aligned along the directions oriented at 45° relative to the shear load, as indicated by the arrows in the image of the $X_2 - X_3$ cross-section in Fig. 14.5a. The degree of structural anisotropy H_1/H_3 and the trabecular orientation angle Θ_i were, respectively, $H_1/H_3 = 1.17$ and $(\Theta_1, \Theta_2, \Theta_3) = (85^\circ, 12^\circ, 79^\circ)$ in region C, $H_1/H_3 = 1.12$ and $(\Theta_1, \Theta_2, \Theta_3) = (52^\circ, 88^\circ, 38^\circ)$ in region S1, and $H_1/H_3 = 1.15$ and $(\Theta_1, \Theta_2, \Theta_3) = (78^\circ, 12^\circ, 90^\circ)$ in region S2, as shown in Fig. 14.5b. The smaller H_1/H_3 values obtained in this case (compared with Ic) indicate a more distributed trabecular structure, as shown in the image of the $X_1 - X_3$ cross-section in Fig. 14.5a.

The change in the contact area S/S_0 depended on the site of the screw threads, as shown in Fig. 14.6. In the Ic case, the contact area S/S_0 increased after initially decreasing at the top of the screw threads (Tt), and decreased on both sides (T_{s1} and T_{s2}) and at the root (Tr), as shown in Fig. 14.6a. In the Is case, the entire contact area S/S_0 decreased, as shown in Fig. 14.6b. The rates of decrease in the contact area

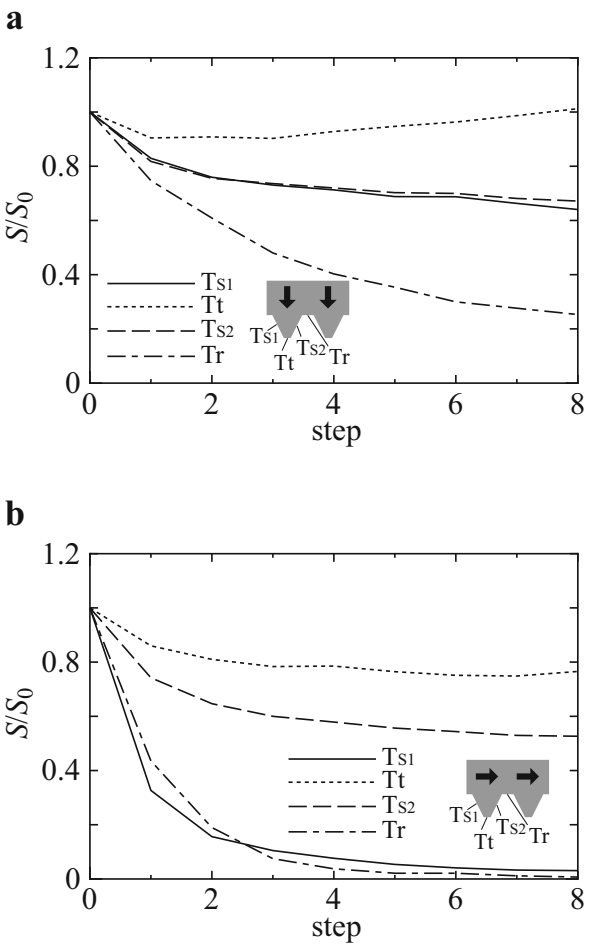

Fig. 14.6 Change in the contact area S/S_0 between the screw threads and the trabeculae for the bone-screw interface (model I), for the cases of (**a**) compressive load (Ic) and (**b**) shear load (Is) (This figure was adapted from Tsubota et al. (2003) with permission from Springer)

S/S_0 at the root (Tr) and on the tensile side (T_{s1}) were higher than those at the top (Tt) and on the compressive side (T_{s2}), and the areas S/S_0 at Tr and T_{s1} were zero in the final state.

While the trabeculae remained near the screw threads with compressive load (case Ic), the bone was resorbed on the tensile side (T_{s1}) and at the root (Tr) of the threads with shear load (case Is). These results show that the direction of the load applied to the screw is one of the critical factors in determining bone resorption at the bone-screw interface, and that pull-out loading is a candidate cause of screw loosening. The bone resorption predicted by the simulation depended on the site of the screw threads, which indicates that the screw threads are important in the remodeling-induced loosening of the fixation screw. In fact, the remodeling simulation by using model S did not predict any trabecular structural changes that would cause screw loosening, because the screw threads were not modeled in detail. In addition, the temporal evolution of the structural changes, as shown in Fig. 14.6, demonstrates that remodeling around the spinal fixation screw is more important for longer-term fixation.

14.4 Trabecular Structural Changes as Causes of Screw Loosening

Trabecular structural changes induced by mechanical bone remodeling were suggested to be important for the proper fixation of bone implants, such as hip joint stems in the proximal femur (Doblare and Garcia 2001; Huiskes et al. 1987; van Rietbergen et al. 1993) and dental implants in the mandible (Stanford and Brand 1999). However, it has not been reported whether the trabecular structure changes when a fixation screw is implanted into a vertebral body. One reason is the difficulty associated with simultaneously observing the trabecular structural changes around the fixation screw *in vivo* and simulating the trabecular structural changes around the screw, by using previously developed computational techniques. In this study, the trabecular structural changes around the screw were simulated using voxel finite element models of trabecular surface remodeling. By using the model S for a vertebral body with a fixation screw, we were able to predict changes in the trabecular orientation in the pedicle region induced by changes in the mechanical environment caused by the implanted screw. Because a change in the trabecular orientation affects the mechanical integrity of the vertebral body, the simulation method is likely to be useful for evaluating trabecular bone remodeling-induced temporal changes in the mechanical integrity of a vertebral body with a screw.

Model S was constructed for investigating the basic effects of the screw implantation on the trabecular structural changes in the vertebral body. For accurate prediction of the trabecular structural changes in the future, it is necessary to develop a model of the ligamentous motion segment in which intervertebral discs

play an important role in transferring the body weight to the vertebral body. For example, if a model of intervertebral discs that consist of annulus fibrosus and nucleus pulposus is developed to precisely capture the vertebral body loading conditions, the predicted trabecular structural changes by using model N for a normal vertebral model (see Appendix. 14.A) would be smaller in the pedicle part than in the central part, as was predicted by Goel et al. (1995). This might lead to the formation of denser trabeculae at the vertebral body center after implanting the fixation screw, because the trabeculae in the pedicle region will provide less support to the load applied to the screw, compared with the trabeculae in the central region.

For model I, the initial trabecular structure was isotropic rather than anisotropic one that was used in model S. The loading conditions that were applied to the screw corresponded to the two cases of simple loading, namely, compressive and shear loading. Despite these simplifications, the bone resorption around the screw thread, observed in the Is case, indicates that the stress-shielding phenomenon can occur in a vertebral body with a fixation screw, as well as in the case of other bone implants (Stanford and Brand 1999; van Rietbergen et al. 1993). The effects of structural anisotropy and realistically complex loading conditions will be taken into account by coupling the two models S and I (describing different structural scales) in future work.

Based on the previous experimental and computational studies of trabecular structural changes around implants (Guldberg et al. 1997; van Rietbergen et al. 1993), the structural changes obtained in the present study can be thought of as occurring on the temporal scale ranging from a few months to a few years. On this time scale, it would be necessary, in spinal fixation, to consider trabecular remodeling, for evaluating the vertebral body with the fixation screw as a load-bearing structure. For example, an experimental result obtained using a canine spine surgery model, in which L1-L5 were immobilized for 9 months by using an instrument with transpedicular screws placed bilaterally at the L1, L3 and L5 pedicles, indicated that loosening of the screw was more pronounced for L1 and L5 than for L3 (Dalenberg et al. 1993). In the immobilized spinal structure, the screws at L1 and L5 outside of the instrument are more affected by the bending load transferred from the fixation device than those placed at L3 in the middle of the instrument. Because the bending load of the screw would cause a pull-out load of the screw, screw loosening at the L1 and L5 obtained in the animal experiment might be owing to the pull-out load applied to the screw. This point corresponds to the simulation result of model I for the bone-screw interface, which indicates that the pull-out load is a candidate cause of the screw loosening.

The simulation method that uses the voxel model is effective for predicting patient-specific remodeling phenomena, the voxel model of the bone structure can be easily constructed from medical imaging data (van Rietbergen et al. 1998; Hasegawa et al. 2016). Thus, the voxel-based simulation method is likely to enable testing various combinations of bone and spinal fixation screws, and can provide useful information for choosing the screw type. In addition, considering that voxel models of a musculoskeletal system, including that of a spinal system, can be

constructed using recently developed imaging techniques (Beuf et al. 2001; Zankl and Wittmann 2001), voxel models of a bone-implant system for various types of implants can be constructed by superimposition of the digital implant data (that is, CAD data) on the spinal voxel model. With this voxel model, the remodeling simulation method is likely to be useful for designing patient-specific spinal fixation systems. Combining the bone remodeling simulations that use the voxel model with advanced techniques for medical imaging and structural optimization is likely to provide a novel computational design system for bone-implant devices.

14.5 Conclusion

In this chapter, fixation screw implantation-induced trabecular structural changes in a vertebral body were investigated by conducting 3D trabecular surface remodeling simulations. By using voxel FEs, computational models of the bone and screw were constructed on two structural scales of the entire vertebral body with the implanted screw and the bone-screw interface. In the simulation of the entire vertebral body, the implantation of the fixation screw induced changes in the mechanical environment of the cancellous bone, leading to trabecular structural changes at the cancellous bone level. The effects of the screw on trabecular orientation were more significant in the regions above and below the screw compared with those in front of the screw. In the case of the bone-screw interface, trabecular structural changes depended on the direction of the load applied to the screw. It was suggested that the bone resorption predicted in the pull-out loading case is a candidate mechanism of screw loosening. The results indicate that the effects of implanted screws on trabecular structural changes are more important for longer-term fixation.

Appendix: Cancellous Bone Remodeling in a Normal Vertebral Body

In the case of a normal vertebral body, the trabecular surface remodeling simulation was conducted using a half-voxel model of a human L3 vertebral body (model N), as shown in Fig. 14.7a. The cortical shape of the model in the midsagittal plane was determined based on the photograph of the cross-section of the human vertebral body, available in the literature (Mosekilde 1990), as shown in Fig. 14.7b. Rotating the midsagittal section with regard to the central longitudinal axis, the three-dimensional shape of the cortical bone was constructed as an axisymmetric shell. The vertebral body diameter was 50 mm in the bilateral and anteroposterior directions, and its height was 25 mm in the axial direction.

The cancellous bone part was filled with toroidal trabeculae to a bone volume fraction of $BVF = 0.46$ and the degree of structural anisotropy of $H_1/H_3 = 1.04$, in

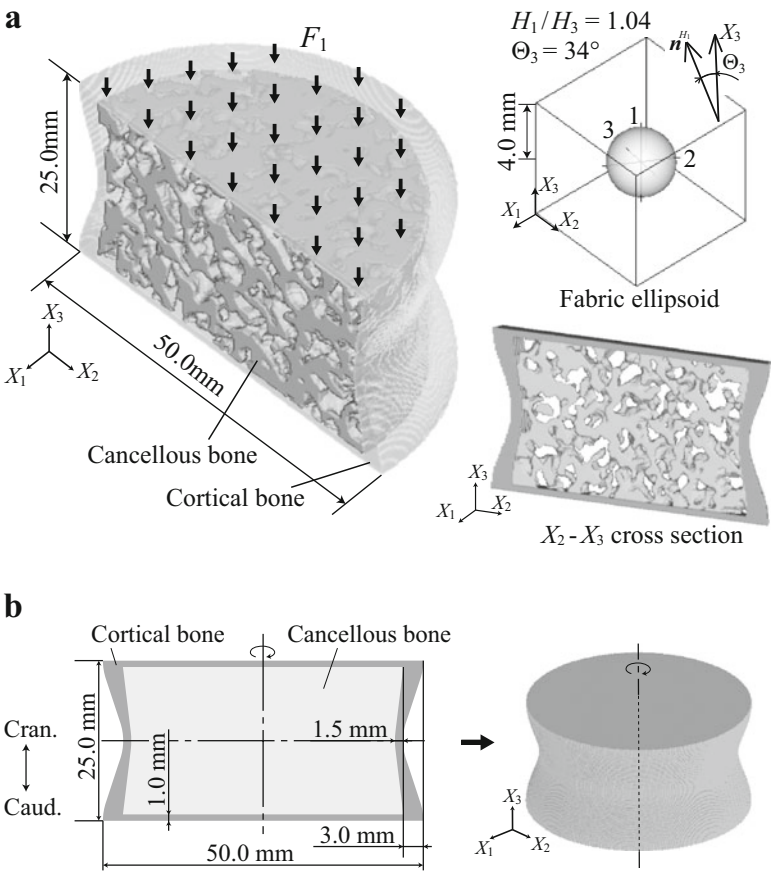

Fig. 14.7 Voxel finite element model of half of a normal vertebral body (model N), assumed to be symmetric with respect to the central sagittal plane. (**a**) A three-dimensional image and compressive loading condition owing to the body weight (*left*), the fabric ellipsoid of the trabecular structure (*top right*), and the $X_2 - X_3$ cross-section (*bottom right*). (**b**) The shapes of the cortical and cancellous bones, constructed by rotating the midsagittal section (This figure was adapted from Tsubota et al. (2003) with permission from Springer)

which H_1 and H_3 were the maximum and minimum principal values of the fabric ellipsoid (Cowin 1985), respectively. As indicated by the fabric ellipsoid and by the image of the $X_2 - X_3$ cross-section in Fig. 14.7a, the trabecular structure was initially isotropic. The number of voxels for describing the bone was approximately 0.85 million, and the volume of each element was 250 μm × 250 μm × 250 μm. The bone part was assumed to be homogeneous and isotropic, and Young's modulus E and Poisson's ratio ν were set as $E_b = 20$ GPa and $\nu_b = 0.3$ (An 1999; Zioupos et al. 1999). As a boundary condition, uniform compressive displacement U_3 was applied to the upper plane at $X_3 = 25$ mm to apply the total load $F_1 = 588$ N as a body weight. The lower plane at $X_3 = 0$ mm was fixed. The model

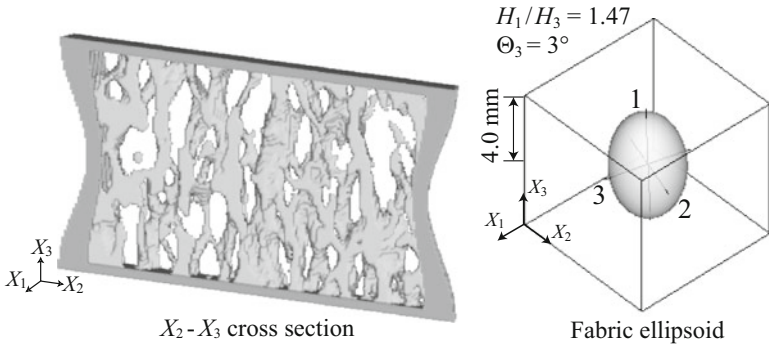

Fig. 14.8 Trabecular structure in a normal vertebral body (model N) obtained from the remodeling simulation: the $X_2 - X_3$ cross-section (*left*) and the fabric ellipsoid (*right*) (This figure was adapted from Tsubota et al. (2003) with permission from Springer)

parameters in the remodeling rate equation (Chap. 9) were set constant as threshold values $\Gamma_u = 1.0$ and $\Gamma_l = -1.25$, and the sensing distance was $l_L = 2.5$ mm.

In remodeling simulation, an anisotropic trabecular structure was obtained owing to the trabecular formation and resorption for converging to a local state of uniform stress, as indicated by the image of the $X_2 - X_3$ cross-section and fabric ellipsoid of the trabecular structure in Fig. 14.8. The angle Θ_3 between the maximum principal direction of the fabric ellipsoid and the X_3 axis was 3°, consistent with the observation that the trabeculae in the vertebral body are oriented along the axial direction (Mosekilde 1990). The bone volume fraction *BVF* decreased to 0.37, and the degree of structural anisotropy H_1/H_3 increased to 1.47. The structural parameters *BVF* and H_1/H_3 obtained in the simulation better captured the experimental observation (Beuf et al. 2001) than the parameters of the initial isotropic structure.

References

An YH (1999) Mechanical properties of bone. In: An H, Draughn RA (eds) Mechanical testing of bone and the bone-implant Interface. CRC, Boca Raton

Beuf O, Newitt DC, Mosekilde L, Majumdar S (2001) Trabecular structure assessment in lumbar vertebrae specimens using quantitative magnetic resonance imaging and relationship with mechanical competence. J Bone Miner Res 16(8):1511–1519. https://doi.org/10.1359/jbmr.2001.16.8.1511

Cowin SC (1985) The relationship between the elasticity tensor and the fabric tensor. Mech Mater 4(2):137–147. https://doi.org/10.1016/0167-6636(85)90012-2

Dalenberg DD, Asher MA, Robinson RG, Jayaraman G (1993) The effect of a stiff spinal implant and its loosening on bone mineral content in canines. Spine (Phila Pa 1976) 18(13):1862–1866

Doblare M, Garcia JM (2001) Application of an anisotropic bone-remodelling model based on a damage-repair theory to the analysis of the proximal femur before and after total hip replacement. J Biomech 34(9):1157–1170

Goel VK, Ramirez SA, Kong W, Gilbertson LG (1995) Cancellous bone Young's modulus variation within the vertebral body of a ligamentous lumbar spine–application of bone adaptive remodeling concepts. J Biomech Eng 117(3):266–271

Guldberg RE, Richards M, Caldwell NJ, Kuelske CL, Goldstein SA (1997) Trabecular bone adaptation to variations in porous-coated implant topology. J Biomech 30(2):147–153

Hasegawa M, Adachi T, Takano-Yamamoto T (2016) Computer simulation of orthodontic tooth movement using CT image-based voxel finite element models with the level set method. Comput Methods Biomech Biomed Eng 19(5):474–483. https://doi.org/10.1080/10255842.2015.1042463

Hughes TJR, Ferencz RM, Hallquist JO (1987) Large-scale vectorized implicit calculations in solid mechanics on a Cray X-Mp/48 utilizing Ebe preconditioned conjugate gradients. Comput Method Appl M 61(2):215–248

Huiskes R, Hollister SJ (1993) From structure to process, from organ to cell: recent developments of FE-analysis in orthopaedic biomechanics. J Biomech Eng 115(4B):520–527

Huiskes R, Weinans H, Grootenboer HJ, Dalstra M, Fudala B, Slooff TJ (1987) Adaptive bone-remodeling theory applied to prosthetic-design analysis. J Biomech 20(11–12):1135–1150

Kuiper JH, Huiskes R (1997) Mathematical optimization of elastic properties: application to cementless hip stem design. J Biomech Eng 119(2):166–174

Lu WW, Zhu Q, Holmes AD, Luk KD, Zhong S, Leong JC (2000) Loosening of sacral screw fixation under in vitro fatigue loading. J Orthop Res 18(5):808–814. https://doi.org/10.1002/jor.1100180519

Luo G, Sadegh AM, Alexander H, Jaffe W, Scott D, Cowin SC (1999) The effect of surface roughness on the stress adaptation of trabecular architecture around a cylindrical implant. J Biomech 32(3):275–284

McCullen GM, Garfin SR (2000) Spine update: cervical spine internal fixation using screw and screw-plate constructs. Spine (Phila Pa 1976) 25(5):643–652

Mosekilde L (1990) Age-related loss of vertebral trabecular bone mass and structure–biomechanical consequences. In: Mow VC, Ratcliffe A, Woo SL-Y (eds) Biomechanics of Diarthrodial Joints II. Springer, New York

Orr TE, Beaupre GS, Carter DR, Schurman DJ (1990) Computer predictions of bone remodeling around porous-coated implants. J Arthroplast 5(3):191–200

Prendergast PJ (1997) Finite element models in tissue mechanics and orthopaedic implant design. Clin Biomech (Bristol, Avon) 12(6):343–366

Sadegh AM, Luo GM, Cowin SC (1993) Bone ingrowth: an application of the boundary element method to bone remodeling at the implant interface. J Biomech 26(2):167–182

Stanford CM, Brand RA (1999) Toward an understanding of implant occlusion and strain adaptive bone modeling and remodeling. J Prosthet Dent 81(5):553–561

Tomita K, Kawahara N, Baba H, Tsuchiya H, Fujita T, Toribatake Y (1997) Total en bloc spondylectomy. A new surgical technique for primary malignant vertebral tumors. Spine (Phila Pa 1976) 22(3):324–333

Tsubota K, Adachi T, Tomita Y (2003) Effects of a fixation screw on trabecular structural changes in a vertebral body predicted by remodeling simulation. Ann Biomed Eng 31(6):733–740. https://doi.org/10.1114/1.1574028

Vaccaro AR, Garfin SR (1995) Internal fixation (pedicle screw fixation) for fusions of the lumbar spine. Spine (Phila Pa 1976) 20(24 Suppl):157S–165S

van Rietbergen B, Huiskes R, Weinans H, Sumner DR, Turner TM, Galante JO (1993) ESB Research Award 1992. The mechanism of bone remodeling and resorption around press-fitted THA stems. J Biomech 26(4–5):369–382

van Rietbergen B, Weinans H, Huiskes R, Odgaard A (1995) A new method to determine trabecular bone elastic properties and loading using micromechanical finite-element models. J Biomech 28(1):69–81

van Rietbergen B, Majumdar S, Pistoia W, Newitt DC, Kothari M, Laib A, Ruegsegger P (1998) Assessment of cancellous bone mechanical properties from micro-FE models based on micro-CT, pQCT and MR images. Technol Health Care 6(5–6):413–420

Zankl M, Wittmann A (2001) The adult male voxel model "golem" segmented from whole-body CT patient data. Radiat Environ Biophys 40(2):153–162

Zioupos P, Smith CW, An YH (1999) Factors affecting mechanical properties of bone. In: An H, Draughn RA (eds) Mechanical testing of bone and the bone-implant Interface. CRC, Boca Raton

Index

Y. Kameo et al., *Bone Adaptation*, Frontiers of Biomechanics 2,
https://doi.org/10.1007/978-4-431-56514-7